The Effects of Energetic Particles on Radiative Transfer and Emission from Hydrogen in Solar Flares

M K Druett

PhD

2017

The Effects of Energetic Particles on Radiative Transfer and Emission from Hydrogen in Solar Flares

Malcolm Keith Druett

A thesis submitted in fulfilment of the requirements of the
University of Northumbria at Newcastle
for the degree of
Doctor of Philosophy

Research undertaken in the Faculty of Engineering and Environment

November 2017

Abstract

The Effects of Energetic Particles on Radiative Transfer and Emission from Hydrogen in Solar Flares

by Malcolm Keith DRUETT

There are rapid increases of hard and soft X-rays (HXR, SXR) and ultraviolet (UV) emission with large Doppler blue-shifts associated with plasma up-flows observed at flare onsets accompanied by broadened chromospheric emission with large red-shifts. Hα shows red-shifts of 1–4 Å in the impulsive phase of solar flares observed with various past (Ichimoto and Kurokawa, 1984; Wuelser and Marti, 1989) and current (the Swedish Solar Telescope, SST) instruments (Druett et al., 2017). HXR footpoints are observed to be co-temporal and co-spatial with increases in white light (WL) and continuous emission during the impulsive phase. These effects point to fast, effective sources of excitation and ionisation of hydrogen atoms in flaring atmospheres associated with HXR emission. Most current radiative hydrodynamic models can account for SXR and UV emission, but fail to explain correctly the strongly red-shifted Hα line emission occurring at the flare onsets or the locations of the white light sources, and offer little explanation of the origin of seismic sources in flaring event.

We investigate electron beams as the agents accounting for the observed hydrogen line and continuum emission by considering a 1D hydrodynamic response of the quiet Sun chromosphere to injection of an electron beam and its conversion into a flaring atmosphere with its own kinetic temperatures, densities and macro-velocities (Zharkova and Zharkov, 2007). A radiative response in these atmospheres is simulated using a fully non-local thermodynamic equilibrium (NLTE) approach for a 5 levels plus continuum hydrogen atom model. Simultaneous steady state and integral radiative transfer equations in all optically thick transitions (Lyman and Balmer series) are solved iteratively for all the transitions to define their source functions with the relative accuracy of 10^{-5}. The solutions of the radiative transfer equations were found using the L2 approximation. Resulting intensities of hydrogen line and continuum emission are calculated for Lyman, Balmer and Paschen series.

The hydrodynamic model is shown to account closely for the timing and magnitude of upward motion to the corona observed in 171Å by the Atmospheric Imaging Assembly/Solar Dynamics Observatory for C1.5 flaring event onset, published in Nature communications (Druett et al., 2017), and suggests that both red and blue Doppler-shifts should be observed in the hydrogen Lyα line (in prep). Inelastic collisions with beam electrons are shown to strongly increase excitation and ionisation of hydrogen atoms at all depths from the chromosphere to photosphere. This leads to an increase in Lyman continuum radiation, which governs the hydrogen ionisation and leads to strong enhancement of emission in Balmer and Paschen continua. The contribution functions for Paschen continuum emission indicate a close correlation of the emission induced by electron beams with the observations of heights of WL and HXR emission reported for limb flares, (Druett and Zharkova, 2018) unlike other published simulations. This process also leads to a strong increase of wing emission (Stark's wings) in Balmer and Paschen lines combined with large red-shifted enhancements of Hα line emission resulting from a downward motion by hydrodynamic shocks. In contrast to other existing simulations, our work reproduces very closely the observed Hα line profiles with large red-shifts in a C1.5 flare by the Swedish Solar Telescope (Druett et al., 2017), the large red-shifts previously observed (Ichimoto and Kurokawa, 1984; Zarro et al., 1988; Wuelser and Marti, 1989) and explains dimming of Hα emission at flare onsets if observed with narrow spectral windows of 2-3Å.

The hydrodynamic models are able to account for the delivery of momentum below the photosphere in the hydrodynamic shocks that result form the beam injection. The supersonic velocities and heights of these shocks can be used to predict a seismic response (in prep), and a method is proposed for detecting the propagation of hydrodynamic shocks that are capable of triggering a seismic response (Druett and Zharkova, 2018).

Contents

"Music, poured out
In silence, sequenced
Note by note -

Bent light, splayed,
Graceful, continuous
As a movie, sliced up

Frame by frame
It radiates
From hot to cool

Each hungry element
Steals from it,
Precise as a scale. "

Katrina Porteous

Acknowledgements

First and foremost I must thank my supervisor, Professor Valentina Zharkova, for her expertise and tireless input without which this PhD would simply not have been possible. *Moreover*, I must mention the scale of academic input she has provided through the vast wealth of her previous and ongoing work on solar flares, and through her guidance on every aspect of our research during the PhD. This work represents my proudest academic achievement, your guidance has been a huge part of bringing that about. I will always be grateful to you, and indebted to you for this.

I also acknowledge my second supervisor, Professor James McLaughlin, for his sage professional advice and guidance, as well as for his support and motivation during difficult times. It has been particularly gratifying to see you achieve the richly deserved and outstanding academic success that you have whilst I have been at Northumbria university.

Doctor Eamon Scullion also stands out as deserving particular thanks. His excellent input to our research as a collaborator has greatly enhanced the quality of the work. You have provided me huge insight into solar flares, as well as valued friendship.

I must also note the outstanding work of my colleagues in the Northumbria University Solar Physics Group and also my collaborators in other institutions: Doctor Sarah Matthews, Doctor Sergei Zharkov, Professor Luc Rouppe van der Voort, and (soon-to-be Doctor) Connor Macrae.

The Solar Physics PGR group at Northumbria university provided a highly enjoyable and productive platform for the completion of this work, and for friendships that will endure beyond: André (7-1) Chicrala, Rytis (sea kelp) Dobranskis, (Ber)Linh Le Phuong, Krishna (Captain Bailout) Mooroogen, Tom Rees-Crockford (whoever that is), Autumn (card only) Rolling, Doctor Ben BJ Snow, and Ajay ('Murica) Tiwari, ably supported by additional visitors. From other parts of the university: Adam (build tall) Bridgewater, Mehrnoush (animal lover) Mokhtarimehr, Rick (and) Morton, Paras (prickly pear) Patel, Doctor Neoh Siew Chin, Doctor Paul (fruit dealer) Worawut. Doctor Ben BJ Snow must receive additional acknowledgement for his advice on academic, programming, and word processing matters.

I would like to thank Northumbria University and its staff for their funding and support, and for offering me the chance to conduct this research.

I would also like to thank my examiners for their effort in assessing this work: Professor Toby Arber, Doctor Sergiy Shelyag, and Professor Nicola Adams.

I acknowledge IDL support provided by STFC.

I am grateful to the staff of the SST for their invaluable support with the observations. The Swedish 1-m Solar Telescope is operated on the island of La Palma by the Institute for Solar Physics at Stockholm University in the Spanish Observatorio del Roque de los Muchachos of the Instituto de Astrofísica de Canarias.

On a personal note, thank you to the many friends whose belief in my capacity and support has greatly aided the completion of this course; Derek, Munzar, Sibyl and Tim to name a few. Meriel, thank you for all of your support and help, and for tolerating the constant teasing that I count as affection. I hope you know how grateful I am, and how happy you make me. I also thank your family for their support and intrigue in my work, but more importantly for the welcoming hearts they have shown. Finally, in so many ways I am more grateful than I am able to adequately express for the lifelong love and support of my family: my parents, Jim and Jane, and my sister, Heather, and her family.

Declaration of Authorship

I, Malcolm Keith DRUETT, declare that this thesis titled, "The Effects of Energetic Particles on Radiative Transfer and Emission from Hydrogen in Solar Flares" and the work presented in it are my own. I confirm that:

- This work was done wholly in candidature for a research degree at Northumbria University.
- The work contained in this thesis has not been submitted for any other award.
- Where I have consulted the published work of others, this is always clearly attributed.
- Where I have quoted from the work of others, the source is always given. With the exception of such quotations, this thesis is entirely my own work.
- I have acknowledged all main sources of help.
- Where the thesis is based on work done by myself jointly with others, I have made clear exactly what was done by others and what I have contributed myself.
- I have indicated instances in the text where the material is associated with a paper that has been submitted for publication in a peer reviewed journal.
- Ethical clearance for the research presented in this thesis has been approved.
- **The word count of this thesis is 45,000 words.**

Signed:

_____

Date:

_____

Chapter 1

Introduction to solar flares

1.1 Observations of solar flares

Flares are spectacular events of enhanced emission in a wide range of the electromagnetic spectrum (Fig 1.1) including hard X-rays (HXR) (Chubb et al., 1957; Warwick and Zirin, 1957; Winckler, 1964; Kontar et al., 2011) and γ-rays (Chupp et al., 1973; Vilmer, MacKinnon, and Hurford, 2011), soft X-rays (SXR) (Acton et al., 1963; Teske, 1967; van Allen, 1967; Meekins et al., 1970; Culhane et al., 1992; Sylwester and Sylwester, 1999; Tomczak and Ciborski, 2007) and ultra-violet (UV) radiation (Fletcher et al., 2011; Liu et al., 2015; Battaglia et al., 2015; Brosius, Daw, and Inglis, 2016), optical (Fletcher et al., 2011) and radio (Smith et al., 2011) emission.

Reid, 1963 suggested classifying solar flares by their *importance class*, which involved a number of different parameters in its calculation. There were also attempts to classify flares by their behaviours (Svestka, 1986; Bai and Sturrock, 1989). Nowadays solar flares are generally classified according to the peak flux in the GOES (Geostationary Operational Environmental Satellite) SXR light-curve in the 1-8Å wavelength channel (see Fig.1.2, top panel,) as per Table 1.1, with the fluxes measured at the orbital distance of the Earth, by GOES. 1-8Å wavelength photons correspond to energies from 1.5 to 12 keV.

Solar flares often show the division into three phases as outlined in Kane, 1974 (See Fig.1.1):

(1) Firstly, some flares have a precursor phase of 10 minutes or so, showing a slow increase in low energy X-rays and EUV radiation.

TABLE 1.1: GOES flare classification system.

Classification	Peak Flux, W·m^2
A	$<10^{-7}$
B	10^{-7}-10^{-6}
C	10^{-6}-10^{-5}
M	10^{-5}-10^{-4}
X	$>10^{-4}$

(2) Then there is an impulsive phase over the course of around one hundred seconds, with a rapid increase of emission in all wavelengths, which may include several maxima or peaks, followed by a swift reduction of emission in some channels (microwaves, EUV and X-rays).
(3) Finally, there is a gradual phase with a slowly increasing flux in optical line emission (see Hα light-curve in Fig.1.1), EUV and low energy X-rays to a maximum, followed by a slow decay phase of over 10 minutes as radiation levels decrease back to pre-flare levels.

Solar flares occur in active regions of the Sun, where magnetic flux emerges, and groups of magnetic field lines form loops through the whole solar atmosphere, extending them into the corona (See Li et al., 2017 Fig. 1.2). We will now take a closer look at the emission from solar flares (shown in Fig.1.1), beginning with the high energy, HXR emission.

1.1.1 Hard X-rays (HXR)

In 1957 Chubb et al., 1957 and Warwick and Zirin, 1957 reported the detection of X-ray emissions during solar flares using rocket observations, confirming the presence of electron beams in these events. Over the next decade a large number of studies attempted to better observe and understand this emission (Anderson and Winckler, 1962; Winckler, 1964; Moreton, 1964; Arnoldy, Kane, and Winckler, 1968; Holt and Cline, 1968; Neupert, 1968; Holt and Ramaty, 1969; Zirin et al., 1969; Zirin and Lackner, 1969), for example the correlations with other emission, e.g. the Neupert Effect: that the gradient of the SXR signature is well correlated with the HXR emission (Neupert, 1968). HXR emission during the impulsive bursts of solar flares proved difficult to detect over thermal background sources at first (Kahler and Kreplin, 1971;

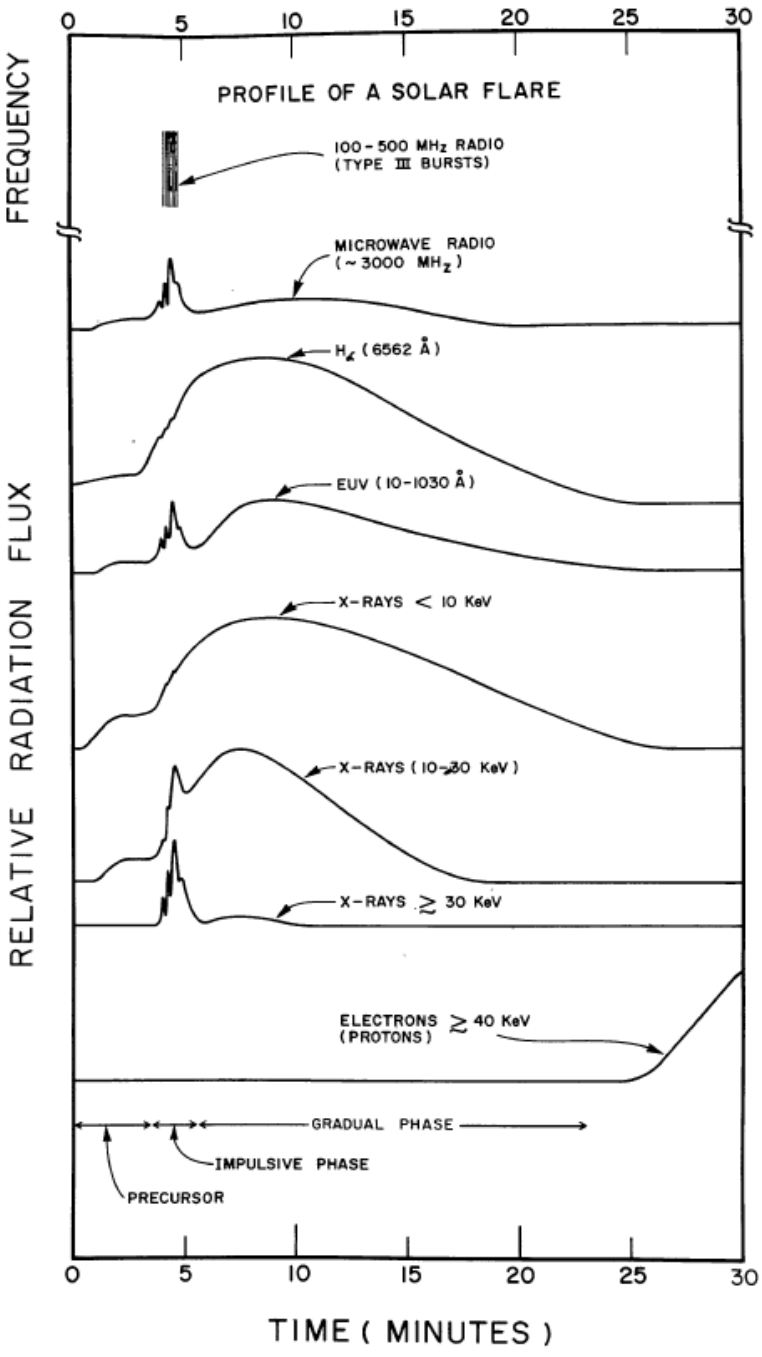

FIGURE 1.1: A schematic representation outlining the precursor, impulsive, and gradual phases of a solar flare. Shown in different parts of the electromagnetic spectrum, taken from Kane, 1974.

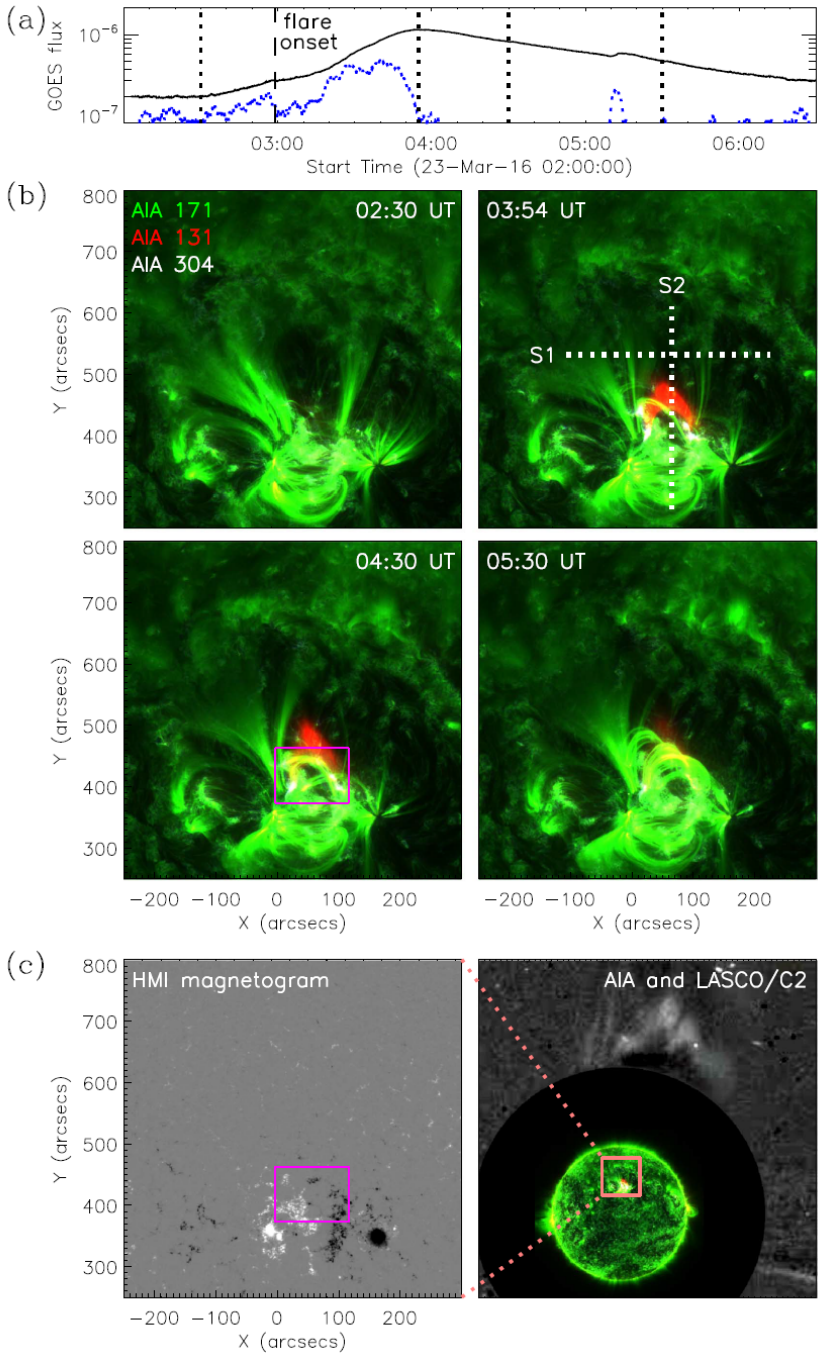

FIGURE 1.2: SXR flux and magnetic structure in a solar flare. The soft X-ray flux over the course of a solar flare in the range 1-8Å (black line) and its time derivative (blue line) (a) with magnetic field loops extending into the corona which are visible in the AIA 171Å and AIA 131Å channels (b), and the location of a flare in an active region in a region (c), taken from Li et al., 2017.

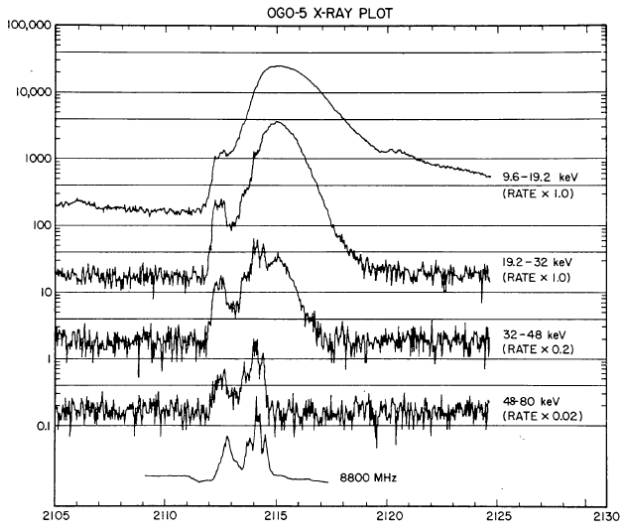

FIGURE 1.3: The timings of the HXR fluxes in the different energy channels, from Zirin, Pruss, and Vorpahl, 1971. Their signal is particularly correlated with the impulsive phase of a solar flare in the high energy channels ($\geq$ 32keV) and the radio emission (8800 MHz), and with the gradual, thermal phase of a flare in the lower energy channels ($\leq$ 32keV).

Peterson, Datlowe, and McKenzie, 1973), as reported in the review paper by Kane, 1974. Nevertheless the findings of these authors propelled missions to move from balloon based observations to satellite observations using the OSO, Yohkoh and RHESSI missions.

Spatially integrated HXR light curves in solar flares reveal many strong impulses throughout the active region (named elementary flare bursts by van Beek, de Feiter, and de Jager, 1974), with durations from fractions of a second up to ten seconds. Observations made with OSO revealed these sharp rises and falls of emission during the impulsive phase, across HXR energy bands from a few keV up to several hundred keV in more powerful flares (Parks and Winckler, 1969, Frost, 1969,Zirin, Pruss, and Vorpahl, 1971 see Fig.1.3, Kane, 1974 see Fig.1.1). After the impulsive phase there is a slow, stronger enhancement leading up to, and decaying from a maximum in the lower energy channels over the course of tens of minutes (Zirin, Pruss, and Vorpahl, 1971 see Fig.1.3, Kane, 1974 see Fig.1.1, Holman et al., 2011).

Winckler, 1964 reported the energetic spectra of HXR in solar flares, finding that they were distributed in energy E with approximately negative power laws, $f(E) \propto E^{-\gamma}$, which varied somewhat over the course of the flare, and from flare to

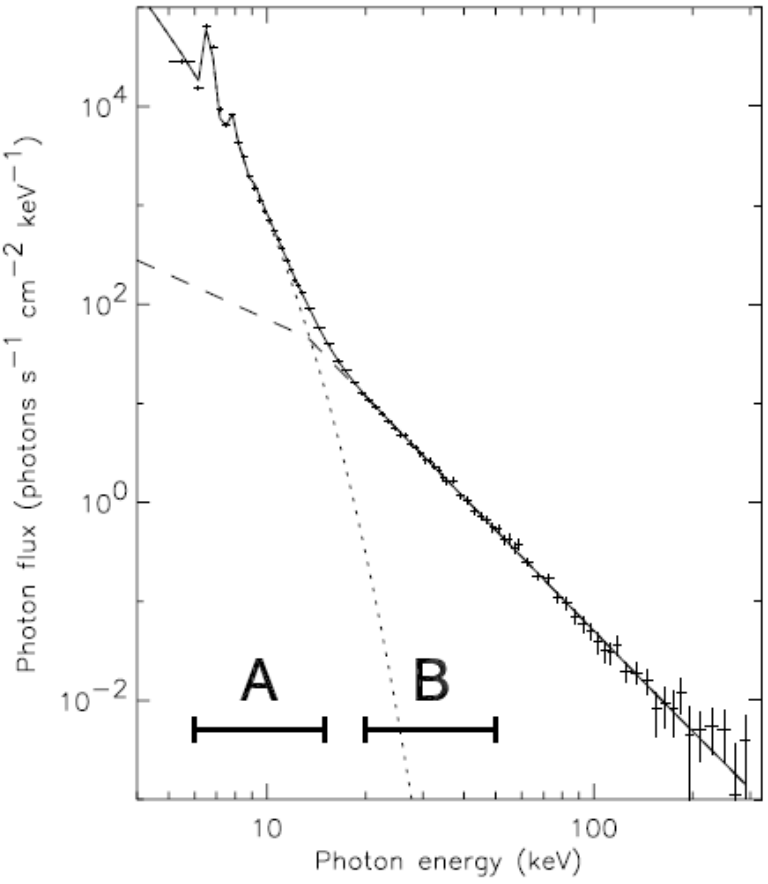

FIGURE 1.4: A RHESSI HXR photon energy spectrum during a solar flare with thermal and power law components (Grigis and Benz, 2004). The thermal component is seen below about 10keV and the non-thermal tail above 20keV

flare. Subsequent investigations have revealed that HXR photon energy spectra in solar flares comprise of thermal emission at low energies (Generally $E < 10$ keV, see Fig.1.4) from plasma with temperatures in the 10^6 K range, and high energy HXR emission with a power-law distribution (Piana et al., 2003; Grigis and Benz, 2004; Holman et al., 2011) from non-thermal sources. The non-thermal tail can reach up to hundreds of keV (Kuznetzov et al., 2006) with spectral indices, γ, between around 3 and 9.

The timing of the peak emission in different energetic channels was studied in detail using data from RHESSI. It was shown that peak emission in the higher energy channels occurred earlier after a flare onset than the peak in the low energy channels (Kontar and MacKinnon, 2005) (See Fig.1.5). Aschwanden, 2007 added detail to this, showing that the signals in higher energy RHESSI channels peaked

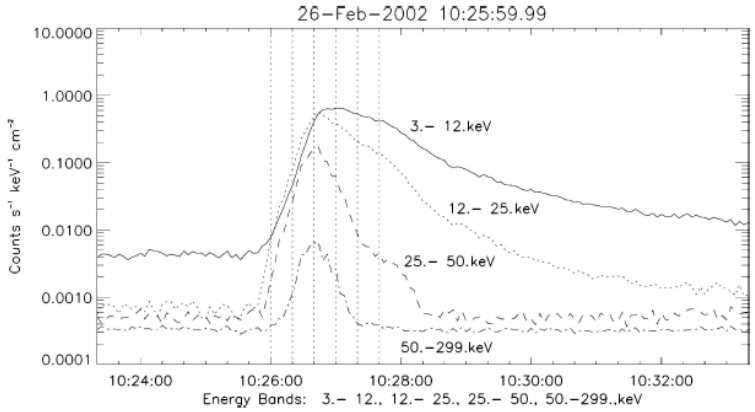

FIGURE 1.5: The temporal profiles of the HXR photon flux in different channels, from Kontar and MacKinnon, 2005.

earlier, and also confirming this fact holds when contributions are decomposed into thermal and non-thermal contributions (Aschwanden, 2007, see Fig.1.6). These findings were later confirmed by Fokker Planck modelling of electron precipitation by Siversky and Zharkova, 2009.

Lin and Schwartz, 1987 observed a flare in which the HXR photon spectrum appeared to show a double power law behaviour (see Fig.1.7), with a switch between gradients happening above a particular break energy, E_B. Later, this behaviour was observed in a number of other flares using RHESSI data, obtaining break energies of between 10 and 30 keV (see Fig.1.8) (Holman et al., 2003; Sui, Holman, and Dennis, 2007).

Balloon-based observations with hard X-ray spectrometers were the first to reveal the HXR photon spectrum varied in time from soft (high) to hard (low) and back to soft (SHS) (Parks and Winckler, 1969; McKenzie, Datlowe, and Peterson, 1973), obtaining a minimum value around the peak of the event. Data from the solar maximum mission confirmed these observations (Benz, 1977; Brown and Loran, 1985). The SHS behaviour of the spectral index of HXR photon spectra is illustrated for four different flares in the panels of Fig.1.9 (Grigis and Benz, 2004). In this figure one can see that the spectral index (thin line) hardens co-temporally with peaks in the non-thermal HXR flux (thick lines) and softens when the flux decreases. Observations with instruments such as RHESSI (Fletcher and Hudson, 2002; Hudson and Fárník, 2002; Grigis and Benz, 2008) revealed that this relationship also generally

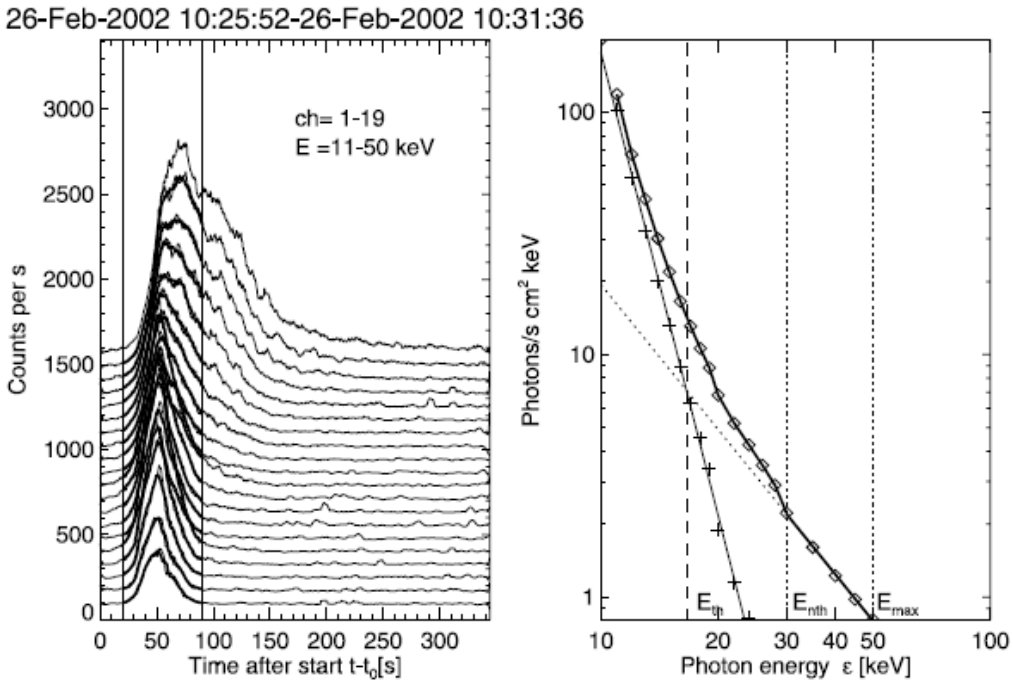

FIGURE 1.6: The X-ray time profiles in 20 energy channels. Shown from 10 to 50 keV from top to bottom (left panel), peaking at later times in the lower energy channels. In the right panel we see the total flux spectrum for time interval for the time interval selected by the vertical bars in the left panel, showing the thermal contributions (crosses), non-thermal contributions (dashes), and the total (boxes) (Aschwanden, 2007).

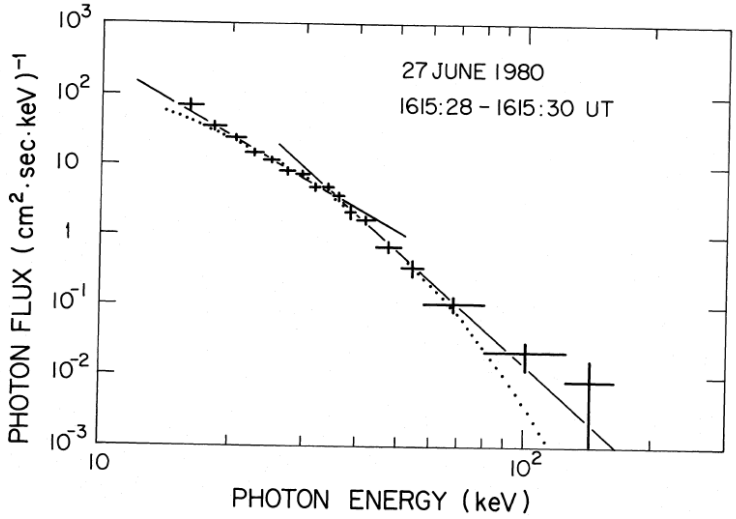

FIGURE 1.7: The double power law photon energy spectrum during a solar flare (crosses). Shown alongside the double power-law (solid lines) and isothermal (dotted curve) model fits from Lin and Schwartz, 1987.

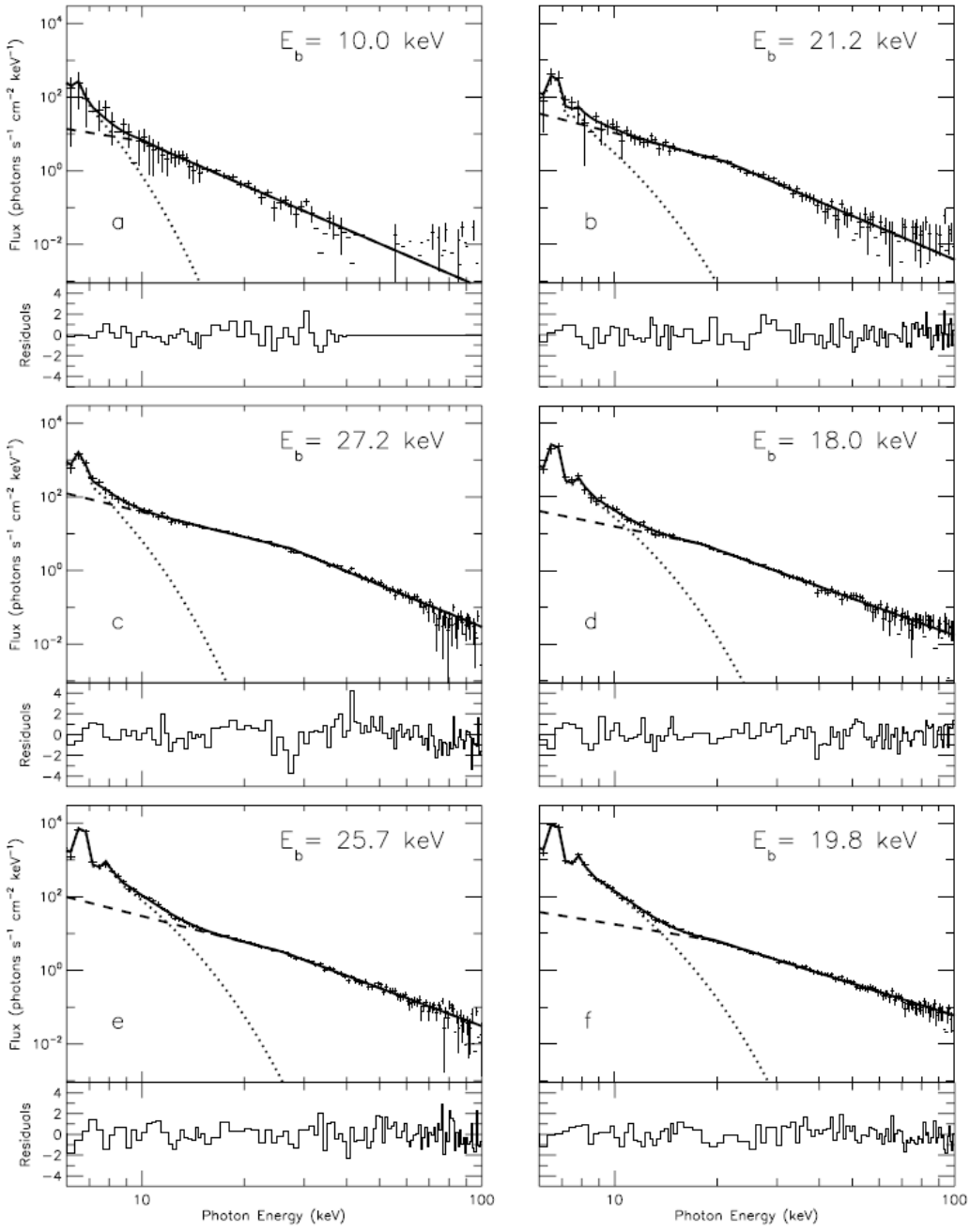

FIGURE 1.8: The break energies, E_b, for double power law photon energy spectrum during solar flares, from Sui, Holman, and Dennis, 2007. Residuals for the regression of the data onto the models are shown. Small, random, unsystematic variation in these residuals indicates a good agreement between the model fitting and the data.

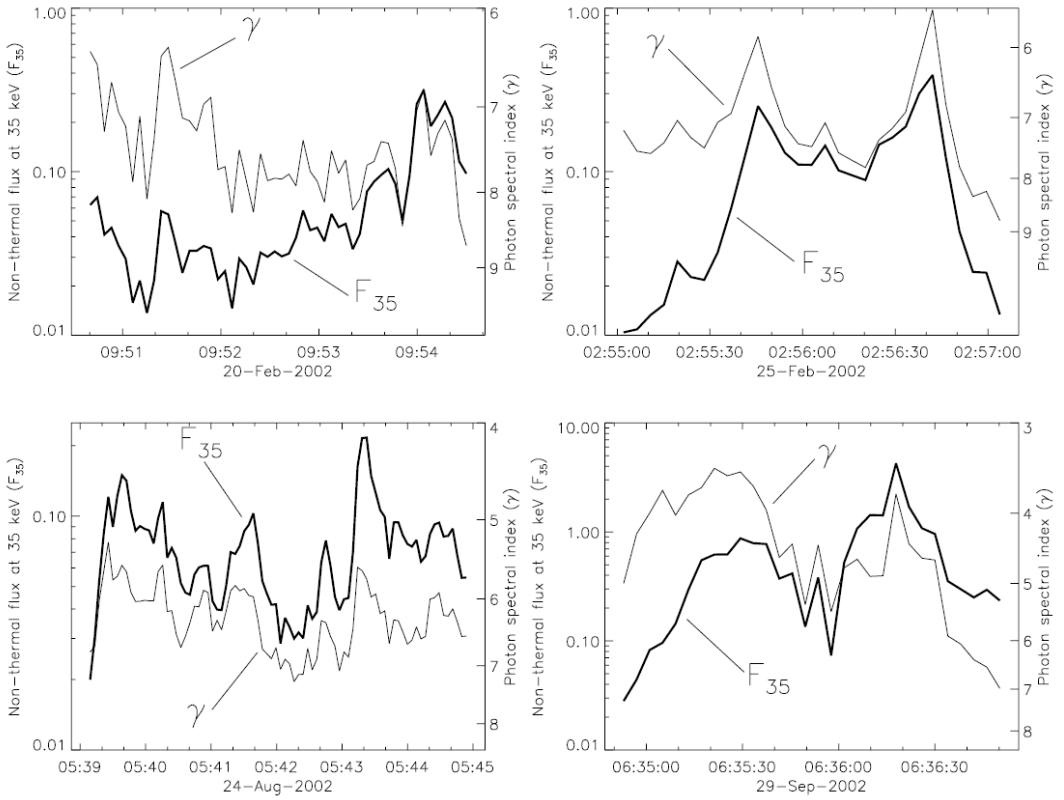

FIGURE 1.9: The time evolution of the photon spectral index (γ, thin line) and the non-thermal flux at 35keV (F_{35}, thick line). Shown for 4 flares (Grigis and Benz, 2004).

holds for the local spectral index in individual flare bursts.

Direct measurements of the location and size of the impulsive HXR bursts are difficult because of the high time-resolution required to provide the necessary context for results. This remains an issue to the current day, with the best angular resolution RHESSI imaging can provide on the order of 2" (1440×1400 km), and only in the case of low photon energies. However HXR sources have been shown to originate both in coronal loop structures and at the flare foot-points (Krucker et al., 2008, see Fig.1.10, Fletcher et al., 2011). Jin and Ding, 2008 observed three HXR sources during an X7.1-class flare, two sources were located in foot-points where chromospheric brightenings were located, but there was also an overlying loop-like structure that emitted in the 25-50keV range. The coronal HXR source, although sometimes reported to appear before the foot-point signatures, is generally well correlated with the foot-point signatures in time and evolution, suggesting a strong coupling between these regions during the flare.

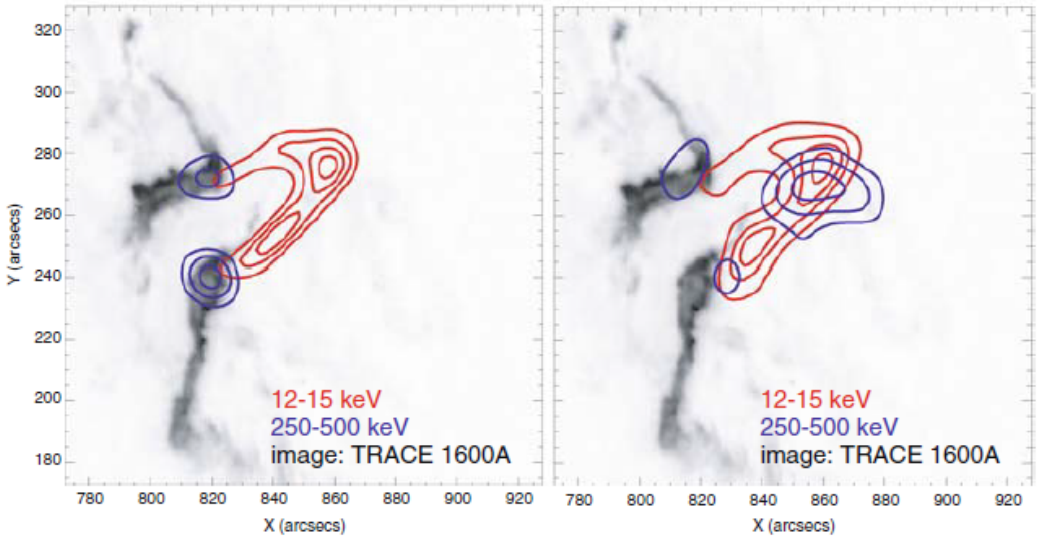

FIGURE 1.10: X-ray sources in a coronal loop. Low energy HXR sources (12-15keV) can be seen in the loop sources of both panels, and the higher energy emission (250-500 keV) are located in the foot-point HXR sources, co-spatial with the foot-point brightenings (Krucker et al., 2008).

The co-temporal HXR photon spectra in the different foot-point sources often have very similar spectral indices, but both these are usually more noticeably different from the loop source. Emslie reported the foot-point spectral index differences to be up to 0.3-0.4 (Emslie et al., 2003), and Battaglia and Benz found that the differences in foot-point spectral indices were only significant in 1 of 5 cases studied, although both differed significantly from the form of the spectral index in the coronal loop source (Battaglia and Benz, 2006, see Fig.1.11 from Holman et al., 2011 based on Battaglia and Benz, 2006).

Recently, the co-alignment and higher spatio-temporal cadence of modern instruments has allowed investigation of the heights of HXR source using limb flares (Battaglia and Kontar, 2011; Martínez Oliveros et al., 2012; Krucker et al., 2015). It was found that the higher energy HXR sources are present near the quiet Sun photospheric heights, with lower energy, thermal sources dominating in the overlying loop structures (Figs.1.12 & 1.13).

In the impulsive phase HXR foot-point sources have been shown to correspond in time with area increases in Hα emission (Zirin et al., 1969; Vorpahl and Zirin, 1970; Zirin, Pruss, and Vorpahl, 1971). Jin and Ding, 2008 observed three HXR

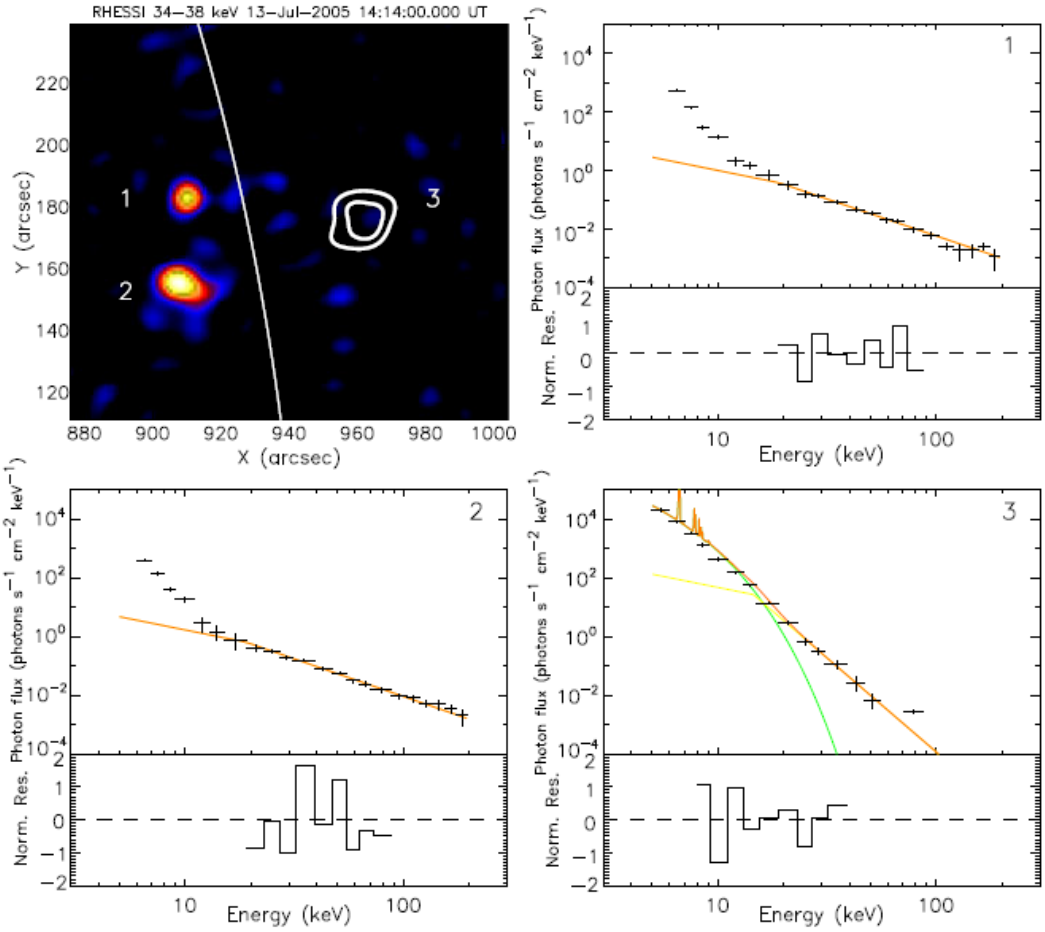

FIGURE 1.11: The CLEAN image of a RHESSI event (top left). The HXR photon energy spectra in the foot-point sources (upper right and lower left panels) are seen to have similar fluxes and show power-law non-thermal emission tails at high energies (> 10keV), unlike the loop-top energy spectrum (Bottom right panel). Taken from Holman et al., 2011, based on the work of Battaglia and Benz, 2006.

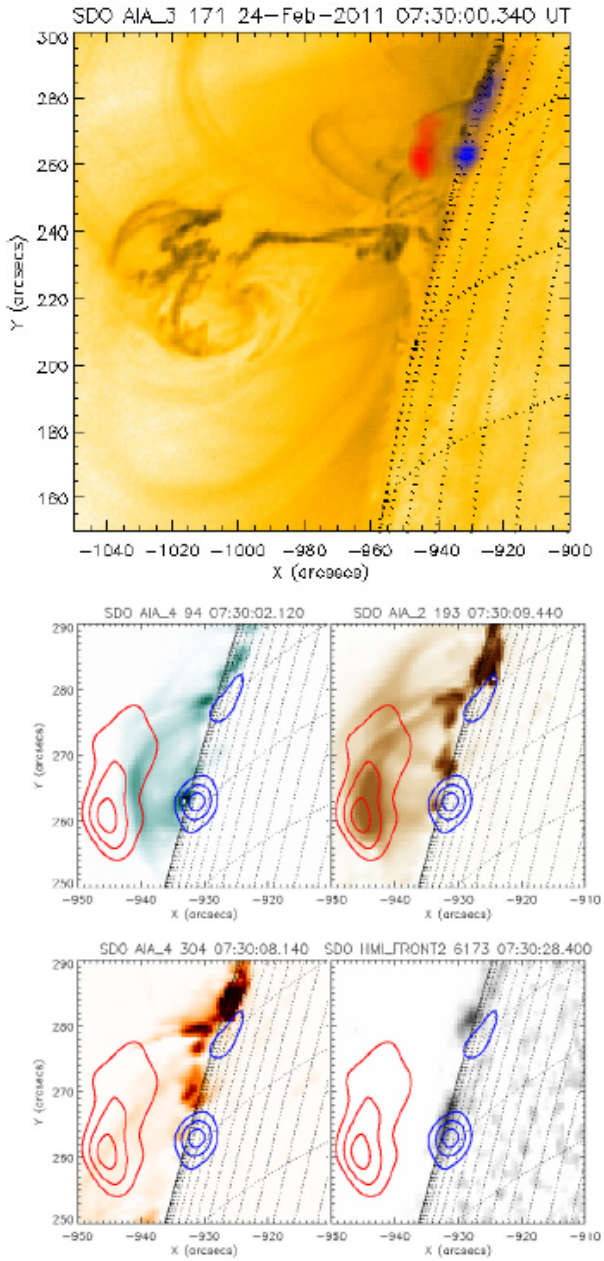

FIGURE 1.12: A RHESSI image showing the location of the HXR sources in the flare foot-points (25-50 keV, blue contours) and SXR sources from coronal temperature plasma in the loop (6-12 keV, red contours), from Battaglia and Kontar, 2011. The top panel shows a context view with RHESSI sources overlaid on the AIA 171Å channel image, and the lower panels show zoomed views at different times of the observed flare.

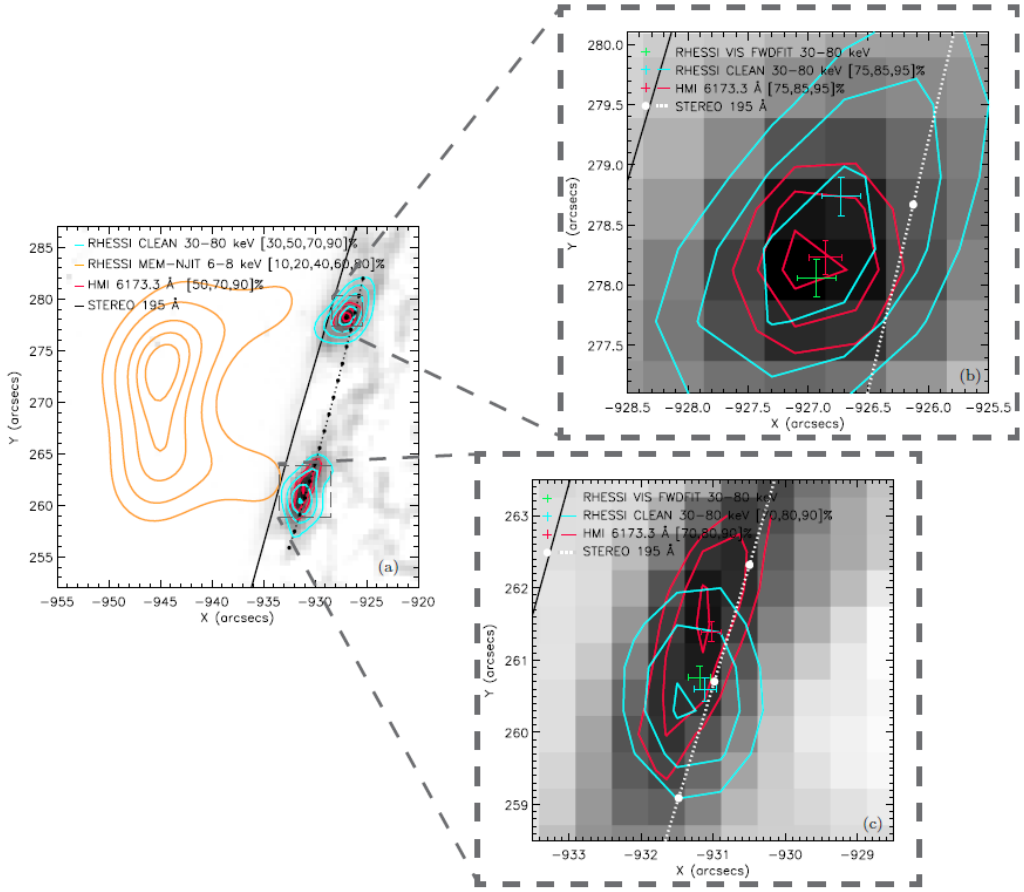

FIGURE 1.13: HMI and RHESSI images overlaid in a solar flare. The HMI intensity continuum difference images (pixelated background images), overlaid with the HXR foot-point sources shown by the RHESSI CLEAN images (blue contours) which are seen to be co-spatial with the WL HMI sources (red contours) in the impulsive phase of a solar flare(Martínez Oliveros et al., 2012). The left panel shows a zoomed-out context image, with the SXR loop source (RHESSI 6-8 keV channel) indicated by the orange contours.

sources during an X7.1-class flare, two sources were located in foot-points where chromospheric brightenings were located, with an additional, overlying loop-like structure that emitted in the 25-50 keV range. Martínez Oliveros et al., 2012 reported foot-point HXR sources of emission at heights that were co-spatial with white light signatures (Fig.1.13).

1.1.2 Soft X-rays (SXR)

Kreplin, Chubb, and Friedmann, 1962 and Donnelly, 1967 reported that the maximum in SXR flux in the wavelength range 1-10Å tends to occur on the scale of minutes after the maximum in the impulsive HXR bursts, associating the signal peak with the gradual phase of the flare (Kane, 1974). Kane and Donnelly, 1971; Zirin, Pruss, and Vorpahl, 1971 noted that lower energy X-ray signals observed in solar flares tend to last longer than the higher energy signals, with thermal emission profiles that occur alongside bright Hα ribbons, after the higher energy HXR and radio bursts have returned to background levels.

Neupert, 1968 reported that the temporal derivative of the HXR signature in solar flares follows the temporal profiles of the SXR emission, this became known as the Neupert effect. Neupert, Thomas, and Chapman, 1974 found that the SXR lightcurve could not be accounted for by models which heated only coronal material through flare mechanisms. They and other authors (e.g. Kane, 1974) pointed out that the excellent temporal agreement of impulsive phase SXR burst radiation with rises in co-spatial Hα emission demanded heating of the chromospheric material by the agents responsible for the SXR. Pintér, 1970 explains this temporal agreement by highlighting that SXR flux experiences rapid growth that coincides with expansion of the flaring area in Hα line that occurs after the impulsive phase. This is compatible with the interpretation of Glencross, 1973, namely that these SXR profiles are produced as the result of a series of spatially separated X-ray source sites throughout the active region over the course of a flare, rather than as bulk emission from one region, which would be expected to produce a signature with the exponential decay during cooling, such as the signals observed at the end of the impulsive phases of flares. Thus, it was suggested that Hα energisation signatures could be used to identify these separate locations.

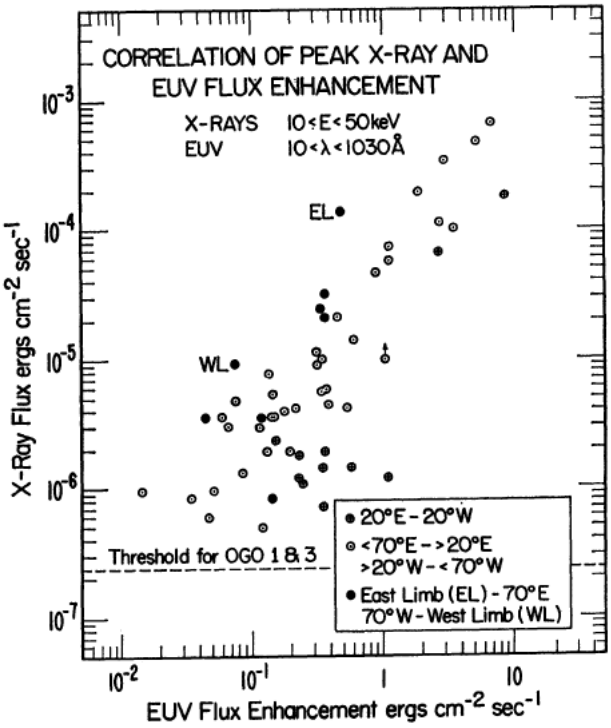

FIGURE 1.14: The correlation between peak values of HXR and EUV fluxes in a number of solar flares. Measurements are taken using the OGO-1 and OGO-3 satellites, from Kane and Donnelly, 1971. Flares observed near the disk centre are shown with shaded circles, those observed off-centre are shown using unshaded circles, and two limb flares are individually labelled.

1.1.3 Emission in the UV and EUV

Extreme ultraviolet (EUV) emission in solar flares (10-1030Å) was first measured directly by Donnelly, 1968. The time profile has impulsive and gradual phases with solar flare, and is confined to an altitude <10 Mm from surface (Kane, 1974). Emission in this band is from lines with temperatures between chromospheric ($T = 10^4$) and coronal ($T = 1.5 \times 10^6$) values. Emission increases more in transition region lines during flares than in coronal lines (Fig.1.1), and the line emission increase was observed to be proportional to the continuum emission increase in the EUV band (Fig.1.1) as well as positively correlated to the strength of the HXR energy flux in an impulsive burst (Kane and Donnelly, 1971, see Fig. 1.14).

UV radiation rises and falls with both impulsive and gradual phase (Fig.1.1). Mrozek, Tomczak, and Gburek, 2007, used TRACE and HXT observations to investigate the time difference between maxima of HXR and UV brightenings. This was

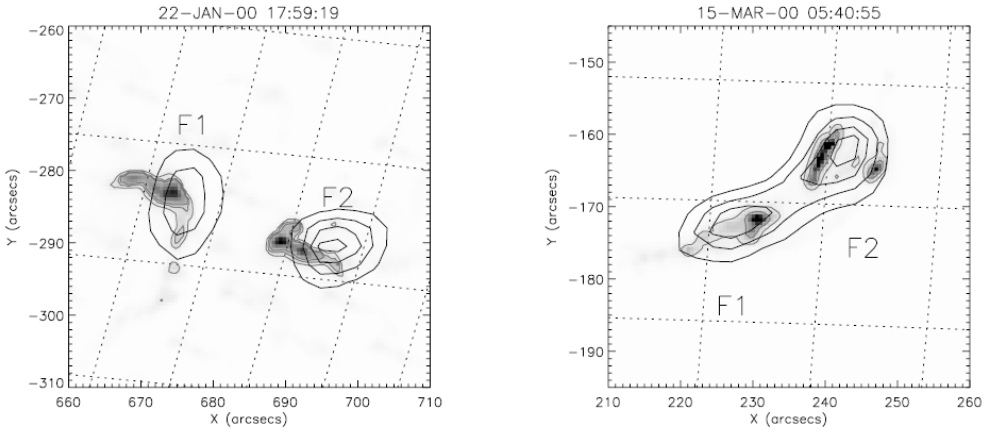

FIGURE 1.15: The HXR emission sources (black contours) in the two foot-points of different flares (left and right panels), from Mrozek, Tomczak, and Gburek, 2007. Co-temporal EUV emission sources are indicated by the grey contours. These are overlaid on the co-temporal full grey-scale UV emission images.

found to be <2 s, taken with 2 s cadence of images, and the signals were cospatial (Fig.1.15). Spatio-temporal correlations between the HXR sources and impulsive EUV and UV sources are frequently reported, showing a slightly stronger correspondence to the UV sources (compare Fig.1.15 a and b, see Fig.1.12), which are more cospatial with flaring foot-points in the optical emission. Mrozek, Tomczak, and Gburek, 2007 found the EUV AIA 171Å signal was delayed by 6 s compared to the maxima of HXR, and appeared slightly offset in images from the HXR foot-point sources.

Hot, coronal Iron lines (Fe XXI, Fe XXIII, Fe XXIV, Fe XXI) generally exhibit profiles with large blue Doppler-shifts during and after the impulsive phases of solar flares, with Doppler velocities of up to 250 km·s^{-1} (Mason et al., 1986; Polito et al., 2016; Polito et al., 2017). A recent example comes from Polito et al., 2016 in which the authors observed blue-shifted profiles in Fe XXI 1354Å emission, emerging from the flaring foot-point regions (3″-5″), and taken to represent 200 km·s^{-1} up-flows during a flare (Fig.1.16), with FeXXIII showing blue-shifts corresponding to Doppler velocities up to 226 km·s^{-1}.

Emission with larger blue-shifts is also recorded in coronal lines, in particular in observations from the Solar Maximum Mission which focussed on the higher temperature coronal lines. For example, upflows of over 350 km·s^{-1} were reported using

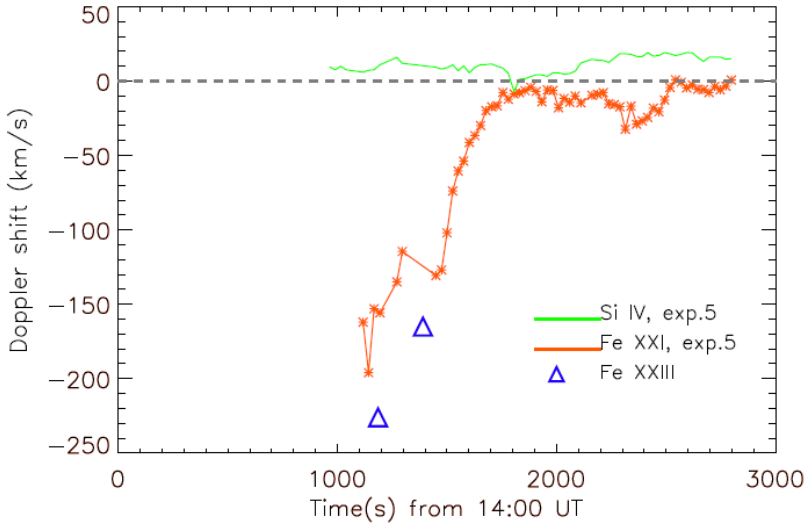

FIGURE 1.16: Blue Doppler-shifts seen in the UV lines (Fe XXI, orange line, and Fe XXIII, blue triangles) as functions of time, from Polito et al., 2016. This illustrates up-flows of hot plasma during and after the impulsive phase of a solar flare (1000 s). The blue-shifted lines observed can be contrasted with the chromospheric Si IV emission line (green line).

observations the Ca XIX line by Antonucci and Dennis, 1983 and 500 km·s^{-1} in Ca XIX, with 800 km·s^{-1} in the FeXXV spectra (Antonucci, Dodero, and Martin, 1990a; Antonucci, Dodero, and Martin, 1990b).

Advances in the observations of the hydrogen Lyman lines and continua are necessarily linked to the space-based missions capable of observing ultraviolet emission. In 1953, detection of the Lyman alpha (Lyα) line was reported in the Sun's spectrum from balloon and rocket missions (Pietenpol et al., 1953; Byram et al., 1953). Soon after, increases in Lyα intensity associated with solar flares (Hallam, 1964) were reported in observations using the OSO I satellite. The earliest qualitative description of Lyman line observations during solar flares was provided by Hall, 1971 using observations from OSO III. The authors reported enhancements of Lyα line emission as a percentage of the full-disk intensity that were similar to the percentages of the disk area covered by the flare areas, and derived a rise time of around 2.4 minutes and a decay time of around 4.4 minutes in the net emission intensity from the Sun.

In the 1970s, higher spatial resolution observations reported brightenings of Lyα in transient flare kernels, with great enhancement of the Lyman continuum and lines. These enhancements were associated with X-ray emission and surrounding

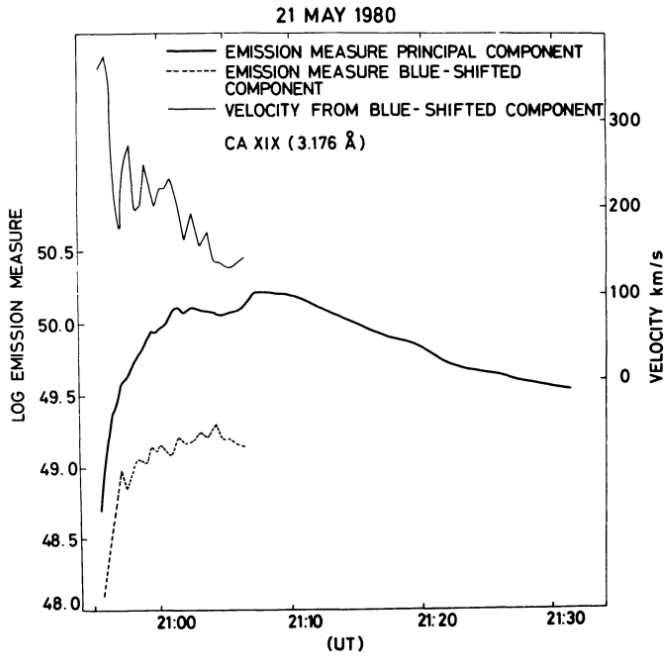

FIGURE 1.17: The evolution of the velocity and emission measure of highly Blue-shifted emission from coronal spectral lines during the impulsive phase of a solar flare, from Antonucci and Dennis, 1983.

Hα emission (Wood et al., 1972; Wood and Noyes, 1972; Křivsky and Kurochka, 1974; Machado and Noyes, 1978), with impulsive and gradual components of flare emission (Kelly and Rense, 1972).

Spectral information about the Lyα line became available in the 1980s. The first complete Lyα line flare spectra were published by Canfield and van Hoosier, 1980 from full disk observations of the Sun, and with low temporal cadence. The observed profiles show the line core with self-absorption, indicating a large optical opacity, throughout the flare and only slightly asymmetric wing intensities, with greater excess in the red wing before the flare maxima and greater excess in the blue wing after the flare maxima.

Lemaire, Choucq-Bruston, and Vial, 1984 reported simultaneous spectrographic observations of many chromospheric lines during a flare including Lyα and Lyβ from the OSO-8 satellite. The Lyα and Lyβ lines both show an impulsive peak, with increased wing emission at the same time as the increased intensity in the core Lemaire, Choucq-Bruston, and Vial, 1984. The rise time was around 60 s and the decay time from this peak was around 200 s.

The practice of using full-disk images of Lyman line profile observations has persisted to the present day (MEGS-B instrument of the Extreme ultraviolet Variability Experiment, EVE (Woods et al., 2012), on board the Solar Dynamics Observatory, SDO (Pesnell, Thompson, and Chamberlin, 2012)). Doppler velocities have been calculated from Ly$\beta - \epsilon$ emission during the impulsive phase of solar flares from full-disk spectral observations (Sun-as-a-star observations) (Brown, Fletcher, and Labrosse, 2016). Flow speeds varying from 10 km·s^{-1} to 60 km·s^{-1} were derived from the similar observations depending on the line-fitting technique used, and whether the full disk intensity profiles or the quiet Sun subtracted intensity profiles were used. The line emission in these observations is the net emission from a variety of solar features: impulsive flare kernels, bright ribbons, and the surrounding active region. Therefore, one can interpret the flow speeds stated in Brown, Fletcher, and Labrosse, 2016, as relating to the net active region emission and resulting from the techniques employed, rather than as indications of flow speeds in the flare foot-points.

Zirin, 1978; Canfield and van Hoosier, 1980; Canfield, Puetter, and Ricchiazzi, 1981 studied the ratio of the integrated intensities of hydrogen Lyα and Hα lines during solar flares. They found that the intensities of emission in these two lines were generally correlated and their ratio was approximately unity. The authors had anticipated a greater increase of Lyman line emission, relative to the Hα line. It was inferred from their observations that the weakness of the Lyα line is due to photon trapping as a result of high optical depth. Hence, the authors concluded that the relative stability of the ratio in emission from these lines is due to their joint roles in the cooling of the plasma.

Lyman alpha is is the brightest line in the UV spectrum, and the Lyman lines are highly optically thick. Therefore, understanding the emission and radiative transfer in the Lyman lines during solar flares is important to understanding the excitation of hydrogen atoms throughout the chromosphere. Moreover, Lyman continuum emission is also highly optically thick in the chromosphere, making it unique amongst the hydrogen continua. Thus, it is key to understanding continuous emission from hydrogen as well as the ionisation degree of the plasma.

In the late 1970s several hydrogen Lyman continuum spectra were reported by

Machado and Noyes, 1978. Sun-as-a-star continuum observations near the Lyman continuum head wavelength (910Å) using the SUMER (Solar Ultraviolet Emission of Emitted Radiation) on-board SOHO (SOlar and Heliospheric Observatory), show a relative signal increase of 70%. Accounting for the area of the flare region, the local increase of the radiance of the Lyman continuum is estimated to be a factor of several thousands, and this increase is sustained for a long time after the impulsive phase (Lemaire et al., 2004).

The Lyman series has been remarkably underused in studies of the solar atmosphere due to a lack of high resolution imaging and spectroscopic instruments available. This state may be remedied by the spate of recently proposed instruments including the Extreme Ultraviolet Imager (EUI) and the Multi-Element Telescope for Imaging and Spectroscopy (METIS) aboard the Solar Orbiter (SO), the Chromospheric Lyman-Alpha SpectroPolarimeter (CLASP), the Lyman Alpha Spicule Observatory (LASSO), and the Lyman-α Solar Telescope (LST) for the ASO-S mission (Li, 2016). Observations from this new generation of the instruments would provide high-resolution imaging of Lyman lines.

1.1.4 Emission in optical lines

In early spectroscopic analysis of the quiet Sun (QS) an obvious characteristic was the deep self-absorption profile of the visible red Hα line, 6562.8Å, resulting from transitions between principal quantum states 3 and 2 of neutral hydrogen atoms and originating from chromospheric temperatures in the range 10-30,000 K in the line core, but down towards the photospheric temperature minimum region in the optically thinner line wings.

This picture was enhanced by observations of what was termed the *Flash* phase, a period showing several peaks in emission occurring at the time of impulsive HXR signatures, with the greatly enhanced emission confined to only a small part of the Hα flaring region (Fig.1.18) (Dodson, Hedeman, and McMath, 1956; Harvey, 1971; Vorpahl, 1972). Flare Hα emission appears in the loops on both sides of the magnetic inversion line (MIL) (Zharkova et al., 2005) in ribbon formations in locations associated with the embedded foot-points of the loops associated with magnetically reconstructed loops.

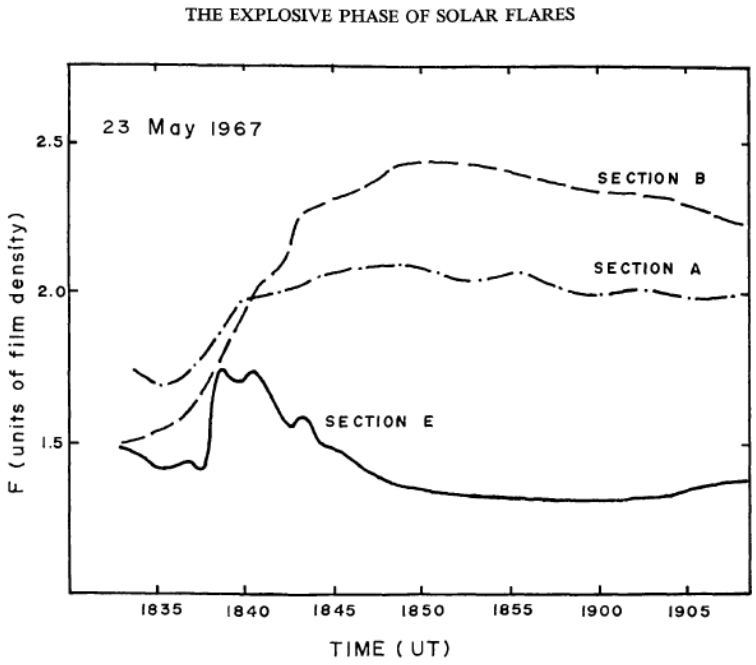

FIGURE 1.18: Time profiles of impulsive and non-impulsive Hα flare kernels. The time profiles of the flux in Hα from an impulsive flare kernel flux (section E, solid line) showing a non-thermal impulsive profile, peaking at the flare onset. Two profiles from general points in the flaring active region are also shown (sections A and B, dashed lines), with longer lasting thermal enhancements peaking in flux later in the flare (Harvey, 1971).

These developments characterised the form of Hα emission during a solar flare:

(1) An impulsive phase in the *flare kernels*. Flare kernels are small areas associated with HXR sources, activated before the HXR sources but showing sharp co-temporal rises in emission with spikes in the HXR channels. These small kernels are located low in the chromosphere, and their size is not related to the size of the total Hα flare, but do occur near steep magnetic gradients (See Fig.1.18 section E, Fig.1.1).

(2) The main flare signature, which is much longer in duration and produces greater emission over a greater area in Hα (See Fig.1.18, sections A and B).

Švestka, Kopecký, and Blaha, 1961; Švestka, Kopecký, and Blaha, 1962 used 92 flares observed using the Ondrejov Observatory to produce a survey of early Hα spectral observations. They found that the maximum flare asymmetry occurs before the flare maximum, around the impulsive phase. This asymmetry then reduces throughout the flare (See Švestka, Kopecký, and Blaha, 1962 Fig.1). They reported that 118 of 244 flaring regions showed Hα and calcium K emission with red asymmetry, 104 had symmetrical profiles and only 18 showed blue asymmetries. 80% of flares were found to display red wing enhancement and 23% of flares showing blue wing enhancement, and only 5% of flares showing only enhancement in the blue wing. They also found that flares with central enhancement of the Hα line, with emission integrated over the active region, also tended to show greater red asymmetry (see table 1.2 where '0' represents deep central reversal of the Hα line profile and '3' represents no central reversal).

Kane, 1974 reports that the impulsive increase in Hα is also associated with increase in line width, and Švestka, Kopecký, and Blaha, 1961; Švestka, Kopecký, and Blaha, 1962 pointed out in their survey that flares with greater Hα line widths were more asymmetric (see Fig.1.2) and that the flares occurring over the sunspot penumbra in general showed greater line width and asymmetry.

Over the next decades, more detailed spectral instruments were developed. By the 1980s, highly detailed spectral profiles of Hα observations in flares became available (Ichimoto and Kurokawa, 1984; Zarro et al., 1988; Wuelser and Marti, 1989; Canfield et al., 1990; Del Zanna, 2008; Milligan and Dennis, 2009; Graham and Cauzzi,

Central reversal scale	**Mean asymmetry**	**n**
3	+1.31	48
2	+0.79	14
1	+0.77	13
0	-1.12	8

TABLE 1.2: The mean asymmetry of flares compared to the central reversal of the Hα line, and the frequencies of each type of flare observed, from Švestka, Kopecký, and Blaha, 1962. Positive asymmetry relates to Hα profiles with greater emission the longer wavelengths (red wing) and negative relates to those showing greater emission in the shorter wavelengths (blue wing). The central reversal scale is greater for flares that have Hα profiles in emission and lower for those with profiles in absorption.

Hα line width scale (right) Asymmetry scale (below)	0	1	2	3	4	5-6
+3	0	0	24	**42**	**44**	**50**
+2	6	25	**57**	29	25	22
+1	16	44	10	10	19	17
+0	**78**	31	19	19	12	11
mean	0.28	0.94	1.67	1.95	2.00	2.11

TABLE 1.3: The relationship between the Hα line asymmetry and the line width for a large number of solar flare observations, from Švestka, Kopecký, and Blaha, 1962. The mean values in the bottom row show the mean asymmetry of each line width category.

2015). These observations were able to provide spectra at high cadence from light integrated over the flaring region, and showed large red Doppler-shifted profiles in Hα emission during the impulsive phases of solar flares (Ichimoto and Kurokawa, 1984 Fig.1.19, Zarro et al., 1988 Fig.1.20, Wuelser and Marti, 1989 Fig.1.21) or more symmetrical profiles in the cases of kernels with a pre-heated atmosphere (Wuelser and Marti, 1989 Fig.5).

With the advances of modern instrumentation at observatories such as the Big Bear Solar Observatory (BBSO), the Dunn Solar Telescope (DST), the Swedish 1-m solar telescope (SST), and the upcoming Daniel K Inoye Solar Telescope (DKIST) it has become feasible to observe more spatially resolved kernels in lines such as Hα (Rubio da Costa et al., 2016). A somewhat perplexing and confounding trend in the modern instrumentation has been towards narrower wavelength windows, around $\pm$1.5Å from the line central wavelength, which are thus unable to capture the full behaviour of the Hα line during flares reported from the 1990s and before. An example of this can be seen in Fig.1.22 (Sánchez-Andrade Nuño, Puschmann, and Kneer, 2007) with the Hα profiles truncated, particularly at 09:28:00, during the impulsive phase. Another example is shown in Fig.1.23, taken from Rubio da Costa et al., 2016, in which the truncated profiles are particularly evident in the impulsive kernel (purple line), and particularly at 17:46:13.

Of course, there are spectral lines from elements other than hydrogen which are formed in the chromosphere and transition region. A few of the more popular lines are included in Table 1.4. Zirin and Tanaka, 1973 concluded there was no real difference between calcium K and Hα responses. However, more modern instruments such as AIA aboard SDO, EIS aboard HINODE and IRIS have allowed authors to investigate the individual idiosyncrasies of each line in Table 1.4. This has enabled the analysis of the complex processes and dynamic conditions of different heights within the flaring chromosphere (Falchi and Mauas, 2002; Solov'ev, Kirichek, and Ganiev, 2013; Kerr et al., 2015; Simões et al., 2016; Zhang, Li, and Ning, 2016; Bamba et al., 2017). For example, the differing sensitivities of the He I 584Å and He II 304Å lines to electron beam heating can be used to diagnose beam heating rates in the chromosphere (Simões et al., 2016), or destabilisation of the foot-points of flare ribbons may be identified through the associated precursor brightenings showing

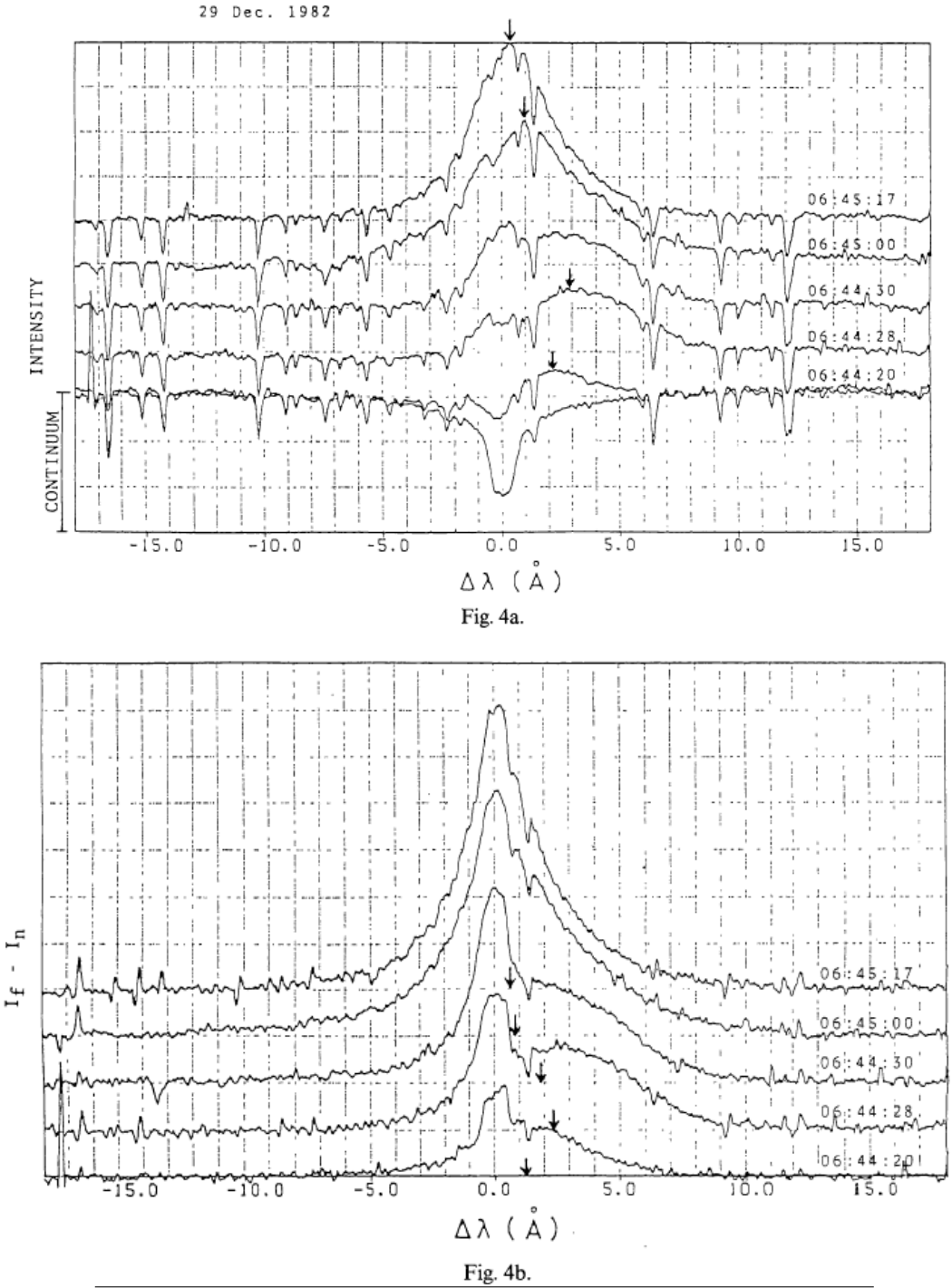

FIGURE 1.19: The Hα profiles during the impulsive phase of a solar flare, from Ichimoto and Kurokawa, 1984. Showing the enhancement over a background-subtracted profile for the same flare, with profile peaks up to 3Å into the red wing, and red wing excess lasting for around 100 s.

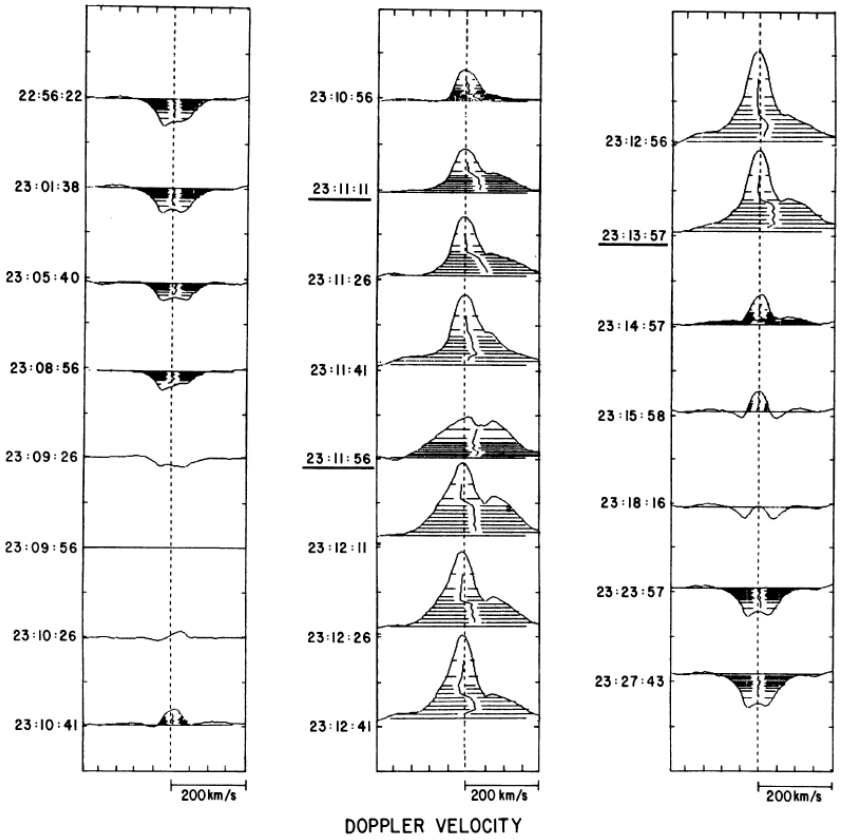

FIGURE 1.20: Hα emission with pre-flare profiles subtracted. These are shown during the impulsive phase (periods of enhanced HXR emission) of a flare with large red Doppler-shifted components lasting on the order of 100 s in the central column. This behaviour was noted in all five flares reported in Zarro et al., 1988.

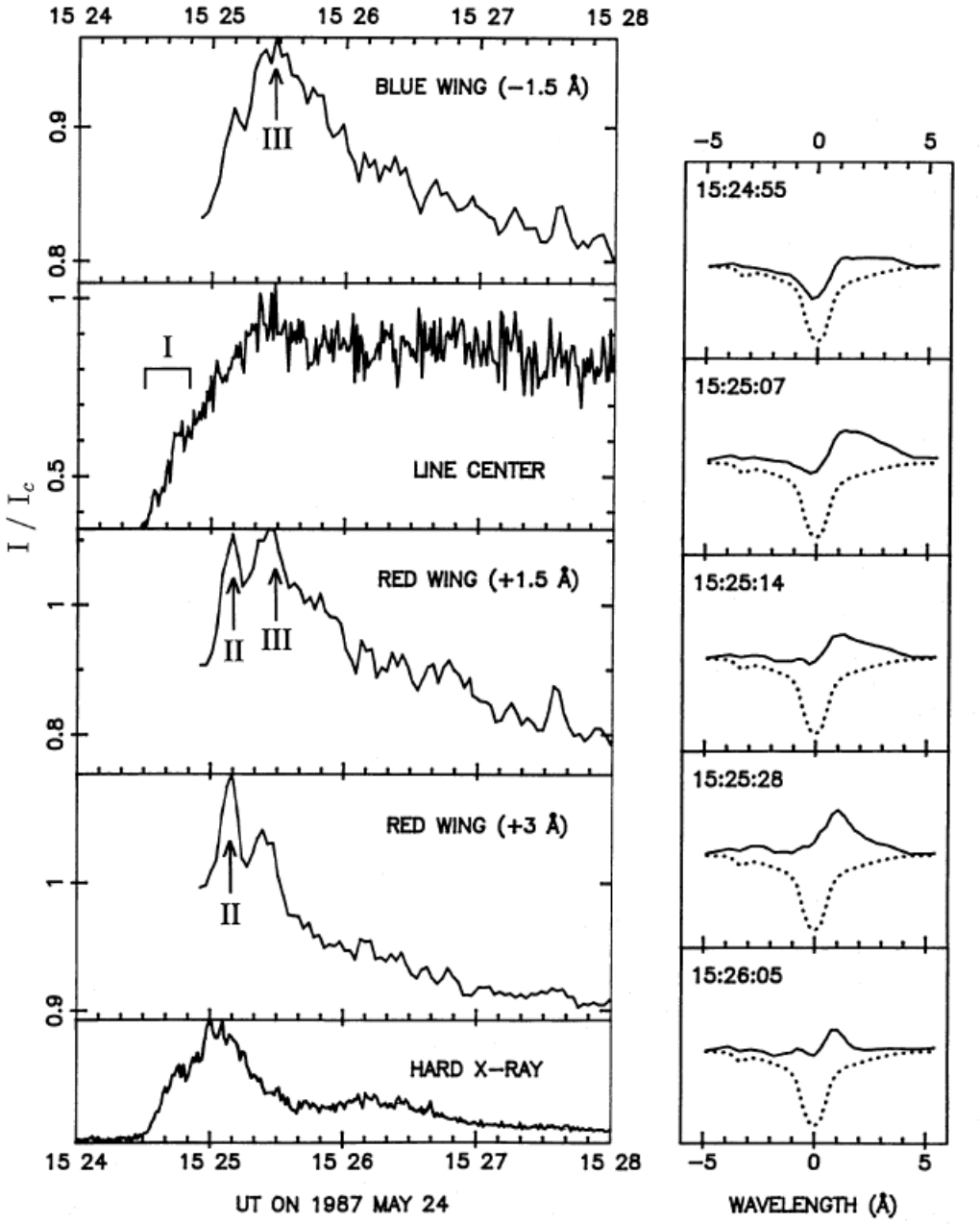

FIGURE 1.21: Hα emission profiles in a flare, taken from Wuelser and Marti, 1989. The left panels show the time evolution of emission intensity in the blue wing of the Hα lines (top), the line centre (second row), the red wing (third row) the far red wing (fourth row) and the HXR count rate (bottom row). The panels on the right show the Hα profiles with large Doppler red-shifted emission during the impulsive phase of a solar flare, with red-wing excess extending up to 4Å and lasting on the order of 100 s (right panels).

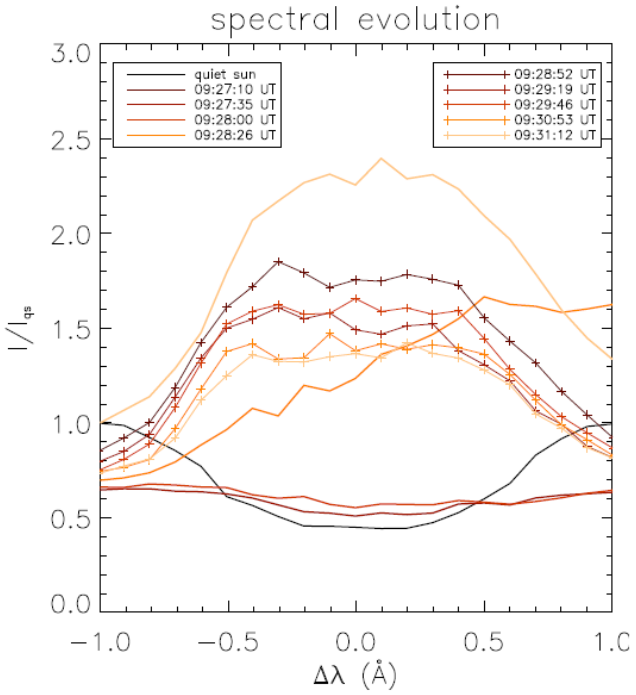

FIGURE 1.22: Truncated Hα profiles observed in a solar flare. See particularly the truncation of the red wing emission profile at 09:28:00, during the impulsive phase of a solar flare, from Sánchez-Andrade Nuño, Puschmann, and Kneer, 2007.

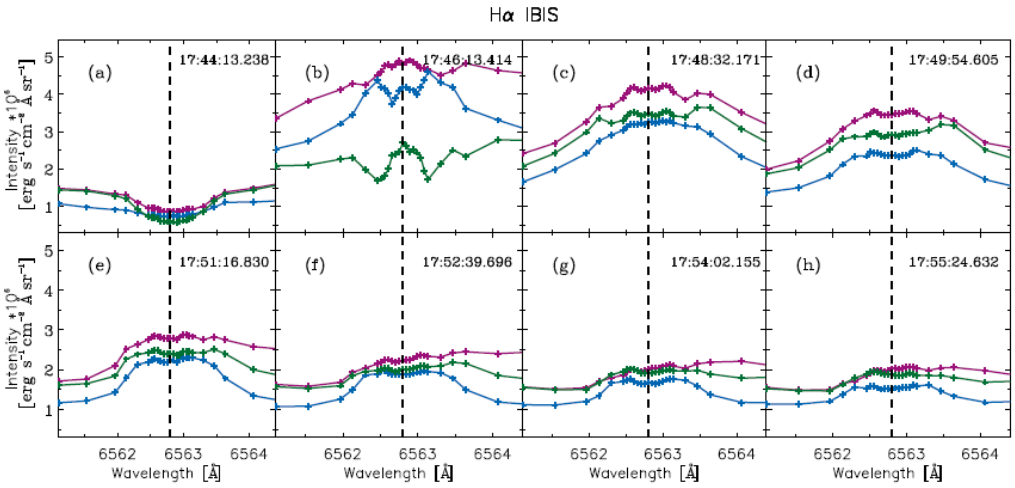

FIGURE 1.23: The temporal evolution of the Hα line in a solar flare. Profiles were observed in flare ribbon locations (purple and blue lines) and in the active region, outside of the flare ribbons (green lines). This figure from Rubio da Costa et al., 2016 illustrates truncated Hα profiles, particularly in the impulsive kernel (purple line), particularly at 17:46:13, 17:51:16, and 17:52:39.

Line	wavelength	formation height	Instrument
Fe IX	17.1Å	Upper TR	AIA
He II	30.4Å	Chromo/TR	AIA
C IV	1600Å	Core in TR	AIA
C II	1330Å	Core in TR	IRIS
Si IV	1400Å	Upper Chromosphere	IRIS
Mg II	2796Å	Chromosphere	IRIS
Ca II	8542Å	Low Chromosphere	DST

TABLE 1.4: List of other commonly observed optical and UV spectral lines.

blue-shifted emission above magnetic field structures (Bamba et al., 2017).

1.1.5 Continuous emission: White light flares

White light (WL) signals in solar flares are broad, continuous emission across the visible spectrum, associated with bound-free and free-free interactions between ions or neutral atoms and electrons. Uchida and Hudson, 1972 pioneered techniques for the observation of short-lived WL flare signatures by using the cancellation of positive and negative time-separated images of the Sun to eliminate permanent features.

Early observations of WL flares (Uchida and Hudson, 1972; Rust and Hegwer, 1975; Hiei, 1987; Kurokawa, Takakura, and Ohki, 1988; Hudson et al., 1992) showed that they often occur simultaneously with HXR bursts, γ-rays, and optical emission in the hydrogen lines. Subsequent observations also confirmed that the WL intensity in a flare generally correlated positively with the intensities in the HXR channels (Neidig and Kane, 1993; Sylwester and Sylwester, 2000; Watanabe et al., 2010). More recently UV Balmer continuum enhancements have also been observed to be co-temporal and co-spatial with HXR sources (Kleint et al., 2016; Kotrč, Procházka, and Heinzel, 2016).

Recent observations have demonstrated the heights where WL emission is formed (Battaglia and Kontar, 2011; Martínez Oliveros et al., 2012; Krucker et al., 2015). High resolution observations of limb flares have enabled observers measure the heights of HXR and WL sources, finding them to be co-temporal, co-spatial, impulsive, and located close to the height the quiet Sun photosphere (see Krucker et al.,

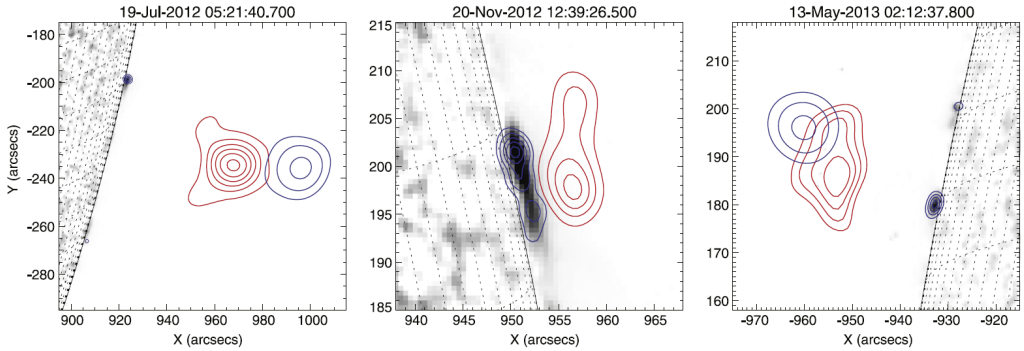

FIGURE 1.24: The co-temporal and co-spatial nature of HXR in the foot-points of a flare during the impulsive phase (blue contours) with the WL flare emission kernels (grey-scale image) at photospheric heights, from Krucker et al., 2015.

2015 Fig.1.24), below the stopping depths for beam electrons derived from the quiet Sun atmospheres of Fontenla et al., 2009.

1.1.6 Seismic responses

Kosovichev and Zharkova, 1998 detected a seismic response in a solar flare through the pattern of accelerating circular ripples that emanated for up to 55 minutes and 120 Mm from a power source associated with an X-class solar flare (see Fig.1.25), they called this phenomenon a *sunquake*. Starting from 2005 the frequency of sunquake detections grew through the use of detection methods such as Time-Distance (TD) diagrams (Zharkova et al., 2005; Kosovichev, 2006b; Kosovichev, 2006a; Zharkova and Zharkov, 2007; Donea, 2011; Zharkova and Siversky, 2011; Zharkova et al., 2011a; Matthews et al., 2015) (see Fig.1.26), and acoustic holography (Lindsey and Braun, 2000). Some of the detections were of anisotropic sources, rather than circular sources. Sunquakes have also often been associated with white light flares and shown to be caused by proton rich beams (Zharkova and Zharkov, 2007). Recently there have been detections reported for events as small as GOES M and C-class flares (Donea et al., 2006; Moradi et al., 2007; Sharykin, Kosovichev, and Zimovets, 2015), as predicted by Donea and Lindsey, 2005.

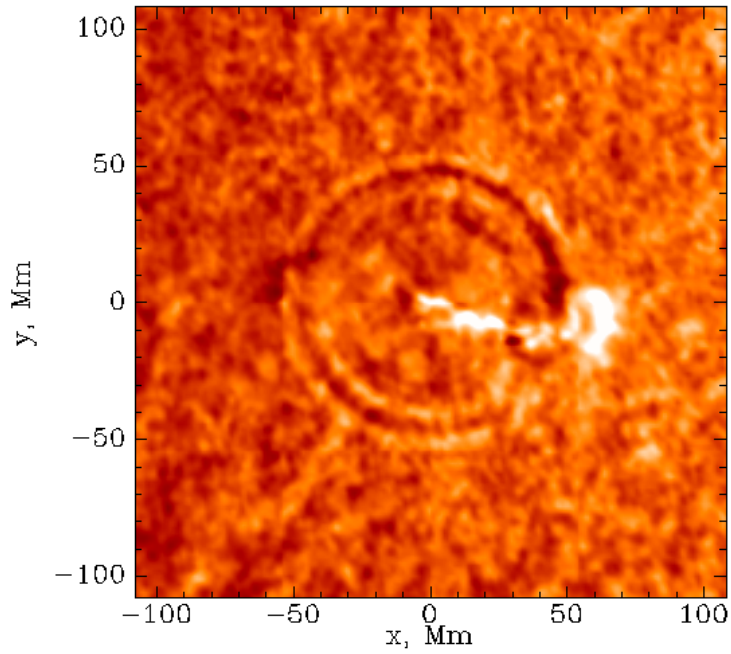

FIGURE 1.25: A sunquake: a seismic response in a solar flare is shown though the concentric ripples that appeared on the solar surface. These ripples appeared at some distance from the central source location and accelerated outward from it, reaching up to 120 Mm from the source location Kosovichev and Zharkova, 1998.

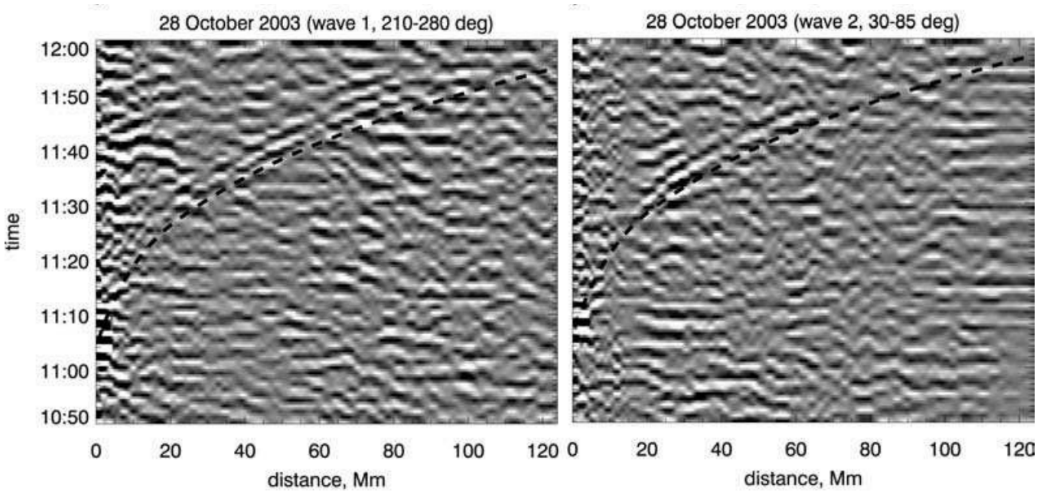

FIGURE 1.26: The detection of a sunquake using Time-Distance (TD) diagrams to identify radially accelerating wavefronts, taken from Kosovichev, 2006a.

1.1.7 Magnetic fields: irreversible, step-like changes

In the 1960s studies first detected magnetic field changes associated with solar flares (Severny, 1964). Subsequent observations have shown that solar flares are the most powerful magnetic events in the solar system, releasing energies up to 10^{32} erg in tens of minutes (Priest and Forbes, 2000; Somov, 2000; Karlický, 2014).

Irreversible magnetic field changes have been observed to be co-temporal with variations in HXR emission (Zharkova and Kosovichev, 2002; Zharkova et al., 2005) and brightenings in flare foot-point ribbons (Sudol and Harvey, 2005). Zharkova et al., 2005 provided the correlation coefficients of ~ 0.6 between HXR counts and magnetic field changes during solar flares (see Fig.1.27). However, there are often additional HXR sources, and foot-point brightenings that are not co-spatial with the step-type magnetic field changes (Kosovichev and Zharkova, 2001; Zharkova et al., 2005; Martínez-Oliveros and Donea, 2009; Matthews, Zharkov, and Zharkova, 2011; Petrie and Sudol, 2010; Petrie, 2012). Song and Zhang, 2016 reported 5 X-class flares in which the continuum emission intensity in a sunspot is highly negatively correlated with the change in magnetic field during a solar flare (see Fig.1.28).

The magnitudes of the step-like changes in magnetic field strength have been shown to be sufficient to account for the total energy budgets deposited in solar flares (Zharkova and Kosovichev, 2002; Zharkova et al., 2005), and have been calculated to be 2 or 3 times bigger than the total energy radiated through HXR, SXR and EUV added together (Holman et al., 2003; Zharkova et al., 2005; Petrie, 2012; Petrie, 2013).

These irreversible, rapid, step-type changes in the magnetic field magnitudes of an active region are detected as sudden, permanent changes in the LOS magnetograms occurring co-temporally with strong solar flares (see Kosovichev and Zharkova, 2001, Fig.1.29, region 1, Song and Zhang, 2016 Fig.1.28) (Kosovichev and Zharkova, 1999; Cameron and Sammis, 1999; Kosovichev and Zharkova, 2001; Spirock, Yurchyshyn, and Wang, 2002; Wang et al., 2002; Zharkova and Kosovichev, 2002; Meunier and Kosovichev, 2002; Schunker and Donea, 2003; Wang et al., 2004b; Wang et al., 2004a; Yurchyshyn et al., 2004; Sudol and Harvey, 2004; Wang, 2006; Song and Zhang, 2016), using instruments such as the Global Oscillations Network

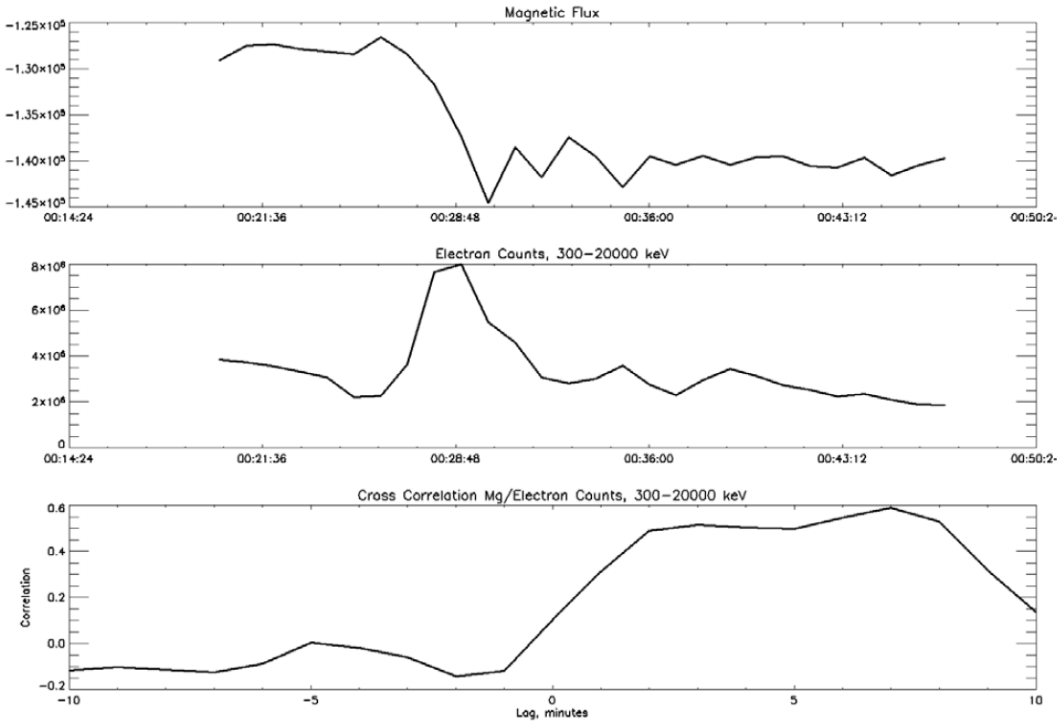

FIGURE 1.27: Total magnetic flux variations (top panel) and the RHESSI hard X-ray emission measured in the band 0.3–2 MeV prior to and during a flare (middle), from Zharkova et al., 2005. The correlation coefficient between these quantities is shown in the bottom panel, with 0 on the X-axis corresponding to the onset of HXR emission.

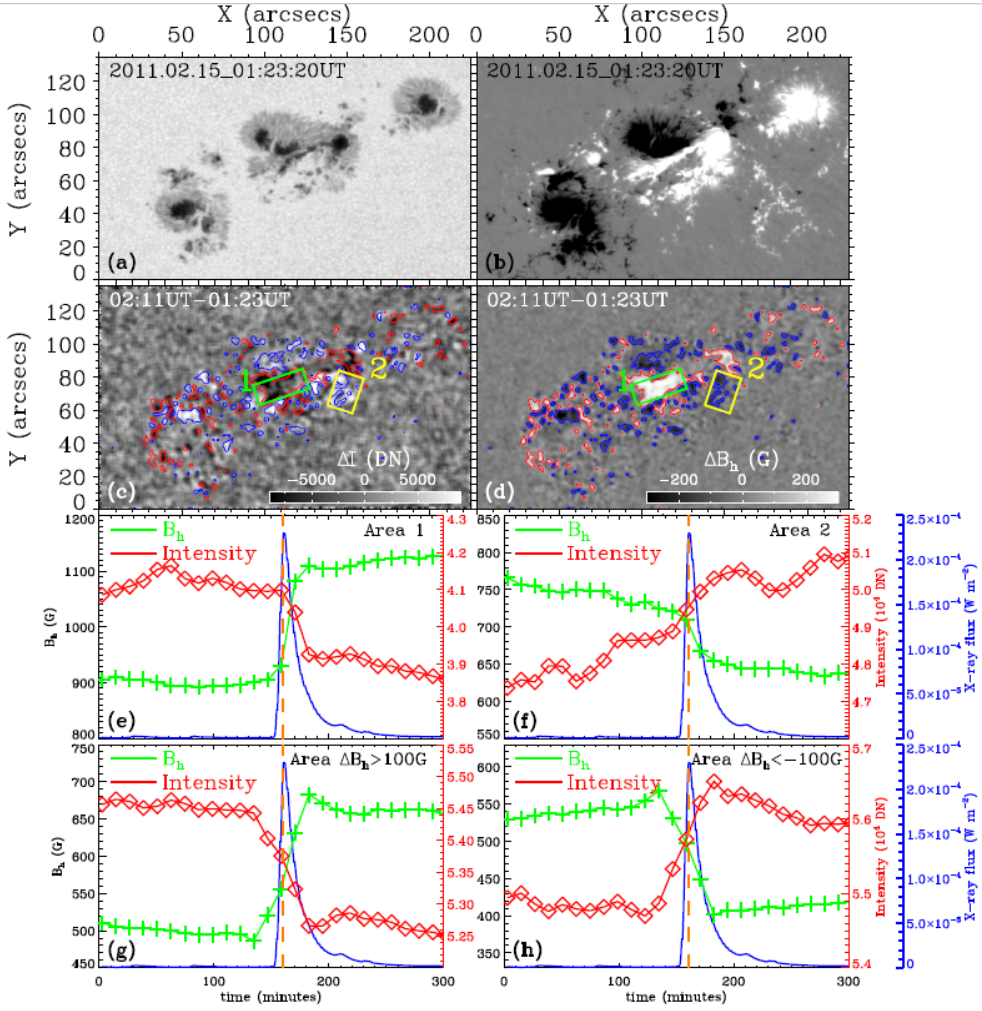

FIGURE 1.28: A continuum intensity map of an active region (a), a magnetic field map of the same active region (b), and the locations permanent of magnetic field changes (green and yellow boxes) (c and d), from Song and Zhang, 2016. The permanent changes in magnetic field (green lines) are shown to be correlated in time with HXR impulses (blue lines) in panels e to h.

Group (GONG) (Sudol and Harvey, 2004; Wang, 2006), the Michelson Doppler Imager on-board the Solar and Heliosperic Observatory (MDI, SOHO) (Zharkova et al., 2005) and the Helioseismic and Magnetic Imager on-board the Solar Dynamics Observatory (Song and Zhang, 2016). The step-like change from pre to post-flare state occurs on short time-scales compared to background trends, usually a few minutes (Sudol and Harvey, 2005), but ranging up to a hundred minutes (Wang et al., 2002; Zharkova and Kosovichev, 2002; Schunker and Donea, 2003).

A magnetic neutral line, or Magnetic Inversion Line (MIL) separates sections of an active region on the Sun containing magnetic fields with opposite polarity signs. MILs can be derived from the magnetic field gradients (Gaussian gradients) in magnetograms (Li et al., 2017 see Fig.1.2, 1c, left panel. Schunker and Donea, 2003 Fig.1.30, Fig.1a, region 1). The irreversible magnetic field changes can reach up to 300G (Sudol and Harvey, 2005; Zharkova et al., 2005) and are located close to the MIL (compare Fig.1.2, b, lower left panel with c, left panel) (Schunker and Donea, 2003; Sudol and Harvey, 2004). Moreover, they tend to occur when the Gaussian gradient of magnetic field across the MIL is steep (Sudol and Harvey, 2004). Fig.1.30a shows the locations of observations of the magnetic field strengths displayed in Fig.1.31 from Schunker and Donea, 2003. The top panels of Fig.1.31, are taken from the area 1 of Fig.1.30a, which straddles the magnetic neutral line. The location shows an irreversible change in magnetic field strength (left panel, black line) that occurs simultaneously with peaks in continuum intensity (grey line). Separated polarity regions frequently each contain one foot-point of a group of field lines that protrude into the solar corona. MILs are often found to have a sigmoid shape before a flare occurs (note, this terminology actually refers to an s-shape, and not the shape of a lower or upper case Greek alphabet sigma).

Yurchyshyn et al., 2004; Zharkova et al., 2005 studied the X4.8 flare on 23rd July 2002, in which Zharkova et al., 2005 reported the permanent, or irreversible, changes in the magnetic flux at the time of the HXR peak occur over the MIL. The MIL was almost stationary ($|v| < 20$ km·s^{-1}) except around the time of the HXR signal where it migrated at up to 250 km·s^{-1}. They used difference magnetograms, between MDI full disk magnetograms taken every minute, to identify and track the motion of a large negative magnetic discharge which migrates at the times of the HXR peak.

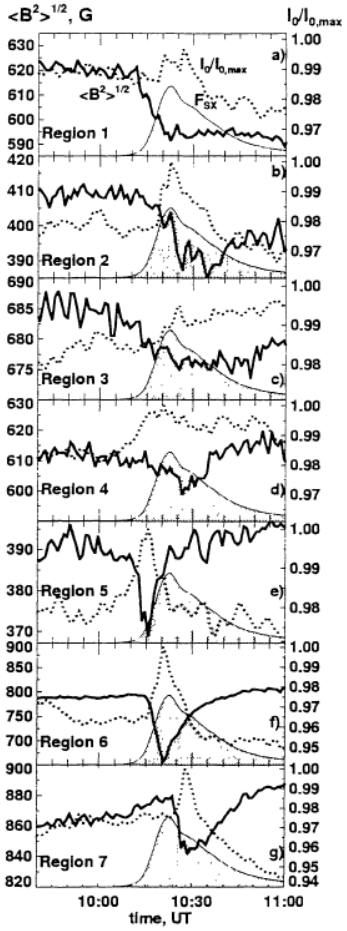

FIGURE 1.29: Permanent changes in magnetic field lines (solid black lines, panels 1-3), and transient changes in magnetic field (solid black lines, panels 5-7) from Zharkova and Kosovichev, 2002, that are co-temporal with intense emission in the background intensity (grey lines, panels 5-7).

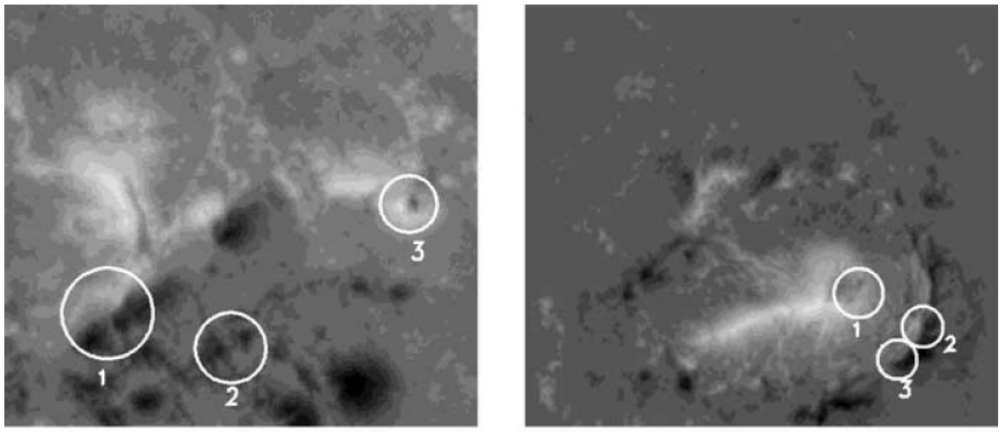

a. 2000 July 14 b. 2000 November 24

FIGURE 1.30: Magnetograms of solar flares, with a MIL separating regions of opposite polarities shown in panel a, region 1, taken from Schunker and Donea, 2003.

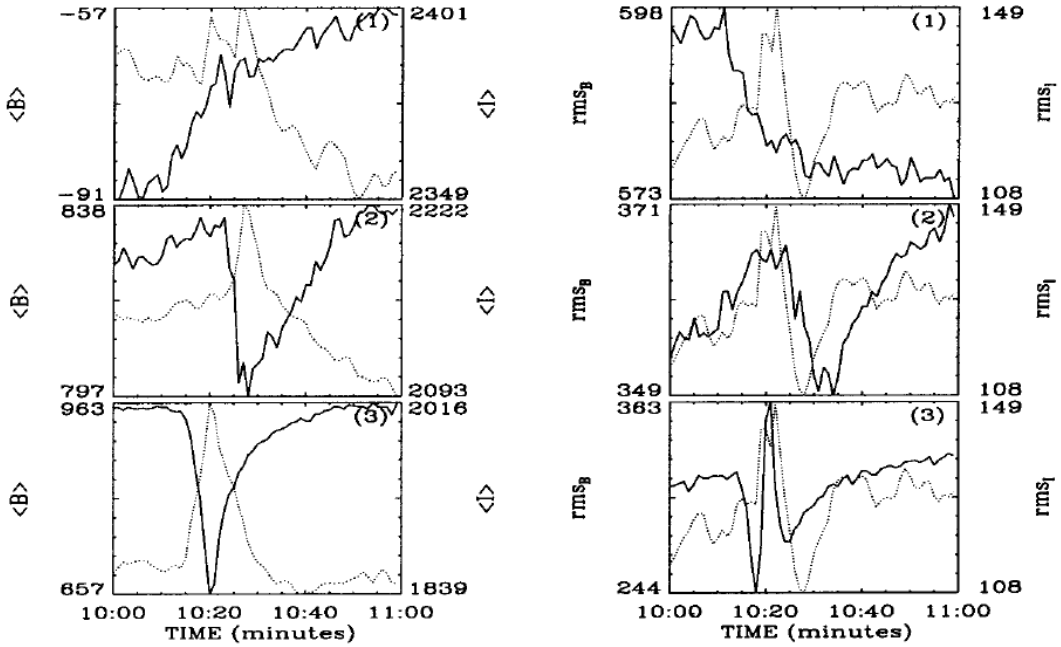

FIGURE 1.31: Irreversible changes in magnetic field from region 1 of Fig.1.30 (Top-left panel, black line) and reversible changes in magnetic field strength (middle and bottom left panels, black lines) from regions 2 and 3 of Fig.1.30 that are co-temporal with intense emission in continuous emission (grey lines) (Schunker and Donea, 2003).

Sudol and Harvey, 2005 noted that in 12 of the 15 X-class flares they studied, the irreversible changes occurred over sunspot penumbrae, and propagated across the solar surface at 5-30 km·s^{-1} for up to an angle of 1°.

1.1.8 Reversible changes in magnetic field

Transient variations of magnetic field during solar flares on the order of 1-10 minutes were detected using video magnetographs by Patterson and Zirin, 1981 and Zirin and Tanaka, 1981 and confirmed by many later observations (Kosovichev and Zharkova, 1999; Kosovichev and Zharkova, 2001; Zharkova and Kosovichev, 2002; Schunker and Donea, 2003; Zharkova et al., 2005).

The upper panel of Fig.1.32 is taken in the flare foot-points with HXR emission (Zharkova et al., 2005), and shows an irreversible change in magnetic field strength of comparable magnitude to the irreversible changes observed in the other regions (middle and lower panels). This has been highlighted using parallel red lines in the upper panel. However, the upper panel also shows reversible changes that last for

the order of 10 minutes starting at the time of the reported impulsive HXR signature. Reversible, or transient, magnetic field changes were interpreted as being caused by the increase of spectral line emission during solar flares (Patterson and Zirin, 1981), as opposed to the true changes in magnetic field strength.

As discussed in section 1.1.7, the top panels of Fig.1.31 are taken from area 1 of Fig.1.30 straddling the magnetic neutral line and show an irreversible change in magnetic field strength. However, the middle and lower panels of Fig.1.31 are taken from areas 2 and 3 of Fig.1.30a, and show fully reversible changes in magnetic field strength, similarly to the observations of Kosovichev and Zharkova, 2001 (see Fig.1.29, panels 5-7), at times coinciding with spikes in continuum intensity. These transients are found near flare foot-points and are associated with intense emission in spectral lines during flares (Patterson and Zirin, 1981; Harvey, Tang, and Gaizauskas, 1986; Schunker and Donea, 2003; Zharkova et al., 2005),

Some authors suggested that these transients result from observational effects due to changes in spectral profiles, or the deposition of supplementary energy into the system (Schunker and Donea, 2003). Kosovichev and Zharkova, 2001 attribute these disturbances to the propagation of charged particles delivering energy from the site of magnetic field energy release in the corona. Accelerated beams of particles excite electrons in the atoms of the ambient plasma and ionise the atoms through inelastic collisions, leading to an increase in spectral line intensity and thus an increase in the LOS magnetogram measurements detected as a reversible change in the magnetic field (Zharkova and Kosovichev, 2002).

More recently, a mechanism to explain the transient changes in magnetic field during solar flares was outlined by Zharkova et al., 2011b. Energetic electron beams precipitating from the coronal loops into their foot-points carry a self-induced electric field. The self-induced electric field produces a force in the direction of the coronal source. This stops beam electrons with lower energies and turns them back towards the corona, generating 'Return currents' (Siversky and Zharkova, 2009). From the differences of photon spectral indices at high and low energies, and the magnitude of the HXR flux increases seen at the peaks of HXR impulses in a flare, one may deduce the induced electric field of the beam. Using the continuity equation

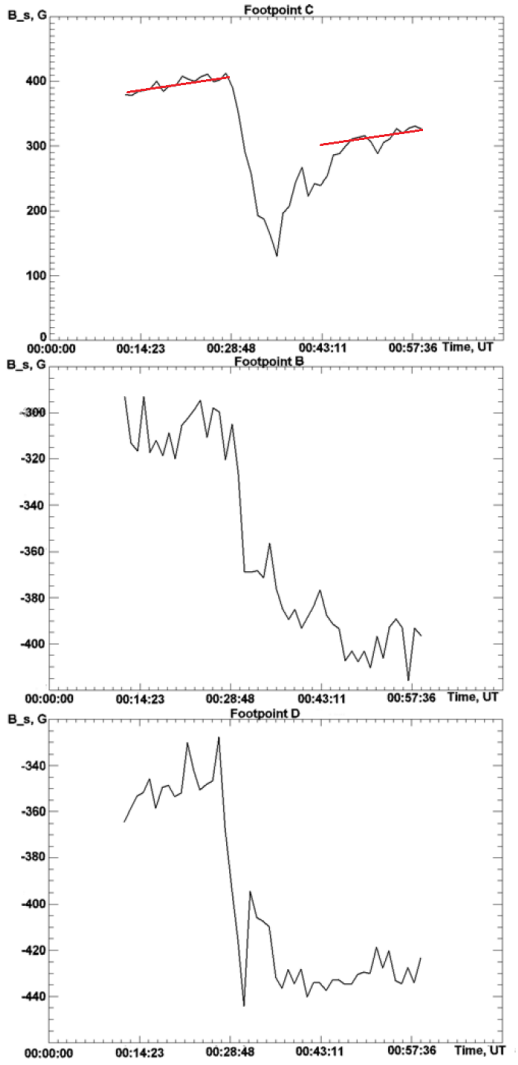

FIGURE 1.32: Permanent and reversible changes in magnetic field in the same location (top panel, with parallel red lines added to the original figure to highlight the magnitude of the reversible and irreversible changes) and two locations showing irreversible magnetic field changes (lower and middle panels), from Zharkova et al., 2005.

approach to beam precipitation Zharkova et al., 2011b found that high energy electrons reach the upper photosphere with a highly anisotropic distribution of pitch angle (Zharkova, Kuznetsov, and Siversky, 2010). The electrons then move across the flux tube and spread at a certain height, quickly changing the induced electric field with height. By Faraday's law a transient magnetic field along the loop length is induced by these electrons, with the opposite polarity to the field that was originally present. This transient is seen as a magnetic field reversal in magnetograms, and disappears once the beam stops, as observed in many observed flares (Kosovichev and Zharkova, 2001; Régnier and Fleck, 2004; Zharkova et al., 2005; Sudol and Harvey, 2005). Magnitudes of 30-130G have been recorded as temporary variations in the magnetic field at flare locations (Kosovichev and Zharkova, 2001; Zharkova and Gordovskyy, 2005a).

The energies released in the temporary magnetic field fluctuations during flares are therefore related to the energies of the particles in injected electron beams.

1.2 Models and interpretation of observations

1.2.1 Magnetic changes in solar flares

It is widely accepted that the primary energy release in a solar flare comes from a reconstruction of magnetic fields in an active region, occuring in the corona (Moore et al., 1984; Priest and Forbes, 2000; Somov, 2000). Magnetic reconnection is the phenomenon of magnetic field lines intersecting and reconnecting with each other (Petschek, 1964 Figs 50-2, and 50-3). Sturrock (1968, 1973) proposed the geometry of a solar flare triggered by magnetic reconnection using the Petscheck mechanism in a simple, bi-polar active region (Sturrock, 1968, see Fig.1.33). In this model, magnetic reconnection rapidly re-structures the magnetic topology of the region above the photospheric foot-points of the field lines and, thus, results in permanent changes to the directivity, helicity and shear of the B-field in large areas. These changes are detected in LOS magnetograms as irreversible, rapid, step-like changes in the LOS magnetic field strength. The energy released due to the reconnecting field lines accelerates high energy particle streams that travel along the magnetic field lines down

through the chromosphere creating bright filaments, as well as ejecting plasma and high energy particles outward into the heliosphere.

These alterations release large amounts of stored energy due to the differences between the initial and restructured B-fields (Sweet, 1958; Syrovatskii, 1963; Petschek, 1964; Somov et al., 1999; Priest and Forbes, 2000; Zharkova and Gordovskyy, 2005a; Hudson, Fisher, and Welsch, 2008; Petrie, 2012; Petrie, 2013; Wang and Liu, 2012). Therefore, magnetic reconnection is the suitable process to explain the step type changes in LOS magnetic field strength, and acts a trigger. Because the energy liberated in irreversible magnetic field changes has been shown to be capable of supplying the energy budget required to power the processes of solar flares (Zharkova and Kosovichev, 2002; Zharkova et al., 2005), such changes are believed to indicate the primary source of energy release in solar flares.

Some of the energy unlocked by magnetic reconnection is released through the acceleration of energetic particles (Zharkova et al., 2005). Acceleration occurs in current sheets in a diffusive region where the reconnecting magnetic field lines intersect and the particles gain their energy due to the electric fields directed along the guiding field (Litvinenko, 1996; Zharkova and Gordovskyy, 2004; Zharkova and Gordovskyy, 2005a; Zharkova and Agapitov, 2009) as they pass through the magnetic field of the current sheet. Particles are accelerated to sub-relativistic energies with power law energy distributions with parameters that depend on the B-field topology of the reconnecting current sheet (Zharkova and Gordovskyy, 2005a; Zharkova and Agapitov, 2009). Table 1.5 of Zharkova and Gordovskyy, 2005a shows the spectral indices of electron beams, γ, generated from reconnection models with an exponential index α (left column), of the horizontal magnetic field B_x,

$$B_x \propto \left(\frac{z}{a}\right)^{\alpha}, \tag{1.1}$$

z is the distance from a null point and a is the thickness of the reconnecting current sheet. λ (top row) is an index of the vertical density variations,

$$N(z) \propto \left(\frac{z}{a}\right)^{\lambda} \exp\left(-\lambda\frac{z}{a}\right). \tag{1.2}$$

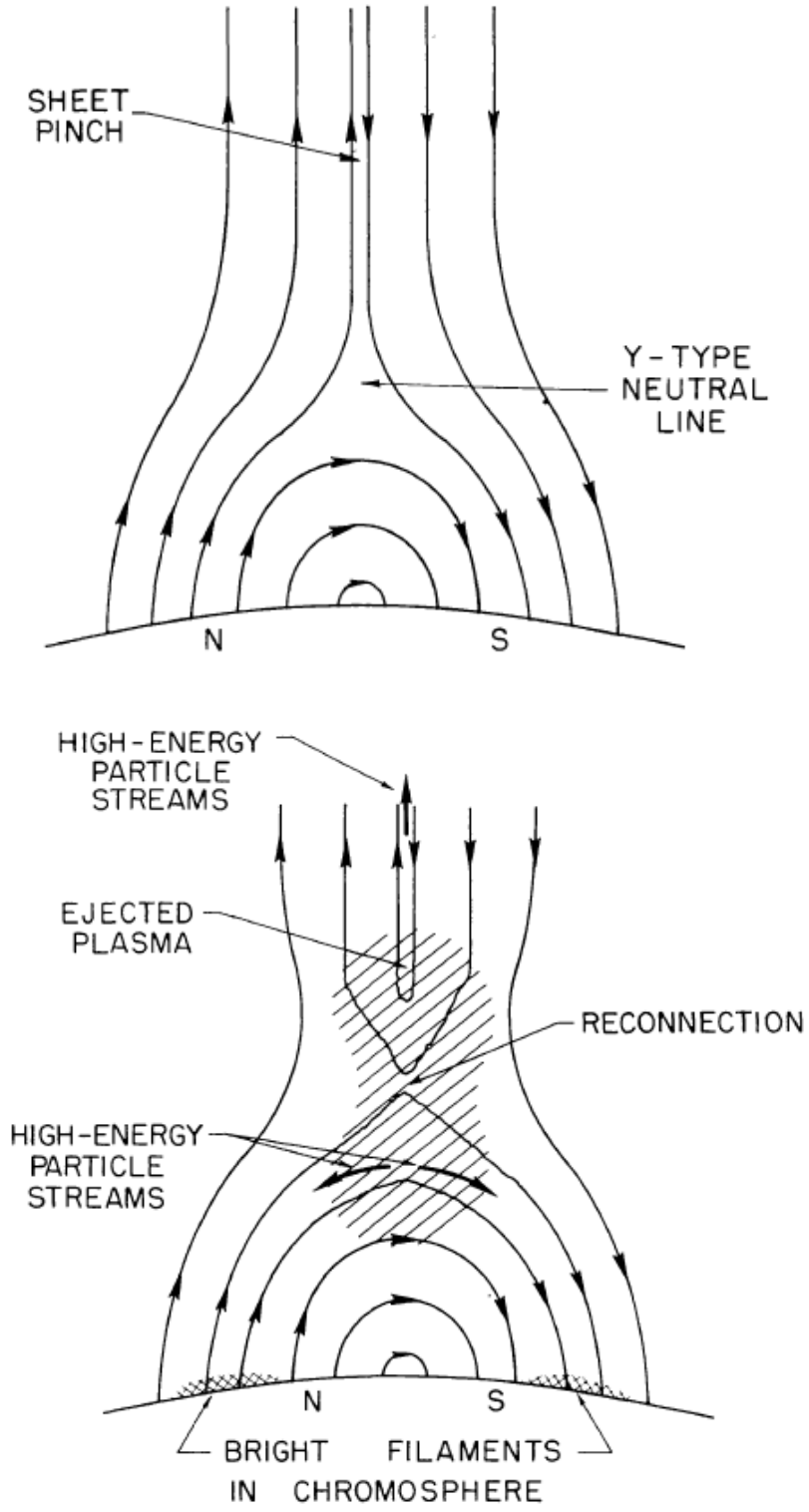

FIGURE 1.33: A schematic representation of magnetic field patterns leading to solar flares above a bipolar region before (top panel) and after reconnection (lower panel) in the corona. The reconnection event triggers a solar flare in the bright foot-points of the reconnecting loops (Sturrock, 1968).

	λ				
α	0	1/2	1	2	3
0.5	3	4	5	7	9
1	2	2.5	3	4	5
2	1.5	1.75	2	2.5	3
3	1.33	1.5	1.67	2	2.33

TABLE 1.5: The spectral indices, γ, of accelerated electron beams in a reconnecting current sheet calculated for exponential indices α and λ, of the magnetic field B_x and density variations across the current sheet. Taken from table III in Zharkova and Gordovskyy, 2005a.

Protons and electrons are accelerated simultaneously in a current sheet, they are dragged by diffusion processes from the neutral ambient plasma into the diffusion region during magnetic reconnection. They undergo a complex energisation in the diffusion region by the Lorentz force at the midplane of current sheet until they gain the energy required to escape from the 3D magnetic trap. Zharkova and Gordovskyy, 2004 showed that electrons are quickly accelerated due to their low mass, escaping within 10^{-6} s, whereas heavier protons take on the order of 10^{-3} s to gain sufficient energy to escape. When they escape the diffusive region, accelerated particles are injected into the lower solar atmosphere following the magnetic field lines of the coronal loop legs. Due to their opposing charges, protons and electrons are often preferentially ejected into the loop legs with opposite polarity (Zharkova and Gordovskyy, 2004).

Particle in cell (PIC) modelling of current sheets in the corona (Siversky and Zharkova, 2009) and in the heliosphere (Zharkova and Khabarova, 2012) shows that the electrons and protons accelerated by magnetic reconnection are fully separated from each other, and ejected into different magnetic leg loops only when the magnetic field topology generates large values of the guiding field. Topologies such as this explain the HXR and γ ray source separations observed in some flaring events (e.g. Hurford et al., 2003, see section 1.1.1).

1.2.2 Interpretation of HXR

When energetic charged particles undergo elastic collisions by passing through the electric and magnetic fields of other particles, high-energy photons are emitted in the form of HXR. This emission is also known as *bremsstrahlung*, which means *braking radiation*, due to the decelerating influence these interactions have on the energetic charged particles.

Energetic electrons, accelerated up to hundreds of keV, have been interpreted as the key agents delivering energy during this phase by authors since the 1960s because of their association with the strong, non-thermal HXR bremsstrahlung in the impulsive phases of solar flares (Brown, 1971; Syrovatskii and Shmeleva, 1972; Hudson, 1972; Brown, 1973; Kane, 1973). Moreton, 1964 concluded such emission was associated with bremsstralung radiation from energetic electrons, and categorised the flare observations into two groups, those characterised by low energy thermal sources and higher energy, non-thermal, impulsive bursts. This interpretation is complementary with the magnetic reconnection models of Alfvén and Carlqvist, 1967; Sturrock, 1968; Syrovatskii, 1969; Takakura, 1971; Sturrock, 1972; Petrosian and Sturrock, 1973 in which particles such as electrons are accelerated by electric fields (see section 1.2.1).

Holt and Cline, 1968 used experimental data from HXR and microwave radio emission to directly infer the electron spectrum generating them, showing that the radiation was due to sub-relativistic electrons. They reasoned that X-rays and gyrosynchrotron microwave radiation for a flare on July 7th 1966 could be explained from an energetic electron source with a negative power-law energy spectrum, located in the chromosphere.

Power law energy distributions of energetic electrons are generated in the models of particle acceleration resulting from magnetic reconnection (Takakura, 1971; Kane, 1973; Kane, 1974; Litvinenko, 1996; Zharkova and Gordovskyy, 2004; Zharkova and Gordovskyy, 2005a; Siversky and Zharkova, 2009; Zharkova and Agapitov, 2009; Holman et al., 2011). These simulations predict emission at low energies, $\sim$ 10keV, from thermal bremsstrahlung (consistent with section 1.1.1) as well that the non-thermal beam electrons with power law distributions are responsible for

the power-law HXR photon spectra at high energies via bremsstrahlung.

The non-thermal electron beams penetrate through the solar atmosphere incurring Ohmic losses due to their own self-induced electric field (Gordovskyy et al., 2005; Zharkova and Zharkov, 2007) as well as heating the plasma through Coulomb collisions and exciting and ionising the plasma through inelastic collisions. The self-induced electric field of these beam particles produces a force in the direction of the coronal source. This stops beam electrons with lower energies and turns them back towards the corona, generating 'return currents'. This occurs at stopping depths of electrons with a lower cut-off energy for the power law distribution. This field exists as long as the beam electrons are injected into the atmosphere (Siversky and Zharkova, 2009). This has been observationally confirmed in many solar flares (Zharkova and Gordovskyy, 2005a; Holman et al., 2011). Return currents also explain how a beam of electrons entering the lower atmosphere can be established without overcharging this atmosphere through a continuous injection of charged particles.

For a beam that generates a strong self-induced electric field, return currents will form in a small fraction of second (Siversky and Zharkova, 2009), decelerating the turning electrons with lower energies back to the source (Zharkova and Gordovskyy, 2006). This reduces the electron population at the lower energies, flattening the electron energy spectrum, as the beam moves down the loop to the foot-point (<100 keV, Holman et al., 2011). Siversky and Zharkova, 2009, showed that these return current electrons can be re-cycled up to 50 times per second, removing the *particle number problem* in which it was observed that a large number of beam electrons are required to produce the emission sources detected in solar flares. Thus in the loop foot-points, double-power-law energy distributions of electrons are detected, with a lower spectral index below some critical energy, which depends on the self-induced electric field (Sui, Holman, and Dennis, 2007; Holman et al., 2011; Kontar et al., 2011).

Additionally return currents will modify the spectrum and reduce the number of low-energy electrons in the beam as it penetrates into the chromosphere (Zharkova and Gordovskyy, 2005a; Holman et al., 2011), giving one explanation of the double power law HXR energy spectra observed at these times (section 1.1.1).

Zharkova and Gordovskyy, 2006 analysed the electron and photon spectral indices in simulations of energetic electron beams precipitating from the corona into the lower atmosphere in the presence of a self-induced electric field. They found that the photon spectral indices flatten more at lower energies for beams with higher initial fluxes. Thus, for the injected electron beams with constant spectral indices and initial fluxes varying in time from low to high and back to low again as observed in elementary flare bursts, a soft-hard-soft variation in the photon HXR spectral index is produced (Zharkova and Gordovskyy, 2006).

The strong coupling between the timings of coronal and foot-point HXR sources during the impulsive phases of solar flares is explained by the acceleration of electrons to sub-relativistic energies in the magnetic reconnection models of solar flares, and their subsequent rapid travel down the loops to the foot-points. The slower, gradual phase variations of the lower energy X-rays signals are explained by the plasma heated to millions of degrees Kelvin by the non-thermal electrons during the impulsive phase.

One of the problems in understanding the acceleration of electrons and other particles is that the radiation they cause through X-rays and γ rays is observed where the densities of ambient plasma are high, rather than in the regions they are produced (Holman et al., 2011). The heated, excited and ionised plasma is confined to the magnetic loops that guides the electrons (Aschwanden, 2004; Holman et al., 2011), and this explains the observations that highest intensity of HXR emission comes from the foot-points of the magnetic loops (see section 1.1.1). The electrons precipitate from the loop top sources where they were accelerated along the magnetic field lines, and they interact with the dense plasma at the foot-points of the loop.

One must be careful in directly inferring the electron energy spectrum from the bremsstrahlung HXR photon spectra they generate. This is beacuse the electron energy spectra may be significantly altered from their originally accelerated forms during transit (Zharkova and Gordovskyy, 2006; Kontar et al., 2011). As the accelerated electrons penetrate downwards through the solar atmosphere, they move from the fully ionised corona into the partially ionised chromosphere and below. Collisional loss rates with depth are higher for lower energy electrons (Brown, 1971; Syrovatskii and Shmeleva, 1972; Emslie, 1978). Therefore, according to the thick target model,

the X-ray photon distribution's spectral index, γ, changes as the beam electrons lose energy at different rates depending on the energy of the electron. Thus, the spectrum of the emerging photon HXR spectrum does not match the electron power-law spectral index δ. Considering only collisional losses $\gamma = \delta - 1$ (Holman et al., 2011). However, the losses due to a variable electric field approximation show a relationship between the HXR photon and electron energy spectral indices that is much closer for harder beams (Syrovatskii and Shmeleva, 1972; Zharkova and Gordovskyy, 2005a). These processes explain why the foot-point HXR sources tend to be similar in the impulsive phase (see Fig.1.11) and the alterations in transit explain the observations from Yohkoh that HXR sources at the top of coronal loops show lower spectral indices (harder beams) than their foot-point counterparts (section 10 of Holman et al., 2011 and Zharkova, 2012).

1.2.3 Hydrodynamic models

In the thick-target model of electron beam propagation energy is transferred from the acceleration region to the lower atmosphere, where the energy is deposited via Ohmic heating from the self-induced electric field of the beam electrons and Coulomb collisions with ambient plasma. These processes transfer energy and rapidly heat the ambient plasma, causing a hydrodynamic response.

There are three types of heating function for the non-thermal beam particles: *CEA* - by beam electrons in Coulomb collisions with electron density derived from a continuity equation approach in which energy is conserved (CEA) (Somov, Spektor, and Syrovatskii, 1981; Zharkova and Zharkov, 2007; Syrovatskii and Shmeleva, 1972); *FCA* - by beam electrons in Coulomb collisions with density derived from a flux conservation equation approach, in which the flux of the beam electrons injected from the corona is conserved (FCA) (Nagai and Emslie, 1984; Fisher, Canfield, and McClymont, 1985; Allred et al., 2005; Emslie, 1978), which has a serious (infinity) limitation (Mauas and Gómez, 1997; Kontar et al., 2011) at the stopping depths in the chromosphere for electrons with the lower cut-off energy; *EED* - by unspecified agents with equal energy deposition (EED) per volume at any depths (Polito et al., 2016; Bradshaw and Cargill, 2006). Heating by particle beams is considered to be either impulsive of 5-10 s(Somov, Spektor, and Syrovatskii, 1981; Fisher, Canfield,

and McClymont, 1985; Allred et al., 2005; Zharkova and Zharkov, 2007), or prolonged (30-300 s) (Polito et al., 2016; Duijveman, Somov, and Spektor, 1983; Nagai and Emslie, 1984; Kennedy et al., 2015; Bradshaw and Cargill, 2006) accounting for different types of flaring events.

There are three types of hydrodynamic models defined by their initial conditions, from which heating starts: *QS type* uses the quiet Sun chromosphere with an initial kinetic temperature of 6700 K (Somov, Spektor, and Syrovatskii, 1981; Duijveman, Somov, and Spektor, 1983; Nagai and Emslie, 1984; Zharkova and Zharkov, 2007) (in Lagrangian coordinates), which is converted by electron beam heating into a flaring atmosphere with its own corona, transition region and chromosphere; *PH type* uses a pre-heated flaring atmosphere comprising of semi-empirical model VAL F (Vernazza, Avrett, and Loeser, 1981) in the chromosphere and the quiet Sun (QS) corona attached above the transition region in Lagrangian (Fisher, Canfield, and McClymont, 1985) or linear (Allred et al., 2005; Kennedy et al., 2015) coordinates, which is also heated by precipitating beam electrons; the *Isotropic type* uses an isotropic atmosphere evenly heated over a linear depth by some unspecified agents (Bradshaw and Cargill, 2006).

The cooling in all hydrodynamic models is provided by radiation from the corona and transition regions, calculated in optically thin emission for the solar abundances (Cox and Tucker, 1969). The additional cooling by hydrogen line emission in the chromosphere is calculated by solving radiative transfer equations (Fisher, Canfield, and McClymont, 1985; Allred et al., 2005) or by adding hydrogen radiative losses for relevant beam parameters as arrays to the cooling function (Zharkova and Zharkov, 2007). A hydrodynamic time-scale (10-100 s)(Shmeleva and Syrovatskii, 1973; McClymont and Canfield, 1983) is much longer compared to a radiative time-scale (0.3 s) (Shmeleva and Syrovatskii, 1973; Somov, 2000) that supports a consequential use of hydrodynamic and radiative models.

Heating of the QS chromosphere by beam electrons in a CEA hydrodynamic model (Somov, Spektor, and Syrovatskii, 1981; Duijveman, Somov, and Spektor, 1983; Zharkova and Zharkov, 2007) is shown to sweep plasma to lower atmosphere, forming a flaring atmosphere with the new corona, transition region and chromosphere. This sweeping is followed by the plasma evaporation back to the corona

combined with formation of a low-temperature condensation in the chromosphere moving as a shock to the photosphere. A hydrodynamic heating in the other two types of models (PH and Isotropic) results in chromospheric plasma evaporation without sweeping, combined with the shock moving downwards to the lower atmosphere with smaller velocities (Polito et al., 2016; Fisher, Canfield, and McClymont, 1985; Allred et al., 2005; Kennedy et al., 2015; Bradshaw and Cargill, 2006).

1.2.4 Interpretation of SXR and UV emission

SXR signatures observed in the Solar Maximum Mission (SMM) (Antonucci et al., 1982) and the RHESSI mission (Lin, Dennis, and Benz, 2003) have been clearly linked to thermal bremsstrahlung and evaporation processes in solar flares, i.e. hot turbulent plasma showing blue-shifted emission lines during the impulsive phase, and lasting for minutes afterwards. It was also shown to be possible to account for the total energy in this SXR emission over the full times of the flare observations by considering the energy supplied by energetic particles in heating the plasma during the impulsive phase (Antonucci et al., 1982; Lin, Dennis, and Benz, 2003).

Models of the evaporation of hot plasma in solar flares have shown good agreement with observed SXR emission as well as the intensities and velocities of observed blue-shifted UV emission in solar flares (Allred et al., 2005; Bradshaw and Cargill, 2006; Del Zanna and Woods, 2013; Kennedy et al., 2015; Polito et al., 2016; Polito et al., 2017).

In section 1.1.3 the lack of high spatial resolution spectral information for hydrogen Lyman line emission was discussed. Higher cadence images have become available from instruments using broadband filters, such as the transition region and coronal explorer, (TRACE), GOES/EUVS-E and PROBA2/LYRA. Rubio da Costa (Rubio da Costa et al., 2009; Rubio da Costa et al., 2010; Rubio da Costa et al., 2012) compared observations from high cadence images with the results from their simulations and concluded that hydrogen Lyα and Hα flare intensities are only weakly affected by the flux of the electron beam causing that flare, with total intensity of each line varying by only a factor of two for beam fluxes varying over 2 orders of magnitude. These conclusions are different from those made from a number other models of Hα emission affected by beam electrons in solar flares, and the simulated

intensities published at the similar times for the F10 and F11 flares of Allred et al., 2005.

Recently, Milligan and Chamberlin, 2016 have shown that inferences of the line and continuum enhancements of Lyman emission made using broadband filters may be anomalous, resulting from the enhancements in the other lines and continuous emission captured by the broadband filter. For example, EVE Lyα light-curves (using a broadband filter) show a rise time of 10 s of minutes at flare onset where other lines show a rapid increase (Hα, Lyβ, Lyman continuum). Whereas, spectrally resolved flare observations of the same event by the Solar Stellar Irradiance Comparison Experiment (SOLSTICE) on-board the SOlar Radiation and Climate Experiment (SORCE) show a well defined peak in Lyα emission during the impulsive phase.

The macro-velocities reported in the higher Lyman line observations of Brown, Fletcher, and Labrosse, 2016 are highly dependent on the method of measurements used. For example, in one flare the maximum Doppler shift calculated from observations of the Lyβ line emission with quiet Sun intensity profiles subtracted varies between 15 and 60 km·s^{-1}, depending on whether the Doppler shift is estimated using a Gaussian, cross correlation function or weighted intensity method. Moreover, the data uses full disk intensities. Thus, even with quiet Sun profiles subtracted the reported Doppler shifts relate to averages over the active region, rather than speeds in the flare kernels.

It is evident that Lyman line emission in solar flares has not yet been comprehensively observed interpreted. It is imperative that emission in the Lyman lines and continuum is considered in the models of solar flares before the advent of the new instruments discussed in section 1.1.3, because this will enable the specification of potential diagnostics of flaring atmospheres provided by the future observations.

1.2.5 Interpretation of optical emission

Simultaneously to a hydrodynamic response to an energetic electron beam, inelastic collisions with beam electrons will excite and ionise the plasma, resulting in UV and optical emission from spectral lines and continuum emission. Therefore the flare dynamics in the lower atmosphere can be derived from observations of optical lines and, in particular, hydrogen Hα line 6563 Å emission with red shifts (Zarro et al.,

1988; Del Zanna, 2008; Milligan and Dennis, 2009; Graham and Cauzzi, 2015; Ichimoto and Kurokawa, 1984; Wuelser and Marti, 1989; Canfield et al., 1990). Observations of flare emission with blue-shifts in coronal lines and red-shifts in chromospheric lines (see section 1.1.4) were interpreted by hydrodynamic responses of flaring atmospheres to heating by particle beams injected from the top and precipitating to lower atmospheric levels (Kostiuk and Pikelner, 1974; Craig and McClymont, 1976; Craig, McClymont, and Underwood, 1978; Somov, Spektor, and Syrovatskii, 1981; Duijveman, Somov, and Spektor, 1983; Nagai and Emslie, 1984; Fisher, Canfield, and McClymont, 1985; Allred et al., 2005).

The radiative models describing hydrogen emission in flares utilise the effects of electron beams in two ways: *via heating of the ambient plasma* by beam electrons as considered in hydrodynamic models and *via non-thermal ionisation and excitation* of hydrogen atoms by beam electrons for a FCA (Aboudarham and Henoux, 1986) and for a CEA (Syrovatskii and Shmeleva, 1972; Zharkova and Kobylinskii, 1993). The heating and non-thermal excitation and ionisation rates of hydrogen atoms are significantly affected by the approaches used for particle kinetics, producing in FCA smaller electron numbers at chromospheric levels compared to CEA. This occurs because of the electron number truncation in FCA at the upper chromosphere (Mauas and Gómez, 1997; Kontar et al., 2011), before a stopping depth of lower energy electrons, in order to avoid the infinite heating (Mauas and Gómez, 1997). This, in turn, shifts to the upper chromospheric depths the effect of beam electrons on hydrogen emission in FCA. The CEA provides very smooth distributions of beam electrons at all precipitation depths, with maximum heating occurring in the chromosphere at the stopping depth of electrons with a lower cut-off energy (Syrovatskii and Shmeleva, 1972). This heating leads to formation of hydrodynamic shocks in the middle chromosphere where the Hα line cores are formed, contrary to the FCA hydrodynamic models (Fisher, Canfield, and McClymont, 1985; Allred et al., 2005) where this shock is formed in the upper chromosphere.

Most models (Polito et al., 2016; Somov, Spektor, and Syrovatskii, 1981; Nagai and Emslie, 1984; Fisher, Canfield, and McClymont, 1985; Allred et al., 2005; Kennedy et al., 2015; Bradshaw and Cargill, 2006) account quite well for evaporation (upward) velocities and intensities of EUV emission. However, hydrodynamic

radiative models using the FCA are less successful in interpreting the red-shifted Hα line profiles (Ichimoto and Kurokawa, 1984; Wuelser and Marti, 1989; Canfield et al., 1990; Wuelser et al., 1994) because the speeds and formation depths of the hydrodynamic shocks in these in FCA models are much smaller than those using the CEA.

Earlier calculations of Hα line profiles (Ricchiazzi and Canfield, 1983; Canfield, Gunkler, and Ricchiazzi, 1984; Canfield and Gayley, 1987) carried out for pre-heated hydrodynamic atmospheres (Fisher, Canfield, and McClymont, 1985), with heating function by Nagai and Emslie, 1984, showed the simulated profiles with blue-shifts (Allred et al., 2005; Kuridze et al., 2015), contrary to the red ones observed (Ichimoto and Kurokawa, 1984; Wuelser and Marti, 1989; Canfield et al., 1990; Wuelser et al., 1994). These discrepancies were previously attributed to a complex geometric multi-thread structure of flares (Ricchiazzi and Canfield, 1983; Canfield, Gunkler, and Ricchiazzi, 1984; Canfield and Gayley, 1987).

Some authors have suggested that the Hα line profiles in flares are determined in a large part by shifts in the maximum opacity of the Hα line, rather than by Doppler shifts, and while this is an eminently reasonable suggestion with regard to the wavelength of the central reversal (Kuridze et al., 2015) it is not responsible for the large red-shifts observed in flare kernels during the impulsive phase of solar flares. Ichimoto and Kurokawa, 1984; Wuelser and Marti, 1989 dismissed the possibility of absorption from rising material accounting for the red wing emission excess compared with the blue wing. Ichimoto and Kurokawa, 1984 did this precisely by showing that optical thickness required for the observed disparity was incapable of resulting in such asymmetry. Therefore, current radiative hydrodynamic models using the FCA and isotropic approaches to beam precipitation do not explain the red-shifted Hα line profiles observed at flare onsets reported since early 80s.

The advances in space and ground-based instruments with high spatial and temporal resolution (IRIS (De Pontieu et al., 2014), the Atmospheric Imaging Assembly (AIA) aboard on the Solar Dynamic Observatory (SDO) (Lemen et al., 2011) and notably the CRisp Imaging Spectro-Polarimeter (CRISP: Scharmer et al., 2003) located at the Swedish 1-m Solar Telescope (SST)(SST: Scharmer, 2006; Scharmer et al., 2008)) helped to eliminate some effects of spatial inhomogeneities in flaring regions

emitting Hα lines (Allred et al., 2005; Heinzel and Kleint, 2014; Kleint et al., 2014; Kuridze et al., 2015; Rubio da Costa et al., 2016). Rubio da Costa et al., 2016 reported simulated Hα line profiles with a small red-shift (about 15 km·s^{-1}) at a flare onset and larger blue-shifts at 52 s later. However, this model still cannot explain the Hα line observations (Ichimoto and Kurokawa, 1984; Wuelser and Marti, 1989; Wuelser et al., 1994) with larger red-shifts taken at the flare onsets.

1.2.6 Interpretation of white light sources

In the 1970s Brown, 1971; Hudson, 1972; Brown, 1973 suggested that accelerated electrons moving downwards as a well directed beam reach the lower chromosphere and deposit energy there, producing localised heating that is responsible for the obsered WL sources in solar flares. Modelling using the FCA predicted that the energetic electrons would be stopped at the top of the chromosphere well above the heights suggested from observations (Brown, 1971; Emslie, 1978). The discrepancy between these suggestions was criticsed by Kane, 1974, who was unaware of the paper by Syrovatskii and Shmeleva, 1972 using the CEA to show that electrons were indeed capable of reaching much greater depths than suggested by the FCA.

Aboudarham and Henoux, 1989 demonstrated that non-thermal ionisation by an electron beam, using the FCA approach of Emslie, 1978, could produce a WL source through Paschen continuum enhancement in the upper chromosphere, they went on to suggest that the chromospheric continuum emission would heat the photosphere via backwarming and result in an increase of H^- emission in the photosphere, explaining the magnitude of WL enhancements that were observed at the time.

The recent observations of co-spatial and co-temporal HXR and WL emission source close to the quiet Sun photosphere in the impulsive phase of solar flares (Battaglia and Kontar, 2011; Martínez Oliveros et al., 2012; Krucker et al., 2015) are clearly at odds with the predictions of models for solar flares using the FCA approach (see section 1.1.5). As a result authors have sought to reconsile the FCA models for beam precipitation by alternative mechanisms that could increase the lower chromospheric and photospheric ionisation degree co-temporally with HXR sources, suggesting energy transport from the corona by Alfven waves (Fletcher and

Hudson, 2008; Kerr et al., 2016). However, these suggestions have yet to provide satisfactory evidence that the proposed alternative mechanisms are responsible for the low height HXR and WL signatutres observed in solar flares, and Krucker et al., 2015 stated that high energy (100keV) beam electrons are the source of the WL emission.

The CEA (Syrovatskii and Shmeleva, 1972; Dobranskis and Zharkova, 2015) to beam electron precipitation does not have such limitations, this is one of the key motivations for the research presented in this thesis. IRIS and the Image Selector offer greater scope for the analysis of high-cadence changes in continuous emission in WL and near-UV, as reported in Heinzel and Kleint, 2014; Kotrč, Procházka, and Heinzel, 2016. Such observations provide an ideal opportunity to examine the predictions of the electron beam delivery model for the locations and intensities of continuous emission, using updated simulations with a dynamic hydrodynamic response to beam heating combined with fully non-LTE radiative modelling.

1.2.7 Seismic responses

There are models that propose energy delivery to the photosphere in solar flares that are sufficient to cause a seismic response (see section 1.1.6). Using the CEA to particle precipitation with mixed particle beams of protons and electrons, Zharkova and Zharkov, 2007 showed that hydrodynamics shocks can reach the photosphere at speeds above the local sound speed. Zharkova and Zharkov, 2015 modelled the deposition of momentum below the heights of surface of the quiet Sun photosphere, and the subsequent production and propagation of acoustic acoustic waves travelling through the solar interior. The waves were shown to return to the surface at their first bounce, with a phase speed relationship that explains the observed acceleration of the quake wave-fronts away from their source.

Donea et al., 2006 suggested that backwarming (heating downward from HXR, SXR etc. in a solar flare) could trigger a seismic response in a solar flare because all examples at the time had been observed to be associated with WL flares. This is no longer the case, therefore backwarming and WL is not a necessary or sufficient condition for a sunquake. Others have suggested that magnetic field changes during the flare release the energy required (Hudson, Fisher, and Welsch, 2008; Fisher et al., 2012). However, incontrovertible confirmation has not yet been found for any of

these triggering mechanisms using observations of flares and their associated sun-quakes.

1.3 Summary

In this chapter we have outlined many advances in the understanding of the physics of solar flares that have been achieved through observations of the emission and modelling. However, we have also highlighted a number of issues associated with solar flares that require explanation. The principle issues are enumerated below for reference:

(1) The lack of high-resolution observations of Lyman line emission profiles in solar flares and the resulting scarcity of comprehensive studies of these emission profiles is problematic in light of the planned missions that will observe Lyman line emission profiles during solar flares (see sections 1.1.3, and 1.2.4).

(2) There is no clear explanation and interpretation of the large red-shifted (1-4Å in Hα) emission in chromospheric line profiles observed during the onsets of solar flares and lasting up to a few minutes (see section 1.1.4).

(3) There are difficulties observing the large red-shifted chromospheric emission resulting from the narrow wavelength windows used in modern spectroscopic observations of Hα (see section 1.1.4).

(4) There is no consistent explanation and modelling that replicates the height and intensity of WL emission observed in the impulsive phase, located at heights close to the photosphere and lasting for minutes after the impulsive phase (see section 1.1.5).

(5) As yet there is not clear evidence of the triggering mechanisms responsible for the seismic responses of the Sun associated with solar flares (see section 1.1.6).

The following chapters present an investigation of solar flares which explains and interprets some of the features of hydrogen emission in order to address the issues listed above, that are not accounted for by existing models. In chapter 2,

the models used for the precipitation of electron beams and the hydrodynamic responses to these beams are presented. In chapter 3, the model for the radiative responses of hydrogen in these atmospheres is described. In chapter 4 the effects of the beam on the optical depths of the hydrogen emission is investigated. Chapter 5 presents the responses in the Lyman lines, and chapter 6 presents the radiative responses in the Balmer and Paschen lines. A case study, comparing our simulations with the observations of the line emission in a C1.5-class flare are presented in chapter 7. Continuum emission from hydrogen is presented in chapter 8, and a summary and evaluation of the findings is given in chapter 9.

Chapter 2

Hydrodynamic Heating of a flaring atmosphere

To simulate radiative responses in a flaring atmosphere one needs to know the physical conditions formed during a solar flare. For this goal we need to consider a hydrodynamic response of the ambient plasma to the heating caused by beam electrons. It has been shown earlier (Somov, Spektor, and Syrovatskii, 1981; Fisher, Canfield, and McClymont, 1985; Nagai and Emslie, 1984; Zharkova and Zharkov, 2007) that the injection into a flaring atmosphere of electrons with power-law energy spectra and their precipitation into deeper atmospheric depths leads to a very fast, within a few seconds, heating of the ambient plasma. This heating is caused by collisions of beam electrons with the ambient particles (Brown, 1971; Syrovatskii and Shmeleva, 1972) or by Ohmic heating (see, for example Emslie, 1981; Zharkova and Gordovskyy, 2006, and references therein).

In this chapter the hydrodynamic response of a flaring atmosphere to the heating by beam electrons is described for different beam parameters.

2.1 Plasma heating by power-law electron beams

2.1.1 Background

In the thick-target model of electron beam propagation (Brown, 1971; Syrovatskii and Shmeleva, 1972) beam electrons lose their energy in collisions with the ambient plasma particles as they are radiating bremsstrahlung as hard X-rays (see section 1.2.2). Electrons are an efficient means of energy transfer from the acceleration

TABLE 1
"STOPPING" COLUMN DEPTHS

	ξ_{max} (cm^{-2})			
E (keV)	$a = 2.7 \times 10^{-12}$ eV^2 cm^2	$\mathcal{E} = 10^{-5}$ V cm^{-1}	$\mathcal{E} = 10^{-4}$ V cm^{-1}	$\mathcal{E} = 10^{-3}$ V cm^{-1}
10	1.8×10^{19}	3.2×10^{19}	3.5×10^{17}	2.2×10^{17}
40	2.9×10^{20}	$>10^{25}$	1.6×10^{18}	2.6×10^{17}
100	1.8×10^{21}	$>10^{25}$	3.2×10^{19}	3.5×10^{17}
400	2.9×10^{22}	$>10^{25}$	$>10^{25}$	1.6×10^{18}

TABLE 2.1: The stopping depths of beam electrons with injected energy shown in the left column (keV), taken from Zharkova and Gordovskyy, 2006. Stopping depths are shown for models considering pure collisional losses (second column) and considering losses due to constant electric fields of difference strengths (three rightmost columns.

region to the lower atmosphere, where the energy is deposited via Ohmic heating and Coulomb collisions, with the ambient plasma that transfers beam electron energy to the plasma and leading to its heating.

Since the 1970s there were two analytical approaches for electron kinetics: the FCA of Brown, 1971 and Emslie, 1978 and the CEA of Syrovatskii and Shmeleva, 1972 considering pure collisional losses, updated recently by Dobranskis and Zharkova, 2015; Zharkova and Dobranskis, 2016 considering both collisional and Ohmic losses. The solutions of Brown, 1971; Emslie, 1978 are restricted to the upper chromosphere because the FCA defines particle numbers at given depths, and it has a singularity when the electron's velocity becomes zero (Mauas and Gómez, 1997). However the solutions by Syrovatskii and Shmeleva, 1972 use a CEA for these abundances. Syrovatskii and Shmeleva, 1972 show that thermalisation of beam electrons happens in the chromosphere only for electron with lower cutoff energies at the collisional (or Ohmic) stopping depths for electrons with given energies (see 2.1, table 1 from Zharkova and Gordovskyy, 2006 or tables in Zharkova and Dobranskis, 2016). While electrons with energies above 80-100 keV can reach deeper photospheric depths of $> 10^{25}$ cm^{-2}.

Moreover, the use of numeric time-dependent solutions describing electron beam kinetics using Fokker-Planck approach (Zharkova, Brown, and Syniavskii, 1995; Zharkova and Gordovskyy, 2005a; Zharkova and Gordovskyy, 2006; Siversky and Zharkova, 2009) helped to describe precipitation of beam electrons, while losing

energy not only in collisions, but also simultaneously in Ohmic losses, and their pitch angles in collisions, electric field and magnetic mirroring. This time-dependent Fokker-Planck approach shows that the beam electrons can still easily reach the photosphere within a very short time-scale (milliseconds). Moreover, heating of the atmosphere is found to start from the photosphere by higher energy electrons (> 100keV), which only later is moving to the upper chromosphere when electrons with a lower cutoff energy reach the collisional stopping depth at this level (Siversky and Zharkova, 2009). The Fokker-Planck approach also shows that electrons precipitating downward naturally produce returning electrons from the same population of energetic electrons (and not from the ambient plasma electrons). The returning electrons (return current) gain large upward velocities, establishing the electric circuit of a direct and return current. Within 1 s a single electron makes up to 100 journeys from the corona where they are injected to the photosphere and back (Siversky and Zharkova, 2009). This electric circuit naturally resolves the 'particle number problem' and at the same time provides strong heating to a flaring atmosphere.

2.1.2 Collisional losses and stopping depths

The power transferred to a plasma through collisions between a beam of particles and the ambient plasma is presented in this section as a function of column depth, so that it is applicable to a stream of electrons travelling down through a flaring atmosphere. It is important that the beam electron densities are calculated as a function of precipitation column depth for use in the calculations of beam electron collisional excitation and ionisation rates in the radiative transfer code, see section 3. Beam electron densities are derived from the CEA discussed in section 1.2.3, and is presented below in the forms given in Syrovatskii and Shmeleva, 1972 and Dobranskis and Zharkova, 2015.

The models we use consider the energy losses of an electron beam due only to collisions (Syrovatskii and Shmeleva, 1972). Future work based on this model could include beam losses due to Ohmic heating and return currents considered using the CEA as presented in the work of Dobranskis and Zharkova, 2015, and for mixed energy losses (Siversky and Zharkova, 2009; Zharkova and Dobranskis, 2016).

Our approach uses the continuity equation (Syrovatskii and Shmeleva, 1972),

$$\frac{\partial}{\partial s}\left[vN\left(E,s\right)\right]+\frac{\partial}{\partial E}\left[\left(\frac{dE}{ds}\right)vN\left(E,s\right)\right]=0, \tag{2.1}$$

rather than the flux conservation equation

$$\frac{\partial}{\partial s}\left[vN\left(E,s\right)\right]=0, \tag{2.2}$$

for a steady flux of energetic particles moving along a definite trajectory under the guide of a strong magnetic field line. s is the displacement downward from the point of injection, and v is the electron mean velocity at this point, E is the energy of the electrons with the number density distribution $N\left(E,s\right)$. The strength of the particle sources is considered to be constant over a time scale required for the beam to cross the absorption region, i.e. no more than a small fraction of a second (Siversky and Zharkova, 2009). The first term of the continuity equation describes the rate of flux loss with the distance travelled through the atmosphere. The second term accounts for the effect of changes to the distribution of the beam at different depths into the plasma. This equation is contrasted with the conservation equation by Emslie, 1978, which uses only the first term of equation (2.1) and ignores the second, and is a valid assumption for the case of laminar flow, that is the case where the the energy distribution of the electrons in the beam does not change with the distance travelled into the plasma.

For non-relativistic collisions, the collisional energy loss rate is (Syrovatskii and Shmeleva, 1972),

$$\frac{dE}{ds}=-\frac{an}{E}, \tag{2.3}$$

where $a\left(E,n(s)\right)$ is the collisional coefficient,

$$a_e=1.3\times10^{-13}\left[\ln\left(\frac{E}{mc^2}\right)-\frac{1}{2}\ln n+38.7\right]. \tag{2.4}$$

m is the mass of an electron and n is number density of the ambient plasma. The terms in the square bracket relate to contributions from electrons, neutral hydrogen atoms, and ions, respectively.

Syrovatskii and Shmeleva, 1972 find the maximum column depth penetrated by

a beam electron, ξ_{max}, with energy E, injected from the corona and undergoing collisional losses with the ambient plasma. To do this one begins from the rate of energy loss of an electron with energy E due to collisions with the ambient plasma,

$$\frac{dE}{d\xi} = \frac{dE}{nds} = -\frac{a}{E}. \tag{2.5}$$

From here the equation is separated and integrated from energy E to 0 and from zero column depth up to ξ_{max} and gives the maximum penetration depth as,

$$\xi_{max} = \frac{E^2}{2a} \tag{2.6}$$

The stopping depths due to collisional losses are calculated by Zharkova and Gordovskyy, 2006 (see Fig.2.1, left column). It was found that the stopping depth due to collisional losses increased from the column depth 1.8×10^{19}cm^{-2} for an electron of kinetic energy 10 keV up to 2.9×10^{22}cm^{-2} for a 400 keV electron. Therefore, the beam electron heating is spread throughout the entire flux tube in our flare models.

Syrovatskii and Shmeleva, 1972 also derive the range of beam electron energies present at depth ξ from a beam of electrons with minimum energy E_1 and maximum energy E_2, injected from the corona and undergoing collisional losses with the ambient plasma. To do this equation (2.5) is again separated and integrated from initial energy $E_{1,2}$ to final energy $E'_{1,2}$. The final values are then set as bounds on the energies as below (with the real part taken to be zero for the answer below the maximum penetration depth),

$$E'_1 = Re\sqrt{E_1^2 - 2a\xi} \leq E \leq Re\sqrt{E_2^2 - 2a\xi} = E'_2 \tag{2.7}$$

The models of Zharkova and Dobranskis, 2016 consider both collisional and ohmic losses. Using these models Zharkova and Dobranskis, 2016 calculated the fractions of precipitating electrons that are present at a given column depth, where 100% represents the total number of electrons including precipitating and returning electrons. An example is shown in Table 2.2, for the precipitating fraction at a column depth of 2.4×10^{19}cm^{-2}. It can be seen from this table that a larger percentage

γ	3		5		7	
$\Delta\mu$	0.2	0.02	0.2	0.02	0.2	0.02
$F = 10^8$	70.8%	71.8%	71.5%	72.1%	71.9%	72.4%
$F = 10^9$	69.2%	69.6%	70.3%	70.5%	71.2%	71.3%
$F = 10^{10}$	63.9%	64.5%	68.2%	68.6%	70.7%	71.1%

TABLE 2.2: The fraction of precipitating electrons at a column depth $\xi = 2.4 \times 10^{19}\text{cm}^{-2}$. Fractions are shown for spectral indices γ, initial fluxes F in units erg·cm^{-2}·s^{-1}, and pitch angle dispersions $\Delta\mu$, where $\mu = \cos\theta$ is the cosine of the angle of precipitation θ.

of precipitating electrons reach a given column depth for a beam with a lower flux, because a weaker beam will induce a weaker electric field. Also, a greater percentage of beam electrons precipitating to a given column depth for a beam of harder spectral index, which has more energy in higher energy electrons than a soft beam.

2.1.3 Continuity equation and the number density of the beam electrons

We now discuss the updated approach from Syrovatskii and Shmeleva, 1972, as presented in Dobranskis and Zharkova, 2015. In this analysis we do not include the self induced electric field of the beam electrons. To make variable dependence explicit we substitute for v in equation (2.1) using the non-relativistic relationship $v = \sqrt{2E/m}$:

$$\frac{\partial}{\partial s}\left[\sqrt{\frac{2E}{m}}N\left(E,s\right)\right] + \frac{\partial}{\partial E}\left[\left(\frac{dE}{ds}\right)\sqrt{\frac{2E}{m}}N\left(E,s\right)\right] = 0, \tag{2.8}$$

$$\frac{\partial}{\partial s}\left[\sqrt{E}N\left(E,s\right)\right] + \frac{\partial}{\partial E}\left[\left(\frac{dE}{ds}\right)\sqrt{E}N\left(E,s\right)\right] = 0. \tag{2.9}$$

The partial differentiation is performed, keeping in mind that $\frac{\partial E}{\partial S} = 0$,

$$\sqrt{E}\frac{\partial N}{\partial s} + \sqrt{E}N\frac{\partial}{\partial E}\left(\frac{dE}{ds}\right) + \frac{1}{2E^{\frac{1}{2}}}N\frac{dE}{ds} + \frac{dE}{ds}E^{\frac{1}{2}}\frac{\partial N}{\partial E} = 0, \tag{2.10}$$

and substitution is performed using the result of equation (2.3)

$$\sqrt{E}\frac{\partial N}{\partial s} + \sqrt{E}N\frac{\partial}{\partial E}\left(-\frac{an}{E}\right) - \frac{1}{2E^{\frac{1}{2}}}N\frac{an}{E} - \frac{an}{E}E^{\frac{1}{2}}\frac{\partial N}{\partial E} = 0. \tag{2.11}$$

This enables the differentiation to be performed, noting that the ambient density n is independent of E, and assuming a_e is slowly varying with E (neglecting the dependence of a_e on E),

$$\sqrt{E}\frac{\partial N}{\partial s} + \sqrt{E}N\frac{an}{E^2} - \frac{an}{2E^{\frac{3}{2}}}N - \frac{an}{E^{\frac{1}{2}}}\frac{\partial N}{\partial E} = 0. \tag{2.12}$$

$$\frac{\partial N}{\partial s} + N\frac{an}{E^2} - \frac{an}{2E^2}N - \frac{an}{E}\frac{\partial N}{\partial E} = 0. \tag{2.13}$$

$$\frac{\partial N}{\partial s} - \frac{an}{E}\frac{\partial N}{\partial E} = -\frac{an}{2E^2}N. \tag{2.14}$$

Now the equations are converted to units of column depth ξ, rather than vertical displacement, s, where $\xi = \int_0^s n(t)dt$, so $d\xi = nds$.

$$\frac{\partial N}{n\partial s} - \frac{a}{E}\frac{\partial N}{\partial E} = -\frac{a}{2E^2}N. \tag{2.15}$$

$$\frac{\partial N}{\partial \xi} - \frac{a}{E}\frac{\partial N}{\partial E} = -\frac{a}{2E^2}N. \tag{2.16}$$

Dobranskis and Zharkova, 2015 solve this equation by the method of characteristics which separates a partial differential equation into a system of ordinary differential equations: An equation

$$a(x,y,z)\frac{\partial z}{\partial x} + b(x,y,z)\frac{\partial z}{\partial y} = c(x,y,z). \tag{2.17}$$

with solution $z(x,y)$ has a normal direction to the surface $z = z(x,y)$ defined by,

$$\left(\frac{\partial z}{\partial x}, \frac{\partial z}{\partial y}, -1\right). \tag{2.18}$$

Thus, by the equation (2.17) and dot product relationship, we see that a tangent direction to the solution surface is given by (a,b,c). This gives the relationship

$$\frac{dx}{a} = \frac{dy}{b} = \frac{dz}{c}, \tag{2.19}$$

which may be separated by use of a chosen parameter to give the ordinary differential equations:

$$\frac{dx}{dt} = a, \frac{dy}{dt} = b, \frac{dz}{dt} = c. \tag{2.20}$$

Therefore the characteristic equations for equation (2.16) are as follows:

$$\frac{d\xi}{dt} = 1, \tag{2.21}$$

which is integrated from the top of the field line where $\xi = 0$ and we choose $t = 0$ here.

$$[\xi]_0^{\xi} = [t]_0^t \tag{2.22}$$

$$\xi = t. \tag{2.23}$$

$$\frac{dE}{dt} = -\frac{a}{E}, \tag{2.24}$$

This is integrated using the condition for the top of the flux tube $E(t = 0) = E_0$,

$$\int_{E_0}^{E} E\frac{dE}{dt}dt = -a\int_0^t dt, \tag{2.25}$$

$$\left[\frac{E^2}{2}\right]_{E_0}^{E} = [-at]_0^t, \tag{2.26}$$

$$E = \sqrt{E_0^2 - 2at} = \sqrt{E_0^2 - 2a\xi}. \tag{2.27}$$

$$\frac{dN}{dt} = -\frac{aN}{2E^2}, \tag{2.28}$$

Here it is defined at the top of the flux tube $N(t = 0) = N_0$, and so (again neglecting the dependence of a on E),

$$\int_{N_0}^{N} \frac{1}{N}\frac{dN}{dt}dt = -\frac{a}{2}\int_0^t \frac{1}{E^2}dt, \tag{2.29}$$

where E is a function of t expressed using the relationship in equation (2.27):

$$\int_{N_0}^{N} \frac{1}{N}dN = -\frac{a}{2}\int_0^t \frac{1}{E_0^2 - 2at}dt, \tag{2.30}$$

$$[\ln N]_{N_0}^{N} = \left[\frac{1}{4}\ln(E_0^2 - 2at)\right]_0^t, \tag{2.31}$$

$$\ln \frac{N}{N_0} = \frac{1}{4} \ln \left(\frac{E_0^2 - 2at}{E_0^2} \right), \tag{2.32}$$

$$N = N_0 \frac{(E_0^2 - 2at)^{\frac{1}{4}}}{E_0^{\frac{1}{2}}} = N_0 \frac{E^{\frac{1}{2}}}{(E + 2at)^{\frac{1}{4}}}, \tag{2.33}$$

$$N = N_0 \frac{(E_0^2 - 2a\xi)^{\frac{1}{4}}}{E_0^{\frac{1}{2}}} = N_0 \frac{E^{\frac{1}{2}}}{(E + 2a\xi)^{\frac{1}{4}}}. \tag{2.34}$$

The initial condition for electron beam energy at the top of the plasma, $\xi = 0$ is a power law spectrum with 0.5 added so that γ is the spectral index for electron flux $F = vN = const \times E_0^{-\gamma}$, where $E_0 = 1/2mv^2$ and so $v = \sqrt{2E_0/m} = const \times E_0^{\frac{1}{2}}$, so we need $N = const \times E_0^{-\gamma - \frac{1}{2}}$,

$$N_0 = N(E_0, 0) = KE^{-\gamma - \frac{1}{2}} \Theta(E_0 - E_{low}) \Theta(E_{upp} - E_0). \tag{2.35}$$

$\Theta(x)$ is a Heaviside function, that is zero when x is negative and one when it is positive. Here it is used to 'zero' the function outside the lower and upper energy bounds E_{low} and E_{upp}. The constant of integration, K, is found from the normalisation of the initial energy flux of the beam electrons at the top of the model,

$$F_0 = \int_{E_{low}}^{E_{upp}} EvN(E, \xi = 0) dE, \tag{2.36}$$

$$F_0 = K \left(\frac{2}{m} \right)^{\frac{1}{2}} \begin{cases} \frac{E_{upp}^{\gamma-2} - E_{low}^{\gamma-2}}{2-\gamma}, & \gamma \neq 2, \\ \ln \left(\frac{E_{upp}}{E_{low}} \right), & \gamma = 2, \end{cases} \tag{2.37}$$

as defined in Syrovatskii and Shmeleva, 1972; Dobranskis and Zharkova, 2015. Thus,

$$N = KE_0^{-\gamma - \frac{1}{2}} \frac{E^{\frac{1}{2}}}{(E + 2a\xi)^{\frac{1}{4}}} \Theta((E + 2a\xi)^{\frac{1}{2}} - E_{low}) \Theta(E_{upp} - (E + 2a\xi)^{\frac{1}{2}}), \tag{2.38}$$

$$N = K((E + 2a\xi)^{\frac{1}{2}})^{-\gamma - \frac{1}{2}} \frac{E^{\frac{1}{2}}}{(E + 2a\xi)^{\frac{1}{4}}} \Theta((E + 2a\xi)^{\frac{1}{2}} - E_{low}) \Theta(E_{upp} - (E + 2a\xi)^{\frac{1}{2}}), \tag{2.39}$$

$$N = K(E + 2a\xi)^{-\frac{\gamma}{2} - \frac{1}{4}} (E + 2a\xi)^{-\frac{1}{4}} E^{\frac{1}{2}} \Theta((E + 2a\xi)^{\frac{1}{2}} - E_{low}) \Theta(E_{upp} - (E + 2a\xi)^{\frac{1}{2}}), \tag{2.40}$$

$$N = K(E + 2a\xi)^{-(\frac{\gamma}{2} + \frac{1}{2})} E^{\frac{1}{2}} \Theta((E + 2a\xi)^{\frac{1}{2}} - E_{low}) \Theta(E_{upp} - (E + 2a\xi)^{\frac{1}{2}}). \tag{2.41}$$

Therefore we arrive at the number of particles of energy E at depth ξ from Syrovatskii and Shmeleva, 1972,

$$N(E,\xi) = KE^{\frac{1}{2}}\sqrt{2a\xi + E^2}^{-\frac{\gamma+1}{2}}\Theta(\sqrt{2a\xi + E^2} - E_{low})\Theta(E_{upp} - \sqrt{2a\xi + E^2}). \quad (2.42)$$

2.1.4 The heating delivered by beam electrons to the plasma at depth ξ

Syrovatskii and Shmeleva, 1972 derive the rate at which energy $\wp(\xi, n)$ is delivered by the beam of electrons with power law energy spectrum to a column depth ξ, but if this energy is equipartitioned to particles we will need to specify the density of the plasma at this depth to work out the total rate of energy delivery to a given depth. We have to work out the contributions from each energy level present in the beam at this depth, namely the energies between E_1' and E_2'. Therefore, we multiply the plasma density at this depth $n(\xi)$ by the rate of energy gained by the plasma, $\frac{dE}{d\xi}$ (the negative of the energy loss rate of the beam) and also by the rate of arrival of beam electrons (Syrovatskii and Shmeleva, 1972).

$$\wp(\xi, n) = \int_0^\infty \left[-n(\xi)\left(\frac{dE}{d\xi}\right)\right] vN(\xi, n)dE = nP(\xi), \quad (2.43)$$

where,

$$P(\xi) = aK\sqrt{\frac{2}{m_e}}(2a\xi)^{-\frac{\gamma}{2}}\frac{1}{2}\int_{t_1}^{t_2}\frac{t^{-\frac{1}{2}}dt}{[1+t]^{\frac{\gamma+1}{2}}}, \quad (2.44)$$

where $t_{1,2}$ relates to the maximum and minimum energies of the electrons in the beam

$$t_{1,2} = \max\left[0, \frac{E_{1,2}^2}{2a\xi} - 1\right], \quad (2.45)$$

and K is the scaling factor, found through the normalisation of the distribution function on electron density.

The term on the right is integrated analytically using Syrovatskii and Shmeleva, 1972's equation 14 for the case $0 \leq (2a\xi/E_1^2) < 1$:

$$\frac{1}{2}\int_{t_1}^{t_2}\frac{t^{-\frac{1}{2}}dt}{[1+t]^{\frac{\gamma+1}{2}}} = \frac{1}{\gamma}t_1^{-\frac{1}{2}}F\left(\frac{\gamma+1}{2}, \frac{\gamma}{2}; \frac{\gamma+2}{2}; -\frac{1}{t_1} - t_2^{-\frac{1}{2}}\right)F\left(\frac{\gamma+1}{2}, \frac{\gamma}{2}; \frac{\gamma+2}{2}; -\frac{1}{t_2}\right) \quad (2.46)$$

and for the case $1 \leq (2a\xi/E_1^2) < (E_2^2/E_1^2)$:

$$\frac{1}{2}\int_{t_1}^{t_2} \frac{t^{-\frac{1}{2}}dt}{[1+t]^{\frac{\gamma+1}{2}}} = \left[\frac{1}{2}B\left(\frac{1}{2},\frac{\gamma}{2}\right) - t_2^{-\frac{1}{2}}\frac{1}{\gamma}F\left(\frac{\gamma+1}{2},\frac{\gamma}{2};\frac{\gamma+2}{2};-\frac{1}{t_2}\right)\right], \tag{2.47}$$

where F is the hypergeometric function,

$$F(\alpha,\beta;\gamma;z) = \frac{1}{B(\beta,\gamma-\beta)}\int_0^1 t^{\beta-1}(1-t)^{\gamma-\beta-1}(1-tz)^{-\alpha}dt \tag{2.48}$$

and B is the beta function.

2.2 Hydrodynamic Response

2.2.1 Governing hydrodynamic equations

In section 1.2.3, the hydrodynamic response of the ambient plasma to an injection of non-thermal beam electrons during a solar flare was discussed. Here we describe the hydrodynamic models that will provide the physical atmosphere used as input by the radiative transfer code described in chapter 3.

The dynamics of a flaring atmosphere was simulated for the two-temperature plasma (electrons and ions) in the work of Somov, Spektor, and Syrovatskii, 1981; Zharkova and Zharkov, 2007; Zharkova and Zharkov, 2015, including the consideration of ion viscosity and radiative colling by optically thin coronal emission and optically thick hydrogen emission (Kobylinskii and Zharkova, 1996). Therefore, the set of hydrodynamic equations they solve self-consistently includes energy equations of ions and of electrons alongside the momentum and continuity equations. The physical conditions derived using the models of Somov, Spektor, and Syrovatskii, 1981; Zharkova and Zharkov, 2007; Zharkova and Zharkov, 2015 are presented in terms of plasma number density n_i, electron temperature T_e, ion temperature T_i, and plasma macro-velocity in the direction of the flux tube v_m. The continuity equation:

$$\frac{\partial n}{\partial t} + n^2\frac{\partial v}{\partial \xi} = 0. \tag{2.49}$$

The momentum equation:

$$\frac{\partial v}{\partial t} + \frac{1}{\mu}\frac{\partial}{\partial \xi}\left[nk_B(T_i + xT_e)\right] = \frac{4}{3}\frac{1}{\mu}\frac{\partial}{\partial \xi}\left(\eta_i n^2 \frac{\partial v}{\partial \xi}\right) + g_\odot. \tag{2.50}$$

Energy equation for ions:

$$\frac{nk_B}{\gamma - 1}\frac{\partial T_i}{\partial t} - k_B T_i \frac{\partial n}{\partial t} = \frac{4}{3}\eta_i n^2 \left(\frac{\partial v}{\partial \xi}\right)^2 + Q(n, T_e, T_i). \tag{2.51}$$

Energy equation for electrons:

$$\frac{nk_B}{\gamma - 1}\frac{\partial xT_e}{\partial t} - xk_B T_e \frac{\partial n}{\partial t} + n\chi_H \frac{\partial x}{\partial t} = n\frac{\partial}{\partial \xi}\left(\kappa n \frac{\partial T_e}{\partial \xi}\right) + P(n, \xi) - L(n, T_e) - Q(n, T_e, T_i). \tag{2.52}$$

These state variables representing number density, plasma macro-velocity, and ion and electron kinetic temperature are presented as functions of time, t sec and the plasma column depth, ξ, in units cm^{-2} representing the total number of particles above a given point, z in the flux tube per centimetre squared, $\xi = \int_0^z n(z)dz$ using the hydrodynamic equations above, presented in Zharkova and Zharkov, 2007, section 3. μ is mean molecular mass $\mu = 1.44m_H$ where m_H is the mass of the hydrogen atom, k_B is the Boltzmann constant, x is the ionisation degree of the plasma, η_i is the ion viscosity, $g_\odot$ is the acceleration due to the gravity of the sun. The energy equation for ions (2.51) relates the thermodynamic energy quantites of the ions to the rate of energy exchange between the ambient electrons and the ions $Q(n, T_e, T_i)$. γ is the adiabatic constant. The energy equation for electrons (2.52) also includes the volume heating rate by beam electrons through collisions $P(n, \xi)$ as defined in section 2.1, and $L(n, T_e)$ is the radiative loss rate $L(n, T_e) = n^2 xL(T_e) + nL_H(n, T)$ erg·cm^{-3}·s^{-1}, where $L(T_e)$ is the loss function from the optically thin coronal emission taken from Cox and Tucker, 1969 and $L_H(n, T_e)$ is the radiative loss function for all hydrogen lines calculated for the optically thick atmosphere from Zharkova and Kobylinskii, 1993. χ_H full ionisation potential of the hydrogen atom.

The continuity equation (2.49) is a statement of the fact that the rate of change of density is dependent on the rate of change in plasma velocity at that point, i.e. if the velocity profile is decreasing with column depth then plasma density increases, if velocity increases with depth then the plasma density decreases, but if the velocity is

constant with depth then the inflow and outflow balance and the density is constant in time. The momentum equation (2.50) relates the factors affecting the average change in velocity of the ambient plasma at a point in time and space. The first term on the left is the rate of change in velocity downwards, which is influenced positively from the acceleration due to gravity (second term on the right side), but is resisted by pressure forces from the ambient ions and electrons (second term on the left side of the equation), there is also an ion viscous heating term considered (first term on the right side). The time-steps in these simulations were $\sim 10^{-4}$ s. Sometimes the time-steps were reduced to $\sim 10^{-5}$ s in order to resolve shocks in the low-temperature condensations.

2.2.2 Initial conditions

In the models we employ there is initially an isothermal temperature distribution, $T_e(0,\xi) = T_i(0,\xi) = T_0 = 6700$ K. The plasma macro-velocities are set to zero $v(0,\xi) = 0$, and the distribution of plasma density is in hydrostatic equilibrium, defined by the relation $n(0,\xi) = n_{min} + h_0^{-1}(\xi - \xi_{min})$, where $n_{min} = 10^{10}$ cm^3 and h_0 is the scale height $h_0 = \frac{k_B[1+x(T_0)]T_0}{\mu g_\odot}$.

Now we define the boundary conditions. The solution is defined in a region limited to the flux tube in terms of column depth $\xi_{min} \leq \xi \leq \xi_{max}$, with an upper boundary $\xi_{min} = 2 \times 10^{17}$ cm^{-2} initially 2500 km above the quiet Sun photosphere and a lower boundary initially at quiet Sun photospheric surface with $\xi_{max} = 1 \times 10^{23}$ cm^{-2}. In this depth there are 150 depth points that are equally spaced in $\ln(\xi)$. There is no initial heat flux at the top of the flux tube, i.e.,

$$\frac{\partial T_e(0,\xi_{min})}{\partial \xi} = \frac{\partial T_i(0,\xi_{min})}{\partial \xi} = 0 \tag{2.53}$$

The top of the flux tube is a free surface with a coronal pressure applied from above,

$$\frac{\partial v(t,\xi_{min})}{\partial \xi} = \frac{4}{3}\frac{1}{n\eta_i}\{p(t,\xi_{min}) - p_{cor}[z(t,\xi_{min})]\} \tag{2.54}$$

with $p(t,\xi_{min}) = nk_B(T_i + xT_e)$ and $p_{cor}[z(0,\xi_{min})] = n_{min}k_B[1 + x(T_0)]T_0$, where x is the ionisation degree defined by a modified Saha formula (Somov, Spektor, and

Syrovatskii, 1981). Somov, Spektor, and Syrovatskii, 1981 note that although these initial conditions are not an excellent approximation, that the beam rapidly heats the atmosphere, and that using various other initial conditions in their models had little affect on the results a few seconds into the simulation.

In contrast, Allred et al., 2005 generate the pre-flare atmosphere for their hydrodynamic models from the PF2 atmosphere of Abbett and Hawley, 1999: A corona is fixed to the atmosphere by holding the top boundary at a temperature of 10^6K and quiescent heating is applied to the bottom of the model to fix the temperature at the base of the photosphere. Then the initial state used by Carlsson and Stein, 1992 was allowed to relax to hydrostatic and energetic equilibrium.

2.3 Hydrodynamic response to a beam heating

Using the code of Zharkova and Zharkov, 2007 described in sections 2.1 and 2.2 the hydrodynamic responses to heating by beams of non-thermal electrons injected from the corona into the quiet Sun (QS) chromosphere are simulated using the methodology described above (Somov, Spektor, and Syrovatskii, 1981; Zharkova and Zharkov, 2007).

The beam electrons are injected with a power-law electron spectrum for energies above a lower energy cut-off $E_c = 10$keV and a power-law spectral index γ. The initial flux of the beam F_0 at the top of the model $\xi_{min} = 2 \times 10^{17}$ cm^{-2} is a function of time matching an elementary HXR burst profile in a flare, with duration of 10 s and a triangular flux profile in time: $F_0 = 0$ at 0 s and 10 s and a maximum at 5 s.

The hydrodynamic responses of the ambient plasma to injection of hard electron beams (spectral index $\gamma = 3$) and initial fluxes 10^{10}, 10^{11} and 10^{12} erg·cm^{-2}·s^{-1} at the top of the flux tube are shown in Fig.2.1. Hereafter, these models are referred to as the F10, F11, and F12 models respectively.

It can be seen from Fig.2.1 that within seconds an electron beam converts the quiet Sun chromosphere into a flaring atmosphere with its own flaring corona, transition region, and chromosphere. After five seconds of beam injection these regions

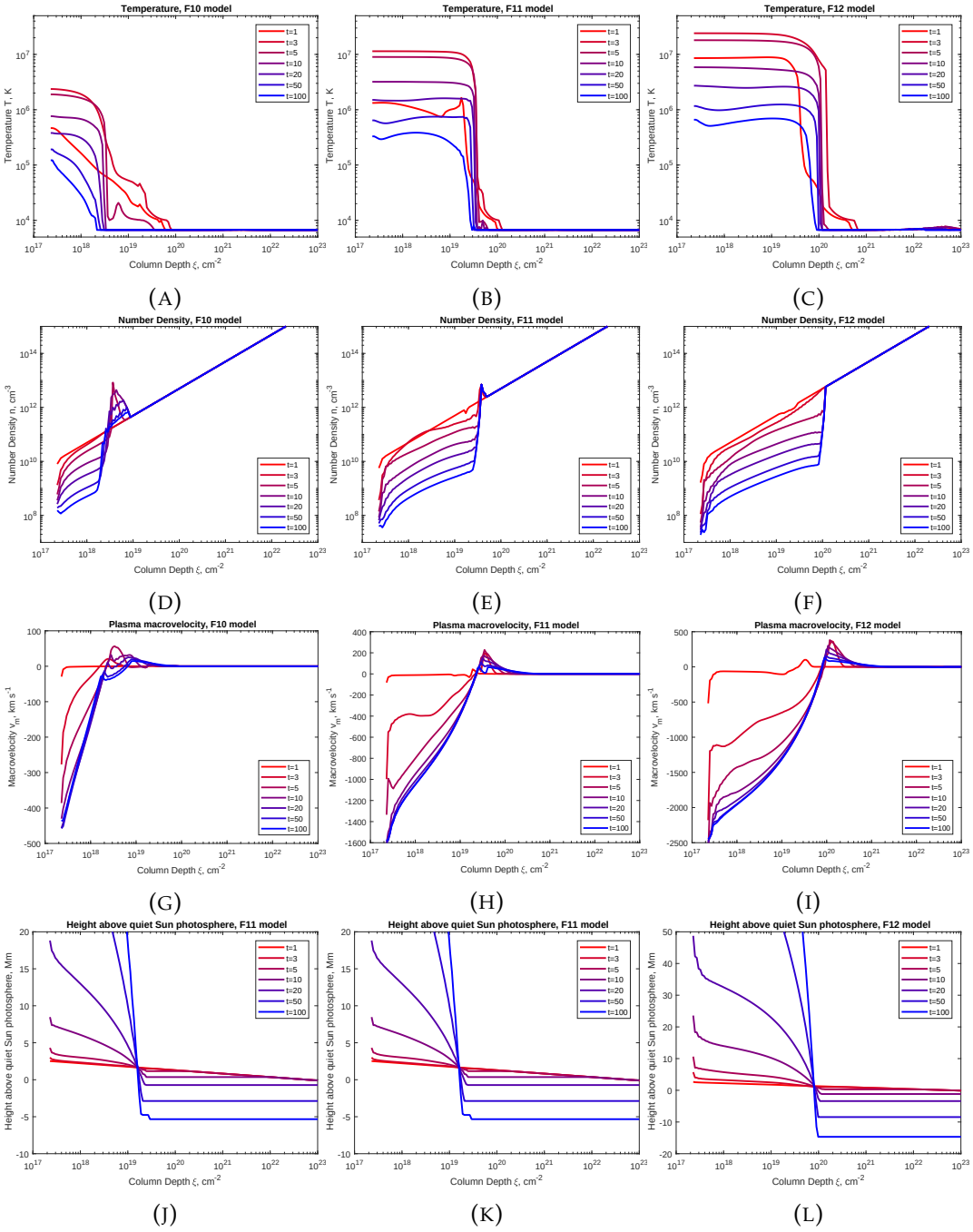

FIGURE 2.1: Hydrodynamic responses of the ambient plasma to electron beam heating for the F10 (a, d, g, j), F11 (b, e, h, k), and F12 (c, f, i, l) models for times from $t = 1$ s (in red) to $t = 100$ s (in blue). The top panels (a, b, c) show the temperatures of the thermal electrons; the panels in the second row (d, e, f) show the plasma densities; the panels of the third row (g, h, i) show plasma bulk macro-velocity, and those in the bottom row (j, k , l) show the relationship between the column depth and height. Each sub-figure is plotted against the column depth in the flux tube (cm^{-2}) from 10^{17} on the left to 10^{23} on the right.

can be clearly discerned from the temperature responses, with the coronal temperatures ($T > 10^6$ K) dropping sharply in the flaring transition regions to the temperatures of flaring chromospheres ($T \sim O(10^4)$ K). Fig.2.1 (top panels) displays the electron temperature responses against column depth for times from 1 (red line) to 100 s (blue line). The magnitudes of the temperature increases in the flaring corona are positively correlated with the initial flux of a beam seen to reach around 2 MK in the F10 model (panel a), 10 MK in the F11 model (panel b) and 25 MK in the F12 model. These temperatures occur at plasma depths smaller than the flare transition region (TR, called flare transition layer in Somov, Spektor, and Syrovatskii, 1981). The beam electrons sweep the coronal plasma to deeper atmospheric levels and create a hydrodynamic shock travelling towards the photosphere and beneath (Zharkova and Zharkov, 2007; Zharkova and Zharkov, 2015). The column depth of the flare transition region is shifted towards deeper atmospheric levels with the increase of the beam's initial flux from 3×10^{18} cm^{-2} for the F10 model to 1×10^{20} cm^{-2} for the F12 model. Once the electron beam stops, at 10 s, the temperature in the flaring corona begins to drop as energy is radiated and conducted away. In the F10 model the flaring corona drops to the sub-million Kelvin range within 20 s, and drops to around 10^5K at the top of the model after 100 s. The temperature drops to 1 MK in the flare corona by around 30 s in the F11 model, and 70 s in the F12 model.

The ambient plasma density also changes following a hydrodynamic response to the beam heating (Fig.2.1, central panel row) showing decreases from chromospheric densities to the coronal ones over the hundred sections simulated above the flare transition region. A high density and low temperature condensation below the flare transition layer due to the formation of shock moving downward to the photosphere.

The plasma heated by beam electrons is swept to deeper atmospheric levels causing the up-flows of chromospheric plasma into the overlying corona and the formation of a hydrodynamic shock of condensed plasma moving downward to the photosphere, which are seen in the macro-velocity responses (Fig.2.1, bottom panels). Since the quiet Sun plasma densities are lower at smaller column depths, the beams of smaller incident flux sweep less plasma. At 5 s we see that the high density

peaks which result from the downward travelling condensations have plasma densities of about 10^{13} cm^{-3} in each model (Fig.2.1). It is evident that for the F10 model the density increase in the condensation appears more noticeable compared to the surrounding plasma than in the F11 and F12 models.

Similarly to the temperature increase, the velocities of generated hydrodynamic shocks are also scaled rather closely by the initial flux of an electron beam. For example, at 5 s after a beam onset the maximum down-flow speed varies from 57 km·s^{-1} for the F10 model, to 382 km·s^{-1} for the F12 model. The hydrodynamic shocks move the flare photosphere downward and penetrate to larger column depths, at the levels of the quiet Sun photosphere and beneath (Zharkova and Zharkov, 2015). The shock reaches the height of the quiet sun photosphere after 13 s in the F11 (Fig.2.1, panel k) and after 6 s in the F12 model (Fig.2.1, panel l). At the same time as the downward condensations there are strong up-flow motions reflecting either gentle (for weaker beams) or explosive (for stronger beams) evaporation of the swept chromospheric plasma back into the corona with the velocities positively correlated to the beam's initial flux (Fig.2.1, third row, at heights above the flare transition layer) (Somov, Spektor, and Syrovatskii, 1981; Fisher, Canfield, and McClymont, 1985; Zharkova and Zharkov, 2007). This evaporation starts after the beam onset and lasts for a few thousand seconds or longer, until the initial quiet Sun atmosphere is restored (Somov, Spektor, and Syrovatskii, 1981; Fisher, Canfield, and McClymont, 1985).

2.3.1 Hydrodynamic response used in chapter 5

The physical conditions of the flaring atmospheres in the F10, F11, and F12 models are presented in Fig.2.2 for use in chapter 5. The temperatures (K), macro-velocities (km·s^{-1}), and densities (cm^{-3}) are shown in the Y-axes of Fig.2.2, versus a column depth (cm^{-2}) on the X-axis on the top, middle and bottom rows, respectively. The profiles are shown for the F10, F11, and F12 atmospheric models from the left to the right column, respectively. For each figure the the initial atmosphere ($t = 0$ s) is shown by the black line, for the impulsive phase ($t = 2, 4$ s) by the red lines, and the gradual phase ($t = 15, 30, 60, 90$ s) by the purple to blue lines. The times of the responses shown in the figure are selected to match the times used in the analysis of the line and continuum profiles in chapter 5.

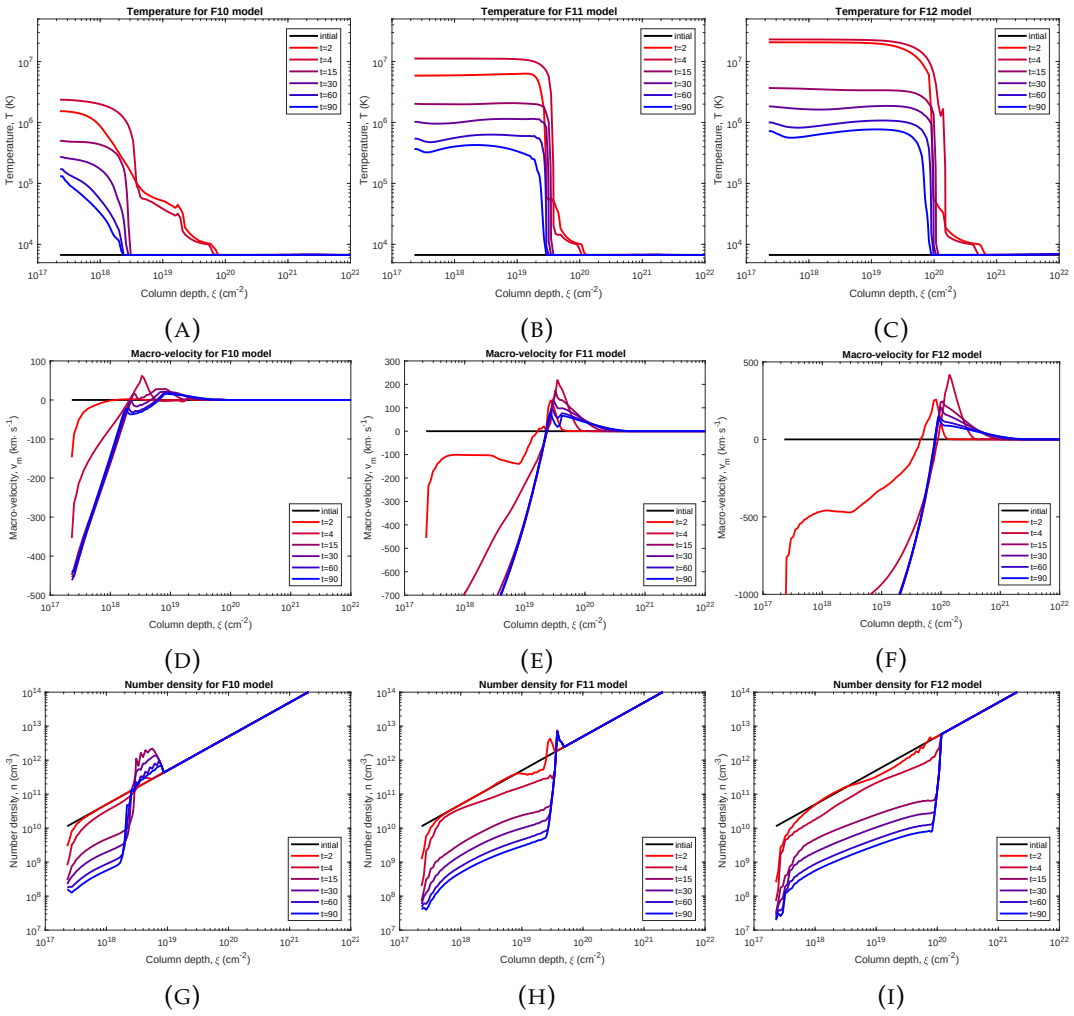

FIGURE 2.2: Simulated hydrodynamic responses for chapter 5. (top row) The temperatures (K), (middle row) macro-velocities (km·s^{-1}), and (bottom row) densities (cm^{-3}) versus column depth (cm^{-2}) are shown for the F10 (left column), F11 (middle column), and F12 (right column) atmospheric models. These profiles are shown for the initial atmosphere ($t = 0$s, black line), impulsive phase atmosphere ($t = 2, 4$s, red lines), and gradual phase ($t = 15, 30, 60, 90$s, purple to blue lines) of the simulation in each figure. The times shown are selected because these are the times used for the spectral profiles shown in chapter 5.

2.3.2 Hydrodynamic response used in chapter 7

For the physical conditions in a flaring atmosphere in chapter 7 the parameters of an injected beam are selected close to the range of parameters of HXR emission derived from RHESSI for the event (see section 7.1.1). Three hydrodynamic models were produced for heating by beam electrons with the initial energy fluxes covering the upper and lower estimates: $F_0 = 7 \times 10^9$ (7F9 model), $F_0 = 10^{10}$ erg·cm^{-2}·s^{-1} (F10 model) and $F_0 = 3 \times 10^{10}$ erg·cm^{-2}·s^{-1} (3F10 model). The duration of beam injection is chosen as 10 s to match the duration of the HXR signatures in a typical elementary flare burst and more specifically, in this case, the fast rise in Hα emission. The initial energy flux of a beam varies as a triangular function in time, with maximum at five seconds (Zharkova and Zharkov, 2007).

Fig.2.3 shows plots of electron kinetic temperatures (a and d), macro-velocities (b and e) and plasma number densities (c and f) as functions of column depth calculated as a hydrodynamic response of the ambient plasma to injection of a power-law beam with the initial flux of 10^{10} erg·cm^{-2}·s^{-1} (F10 model, left panels) and 3×10^{10} erg·cm^{-2}·s^{-1} (3F10 model, right panels). The initial QS chromosphere density is indicated by the straight lines in Figs.2.3c and f. The flaring transition region is swept by the beam towards 3×10^{18} cm^{-2} (F10 model) or 9×10^{18} cm^{-2} (3F10 model), with the flaring chromosphere extending to 8×10^{19} cm^{-2} (F10 model) or 2×10^{20} cm^{-2} (3F10 model) followed by a flaring photosphere (Fig.2.3).

Temperatures in the flaring corona are strongly increased compared to the initial chromospheric temperature, with the magnitude scaled proportionally with the beam initial flux (compare Figs.2.3a and d). While the ambient density is significantly reduced from the initial QS chromospheric magnitude (10^{10} cm^{-3}) to $10^9 - 10^8$ cm^{-3} to form the new corona of a flaring atmosphere (Somov, Spektor, and Syrovatskii, 1981) (Fig.2.3c). These trends are similar to hydrodynamic models heated by electron beams with the same parameters reported by Fisher, Canfield, and McClymont, 1985. The beams with moderate initial fluxes considered in this study do not heat the flaring corona to 10 MK (see Figs.2.3a and d) that is fully acceptable according to the statistical analysis of SXR emission in flares (Ryan et al., 2012). However, our hydrodynamic model heated by beams with the initial energy fluxes of

10^{11} erg·cm^{-2}·s^{-1} or greater is proven to produce coronal temperatures of 10-20 MK (Somov, Spektor, and Syrovatskii, 1981; Zharkova and Zharkov, 2007; Zharkova and Zharkov, 2015) (see Fig.2.3).

The upward motion of a flaring plasma is reflected in the macro-velocity plots (Figs.2.3 b and e) showing evaporation of chromospheric plasma upwards to the newly formed corona at the column depths between 10^{17} and 10^{19} cm^{-2}) (Figs.2.3b, area below the box 1). This evaporation lasts, in general, for a few thousand seconds expanding upwards with increasing velocities even after the beam is stopped (Somov, Spektor, and Syrovatskii, 1981; Zharkova and Zharkov, 2007). The evaporation velocities range from a few tens of km·s^{-1} (at 1 s) to four hundred km·s^{-1} (at 20-100 s). The evaporation will increase the coronal density at later times (>3-5 min) as reported from observations (Polito et al., 2016; Duijveman, Somov, and Spektor, 1983).

At the same time, the beam energy deposition leads to formation of a low temperature condensation in the flaring chromosphere seconds after beam injection begins (Figs.2.3a, b, box 2) with a slightly increased temperature up to 10^4 K. This condensation moves as a shock towards the photosphere and interior (Zharkova and Zharkov, 2015) with velocities from 30-35 km·s^{-1} (7F9 model) up to 50 km·s^{-1} (F10 model) (Fig.2.3b) and up to 90 km·s^{-1} (3F10 model) (Fig.2.3e). The density of this shock is about 10^{13} cm^{-3} (Fig.2.3c). This is different from the results of hydrodynamic models using the FCA in a pre-heated atmosphere, where the shock is formed at upper atmospheric depths (Allred et al., 2005; Kennedy et al., 2015; Polito et al., 2016), because of their different initial atmospheres and heating functions (see section 1.2.3). However, hydrodynamic models using both the FCA and CEA, when simulated for a longer time (above 100 s considered in this paper), consistently show chromospheric plasma evaporation to the corona (Somov, Spektor, and Syrovatskii, 1981; Zharkova and Zharkov, 2007; Zharkova and Zharkov, 2015) with similar velocities up to 1000 km·s^{-1} (Fisher, Canfield, and McClymont, 1985; Polito et al., 2016) or up to 1500 km·s^{-1}(Somov, Spektor, and Syrovatskii, 1981; Zharkova and Zharkov, 2007; Zharkova and Zharkov, 2015).

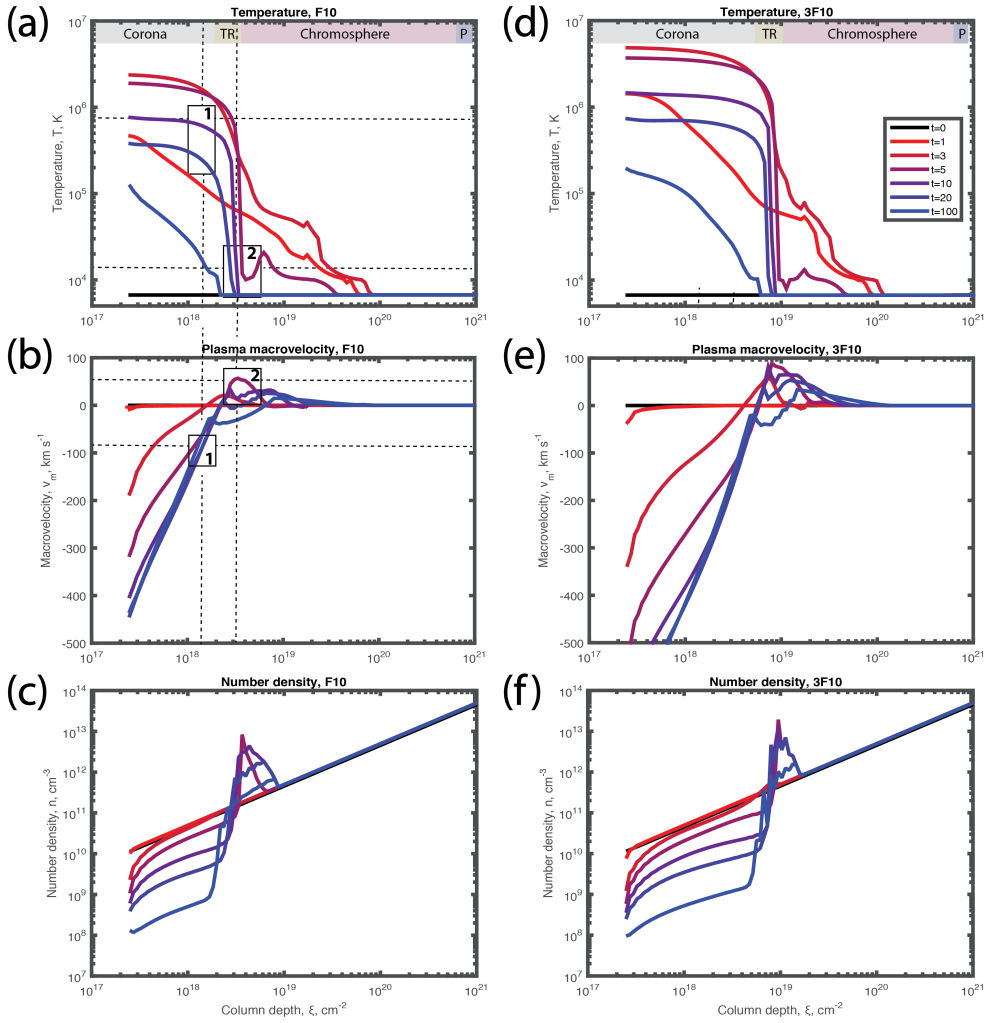

FIGURE 2.3: Simulated hydrodynamic responses for the observed flare studied in chapter 7. The simulated hydrodynamic responses of a flaring atmosphere to injection of a beam with the initial flux of 10^{10} erg·cm^{-2}·s^{-1} (F10 model, left panels) and 3×10^{10} erg·cm^{-2}·s^{-1} (3F10 model, right panels) following Zharkova and Zharkov, 2007 showing column depth dependencies of: (a and d) - the electron kinetic temperature, K, (b and e) - the plasma macro-velocity, km·s^{-1}, and (c and f) - the plasma number density, cm^{-3} forming a flaring corona, chromosphere and photosphere (see the text for more details).

2.4 Comparison with hydrodynamic responses using RADYN

In section 1.2.3 the differences were described between the hydrodynamic models that use FCA to beam precipitation, and those using the CEA. In this section we directly compare the results of the hydrodynamic model used as input to our radiative transfer code, which uses the CEA, with the RADYN model of Allred et al., 2005, which uses the FCA.

The hydrodynamic response to beam heating in the F10 model of RADYN (Allred et al., 2005) is shown in Figs.2.4 and 2.5. In this model the beam flux of 10^{10}erg·cm^{-2}s^{-1} is applied throughout the full duration of the simulation (for 226 s). In the top rows we see the temperature distribution as a solid line and the initial temperature as a dotted line. The middle panels show the electron density (solid lines) and pre-flare electron density (dotted lines), additionally there is a dashed line showing the beam heating function in each panel with its scale on the right hand Y-axis. The lower panels show the density functions (solid lines) and the initial density functions (dotted lines), additionally Fig.2.4 shows the hydrogen ionisation degree of the as a dashed line and Fig.2.5 shows the He III fraction (completely ionised helium fraction) as a dashed line.

One can immediately see for the F10 model of RADYN that the beam heating function is very highly peaked in the mid-upper chromosphere at the stopping depths of their lower energy cut-off electrons in the first seconds of their simulations (panels 5, 6, 7). This is because the RADYN code (Allred et al., 2005) uses the heating function of Brown, 1971; Nagai and Emslie, 1984 which generates what the authors refer to as a *chromospheric hot spot* due to the abrupt cut-off in the injected power law energy distribution at the stopping depth of the electrons with the lower cut-off energy. However, Mauas and Gómez, 1997 compared these results with those generated by solving the full relativistic Fokker-Planck (FP) equation, and concluded that a beam's energy is deposited in a deeper and much broader range of atmospheric column depth than suggested by Nagai and Emslie, 1984. Although the full FP approach also has a plasma depth with a maximum of heating rate, it is found to be in

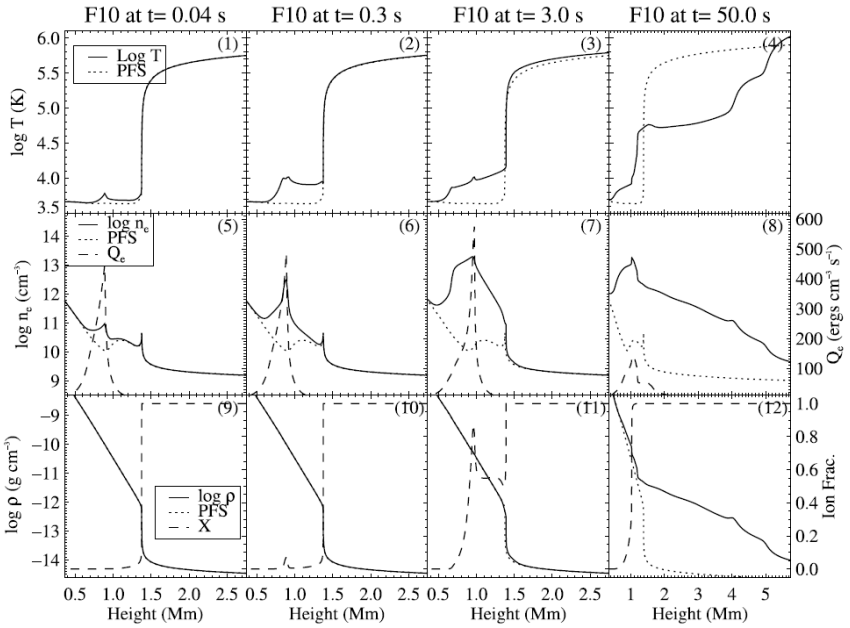

FIG. 3.—Solar atmosphere at four times during the gentle phase of the F10 flare. The top row shows the logarithm of the temperature T as a function of height compared with the preflare state (PFS). In the middle row, the electron density n_e (*left axis*) and beam heating rate Q_e (*right axis*) are plotted. The bottom row shows the mass density ρ (*left axis*) and hydrogen ionization fraction X (*right axis*). Note the change in scale of the horizontal axis in the last column.

FIGURE 2.4: The hydrodynamic response to the the F10 beam heating model from 0 to 50 s, simulated using the RADYN code of Allred et al., 2005.

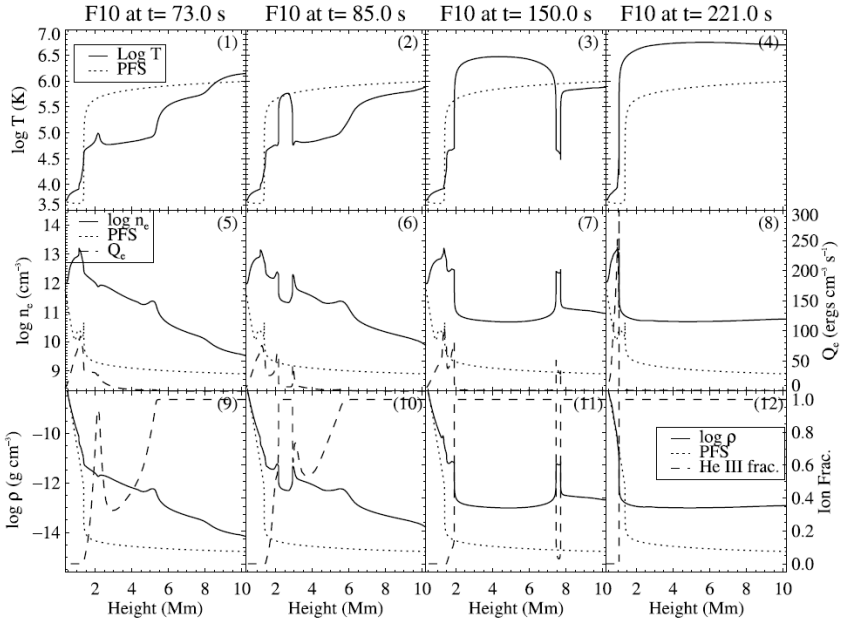

FIGURE 2.5: The hydrodynamic response to the the F10 beam heating model from 72 to 221 s, simulated using the RADYN code of Allred et al., 2005.

agreement with the heating function from Syrovatskii and Shmeleva, 1972 (Dobranskis and Zharkova, 2015; Zharkova and Dobranskis, 2016) used in our work considering collisional losses only, as in the hydrodynamic models of Somov, Spektor, and Syrovatskii, 1981; Zharkova and Zharkov, 2007. Additionally, RADYN adjusts the coronal beam flux to avoid exceeding the saturation limit of Smith and Auer, 1980, which would result in overheating the transition region (Abbett and Hawley, 1999; Allred et al., 2005). Therefore, in our model (see section 2.1.4) the heating is more evenly spread through the atmosphere, with a maximum located deeper in the atmosphere.

In RADYN, the F10 beam results in a slight sweeping of the flare transition region downwards from 1.4 Mm to 1.2 Mm over the course of 50 s (Fig.2.4, panels 1-4). This is slower and over a smaller distance than the sweeping of the ambient plasma by the similar beam in the models used in our work (see Fig.2.1, panel j). The dramatic difference in the sweeping of the plasma results from the the contrast in approaches used for the beam electron heating function (see section 2.1.4) as well as the contrasting initial conditions used on our models. In the RADYN F10 model we see that the upper chromosphere is gently heated from around 5000 K to around 500000 K in the first 50 s (see Fig.2.4 panels 1-4 at 1-1.5 Mm). The gradual heating causes up-flows of hot plasma that increase densities in the lower corona (compare Fig.2.4 panels 11 and 12 at 1.5-4 Mm) and therefore decrease the temperatures there, converting it to an extended transition region (compare Fig.2.4 panels 3 and 4 at 1.5-4 Mm). The overall scheme of evaporation is somewhat similar to that in our model, where plasma initially at chromospheric temperatures and densities is heated, but instead our heating raises this plasma to coronal temperatures (1-2 MK) and flows upward to the overlying corona. The densities of this up-flowing plasma in our model ($\sim 10^9$-10^{10} cm^{-2}) are still higher than the coronal ones ($\sim 10^8$ cm^{-2}).

Differences between up-flows in the F10 models of RADYN and the code presented in this work (that we have named named 'HYDRO2GEN') result also from the scenarios of beam heating that they describe. In our model the beam is stopped after 10 s, simulating a flare burst. Chromospheric evaporation continues after the beam is stopped, although their temperature begins to decrease once the heating is removed (see Fig.2.1, panel a). However, the sustained heating throughout the 226 s

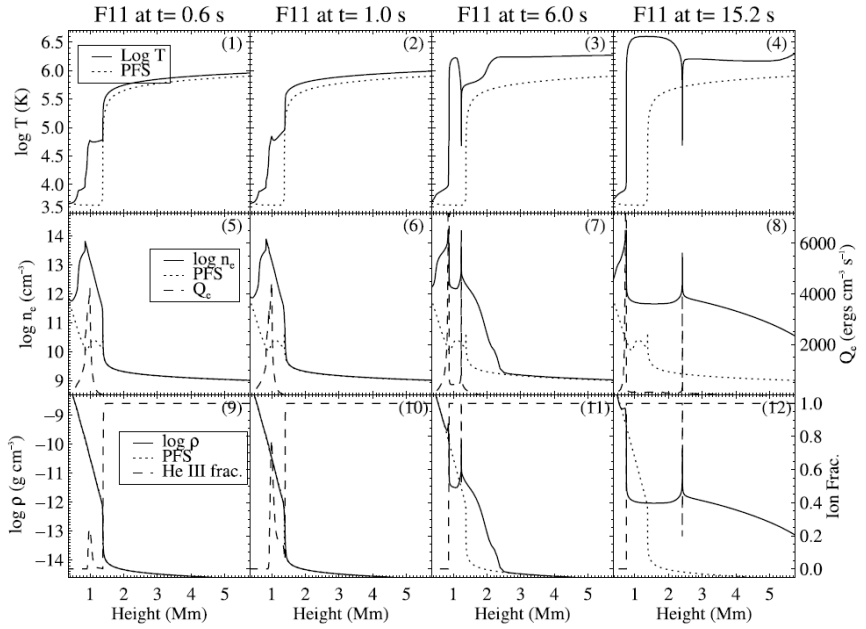

FIGURE 2.6: The hydrodynamic response to the the F11 beam heating model from 0 to 15 s, simulated using the RADYN code of Allred et al., 2005.

of the F10 RADYN simulation results in a continued increase of temperatures over this duration. Eventually, an explosive heating and evaporation event occurs high in the transition region from 73-150 s (see Fig.2.5, panels 1-3 from 3 to 8 Mm).

In the F11 model of RADYN, (see Fig.2.6 showing quantities similar to Fig.2.5) rapid heating occurs in the chromosphere, raising the temperatures to the million Kelvin range in seconds (see Fig.2.6, panels 1-4 from 0.5 to 2 Mm). This is comparable to the height of the heating in our F10 model, although the heating is more smoothly distributed in our models (See the heating functions in Fig.2.6, panels 5-8, particularly the delta-like heating functions in panels 7 and 8). The beam heating results in both up-flows and down-flows, as in our models (see Fig.2.1, panels g-i), but with down-flows at lower velocities < 50 km·s^{-1} than are present in our models (See Fig.2.1). The up-flowing chromospheric material decreases from chromospheric densities towards coronal ones (see Fig.2.6, panels 9-12, at 0.8 to 1.3 Mm), but is also heated to coronal temperatures (see Fig.2.6 panels 1-3, at 0.8 to 1.3 Mm). For this reason one could alternatively describe the up-flows in terms of 'raising the density in the corona'.

In summary, the differences between the hydrodynamic models used in our HYDRO2GEN code and those in RADYN (Allred et al., 2005) arise as a result of the contrast in approaches used for the beam electron heating function (see section 2.1.4), the duration and form of the applied heating, and the different initial conditions used in the simulations: Where RADYN considers an atmosphere with an attached and pre-heated corona, our model begins from the QS chromosphere and converts it through beam heating into a flaring one with its own corona, transition region and chromosphere (see section 2.3). Despite these differences both models predict strong chromospheric heating and evaporation at large upward velocities into the transition region and corona. However the deeper and smoother heating functions, as well as the QS initial conditions, used in the HYDRO2GEN models result in higher velocity, deeper, longer-duration chromospheric condensations.

Chapter 3

Radiative Transfer Method

3.1 NLTE model for hydrogen

In chapter 1 observations of the emission of hydrogen lines and continua were discussed, as well as the models that have been used to interpret this emission. In order to address the problems in interpreting this emission that were identified in 1.3, let us consider that flaring atmospheres of hydrogen atoms are formed in a hydrodynamic response to the injection of electron beams with energy power-law distributions as discussed in the chapter 2. For these atmospheres we describe here a radiative model of hydrogen atoms with given physical conditions.

3.1.1 Statistical Equilibrium

We consider a five levels plus continuum hydrogen model atom. It is assumed that statistical equilibrium is established for each level of the hydrogen atom modelled at each instant of the hydrodynamic responses described above, similarly to Zharkova and Kobylinskii, 1993. This assumption is based on the fact that the time-scale for each radiative process is much shorter than a hydrodynamic characteristic time of tens of seconds (Shmeleva and Syrovatskii, 1973; Somov, Spektor, and Syrovatskii, 1981; McClymont and Canfield, 1983).

Statistical equilibrium for each bound level, i, of the model hydrogen atom at each plasma column depth, ξ (cm^{-2}), is constrained as follows:

$$\frac{\partial n_i(\xi)}{\partial t} = -n_i(\xi)\left(\sum_{k=1,k\neq i}^{N} R_{ik}(\xi) + R_{ic}\right) + \sum_{k=1,k\neq i}^{N} n_k(\xi)R_{ki}(\xi) + n_e n^+(\xi)R_{ci}(\xi) = 0, \tag{3.1}$$

and in the continuum:

$$\frac{\partial n_+(\xi)}{\partial t} = -n_e n_+(\xi) \sum_{i=1}^{N} R_{ci}(\xi) + \sum_{i=1}^{N} n_i(\xi) R_{ic}(\xi), \tag{3.2}$$

where $N = 5$ for a 5 level plus continuum model atom. R_{ik} is the net probability of an atom moving from state i to state k. Note that the recombination terms, R_{ci} are multiplied by the product of the free electron and ionised hydrogen number densities $n_e n^+(\xi)$. This is because both constituents are required for the recombination to occur and therefore the recombination rate coefficients R_{ci} are defined below in units cm^{-6}·s^{-1}, whereas the other rate coefficients R_{ik} and R_{ic} are defined in units cm^{-3}·s^{-1}. In the case of bound levels (equation (3.1)) the first summation term represents deactivation, out of level i, to other levels. The second summation term represents activation, into level i, from other levels. In the continuum case (equation (3.2)) these terms represent recombination and ionisation respectively. The rate coefficients are calculated using the formulae below:

$$R_{ik}(\xi) = \begin{cases} n_e(\xi) C_{ik}(\xi) + A_{ik} & k < i \\ n_e(\xi) C_{ik}(\xi) + n_e^b(\xi) C_{ik}^b(\xi) + Q_{ik}(\xi) + D_{ik}(\xi) & k > i \end{cases} \tag{3.3}$$

$$R_{ki}(\xi) = \begin{cases} n_e(\xi) C_{ki}(\xi) + A_{ki} & k > i \\ n_e(\xi) C_{ki}(\xi) + n_e^b(\xi) C_{ki}^b(\xi) + Q_{ki}(\xi) + D_{ki}(\xi) & k < i \end{cases} \tag{3.4}$$

$$R_{ic}(\xi) = n_e(\xi) C_{ic}(\xi) + n_e^b(\xi) C_{ic}^b(\xi) + Q_{ic}(\xi) + D_{ic}(\xi) \quad \text{ionisation} \tag{3.5}$$

$$R_{ci}(\xi) = A_{ci}(\xi) + n_e(\xi) C_{ci}(\xi) \quad \text{recombination} \tag{3.6}$$

Excitation and de-excitation rates for collisions between hydrogen atoms and thermal electrons, C_{ik}, C_{ki}, are taken from Johnson, 1972. For excitation, de-excitation, and ionisation the rates per second, $n_i C_{ik}$ and $n_i C_{ic}$ are formed by multiplying these coefficients by the abundances in the initial state, i, of each process. In three-body recombination electrons transfer energy and momentum to another electron in the vicinity of a hydrogen ion, resulting in recombination to a bound level, i. Coefficients for this process are taken from Zharkova, 1984; Zharkova and Kobylinskii, 1989a and multiplied by the product of abundances of hydrogen ions and free electrons, $n_e n^+$, and again by the abundance of free electrons, n_e. This process produces

lower rates per second than others considered in all conditions used in our simulations. For excitation and ionisation due to collisions between hydrogen atoms and the beam electrons C^b_{ik}, C^b_{ic}, we use the analytical formulae devised by Zharkova and Kobylinskii, 1993. The depth distribution of the beam electron number densities, n^b_e, is modelled using the work of Zharkova and Kobylinskii, 1993 using the continuity equation approach (Syrovatskii and Shmeleva, 1972). To generate rates per second, the coefficients are multiplied by the abundance of hydrogen in the initial state for a transition to state k or ionisation to continuum, c, $n^b_e C^b_{ik}$, $n^b_e C^b_{ic}$.

The hydrogen spontaneous radiative rates (Allen, 1977) are calculated by multiplying the coefficient of single interaction, A_{ji}, by the number density of hydrogen atoms in the upper state n_j of the transition from j to i, $n_j A_{ji}$. Recombination rates are derived by multiplying the coefficient by the product of the abundances of the hydrogen ions and free thermal electrons required for recombination to occur, $n_e n^+$, to level i, $A_{ci} n_e n^+$. Stimulated excitation or de-excitation, Q_{ik}, and ionisation, Q_{ic}, coefficients in the model due to the external radiation (sometimes called 'backwarming') entering from the levels above and below are taken from Zharkova and Kobylinskii, 1991.

$$Q^{\odot}_{ik}(\xi) = B_{ik} j^{\odot}_{ik}(\xi) = \frac{g_k}{g_i} \frac{c^2 A_{ki}}{2h\nu^3_{ik}} \frac{W_{ik}}{2\sqrt{\pi}} \int_{\infty}^{\infty} I^{\odot}_{ik} \alpha(x) E_2(\alpha(x)\tau_{ik}(\xi)) dx \tag{3.7}$$

$$Q^{\odot}_{ic}(\xi) = B_{ic} j^{\odot}_{ic}(\xi) = 4\pi\kappa^0_{ic} \frac{W_{ic}}{2h} \int_{\nu_{ic}}^{\infty} I^{\odot}_{ic} f_i(\nu) E_2(f_i(\nu)\tau_{ic}(\xi)) \frac{d\nu}{\nu} \tag{3.8}$$

They take the forms $Q_{ik} = B_{ik} j^{\odot}_{ik}$, $Q_{ki} = B_{ki} j^{\odot}_{ik}$ and $Q_{ic} = B_{ic} j^{\odot}_{ic}$ where the coefficients B_{nm} are the Einstein coefficients for stimulated emission and absorption, and $j^{\odot}_{nm}$ is the average intensity of radiation at depth ξ from sources entering from the top and bottom of the model for the transition $n \rightarrow m$. These are multiplied by the abundance in the initial states of the processes to produce excitation and ionisation rates, $n_i Q_{ik}$ and $n_i Q_{ic}$.

D_{ik} and D_{ic} are the coefficients for transitions and ionisation due to internal diffusive radiation. They take the forms $D_{ik} = B_{ik} j^{\partial}_{ik}$, $D_{ki} = B_{ki} j^{\partial}_{ik}$ and $D_{ic} = B_{ic} j^{\partial}_{ic}$ where j^{∂}_{nm} is the average emission intensity of diffusive radiation within the model, for the transition $n \rightarrow m$. These rates are incorporated by solving radiative transfer

equations and converting the steady-state algebraic equations into integral radiative transfer equations of Fredholm second type. The Fredholm integral equations are solved using the L2 approximation method described in section 3.1.6.

3.1.2 Particle conservation

Since the flaring plasma remains neutral, the sum of the number densities of hydrogen ions and atoms, $n(\xi)$, at a column depth ξ is conserved during the radiative processes leading to the following equation to hold:

$$n(\xi) = \sum_{i=1}^{N} n_i(\xi) + n^+(\xi). \tag{3.9}$$

This equation combined with equations (3.1) and (3.2), and allows calculation of the hydrogen ionisation degree.

3.1.3 Comparison of thermal and non-thermal excitation and ionisation rates

Zharkova and Kobylinskii, 1993 and Zharkova, 2008 compared the overall collisional rates in a simulated flare, s^{-1}, between a model with only thermal collisional processes and those including non-thermal electron beams using a variety of parameters for a single power-law energy spectrum. These comparisons were made in a differential study, that is, where the temperature and density profiles were taken from a single hydrodynamic response model, rather than varied to match the response to the particular beam used in the radiative code. Fig.3 in Zharkova and Kobylinskii, 1993 (see Fig.3.1) compares the collisional rates for hydrogen in the Lyman alpha transition (top left panel), ionisation from ground state (top right panel), the Hα transition (bottom left panel), and ionisation from the second state (bottom right panel) as functions of column depth. The rates due to collisions between ambient hydrogen atoms and thermal electrons (line 1), beam electrons for beam of various parameters (lines 2-5) and external photo excitation/ionisation (line 6) are presented.

We note the following relationships based on their work using the F10 hydrodynamic model, with different beam fluxes included in the radiative part of their code

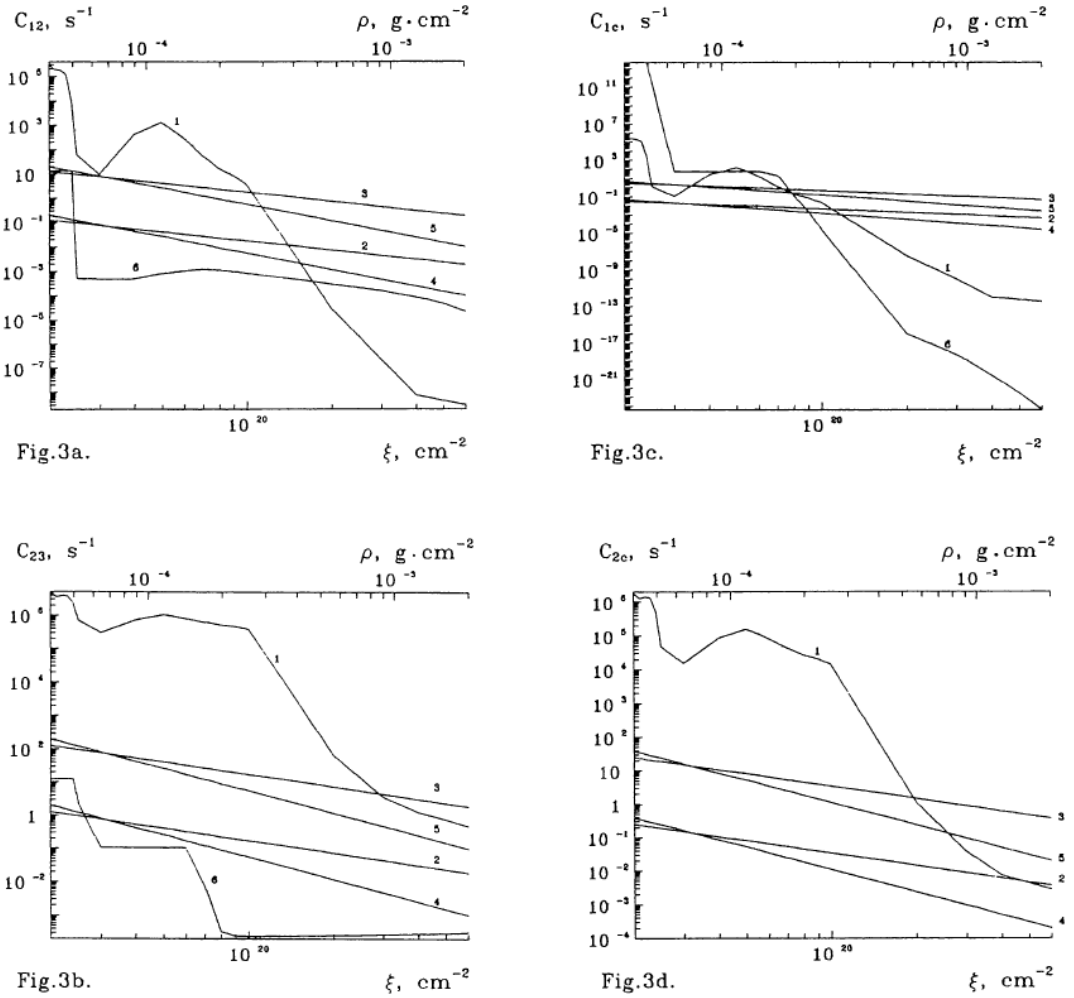

FIGURE 3.1: The collisional excitation/ionisation rates. Rates due to collisions between ambient hydrogen atoms and thermal electrons (line 1), beam electrons for beam of various parameters; $\gamma = 3$, F9 (line 2), $\gamma = 3$, F11 (line 3), $\gamma = 5$, F9 (line 4), $\gamma = 5$, F11 (line 5), as well as external photo excitation/ionisation (line 6). This is shown for excitation from level $1 \rightarrow 2$ (top left panel) and level $2 \rightarrow 3$ (bottom left), and for ionisation from level 1 (top right) and level 2 (bottom right) plotted as functions of column depth ξ. Taken from Zharkova and Kobylinskii, 1993

(see Fig.3.1): (a) Non-thermal collisional processes dominate thermal collisional processes below the flare transition layer ($\xi > 10^{20}\text{cm}^{-2}$). This is particularly evident for ionisation from the ground state of hydrogen in which the collisional rates from non-thermal processes are more than 5 orders of magnitude greater than those for thermal processes for all the models used (Fig.3.1, top right panel). (b) The magnitude of the dominance noted in point (a) is increased for a beam with a higher initial flux if both have the same spectral index. This is due to the greater beam electron density at each depth. (c) Beams of a lower spectral index (harder beams) deposit

their energy deeper in the atmosphere than softer beams, as they contain more high energy particles that penetrate to greater column depths. This means that the ionisation and excitation rates are higher in the deep atmosphere for harder beams, and higher in the upper atmosphere for softer beams.

3.1.4 Optical depth

The optical depth τ of a particular wavelength of light, λ, is the product of the absorption coefficient at that wavelength, κ, and the number density of the absorbing medium through which it is passing, n_λ, multiplied by the distance through which it passes, ΔS. This leads to the well-known formula for optical depth $\tau_\lambda(s) = \int_{s_0}^{s} \kappa_\lambda n_\lambda ds'$. s_0 is the height at the top of the model, and s that at the point under inspection.

Hydrogen in excitation state i is able to absorb light produced by the atomic transition, $j \rightarrow i$ with lower state i. Modelling hydrogen in the lower state of a line or continuum transition as the only absorbing material for photons produced by that transition, therefore, gives that $n_\lambda = n_i$. Thus we have, for a 5-level plus continuum hydrogen atom in a stationary medium, in the line central wavelength λ_0,

$$\tau_{ij}(\xi) = \int_{\xi_{min}}^{\xi} \frac{\kappa_{ij}(\lambda_0)(1-\chi)\frac{n}{n_0}}{\sum_{j=1}^{5} \frac{n_j}{n_i}} d\xi'. \tag{3.10}$$

τ_{ij} is the line centre optical depth, or continuum head optical depth in the case $j = c$, ξ_{min} is the column depth at the top of the model and ξ that at the point in question, n is the total number density of hydrogen atoms and protons, and χ is the ionisation degree of hydrogen atoms.

3.1.5 Radiative Transfer

The radiative transfer equation for an intensity of light with frequency ν, travelling towards the corona is,

$$\mu \frac{\partial I(\nu,\tau)}{\partial \tau} = \alpha(\nu) I(\nu,\tau) - \alpha(\nu) S(\tau). \tag{3.11}$$

τ is the optical depth (section 3.1.4), $\alpha(\nu)$ is the normalised absorption profile at frequency ν, and the source function S is the coefficient of emissivity divided by that for absorption for the line, at optical depth, τ. In the hydrogen transition lines this becomes

$$\mu \frac{\partial I_{ij}(\nu,\tau)}{\partial \tau} = \alpha_{ij}(\nu) I_{ij}(\nu,\tau) - \alpha_{ij}(\nu) S_{ij}(\tau). \tag{3.12}$$

Here α_{ij} is the normalised absorption profile of radiation from a spectral line for the transition from $j \rightarrow i$, assumed to be Voigtian (equation (3.40) in section 3.2.5), μ is the cosine of a propagation angle of radiation with respect to the local vertical in the flaring atmosphere, I_{ij} is the intensity in the spectral line for the transition $j \rightarrow i$. τ is the optical depth in the relevant line centre, $\nu = c/\lambda$ is the frequency and λ a wavelength of line radiation. The source functions $S_{ij}(\tau)$, are related to the relative populations of the atomic levels for the bound-bound transitions (Eq. 3.13)

$$S_{ij}(\tau) = \frac{2h\nu_{ij}^3}{c^2} \left(\frac{n_i g_j}{n_j g_i}(\tau) - 1 \right)^{-1}. \tag{3.13}$$

In the continua the source functions are related to the relative emission measure. The intensity of radiation travelling towards the corona in the ith continuum of hydrogen I_{ic} is derived from section 7.5 in Mihalas, 1978

$$\mu \frac{\partial I_{ic}(\nu,\tau)}{\partial \tau} = f_i(\nu) I_{ic}(\nu,\tau) - \frac{\epsilon_{ic}(\nu_{ic},\tau)}{n_i(\tau)\kappa_{ic}(\tau)} \exp\left(-\frac{h(\nu-\nu_{ic})}{k_B T(\tau)} \right) f_i(\nu)\nu^3, \tag{3.14}$$

with emissivity $\epsilon_{ic}(\nu_{ic},\tau')$

$$\epsilon_{ic}(\nu_{ic},\tau') = \frac{n_e n_+(\tau') A_{ci}(\tau') h}{4\pi \int_{\nu_{ic}}^{\infty} f_i \nu^2 \exp\left(-\frac{h(\nu-\nu_{ic})}{k_B T(\tau')} \right) d\nu}. \tag{3.15}$$

τ is the optical depth in the continuum head, c is speed of light and ν_{ic} is the frequency in the head of the ith continuum. $\kappa_{ic}(\tau)$ is the absorption coefficient in the ith continuum head. h is Planck's constant, k_B is Boltzmann's constant, $T(\tau)$ is the kinetic temperature of the ambient plasma. $f_i(\nu)$ is the absorption profile of the ith continuum, the form of which is taken from the work of Morozhenko and Zharkova, 1980; Morozhenko and Zharkova, 1982; Morozhenko, 1983; Morozhenko, 1984 following the approach proposed by Canfield and Athay, 1974; Canfield and Puetter,

1981; Neidig and Wiborg, 1984:

$$f_i = \begin{cases} \frac{\lambda^3}{\lambda_{ic}^3} = \frac{\nu_{ic}^3}{\nu^3} & i = 1, 2, 3 \text{ (Ly, Ba, Pa)} \\ \frac{\lambda^2}{\lambda_{ic}^2} = \frac{\nu_{ic}^2}{\nu^2} & i = 4, 5 \text{ (Br, Pf)} \end{cases} \tag{3.16}$$

The lines of Lyman series and Lyman continuum are optically thick in all of the models presented. The α lines of the Balmer, Paschen and for some models even Bracket series' become optically thick. Moreover, the Paschen beta (Pβ) spectral line becomes optically thick if affected by powerful beams (model F12) in strong flares.

The formal solutions of radiative transfer equations for upward travelling intensity are:

$$I(\nu, \tau_\nu) = \int_{\tau_\nu}^{\infty} \frac{\alpha}{\mu} e^{-\frac{\alpha}{\mu}(t_\nu - \tau_\nu)} S_\nu dt_\nu \tag{3.17}$$

and in the downward travelling intensity

$$I(\nu, \tau_\nu) = \int_{0}^{\tau_\nu} \frac{\alpha}{\mu} e^{-\frac{\alpha}{\mu}(\tau_\nu - t_\nu)} S_\nu dt_\nu \tag{3.18}$$

Complete redistribution of frequencies is a situation in which the frequency of an absorbed photon and that of the next subsequently emitted photon are independent of each other. Assuming complete redistribution of frequencies, the mean intensities give the following expressions for the simulated rates of excitation, de-excitation and ionisation due to internal diffusive radiation, as stated in equations 11 and 12 of Zharkova and Kobylinskii, 1991:

For excitation and de-excitation in the lines:

$$B_{ik} j_{ik}^{\partial}(\tau) = \frac{A_{ki}}{2} \int_{0}^{\tau_{ik}^0} \frac{n_k}{n_i}(t) K_1(|\tau - t|) dt, \tag{3.19}$$

and for ionisation in the optically thick Lyman continuum:

$$B_{1c} j_{1c}^{\partial}(\tau) = \frac{A_{c1}}{2} \int_{0}^{\tau_{1c}^0} \frac{n_e n_+}{n_1}(t) K_1(|\tau - t|) dt. \tag{3.20}$$

with first kernel functions in the lines:

$$K_1(|\tau|) = A \int_{-\infty}^{\infty} \alpha^2(\nu) E_1(\alpha(\nu)|\tau|) d\nu, \tag{3.21}$$

and in the continuum:

$$K_1(|\tau|) = F(T) \int_{\nu_{ic}}^{\infty} f_i \nu^2 exp\left(-\frac{h(\nu - \nu_{ic})}{k_B T(\tau)}\right) E_1(f_i|\tau|) d\nu. \tag{3.22}$$

The absolute value of the input to the kernel function $K_1(|\tau - t|)$ is used in equations (3.19) and (3.20) so that contributions from upward and downward travelling radiation are both included in one integral. These formulae are substituted into the steady-state equations (equation (3.1)) via the diffusive rates of excitation D_{ij}, de-excitation D_{ji}, and ionisation D_{ic}, for all the diffusive terms relating to radiation that is not optically thin, i.e. non-zero D values. This substitution leads to the integral form of the radiative transfer equations as below:

$$S(\tau) = \frac{P_s(\tau)}{2} \int_0^{\tau_0} K_1(|\tau - t|) S(t) dt + S^*(\tau). \tag{3.23}$$

$S(\tau)$ is the source function. $S^*(\tau)$ is the primary source function, which is the source function resulting from all the rates from equations (3.1) and (3.2) other than the rates for internal diffusive radiation. The limits of integration are taken from the top and bottom of the model, where optical depths for the line centre or continuum head are zero and τ_0 respectively. $P_s(\xi)$ is the survival probability of a scattered photon at optical depth τ, i.e. the chance that an absorbed photon of this wavelength is re-emitted with the same frequency in the next atomic transition:

$$P_s(\tau) = \frac{A_{ci}(\tau)}{\sum_{k=1}^{5} R_{ck}(\tau)}. \tag{3.24}$$

Equation (3.23) is a Fredholm's integral equation of the second kind, $\alpha(\nu)$ is the line absorption coefficient and $f_i(\nu)$ are the relevant continuum absorption coefficients described above. F(T) is the normalisation function in the continuum and A is the

normalisation coefficient in the lines, defined as

$$A \int_{-\infty}^{\infty} \alpha(\nu) d\nu = 1. \tag{3.25}$$

In the continuum the source functions are related to the relative emission measure $\frac{n_e n_+}{n_i}(\xi)$ (REM) via the relationship,

$$\frac{n_e n_+}{n_i}(\xi) = \frac{P_s(\tau)}{2} \int_0^{\tau_0} \frac{n_e n_+}{n_i}(t) K_1(|\tau - t|) dt + \frac{P_s(\xi)}{A_{ci}(\xi)} \sum_{k=1, k\neq i}^{5} \frac{n_k}{n_i}(\xi) R^*_{kc}(\xi). \tag{3.26}$$

R^*_{kc} are the rate coefficients for ionisation from level k (see equation (3.6)) without considering internal diffusive radiation.

3.1.6 Method of solution

For each second of the hydrodynamic response, the system of equations from section 3.1.5 including Fredholm integrals (for optically thick transitions),

$$S_{ij}(\tau) = \frac{P_s(\tau)}{2} \int_0^{\tau_0} K_1(|\tau - t|) S_{ij}(t) dt + S^*_{ij}(\tau), \tag{3.27}$$

$$S_{ic}(\tau) = \frac{P_s(\tau)}{2} \int_0^{\tau_0} S_{ic}(t) K_1(|\tau - t|) dt + \frac{P_s(\xi)}{A_{ci}(\xi)} \sum_{k=1, k\neq i}^{5} \frac{n_k}{n_i}(\xi) R^*_{kc}(\xi), \tag{3.28}$$

and algebraic steady-state equations (for optically thin transitions) from section 3.1.5, are solved using the iterative method first proposed by Zharkova and Kobylinskii, 1993. For all the integral radiative transfer equations, the solutions are found in terms of the source functions S using the approximate method of L2 solutions developed by Ivanov and Serbin, 1984. The L2 approximation is related to the second order escape probability methods described by Rybicki, 1984, but does not suffer from the same shortcomings of methods described therein. This is because it is based on a more rigorous analysis of the asymptotic behaviour of the solutions of the equations of radiative transfer, and is accurate with maximum error 20%, only present in the few top layers of the model (Ivanov and Serbin, 1984). The form of the

L2 approximate solution is

$$S(\tau) \simeq \frac{S^*(\tau)}{\sqrt{1-P_s(\tau)+P_s(\tau)K_2(\tau)}\sqrt{1-P_s(\tau)+P_s(\tau)K_2(\tau_{max}-\tau)}}, \tag{3.29}$$

and the use of L2 approximation significantly improves the accuracy of the solutions (Ivanov and Serbin, 1984) in comparison with L1 solutions used by Zharkova and Kobylinskii, 1993, due to the consideration of the asymptotic nature of the solutions used in the derivation of this result. The second kernel functions employed in this technique are found numerically using Chebyshev-Laguerre quadrature:

$$K_2(\tau) = \int_{\tau}^{\infty} K_1(t)dt. \tag{3.30}$$

The ratios of atoms with electrons in levels i and j, $\frac{n_j}{n_i}(\xi)$, are initially set using the Boltzmann distribution.

The source functions are related to the relative populations of atoms with electrons in each level $\frac{n_j}{n_i}(\xi)$ in the transition lines via equation (3.13), and the Relative Emission Measure $\frac{n_e n_+}{n_i}(\xi)$ (REM) in the continuum (3.26).

The system of equations formed by the statistical equilibrium and radiative transfer equations are solved jointly by calculation of the source functions in the lines and continua using equation (3.29), each implementation of this solution marks the end of an iteration of this radiative transfer code. After each iteration, The new values are checked for convergence against the values of the source functions calculated in the previous iteration at each depth point, with the relative accuracy of $\varepsilon = 10^{-5}$ i.e.,

$$\left|\frac{S_n - S_{n-1}}{S_n}\right| < \varepsilon. \tag{3.31}$$

If the source functions have not all converged at every point then the new source function values are used in the next iteration of the solution method, until convergence is reached.

3.2 Line Formation

The widths of hydrogen spectral lines in the Sun's atmosphere are affected by natural broadening, collisional broadening, the Stark effect and Doppler broadening and result in a Voigtian emission profile (section 3.2.5). Doppler shifts due to line of sight motions further complicate the emission profile (section 3.2.7). In this section we summarise the implementation of these effects in the HYDRO2GEN code.

3.2.1 Natural broadening

The Heisenberg uncertainty principle of quantum mechanics implies there is an uncertainty to the energy level of an excited state of hydrogen due to the finite lifetimes of the electron in these excited states. This uncertainty of a natural line width is not often observed except in cool nebulae because other broadening mechanisms dominate it, but is included in our modelling through the natural wavelength broadening parameter of the excited state i,

$$\gamma_i = \begin{cases} 1 & i = 1 \\ \sum_{j=1}^{i-1} A_{ij} & i \geq 2 \end{cases} \tag{3.32}$$

of the Lorentzian profile, ϕ,

$$\phi(\nu) = \frac{\gamma}{4\pi^2} \frac{1}{(\nu - \nu_0)^2 + \left(\frac{\gamma}{4\pi}\right)^2}, \tag{3.33}$$

where A_{ij} are the rate coefficients of spontaneous decay defined in section 3.1.1.

3.2.2 Collisional Broadening

When the atoms responsible for emission and absorption undergo frequent collisions with other atoms and ions the energy levels are further broadened in a Lorentzian profile. The magnitude of this effect depends on the frequency of the collisions,

$$\gamma_c = \frac{\pi Z^2}{4 m_e c} \lambda_{nm} f_{nm} n \tag{3.34}$$

where Z is the charge of the electron, m_e is its mass, λ_{nm} is the the central wavelength for the transition, f_{nm} is the oscillator strength and n is the density of the ambient hydrogen atoms and ions.

3.2.3 Broadening of Balmer lines by Stark's effect

The Stark Effect is the shifting effect on spectral line emission from atoms due to the presence of an external electric field caused by the charges of the particles in the ambient plasma. The ambient free electrons in the solar atmosphere thus lead to a broadening of the hydrogen spectral lines. Our model accounts for broadening of the hydrogen Balmer α and β via the quadratic Stark broadening by including it as a Lorentzian style broadening parameter, γ_s

$$\gamma_s = \begin{cases} 1.55 \times 10^{-4} \frac{n_e}{\sqrt{T}} \left(26.85 + \log_{10} \frac{T^2}{n_e}\right) + & \text{H}\alpha \\ 6.64 \times 10^{-3} \frac{n_e}{\sqrt{T/2}} \left(19.33 + \log_{10} \left(\frac{T^2}{\frac{n_e}{2}}\right)\right) & \\ 0.5(3m^4 - 27m^2 + 36) 3.69 \times 10^{-4} \frac{n_e}{\sqrt{T}} \left(22.22 + \log_{10} \left(\frac{T^2}{\sqrt{\frac{n_e}{2}}}\right)\right) & \text{H}\beta \\ - \log_{10} \left(0.5(3m^4 - 27m^2 + 36)\right) & \end{cases}, \quad (3.35)$$

where m is the upper level of the transition, for the Hβ line, therefore $m = 4$. Since our work does not model polarised light we do not include the linear Stark effect.

3.2.4 Broadening due to thermal motions

The mean random motion of hydrogen atoms due to thermal motions is given by the formula,

$$v_{rand} = \sqrt{v_{thermal}^2} = \sqrt{\frac{2k_B T_e}{m_H}}, \quad (3.36)$$

where we have set the turbulent velocity to zero and the thermal velocity is the thermal Doppler velocity of the layer,

$$v_D = \sqrt{\frac{2k_B T_e}{m_H}}. \quad (3.37)$$

This gives a Gaussian frequency width of,

$$\Delta\nu_D = \frac{\nu_{nm}}{c} v_{rand}, \quad (3.38)$$

or a Gaussian wavelength width of,

$$\Delta\lambda_D = \frac{\lambda_{nm}}{c} v_{rand}, \tag{3.39}$$

where n and m are the lower and upper levels of the transition in question.

3.2.5 Voigt profile

The Voigt profile, used to describe the shape of spectral line broadened by a combination of Lorentzian and Gaussian broadening mechanisms, is given in Ivanov and Serbin, 1984 as,

$$U(a,x) = \frac{a}{\pi^{3/2}} \int_{-\infty}^{\infty} \frac{e^{-y^2}}{(x-y)^2 + a^2} dy. \tag{3.40}$$

In our context x is a dimensionless wavelength measurement, measured in Doppler half widths. a is a broadening term for Doppler and Lorentzian broadening, in our code:

$$a = \left(\frac{\gamma_n + \gamma_m + \gamma_c}{4\pi} + \frac{\gamma_s}{\pi^2} \right) \frac{1}{\Delta\nu_D}. \tag{3.41}$$

An un-normalised form of this function was analysed by Harris, 1948 using a Taylor series

$$H(a,x) = \frac{a}{\pi} \int_{-\infty}^{\infty} \frac{e^{-y^2}}{(x-y)^2 + a^2} dy. \tag{3.42}$$

Harris gave the form

$$H(a,x) = H_0(x) + aH_1(x) + a^2H_2(x) + a^3H_3(x) + ... + a^nH_n(x) + ... \tag{3.43}$$

with

$$\begin{aligned}
H_0(x) &= e^{-x^2} \\
H_1(x) &= -\tfrac{2}{\sqrt{\pi}}(1 - 2xF(x)) \\
H_2(x) &= (1 - 2x^2)e^{-x^2} \\
H_3(x) &= -\tfrac{2}{\sqrt{\pi}}[\tfrac{2}{3}(1 - x^2) - 2x(1 - \tfrac{2}{3}x^2)F(x)] \\
H_4(x) &= (\tfrac{1}{2} - 2x^2 + \tfrac{2}{3}x^4)e^{-x^2},
\end{aligned} \tag{3.44}$$

where F(x) is the Dawson function

$$F(x) = e^{-x^2} \int_0^x e^{-t^2} dt. \tag{3.45}$$

The Dawson function

In our code the modified Dawson function, $MD(x) = 1 - 2xF(x)$, is calculated using procedures for the Dawson function outlined in Cody, Paciorek, and Thacher, Jr., 1970. For the domain $|x| \leq 2.5$ we use the $n = 5$ form. For the $2.5 < |x| \leq 3.5$ scheme we use the $n = 4$ form. $n = 3$ is employed for cases $3.5 < |x| \leq 5$, and $n = 1$ for $5 < |x|$.

Taylor expansion coefficients

We now calculate the Taylor expansion terms. Mihalas, 1978 (p280, 9-40) gives that:

$$H_n(x) \equiv \frac{(-1)^n}{\sqrt{\pi}(n!)} \int_0^\infty y^n e^{-\frac{y^2}{4}} \cos(xy) dy. \tag{3.46}$$

Let us introduce the notation

$$\begin{aligned} C_n(x) &\equiv \int_0^\infty y^n e^{-\frac{y^2}{4}} \cos(xy) dy, \\ S_n(x) &\equiv \int_0^\infty y^n e^{-\frac{y^2}{4}} \sin(xy) dy. \end{aligned} \tag{3.47}$$

This gives

$$C_0 = \sqrt{\pi} e^{-x^2}, \quad S_0 = 2F(x). \tag{3.48}$$

Integrating by parts gives

$$\begin{aligned} C_1 &= 2(1 - 2xF(x)) & S_1 &= 2x\sqrt{\pi} e^{-x^2} \\ C_n &= 2(n-1)C_{n-2} - 2xS_{n-1} & S_n &= 2(n-1)S_{n-2} + 2xC_{n-1}. \end{aligned} \tag{3.49}$$

It would be preferable to create equivalent recurrence formulae for the Taylor expansion coefficients themselves:

$$H_n(x) \equiv \frac{(-1)^n}{\sqrt{\pi}(n!)} \int_0^\infty y^n e^{-\frac{y^2}{4}} cos(xy) dy \equiv \frac{(-1)^n}{\sqrt{\pi}(n!)} C_n(x). \tag{3.50}$$

Let us also define

$$I_n(x) \equiv \frac{(-1)^n}{\sqrt{\pi}(n!)} \int_0^\infty y^n e^{-\frac{y^2}{4}} sin(xy) dy \equiv \frac{(-1)^n}{\sqrt{\pi}(n!)} S_n(x), \tag{3.51}$$

then we also see that

$$S_n = (-1)^n \sqrt{\pi}(n!) I_n \quad C_n = (-1)^n \sqrt{\pi}(n!) H_n, \tag{3.52}$$

and, by substitution:

$$\begin{array}{ll} H_0 = \frac{(-1)^0}{\sqrt{\pi}(0!)} \sqrt{\pi} e^{-x^2} = e^{-x^2} & I_0 = \frac{(-1)^0}{\sqrt{\pi}(0!)} 2F(x) = \frac{2}{\sqrt{\pi}} F(x) \\ H_1 = \frac{(-1)^1}{\sqrt{\pi}(1!)} 2(1 - 2xF(x)) = \frac{2}{\sqrt{\pi}}(2xF(x) - 1) & I_1 = -2xe^{-x^2} \\ H_n = \frac{2H_{n-2} + 2xI_{n-1}}{n} & I_n = \frac{2I_{n-2} - 2xH_{n-1}}{n}. \end{array} \tag{3.53}$$

The coefficients in the Taylor expansion of the line broadening function can be calculated using these recurrence relations. Note that the area under the curve is normalised to $\sqrt{\pi}$ so when the normalisation required is 1, division of the result by $\sqrt{\pi}$ is necessary. The advantages of this scheme over the differentiation based recurrence method discussed in Mihalas, 1978 exercise 9.2 are that the calculations do not require retention of the explicit, ever-expanding, polynomial forms of factors in the coefficients. The additional calculation cost of terms is linear beyond the second term. Values from the process are compared against tables in Finn and Mugglestone, 1965 and are seen to agree to the five significant figures used in saving values from our Fortran process for a values from 0 to 1 is steps of 0.1 and for x values from 0 to 6 in steps of 0.5 and to a slightly lower, but tolerable accuracy for x from 6.5 to 15.

3.2.6 Line absorption coefficients

The hydrogen line absorption coefficient profiles are Voigtian with wavelength, and have a maximum at the line central wavelength, κ^0_{nm},

$$\kappa^0_{nm} = \frac{Z^2\sqrt{\pi}}{m_e c^2} g f_{nm} \frac{\lambda_{nm}}{\Delta\lambda_D}, \tag{3.54}$$

here gf_{nm} are the Gaunt factors for the lines with lower and upper levels n and m.

3.2.7 Doppler Shifts

To accurately replicate the emission from a plasma undergoing macroscopic mass motions in the line of sight, one must account for Doppler shifts in the emission wavelengths. The Doppler shift of wavelength for a plasma of velocity heading away from us at angle θ, $\mu = cos\theta$ is,

$$\lambda_s = \frac{\lambda_o}{1 + \frac{v_m}{c}\mu}. \tag{3.55}$$

λ_s is the wavelength in source frame and λ_o is the wavelength in observation frame. This equation is set for positive macro-velocity, v_m, heading into the Sun (positive with increasing plasma depth), which therefore increases the wavelength of the emission. Therefore we have the orientation shown in Fig.3.2. We define positions in the emission profile relative to the line centre, in terms of a rest frame X, and a Doppler shifted frame X_i, the Doppler shift, X_{DS}, relates the two as in Fig.3.2,

$$X_i = X - X_{DS}. \tag{3.56}$$

The units we will use for this are defined to be dimensionless and scaled to the Doppler half width of the profile at a given layer

$$X_{DS} = \frac{\lambda_{ij,o} - \lambda_{ij,s}}{\Delta\lambda_D}. \tag{3.57}$$

Therefore we have

$$X_{DS} = \frac{\lambda_{ij} - \frac{\lambda_{ij}}{1+\frac{v_m}{c}\mu}}{\Delta\lambda_D} = \frac{1 - \frac{1}{1+\frac{v_m}{c}\mu}}{\frac{1}{c}v_D} = \frac{\frac{v_m}{v_D}\mu}{1 + \frac{v_m}{c}\mu}. \tag{3.58}$$

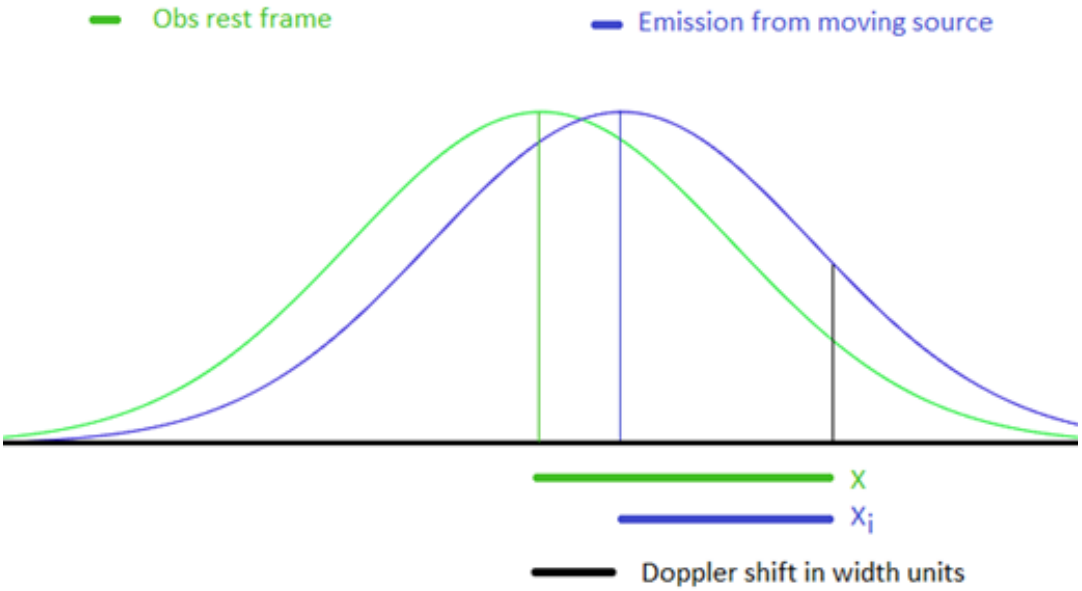

FIGURE 3.2: The relationship between emission in the rest frame and Doppler shifted emission

In the low velocity limit $v_m/c \ll 1$ therefore

$$X_{DS} \approx \frac{v_m}{v_D}\mu, \tag{3.59}$$

and thus we have an expression for the Doppler shifted emission wavelength variable,

$$X_i = X - \frac{v_m}{v_D}\mu. \tag{3.60}$$

The model atmospheres have 150 depth points, each with individual thermal Doppler velocities, and plasma macro-velocities. The radiative code is written to correctly align the emission from each individual layer taking the different thermal Doppler velocities and plasma macro-velocities into account.

3.2.8 Smoothing the line profiles

We generate hydrogen emission profiles for a line with central wavelength λ_0 from the modelled depth points, with each layer having an associated Doppler shift $\Delta\lambda = -\frac{V_m(i)}{c}\mu\lambda_0$, from the layer i due to macro-velocity $V_m(i)$. For smoothing of the contributions of different layers considered, cubic splines were applied to the line profile merged from these layers.

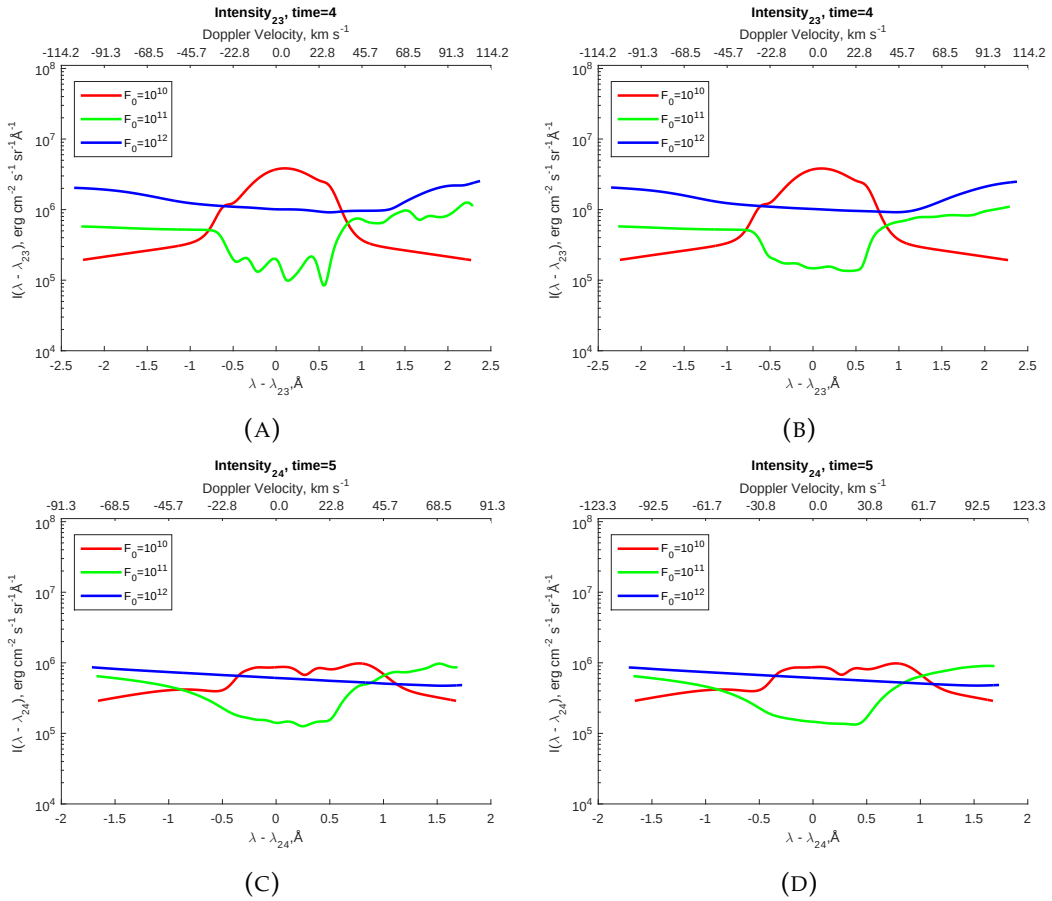

FIGURE 3.3: Balmer line profiles calculated without (a) (c) and with (b) (d) including the line smoothing technique described in section 3.2.8. Line profiles are shown 4 s after the beam onset begins for the Hα line (top panels, a and b), and in the Hβ line at 5 s (lower panels, c and d).

When the differences in Doppler shifts of the adjacent layers are large, this process produces numeric oscillations in the intensity of the line profile (Fig.3.3, left panels). This is a characteristic of the discrete model used, rather than the continuous plasma being modelled and will mask useful information, preventing the accurate analysis. This can be repaired by interpolating between the discrete macro-velocity values (Fig.3.3, right panels).

Therefore, the cubic spline functions of macro-velocities against the data point number are generated. Lower order splines do not produce smooth profiles, and higher order splines produce negligible improvements on the cubic spline function or in some cases grant too many degrees of freedom. Each of the transition lines has a set of 200 wavelength data-points. The intensity contribution to the emission produced at a data point i (found from the contribution functions) is redistributed

uniformly across a continuous data-point-number axis from $i - 0.5$ to $i + 0.5$ and then mapped, via the macro-velocity spline, to be centred on the closest wavelength data point. This model produces a clearer picture of the relevant physical processes, smoothing out the cases where intensity changes result from the discrete modelling distribution. An example of this is the oscillations that are removed from the Hα profile in the F11 model at 4 seconds (Figs.3.3a, b). Note though, the process described above does not remove oscillations in the profiles that result from the physical mechanisms, for example the shape of the Hβ core at five seconds in the model F10 flare (Fig.3.3c, d).

3.3 Formulae for the intensities of emission and contribution functions in hydrogen lines and continua

3.3.1 Line emission

The converged source functions are then used to calculate the overall intensities of emission, integrating over contributions from all depth points and angles. The formula for transition lines is:

$$I_{ij}(\lambda) = 2\pi \frac{c}{\lambda^2} \frac{2hc}{\lambda^3} \int_0^{\tau_{max}} \left(\frac{n_i g_j}{n_j g_i}(\tau) - 1 \right)^{-1} e^{\left(-\frac{\alpha_{ij}(\lambda)}{\mu} \tau \right)} \frac{\alpha_{ij}(\lambda)}{\mu} d\tau. \tag{3.61}$$

In this equation, the coefficient 2π accounts for axial symmetry of the generated emission from different azimuthal angles, the relationship $d\nu = -\frac{c}{\lambda^2} d\lambda$ generates a factor of $\frac{c}{\lambda^2}$ to convert between the intensity formulae given per unit frequency (in equations (3.17) and (3.18)) and per unit wavelength used here. Additionally the formulas for the source functions in the lines (equation (3.13)) have been converted into the functions of a wavelength. g_i is the degeneracy of the quantum state i.

3.3.2 Continuum emission

The formula for the intensity of continuum emission escaping from the top of the model is derived below. We begin from the radiative transfer equation in the continuum for radiation travelling towards the corona, equation (3.14). This is solved

using the integrator factor method and to arrive at the formulation as follows, considering contributions from all depth points and angles,

$$I_{ic}(0,\nu) = \frac{h}{2}\int_0^{\tau_{max}} \left[\frac{A_{ci}(\tau')}{\kappa_{ic}} \frac{n_e n_+}{n_i}(\tau') \frac{exp\left(-\frac{h(\nu-\nu_{ic})}{k_B T(\tau')}\right) \frac{f_i}{\mu}\nu^3 exp\left(-\frac{f_i}{\mu}\tau'\right)}{\int_{\nu_{ic}}^{\infty} f_i \nu^2 exp\left(-\frac{h(\nu-\nu_{ic})}{k_B T(\tau')}\right) d\nu} \right] d\tau'. \quad (3.62)$$

The normalisation term $I_N = \left[\int_{\nu_{ic}}^{\infty} f_i \nu^2 exp\left(-\frac{h(\nu-\nu_{ic})}{k_B T(\tau')}\right) d\nu\right]^{-1}$ depends on the form of the absorption coefficient for the continuum f_i (equation **??**eq:AbsoProf)), and takes the form:

$$I_N = \begin{cases} \left[\nu_{ic}^3 exp\left(\frac{h\nu_{ic}}{k_B T(\tau')}\right) E_1\left(\frac{h\nu_{ic}}{k_B T(\tau')}\right)\right]^{-1} & i = 1,2,3 \\ \left[\frac{k_B T(\tau')}{h}\nu_{ic}^2\right]^{-1} & i = 4,5. \end{cases} \quad (3.63)$$

The resulting formula is given in wavelength units below (equation (3.64)), with the explicit τ dependence is removed, for compactness. The relationship $d\nu = -\frac{c}{\lambda^2}d\lambda$ is used to convert these formula for use with the results in wavelength units.

$$I_{ic}(\lambda) = \begin{cases} \frac{h}{2}\frac{c}{\lambda^2}\int_0^{\tau_{max}} \frac{A_{ci}}{\kappa_{ic}}\frac{n_e n_+}{n_i}\frac{\lambda_{ic}^3}{\lambda^3}\frac{exp\left(-\frac{hc}{k_B T\lambda}\right)\frac{f_i}{\mu}exp\left(-\frac{f_i}{\mu}\tau'\right)}{E_1\left(\frac{hc}{k_B T\lambda_{ic}}\right)}d\tau' & i = 1,2,3 \\ \frac{h}{2}\frac{c}{\lambda^2}\int_0^{\tau_{max}} \frac{A_{ci}}{\kappa_{ic}}\frac{n_e n_+}{n_i}\frac{\lambda_{ic}^2}{\lambda^2}\frac{exp\left(-\frac{hc\left(\frac{1}{\lambda}-\frac{1}{\lambda_{ic}}\right)}{k_B T}\right)\frac{f_i}{\mu}exp\left(-\frac{f_i}{\mu}\tau'\right)}{\frac{k_B T\lambda}{hc}}d\tau' & i = 4,5. \end{cases} \quad (3.64)$$

This formulation uses radiative transfer in the continuum (governed by the optically thick Lyman continuum) to define the ambient ionisation and is affected by collisions, external and internal diffusive radiation. This approach is different from codes such as RADYN (Allred et al., 2005) which uses modified Saha equations to define the ambient ionisation. Moreover our code uses ionization and excitation rates for inelastic collisions by beam electrons following the analytical formulae derived by Zharkova and Kobylinskii, 1989b; Zharkova and Kobylinskii, 1993. These rates were carefully compared with those by thermal electrons in Zharkova and Kobylinskii, 1993, for one-to one and for the volume rates. This differs from RADYN also as a result of the number of beam electrons at a given depth and the depth where these electrons can reach.

3.3.3 Contribution functions

We investigate the emission of hydrogen in Balmer and Paschen series formed in the model atmospheres described in chapter 2 which have 150 points of column depth, converted into an optical depth. The emission from each layer contributes to the overall intensity at each wavelength, and this emission from the layer is a contribution function, which give the contribution from a specific depth point to the total emission measured from the top of the flaring atmosphere at a given wavelength. The contribution functions are functions of depth point number and wavelength.

Thus a contribution function for the depth point m is derived by taking the relevant intensity integral (equations (3.61) and (3.64)) with the integration limits between the optical depths of the layer with the depth point m, i.e. $\tau(m-1)$ and $\tau(m)$. These contribution functions are utilised to investigate the origin of emergent radiation observed from the top of a flaring model.

3.4 Notes

Much of the work in this chapter is taken from the published paper Druett and Zharkova, 2018, and was completed in collaboration between Prof. Valentina Zharkova and I.

Chapter 4

Optical depths of hydrogen emission

4.1 Differential and matched optical depth studies

The optical depths of hydrogen lines are investigated using two approaches. In the first instance, using a differential study: the radiative responses to thermal collisions and to collisions with electron beams with the initial energy fluxes F_0 ranging $10^9 - 10^{12}$ erg·cm^{-2}·s^{-1} are calculated for the same flaring atmosphere with the physical conditions defined by the hydrodynamic response to a beam with $F_0 = 10^{10}$ erg·cm^{-2}·s^{-1}. In the second instance, we use the matched hydrodynamic and radiative responses to complete the investigation.

There are several effects that can be derived from the expressions for optical depth (see section 3.1.4): (1) A higher ionisation degree implies a lower optical depth, all other things being equal, as this will result in fewer hydrogen atoms being present that can absorb photons of the given wavelength. (2) The greater the proportion of neutral hydrogen atoms with electrons in the lower excited state of the transition, n_i, the higher the optical depth, as there will be more material present that can destroy photons of the relevant wavelength by stimulated excitation or ionisation. (3) The only difference in the formulae for optical depths of lines in the same series is the absorption coefficient in the central wavelength (see equation (3.10)). Therefore, aside from a multiplicative constant, the profiles of the optical depths in the line central wavelengths (plotted against column depth) are the same for all the lines of a hydrogen series, as well as for the optical depth of the continuum head wavelength for the

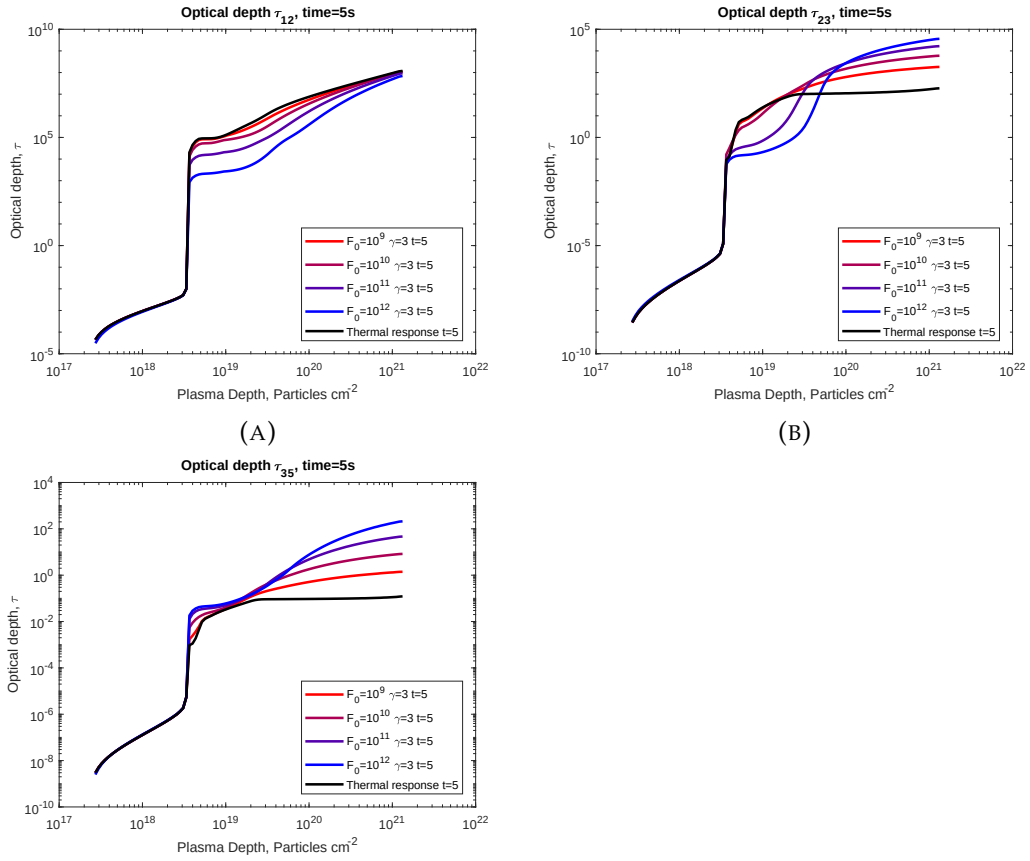

FIGURE 4.1: The optical depths calculated in the differential study for (a) the Lyman alpha line (b) the Hα line (c) the Pβ line, 5 s after the onset of the beam, plotted against column depth (cm^{-2}). Each sub-figure shows the optical depth in the central wavelength of the line profile calculated for the thermal response (black line) and for models including excitation and ionisation rates from electron beams with fluxes in the range $10^9 - 10^{12}$ erg·cm^{-2}·s^{-1}.

same series.

For the first part Fig.4.1 shows the optical depths calculated in the differential study for (a) the Lyman alpha line (b) the Hα line (c) the Pβ line, 5 s after the onset of the beam. The optical depths are plotted against column depth, ξ (cm^{-2}). In each sub-figure the optical depth in the central wavelength of the line profile is displayed for the thermal response (black line) and for models including excitation and ionisation rates from electron beams with fluxes in the range $10^9 - 10^{12}$ erg·cm^{-2}·s^{-1}.

The major radiative processes occurring directly as a result of inelastic collisions with beam electrons, i.e. non-thermal collisional excitation and ionisation, both cause a decrease in optical depth in the Lyman series. Both act to reduce the number density of hydrogen atoms with electrons in the ground state, which could otherwise

absorb Lyman radiation. Thus, the stronger the beam the lower the optical depth for all Lyman lines. This is shown in Fig.4.1a where for all column depths modelled, the optical depth that results from a model using a beam with a higher initial flux is less than or equal to the optical depth from a model using a lower initial flux. However, since the Lyman line cores become very optical thick just below the transition region, the effect this has on the column depths of their formation regions will be minimal.

Whereas both non-thermal ionisation and excitation decrease optical depth for Lyman lines, the processes work against each other for the Balmer series and continuum (Fig.4.1b). Ionisation continues to decrease the amount of absorbing material, but excitation from the ground state into the second level will create more absorbing material for Balmer radiation and, thus, increase the optical depth. At the depth where the plasma drops below the temperature of full ionisation the optical depths rise steeply (Fig.4.1b). However, because a higher proportion of neutral hydrogen (and thus absorbing material with electrons in level 2 of a hydrogen atom) is ionised by stronger beams, this increase of optical depth is reduced for the simulations with higher initial fluxes of electron beams (see Fig.4.1b, at column depths around 10^{19} cm^{-2}).

In a deeper flaring atmosphere the plasma density becomes higher and the hydrogen ionisation degree is lower (Fig.2.1, central panels, Fig.6.3). As a result, the excitation of electrons to level 2 of hydrogen by collisions with beam electrons greatly increases. The number of hydrogen atoms with electrons in level 2 defines optical thickness of the Balmer transitions (see 3.1.4). Thus, stronger beams result in Balmer emission with higher optical thickness (see Fig.4.1b, at column depths around $10^{21} - 10^{21}$ cm^{-2}).

The excitation by non-thermal beam electrons is an important mechanism for increasing the optical depth in Paschen lines. Non-thermal excitation dominates higher in the atmosphere and is more significant for the Paschen series than for the Balmer one (Fig.4.1c). Without the additional excitation supplied by non-thermal collisions there are many fewer electrons in level 3 of hydrogen atoms that can absorb Paschen radiation. In the events excited by stronger electron beams Paschen Pα and Pβ line cores become optically thick (Fig.4.2,b). Also the formation regions of these lines can expanded closer to the flare's transition region for more intense

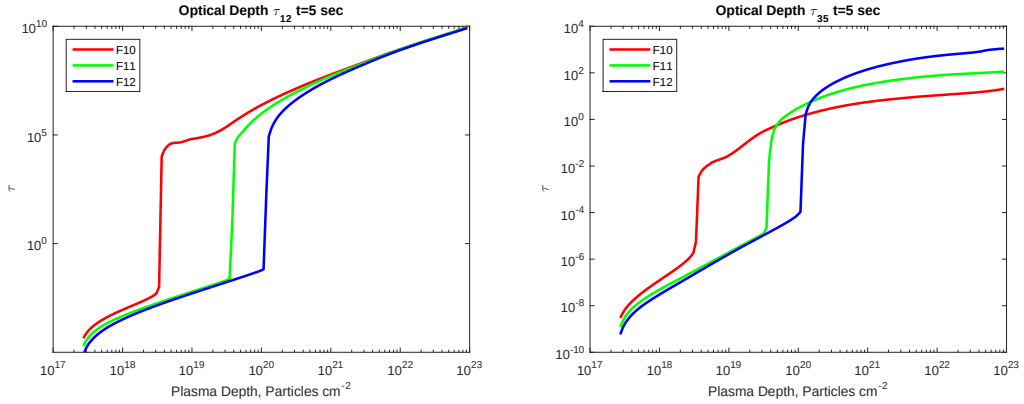

(A) (B)

FIGURE 4.2: Optical depths in coupled hydrodynamic and radiative models, 5 s after beam onset in (a) the Lyman alpha line and (b) the Pβ line, plotted against plasma column depth (cm^{-2}). Simulations are made with for beams with fluxes of 10^{10} (red line), 10^{11} (green line) and 10^{12} (blue line) erg·cm^{-2}·s^{-1}.

events.

For the second part of this investigation the hydrodynamic and radiative models are calculated for the same beam parameters. The optical depths 5 s after beam onset are shown in Fig.4.2 for (a) the Lyman alpha line and (b) the Pβ line, plotted against plasma column depth (cm^{-2}). Results are displayed for beams with fluxes of 10^{10} (red line), 10^{11} (green line) and 10^{12} (blue line) erg·cm^{-2}·s^{-1}.

When the matched radiative and hydrodynamic simulations are used, we can still observe the effects derived from the differential study earlier in this section, i.e. the reduction in optical depths of Lyman lines due to ionisation and excitation by collisions with non-thermal electrons (Fig.4.2a), and the increase in Paschen line optical depths due to excitation by beam electrons (see Fig.4.2b at column depths deeper than 2×10^{20} cm^{-2}). However, understanding of the radiative effects derived from the differential study must be combined with an appreciation of differences in hydrodynamic atmospheres generated by appropriate beams, such as the different column depths of the flare transition layer for each flux (see Fig.4.2). This helps to complete our understanding of the beam's effects on optical depths in the hydrogen lines in real dynamic atmospheres.

4.2 Summary

In summary,

(4.1) The Lyman lines are highly optically thick in the upper chromosphere for all of the simulations. The reductions in optical depth resulting from excitation and ionisation of electrons from the ground state hydrogen caused by collisions with non-thermal beam electrons are negligible when considering the formation regions of these lines. This is also true for the Lyman continuum, which is the only optically thick hydrogen continuum in each of the simulations.

(4.2) Ionisation of the hydrogen atoms by collisions with the non-thermal beam electrons acts to reduce the optical thickness of the Balmer lines. The excitation of electrons to level 2 of hydrogen through collisions with the beam particles acts to increase the optical thickness. This results in Balmer lines becoming optically thinner at the top of the chromosphere during the impulsive phase, where the ionisation dominates, and simultaneously optically thicker in the lower chromosphere where the excitation dominates.

(4.3) The excitation of electrons to level 3 of hydrogen, by collisions with the non-thermal beam electrons, has a greater influence in increasing the optical thickness of Paschen lines during the impulsive phase than depopulation, by ionisation, has in reducing the optical thickness. Therefore the Paschen lines become optically thick in the chromosphere during the impulsive phase of a flare for beams with high initial fluxes, such as the F11 and F12 models.

4.3 Notes

The work in this chapter is taken from the published paper Druett and Zharkova, 2018, and was completed in collaboration between Prof. Valentina Zharkova and I.

Chapter 5

Hydrogen Lyman line and continuum emission

5.1 Introduction

In sections 1.1.3 and 1.2.4 the lack of high spatial resolution spectral profiles of Lyman line emission was discussed, as well as the problems that have resulted from attempts to interpret full-disk intensities in the Lyman lines. The need to comprehensively study emission in the Lyman lines and continuum in the models of solar flares was presented in section 1.3, because of the potential diagnostics of flaring atmospheres provided by the future observations. This task can be performed with the HYDRO2GEN approach and codes presented in chapters 2 and 3.

In this chapter we simulate the emission in the Lyman series and continuum, and probe these simulations with existing observations. In addition, we attempt to predict the features that could be observed using the next generation of the satellite payloads.

5.2 Physical conditions and NLTE modelling

The physical conditions presented in Fig.2.2 for the F10 F11 and F12 models, are used as the input to the hydrogen radiative models described in chapter 3. In order to resolve the upper chromosphere and transition region more clearly, 20 additional depth points are included in our radiative model by interpolating the hydrodynamic

model in the regions of the plasma with clearly monotonic variations in the plasma density, kinetic temperature and macro-velocity.

5.3 Results of simulations

5.3.1 Profiles of the Lyman alpha line

The Lyα profiles simulated during the beam injection phase are shown in Fig.5.1 from 1 second (a) to 4 seconds (d), respectively. The wavelength relative to the line centre is plotted on the X-axis of the line profile plots, and emission intensity on the Y-axis. For the figures in this paper, Lyman line profiles are shown for the F10 model (red lines), F11 model (green lines), and F12 model (blue lines) (see chapter 2). The Lyα line contribution functions and optical depths during the beam injection are shown in Fig.5.2. The logarithm of a column depth is shown on the X-axis, and the wavelength relative to the line centre (1216Å) is shown on the Y-axis. In the top row the contributions to the Lyα emission intensity are shown at 4 seconds in the F10 model (a) and at 2 seconds in the F12 model (b). The colour scale runs from light (low contribution) to dark (high contribution). The lower panels (c and d) display the optical depths at the same times and the same models. The optical depths are shown starting from a value of 1 (light blue) and increasing to an optical depth of $> 10^9$ in the line centre at the base of the model (see Fig.4.2).

During a beam injection, from the first seconds the non-thermal beam electrons ionise and excite the flaring plasma through inelastic collisions as well as heating the ambient plasma through elastic collisions. Two effects of the beam immediately increase the ratio of hydrogen atoms with orbital electrons in level 2 or higher compared to those with orbital electrons in the ground state: (1) plasma heating, (2) collisional excitation of the electrons from ground state by beam electrons. This has the effect of increasing the source functions used in the Lyman line emission functions (chapter 3). Thus, the beam converts the core of the Lyα line into emission in the models with stronger electron beams (see the F11 and F12 Lyα line cores for 1 second, Fig.5.1a). The core is broadened more in the models with stronger electron beams due to the greater heating in these models that result in higher Doppler widths, and the wing emission is also increased by collisional broadening (Fig.5.1a). From

Fig.2.2d, e, and f, one can see that the downward moving hydrodynamic shocks (positive macro-velocity) are formed in the flare transition regions and upper chromospheres of the models. These shocks are formed more swiftly for the hydrodynamic models with stronger beams, appearing in the formation region of the Lyman lines for the F11 and F12 models 2 seconds after the beam onset. Thus, the shock Doppler-shifts the core emission of Lyα to the red wing after 2 seconds for the F11 and F12 models (Fig.5.1). The lower velocity shock that is formed in the F10 model occurs later, and significantly transforms the Lyα line core profile obtained for 4 seconds of the beam onset (Figs.5.1d, 5.2a and c). In the central wavelength of Lyman lines, the emission intensity is sustained by a combination of the wing emission from the depths, in which the core emission is Doppler-shifted to the red wing, and the core emission from the material at slightly deeper levels with the lower Doppler shifts (Fig.5.1c, F11 and F12 models, Fig.5.2b and d).

The Lyα line profiles simulated at the times after the beam has been switched off, at 15 seconds (a), 30 seconds (b), 60 seconds (c) and 90 seconds (d) are shown in Fig.5.3. The Lyα line contribution functions and optical depths during the beam injection are shown in in Fig.5.4 at 30 seconds in the F10 model (panels a and c) and at 90 seconds in the F12 model (panels b and d). The axes and layout are the same as for Fig.5.2.

Once the beam has stopped the atmosphere continues with a hydrodynamic response on a gradual phase (see Fig.1.1) hydrodynamic time-scale of minutes. The recombination rate of free electrons to protons is slower by orders of magnitude than the bound hydrogen radiative transition rates. This sustains the ionisation degree of the plasma for a long period, and is known as a slow recombination. Moreover, radiative transfer in the optically thick Lyman continuum sustains the ionisation degree of the plasma, with radiation escaping from only the top layers of the model. The effect of this sustained ionisation throughout the atmospheric depths is that profiles are highly broadened. Therefore, the deeper atmosphere produces sustained wing emission, which has a lower optical depth than the radiation in the Lyα line core, and thus, it can escape. Core emission from deeper levels is trapped due to the high optical depth and this absorption creates a double reversed self-absorption line

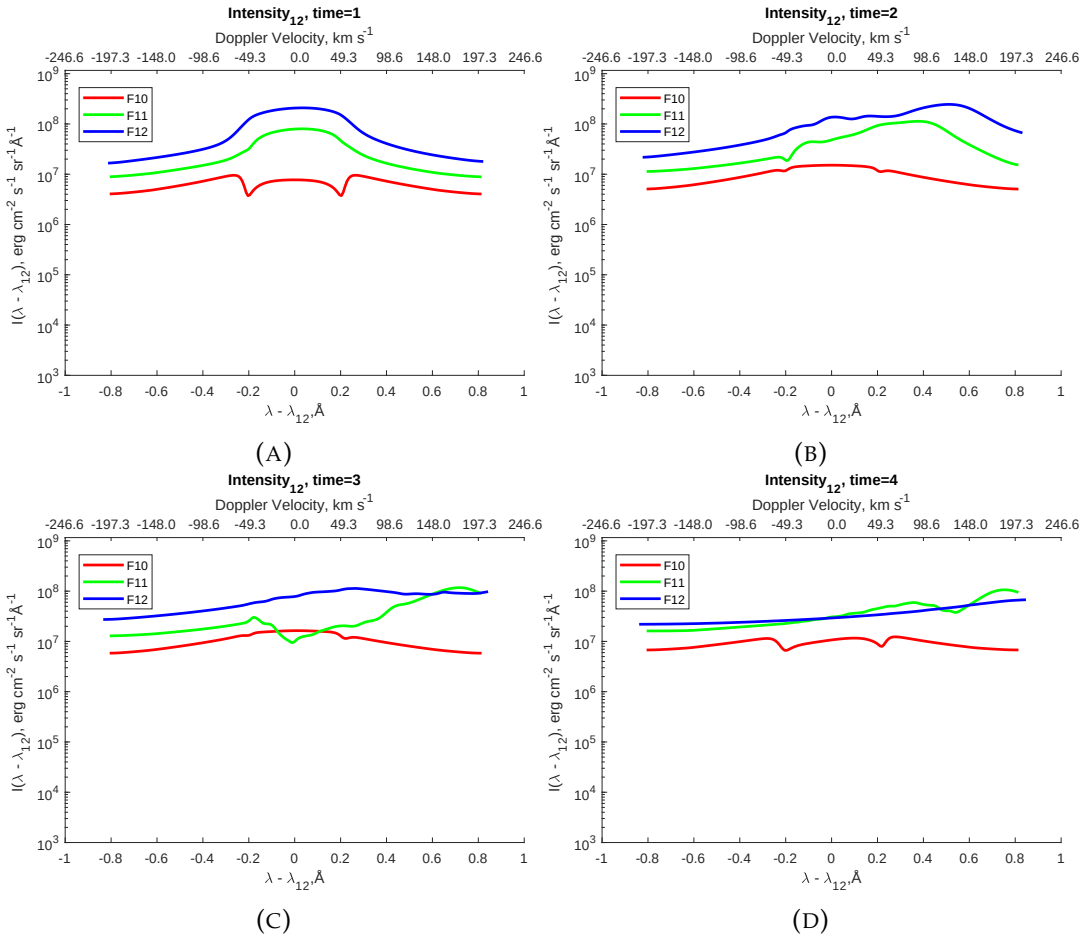

FIGURE 5.1: The Lyα line profiles during the impulsive phase. The profiles for the F10 model are shown with a red line, the F11 with a green line and the F12 with blue for the times 1-4 seconds after beam injection in panels (a) to (d). The Lyα line profiles show Doppler red-shifted emission during the impulsive phase of a solar flare, with more enhanced emission and larger Doppler shifts in models including beams with higher initial fluxes.

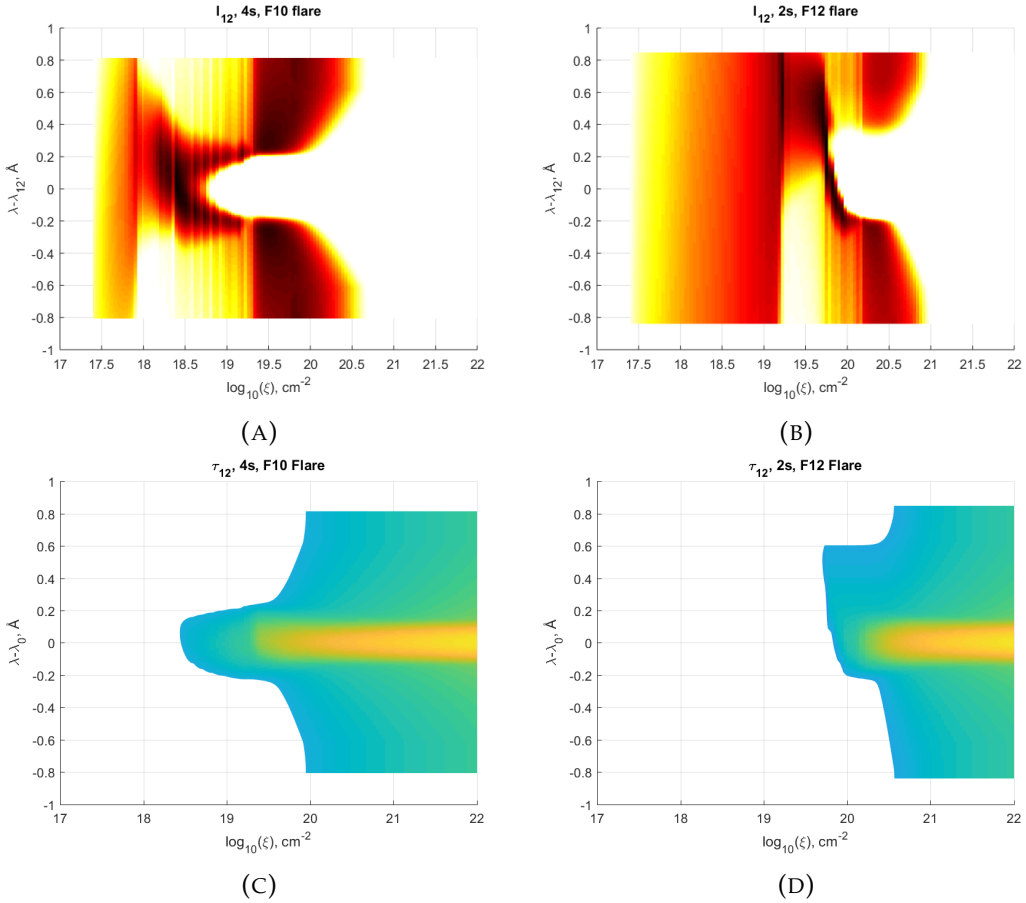

FIGURE 5.2: The Lyα line contribution functions (top row) and optical depths (bottom row) during the beam injection. The logarithm of column depth is shown on the x-axis, and the wavelength relative to the line centre (1216Å) is shown on the y-axis. The logarithms of the contribution functions +1, for the Lyα emission intensity are shown in panels (a) at 4 seconds in the F10 model and panel (b) at 2 seconds in the F12 model. The colour scale runs from light (low contribution) to dark (high contribution). The bottom panels display the optical depths at similar times. The optical depths are shown starting from a value of 1 (light blue) and increasing to an optical depth of $> 10^9$ in the line centre at the base of the model. The red-shifted emission in the Lyα line core in the impulsive phase of the flare is seen to be produced at the column depth at which the optical depth in the line core is just less than unity.

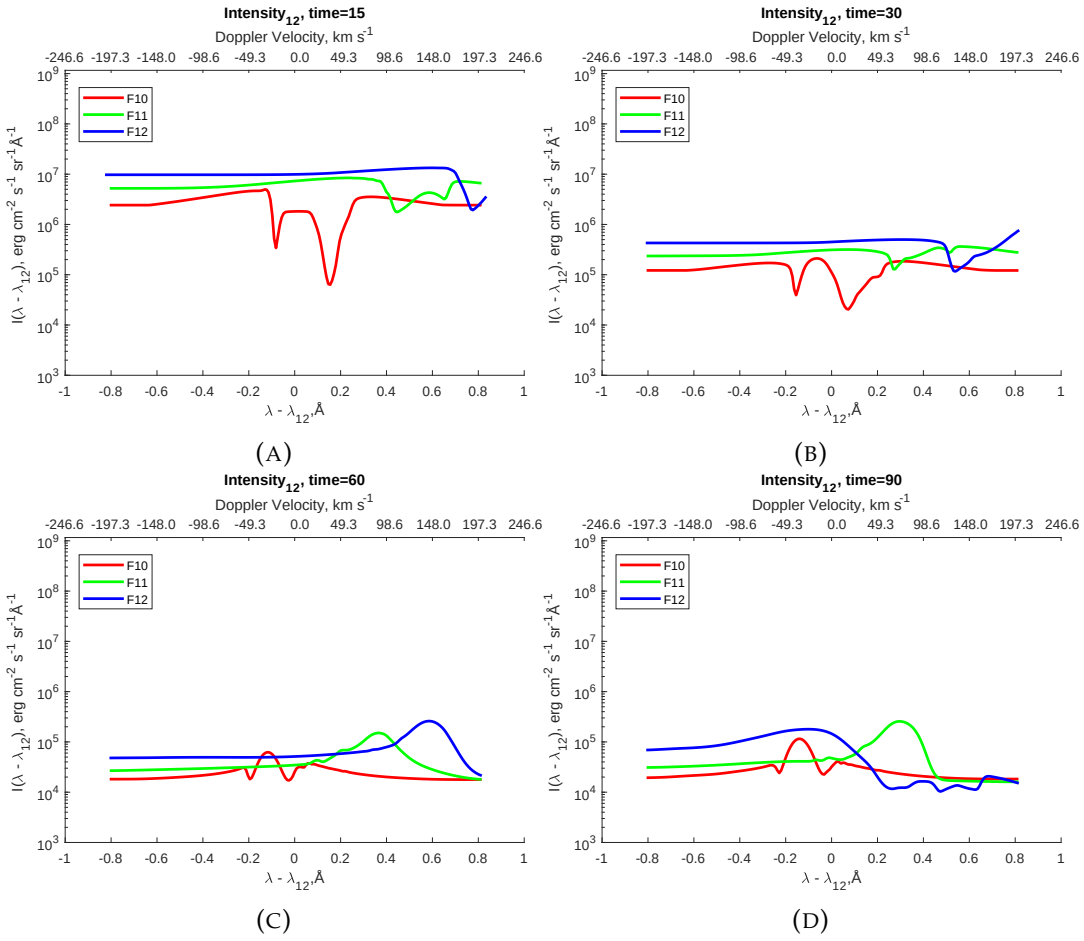

FIGURE 5.3: The Lyα line profiles after the electron beam stops. The profiles for the F10 model are shown with a red line, the F11 with a green line and the F12 with blue for the times 15, 30, 60 and 90 seconds after beam injection in panels (a) to (d). At later times in the simulations the Lyα line profiles begin to exhibit blue-shifted emission.

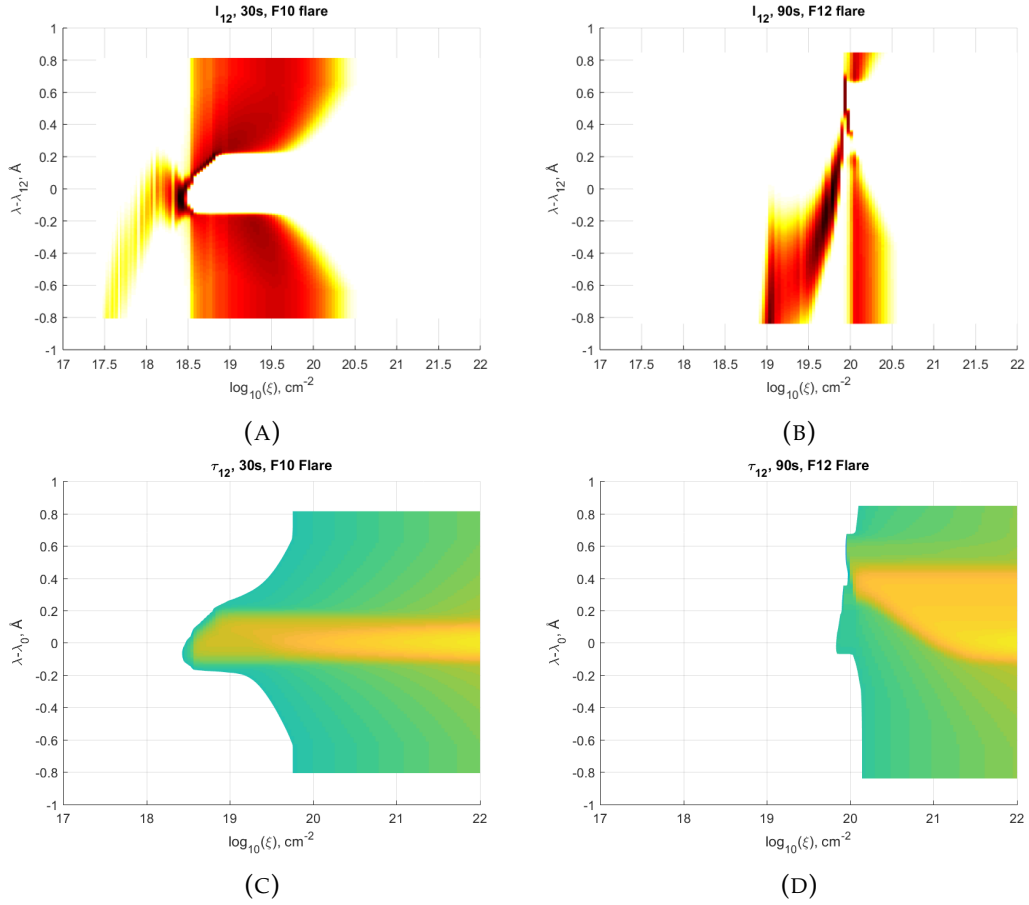

FIGURE 5.4: The Lyα line contribution functions (top row) and optical depths (bottom row) after the beam injection. The logarithm of column depth is shown on the x-axis, and the wavelength relative to the line centre (1216Å) is shown on the y-axis. The logarithms of the contribution functions +1, for the Lyα emission intensity are shown in panels (a) at 30 seconds in the F10 model and panel (b) at 90 seconds in the F12 model. The colour scale runs from light (low contribution) to dark (high contribution). The bottom panels display the optical depths at the similar times. The optical depths are shown starting from a value of 1 (light blue) and increasing to an optical depth of $> 10^9$ in the line centre at the base of the model. The blue-shifted emission is seen to be core emission from optically thin, evaporating plasma.

core with high horns, and the small emission peak due to the emission from the optically thin top layers of the chromosphere (Fig.5.3a, b and Fig.5.4). As the electrons slowly recombine and the plasma cools off, emission intensities are decreased in the Lyα line (Fig.5.3).

Lyman continuum radiation is optically thick (see chapter 4), and escapes the model only from the top layers of the flux tube. Thus, the non-thermal Lyman continuum radiation generated by the beam electrons is trapped after the beam has stopped. This sustains the high radiation temperature and ionisation degree of the plasma for a long time. Moreover, the recombination rate of free electrons to protons is slower, by orders of magnitude, than the bound hydrogen radiative transition rates. Slow recombination, thus, works in conjunction with the radiative transfer in the Lyman continuum to sustain the ionisation degree of the plasma.

The effect of this sustained ionisation throughout the atmospheric depths is that the Lyman line profiles are highly broadened. Therefore, the deeper atmosphere produces sustained wing emission, which has a lower optical depth than the radiation in the Lyα line core, and thus, the radiation from the wings can escape. Core emission from deeper levels is trapped due to the high optical depth. This absorption creates a double reversed self-absorption line core with high horns, and the small emission peak, due to the emission from the optically thin top layers of the chromosphere (Fig.5.3a, b and Fig.5.4). As the electrons slowly recombine and the plasma cools off, emission intensities are decreased in the Lyα line (Fig.5.3).

After the beam is switched off, the temperatures of the models decrease but the plasma still continues to up-flow from greater column depths with the increasing time for another hundred seconds. One sees the evidence of this up-flowing material in the profiles of the Lyα line, from the emission observed from the flare transition region and upper chromosphere at later times of the simulation. For plasma with the temperatures $< 50,000$K, which emit radiation in the Lyα line core, the up-flows occur at around 30 s for the F10 model. One can compare the column depth of $50,000$K plasma in Fig.2.2a with the column depths showing the up-flows in Fig.2.2b. These column depths match with the blue-shifted core emission evident in the contribution function, Fig.5.4a). The result of this up-flow is clearly seen in the blue-shift of the Lyα line core in the F10 model at 30 s (Fig5.3b). This blue-shift increases

throughout the rest of the 100 second simulation. For the models with stronger electron beams, plasma heating becomes much greater and the flare transition region is shifted downward to greater column depths (chapter 2). Plasma up-flows also occur from deeper column depths in the models with stronger beams. For stronger beams, the net result is that the regions in which the Lyman line cores form do not contain up-flows until later in the simulation. A strong blue shift is seen in the Lyα line core at 90 s in the F12 model (Fig.5.3d). This emission originates from the optically thin upper levels of the line formation region (see Fig.5.4b and d, with column depths less than 10^{20}cm^{-2}), which has a large spread of macro-velocities and, thus, appears almost like a wing emission. The fact that this is blue Doppler-shifted core emission and not wing emission can be seen from the contribution functions (Fig.5.4d), as well as the much greater emission in the blue wing of the Lyα line profile than in the red wing (Fig.5.3d, blue line).

5.3.2 Profiles of other Lyman lines

The profiles for the Lyman beta (Lyβ) line simulated during the beam injection phase are shown in Fig.5.5a to d, at 1 to 4 seconds into the simulation, respectively. It was found that the Lyman gamma (Lyγ) and delta (Lyδ) line profiles are similar to the Lyβ line profiles. Fig.5.6 illustrates this fact, showing the Lyγ line profiles at 1 and 4 seconds of the simulation, which can be directly compared with the profiles of the Lyβ lines at the same times. At the top of the flaring chromosphere, the Lyβ line core wavelengths are significantly less optically thick than the Lyα line core and, therefore, Lyβ core emission escapes from this region from the first second of each simulation, forming the emission profiles with absolute intensities in the line core that are lower than Lyα. Broader cores are again seen in the simulations using more powerful electron beams (see Fig.5.5a). The core formation regions of the higher lines in the Lyman series start at the same column depth as the Lyα lines, but extend to slightly greater column depths. Thus, after 2 seconds there is a significant enhancement seen in the red-wing of the F11 and F12 models (see Fig.5.5b) due to Doppler-shifted core emission from the upper layers of the chromosphere. However, unlike the Lyα line, the intensity in the Lyβ line central wavelength is fully sustained by emission from the deeper plasma layers, which have smaller associated Doppler

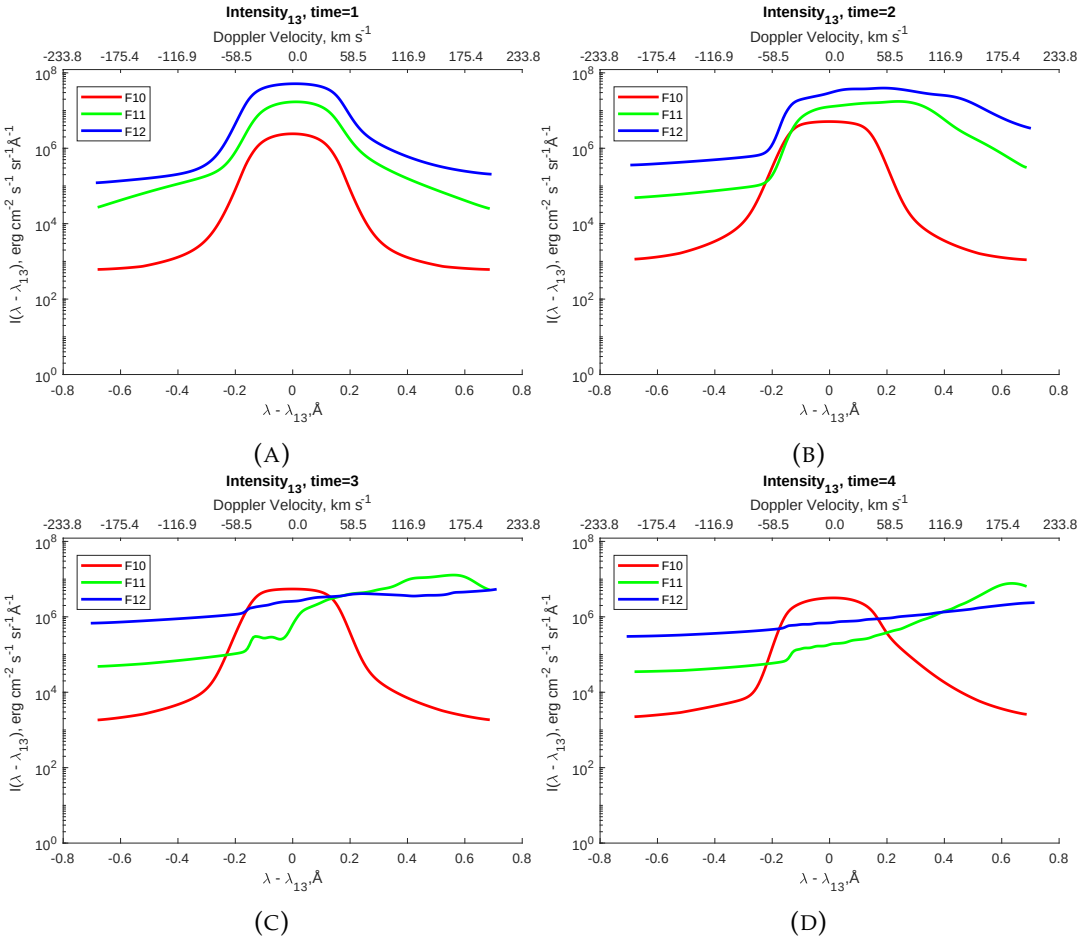

FIGURE 5.5: The Lyβ line profiles during the impulsive phase. The profiles for the F10 model are shown with a red line, the F11 with a green line and the F12 with blue for the times 1 and 4 seconds after beam injection in panels (a) and (b).

shifts at this time. In Fig.5.5c and d after 3 and 4 seconds of the beam injection respectively, we see the emission profiles peak for the F11 and F12 models in the far red wings of the lines. This is because the downward moving hydrodynamic shock occupies a greater portion of the core formation region at these times. In the F10 model, the Doppler shifted Lyβ core emission occurs later than in the models with more powerful beams, and the extent of the Doppler shift is smaller (see Fig.5.5d).

The profiles of the Lyβ lines occurring after the beam is switched off are shown Fig.5.7a-d, at 15, 30, 60, and 90 seconds of the simulation respectively. In the F10 model, the Lyβ line core is much less broad than during the beam injection phase. Also, there is a blue asymmetry of the wing emission, clearly evident at 60 and 90 seconds due to the core emission coming from the very top of the line formation

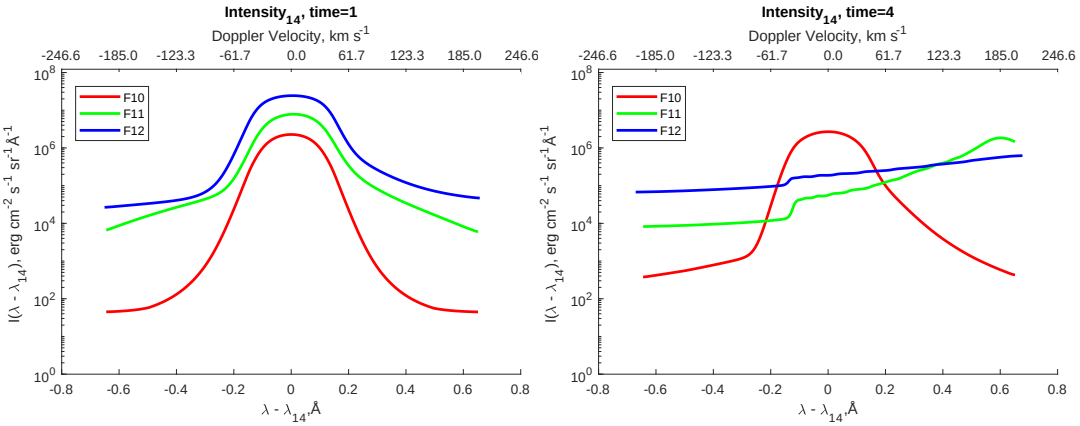

(A) (B)

FIGURE 5.6: The Lyγ line profiles during the impulsive phase. The profiles for the F10 model are shown with a red line, the F11 with a green line and the F12 with blue for the times 1-4 seconds after beam injection in panels (a) to (d).

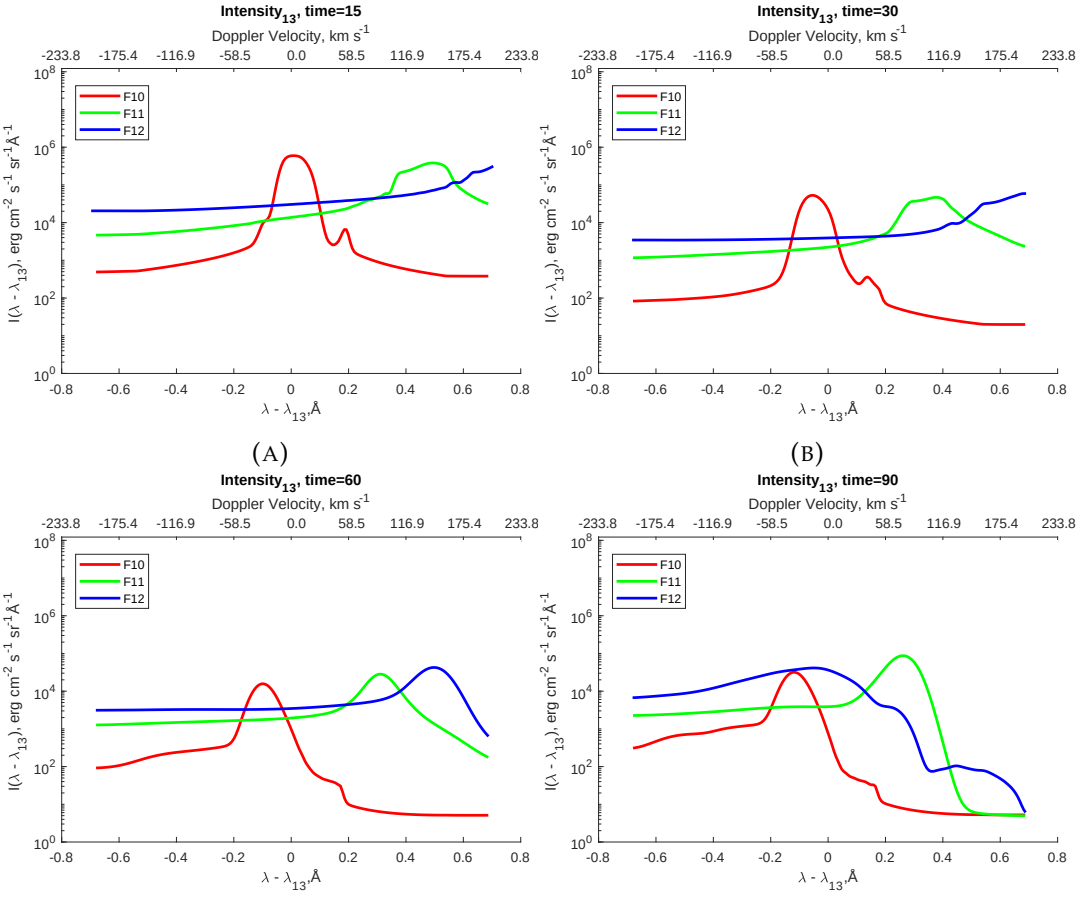

(A) (B)

(C) (D)

FIGURE 5.7: The Lyβ line profiles during the gradual phase. The profiles for the F10 model are shown with a red line, the F11 with a green line and the F12 with blue for the times 15, 30, 60 and 90 seconds after beam injection in panels (a) to (d).

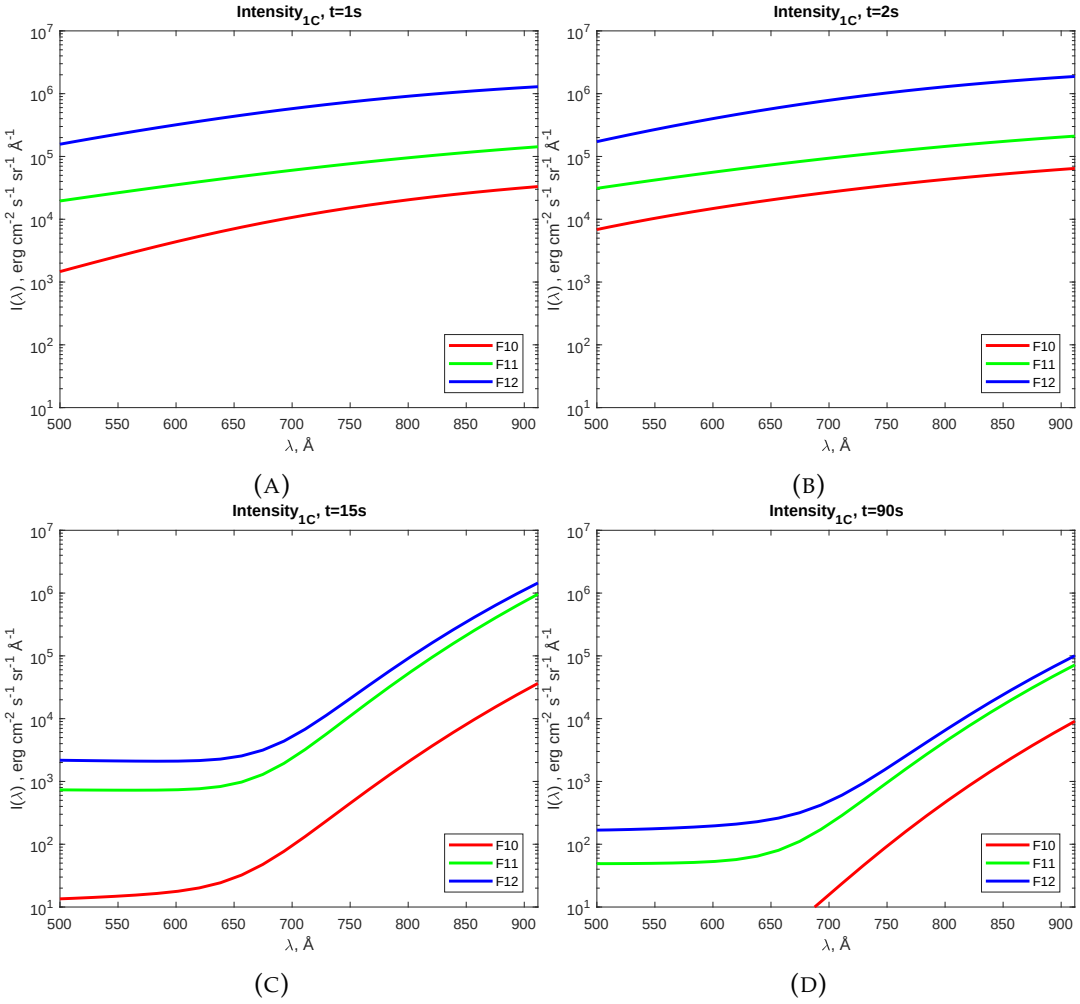

FIGURE 5.8: The Lyman continuum emission. Profiles are shown during the impulsive phase after 1 second (a) and 2 seconds (b), and during the gradual phase after 15 seconds (c) and 90 seconds (d), calculated for the F10 (red line), F11 (green line) and F12 (blue line) models.

region, in the transition region, in which evaporation occurs. In fact, the blue asymmetries after the flare maximum are evident across all of the simulations presented in all Lyman lines.

5.3.3 Simulations of Lyman continuum emission

The Lyman continuum emission, calculated for the same models, are shown in Fig.5.8 with the wavelength on the X-axis and the emission intensity on Y axis during the beam injection phase at 1 second (a) and 2 seconds (b) of the simulation respectively. The emission after the beam is switched off is shown at 15 seconds (c) and 90 seconds (d).

The Lyman continuum is optically thick in the flaring chromosphere for any of the hydrodynamic models (F10, F11, or F12, see Fig.2.2). The optical depth at the continuum head wavelength reaches $> 10^5$ at all times at the base of the flux tube for the F10, F11, and F12 simulations. Moreover, it becomes optically thick at depths on the top of the flaring chromosphere. Therefore, Lyman continuum radiation escapes only from the very upper layers of the chromosphere in the models where its optical depth is about unity, thus governing the hydrogen ionisation in the underlying levels.

During an injection phase, beam electrons quickly (1 s) ionise the plasma, raising the intensity in the Lyman continuum at the same time as they heat the plasma to high temperatures. This process creates a low gradient of intensity variation away from the continuum head (Figs.5.8a and b). The intensity of the emission scales with the intensity of an electron beam, and the intensity peaks co-temporally with the flux of the beam.

After the beam is switched off, the ionisation degree of hydrogen plasma is sustained by radiative transfer in the Lyman continuum and slow recombination of the ambient electrons with hydrogen atoms. Thus, the intensity of emission in the Lyman continuum head reduces very slowly (Figs.5.8c and d). However, the plasma also cools off, meaning that the recombinations are happening at lower temperatures than during the impulsive phase. Therefore, one sees a steepening of the gradient of the Lyman continuum after the beam is switched off (Figs.5.8c and d). The ionisation degree is kept at the same level for tens of minutes, leading to white light flares. This reduction of the gradient of the Lyman continuum during the beam injection is consistent with those reported for the F1 and F2 flare models of Ding and Schleicher, 1997, when compared with their spectra from quiet Sun emission.

5.3.4 Comparison with the Lyman line observations

Let us first discuss the caveats regarding the suitability of comparisons of Lyman line observations in flares with the simulated emission profiles based on a 1D flux tube model.

For other chromospheric lines, 1D flux tube models may accurately reproduce

the observed emission profiles in small flare kernels at the foot-points of the reconnecting magnetic field lines. Lyman line profiles are generally made using low-resolution observations, or even full solar disk images, meaning the collected light from these large areas are clearly not representative of the small flare kernel. For this reason, these observations are not really comparable to 1D flux tube flare models. However, there are certainly some qualitative comparisons possible that can potentially provide valuable insight on Lyman series emission.

Firstly, flare kernels are observed to be particularly bright in Lyman emission (Wood et al., 1972; Wood and Noyes, 1972; Křivsky and Kurochka, 1974; Machado and Noyes, 1978). Secondly, these kernels are particularly associated with strongly asymmetric line profiles during the impulsive phase of the flare (Švestka, Kopecký, and Blaha, 1961; Ichimoto and Kurokawa, 1984; Wuelser and Marti, 1989; Li, Ning, and Zhang, 2015; Kowalski et al., 2017). Therefore, even with low resolution flare observations, it may be possible for 1D models to reproduce the overall trends in the Lyman line asymmetry throughout a flare. Such attempts may, however, be confounded by the fact that flares generally show multiple beam injection locations with different timings and time-profiles that will complicate the interpretation.

Slight asymmetries in Lyα lines profiles obtained from full disk images of the Sun, with an excess in the red wing before the flare maximum and an excess in the blue wing after the flare maximum, were reported by Canfield and van Hoosier, 1980. This is in line with our findings for the Lyα flare kernels emission in the F10, F11 and F12 models, which show the red-shifts at the beginning of the impulsive phase, which last for around 30 to 90 seconds, before being replaced by blue shifts due to evaporation from the flaring plasma from the upper chromosphere (Figs5.1, 5.3).

The observations of Lyman lines by Lemaire, Choucq-Bruston, and Vial, 1984 are also in general agreement with the kernel emission simulated in our models, namely: they show an impulsive peak, which is co-temporal with the increased wing emission. We also note that in our models the variations of Lyman line intensities with time are in a much closer agreement with the impulsive phase of the solar flares than with the gradual phase, since we model the impulsive phase.

It is particularly tricky to compare our simulations with the macro-velocities reported in the higher Lyman line observations of Brown, Fletcher, and Labrosse, 2016 because the reported macro-velocities are highly dependent on the method of measurements used, as discussed in section 1.2.4. We note that the Doppler-shifts reported are generally in line with those seen in the F10 model ($\pm 60 \text{km} \cdot \text{s}^{-1}$) and lower than the velocities seen in the F11 and F12 simulations. This can be a reflection of both the methods and the specific events considered.

5.3.5 Comparison with the observations of Lyman continuum enhancement

Lemaire et al., 2004 report impulsive enhancements of Lyman continuum emission at ~ 900Å in the bright flare kernels that is several thousand times greater than the background enhancements. The similar emission intensity increase in the hydrogen Lyman continuum head ($\lambda = 910$Å) is simulated during the beam injection for the F12 model (see Fig.5.8b, blue line). This is more than 100 times the emission after 90s in the F10 model (see Fig.5.8d, red line), which is again greater than the emission from the quiet Sun. The quiet Sun emission intensities in the Ly continuum head provided in the models of Ding and Schleicher, 1997 are all in the range $10^2 - 10^3 \text{erg} \cdot \text{cm}^{-2} \cdot \text{s}^{-1} \cdot \text{sr}^{-1} \cdot \text{Å}^{-1}$. The enhancements observed by Lemaire et al., 2004 are, thus, shown to be consistent with the enhancement from ionisation of the ambient plasma by the non-thermal beam electrons through elastic collisions, as shown in our models.

The intensities of emission in the Lyman continuum heads only drop by a factor of ~ 10 in each model during the 80 s after the beam is switched off (see Fig.5.8d). This decay rate agrees well with the reports of particularly bright impulsive enhancements above the general flare continuum increase, lasting around 2 minutes in small kernels (Machado and Noyes, 1978). The slow decay of impulsive brightening results from radiative transfer in the Lyman continuum, which is highly optically thick and traps the radiation, sustaining the ionisation degree throughout the depths of the model. Lyman continuum emission only escapes from the optically thin upper layers of the chromosphere with optical depth ~ 1, controlling the radiative loss of energy that was originally supplied to the atmosphere by collisions with

the non-thermal beam electrons.

5.4 Discussion and conclusions

Our simulations illustrate that the Lyman lines in flaring atmospheres are affected by the dual effects of an injected electron beam via hydrodynamic and radiative responses, and the Lyman line responses are strongly indicative of the conditions at the top of the chromosphere and transition region.

Heating and excitation by beam electrons increase the emission intensities in the Lyman line cores during the impulsive phase. At the same time, heating by the beam electrons broadens the profiles by greatly increasing the Doppler widths of the lines at the top of the chromosphere, and ionisation by the beam electrons increases the electron densities leading to greater broadening by collisions with ambient electrons. The broadening and the increases in intensity of the Lyman lines scale with the flux of the beam (Fig.5.3). This matches the description given by Lemaire, Choucq-Bruston, and Vial, 1984 of broadened Lyα lines showing intensity peaks in the impulsive phase of flares. The Lyα line cores are not observed in emission in the profiles reported by Canfield and van Hoosier, 1980, but it must be recalled that these profiles were made from full-disk observations, and thus will not fully reflect the emission from the small flare kernels modelled in this paper.

The conversion of the quiet Sun chromosphere into a flaring atmosphere described in chapter 2 results in sweeping of the chromospheric plasma down to the photosphere via a hydrodynamic shock. This shock forms in the regions of the Lyman lines in all the simulations presented in this paper, leading to red-shifted Lyman emission in the line profiles. Intensities in the line central wavelengths are maintained by the emission from the material below the shock (Fig.5.1).

The ionisation degree of the plasma is strongly increased during the beam injection by collisions between the non-thermal electrons and the ambient plasma. After the beam is switched off, the ionisation degree is maintained by radiative transfer in the Lyman continuum combined with slow recombinations, leading the to wing emission that decreases slowly over the remainder of the simulation. The line cores with strong self-absorption are seen in the simulated profiles. When the

beam is switched off, the temperature of the flaring corona reduces, and the hydrodynamic shock continues to move down through the atmosphere, this results in evaporation from the transition region and chromospheric plasma to the corona. Blue-shifted, optically thin core emission is often seen in the simulated Lyman line profiles (Fig.5.3), sometimes at the same time as the red shifted core emission from deeper atmospheric layers (see F11 and F12 models, Fig.5.3). The pattern of Lyman line profiles with the red-wing excess in the impulsive phase, with blue-wing excesses seen at later times is consistent with the observations taken before and after the flare maximum reported by Canfield and van Hoosier, 1980.

The magnitudes of the Doppler shifts in the Lyman line profiles of the F10 model are comparable with the values of up to ± 60 km·s^{-1} reported by Brown, Fletcher, and Labrosse, 2016, although they report no observations of the greater Doppler shifts suggested by the F11 and F12 models. However, the observed profiles reported in Brown, Fletcher, and Labrosse, 2016 are from full disk images of the Sun, and the difficulty in reporting average Doppler velocities from the whole active region is clear from the variation in values produced when different methods were used by the authors, such as Gaussian fitting or cross correlation functions. It is not surprising that the observed velocities are lower than for our simulations: the background subtracted intensities analysed are the net emission over the whole active region and not the small, impulsive foot-points of the reconnecting loops which are known to have quite different characteristics from observations in other transition region and chromospheric line observations.

Non-thermal particles beams are shown to be capable of producing the red-shifted Lyman line emission observed before a flare maximum, and the subsequently blue-shifted emission at later times. The Lyman line emission intensities are shown to peak in the impulsive phase.

In the optically thick Lyman continuum, radiation only escapes from the top layers of the chromospheric temperature plasma. Therefore emission intensities are sustained after the beam has stopped. Radiative transfer in the Lyman continuum regulates the slow decrease of the ionisation degree in flare plasma.

These findings are important for understanding the dynamics of the upper chromosphere and transition region in solar flares, and can be useful to diagnose the

formation height of hydrodynamic shocks in the chromosphere that result from non-thermal beams of energetic particles. Analysing emission and radiative transfer in the Lyman continuum provides important insight into the dissipation of a flare energy delivered to the chromosphere.

Thus, it is highly encouraging that these theoretical findings can be compared with new observations by recently proposed instruments such as the Extreme Ultraviolet Imager (EUI) the Multi-Element Telescope for Imaging and Spectroscopy (METIS), the Chromospheric Lyman-Alpha SpectroPolarimeter (CLASP), the Lyman Alpha Spicule Observatory (LASSO), and the Lyman-α Solar Telescope (LST).

In summary,

(5.1) We predict that the Lyman lines will show an impulsive phase enhancement in the flaring foot-points of the loops due to excitation of the plasma by collisions with the non-thermal electron beam producing the HXR signal.

(5.2) The Lyman line profiles can be used to understand the conditions at the top of the flaring chromosphere. Red-shifted emission will be evident during in the impulsive phase, and blue-shifted emission will occur around 20-80 seconds later, depending on the parameters of the injected beam.

(5.3) Lyman continuum emission shows long lasting enhancement that begins with the onset of the non-thermal HXR as a result of the trapping of optically thick Lyman continuum radiation. The profile of the continuum enhancement shows a lower gradient during the impulsive phase, than in the gradual phase as a result of the higher energy and higher temperature emission at these times.

(5.4) This work addresses the lack of predictions from models, regarding the forthcoming missions that will provide high resolution observations of the Lyman lines and continuum. This was highlighted in point **1** of section 1.3 and discussed in sections 1.1.3, and 1.2.4.

5.5 Notes

Much of the work in this chapter is taken from a paper in preparation, and was completed in collaboration between Prof. Valentina Zharkova and I.

Chapter 6

Hydrogen line emission: Balmer and Paschen series

6.1 Line intensity profiles: core, wings, and macro-velocity

To analyse emission from a flaring atmosphere in the hydrogen Balmer and Paschen lines and continua we use the full NLTE radiative code for the relevant hydrodynamic atmospheres with matching beam parameters. At first, in order to discern direct effects of energetic particle beams on the line profiles, let us consider emission without including any shifts due to plasma macro-velocities as presented in section 6.1.1. Subsequently, in section 6.1.2, we consider line profiles with the Doppler shifts included to produce a more complete picture of the resultant line profiles and to compare them with observations.

6.1.1 Balmer and Paschen lines: core and wing responses

Fig.6.1 shows the simulated enhancements of the Hα line profiles for 1-5 s after a beam onset (panels a-e respectively), with intensity (I) presented on the y-axis in erg·cm^{-2}·s^{-1}·sr^{-1}·Å^{-1} and distance from a line centre ($\lambda - \lambda_0$) in Å on the x-axis. Hereafter, the lines show the profiles for the F12 model (blue), the F11 model (green) and the F10 model (red). When a beam of energetic electrons is injected down through the solar atmosphere from the corona, inelastic collisions between beam electrons and the neutral hydrogen cause electrons in hydrogen atoms to move into excited states of the upper atomic levels and to become quickly ionised.

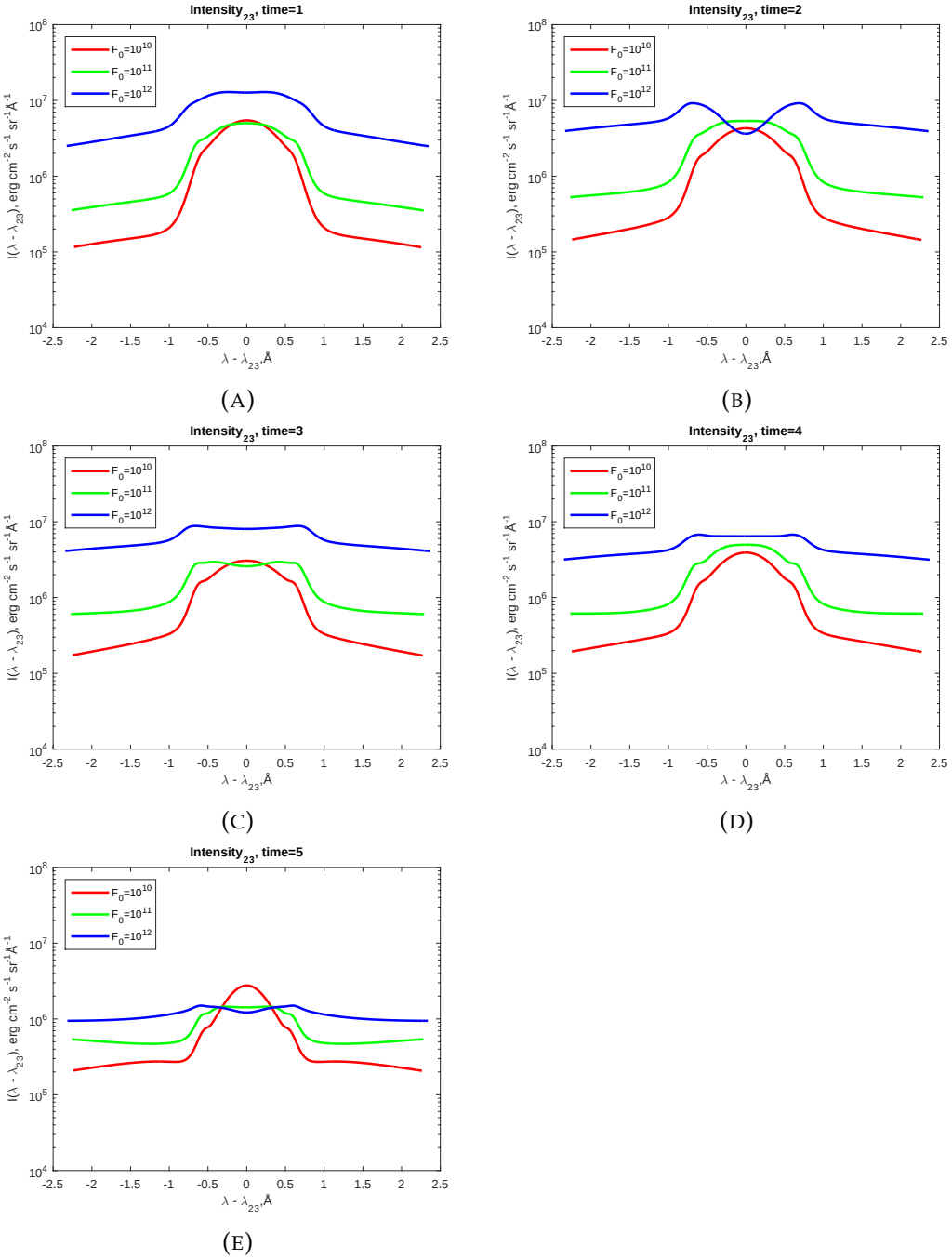

FIGURE 6.1: Profiles of Hα line intensity enhancements, in erg·cm^{-2}·s^{-1}·sr^{-1}·Å^{-1}, plotted versus distance in Å from the line central wavelength for times from 1 to 5 seconds in panels (a) to (e) respectively. Results are shown for the F12 (blue line), F11 (green line) and F10 (red line) beam models. The colour scheme for the lines representing these models is also used in Figs.6.2 to 8.1

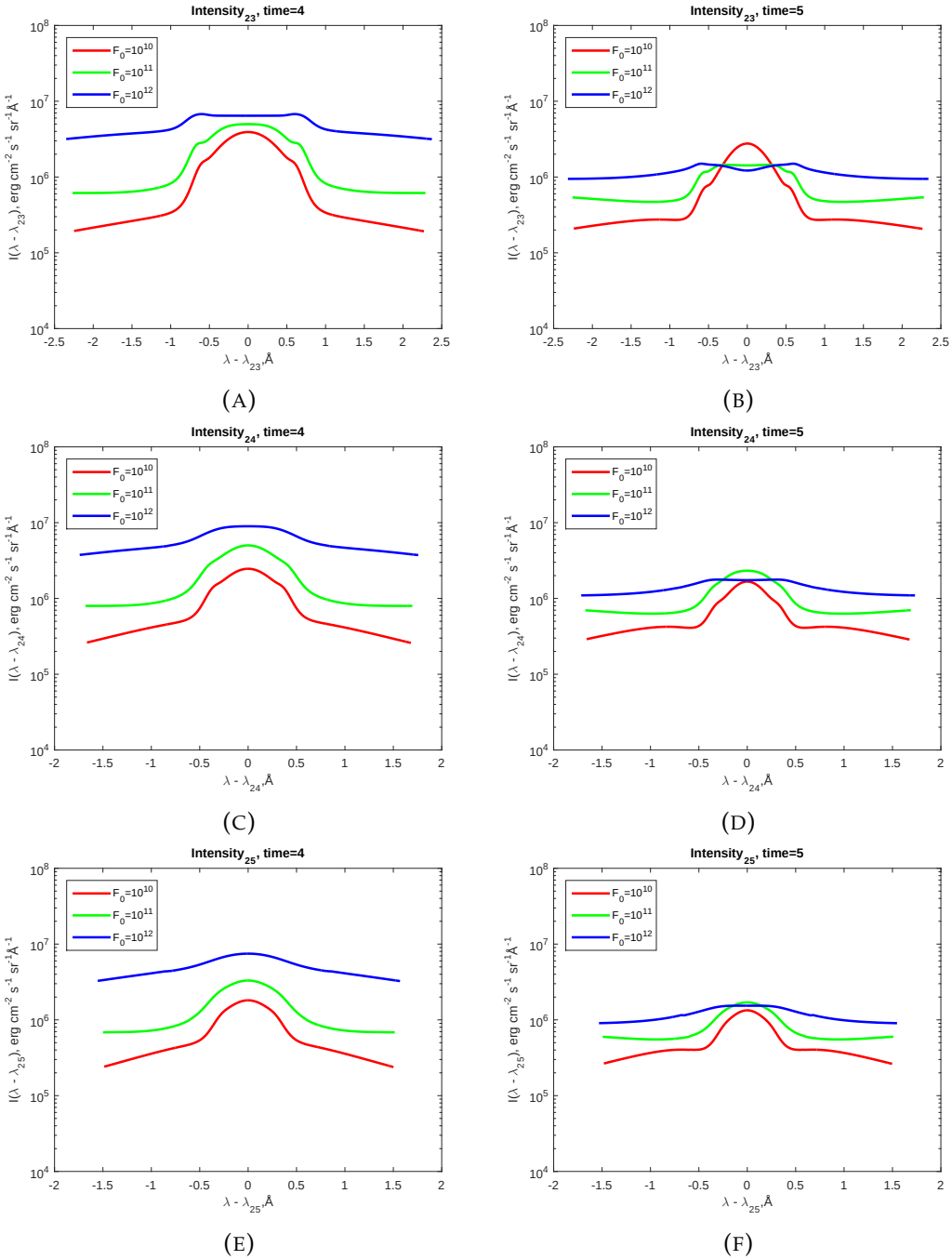

FIGURE 6.2: Intensity enhancements in erg·cm^{-2}·s^{-1}·sr^{-1}·Å^{-1} against distance from line centre in Å for the Hα (top panels, a and b), Balmer beta (Hβ) (middle panels, c and d), and Hγ (bottom panels, e and f) lines 4 s (left panels) and 5 s (right panels) seconds after the beam injection begins.

This increases the source functions of the hydrogen line and continua so that the lines, like Hα, which are in absorption in the quiet sun are converted into emission lines in flaring atmospheres. When in emission, these line profiles have a Doppler-broadened core around the central wavelength (see Fig.6.1a, at wavelengths between ± 0.5Å). If the optical thickness is high in this transition, there is significant self-absorption in the central wavelength of the line with the horns of increased intensity appearing in the near wings of the profile (see Fig.6.1b and e at ± 0.7Å and ± 0.5Å in the F12 model). There are also extended wings in these profiles due to Stark's effect. These extended wings can be seen between 1 and 2.4Å from the central wavelength in Fig.6.1.

Let us inspect these profiles in a greater detail as shown in table 6.1, which presents the number density (n_{tot}), ionisation degree (χ) and ratio of hydrogen atom numbers with electrons in level 3 to those with electrons in 2 ($\frac{n_3}{n_2}$) one second after beam onset. This information is presented for each of the models at the point where the optical depth (τ) of the Hα line is $= 1$. Simulations showed that one second after a beam onset all the Hα line cores become optically thick at the depths where the kinetic temperature approaches 18,000K.

Zharkova and Zharkov, 2007 show that electron beams with higher initial fluxes of electron beams result in the flare transition region is formed at a greater column depths. This effect can lead to an increase of the column depth and, therefore, densities of the formation regions for hydrogen lines (see table 6.1). This can be an essential addition to the influence of radiative processes on resulting intensities in lower transitions (Lyman series) or in opposition to radiative processes acting to form the core higher in the atmosphere in upper transitions (Paschen Series) (see section 4). In the Balmer line formation regions there are greater non-thermal excitation and ionisation rates for beams with higher initial fluxes. Therefore, there is more hydrogen atoms with electrons in the upper excited levels (table 6.1). The greater ratio of atoms with electrons in the upper levels of Balmer lines to those in the lower state ($n = 2$) explains an increase of the emission in Balmer lines for stronger beams. (Fig.6.1).

The line broadening results from collisional broadening caused by ambient and beam electrons and Stark effect caused by local electric fields produced by them.

Flare Model	$n_{tot}(\tau = 1)$ (cm^{-3})	$\chi(\tau = 1)$	$\frac{n_3}{n_2}(\tau = 1)$
F10	$7.9E + 11$	0.90599	$1.02E - 2$
F11	$2.1E + 12$	0.93240	$2.22E - 2$
F12	$5.8E + 12$	0.97239	$2.68E - 2$

TABLE 6.1: Characteristic core formation conditions for the Hα line at $t = 1$ second: values of the number density n_{tot}, the ionisation degree χ, and the ratio of neutral hydrogen atoms with electrons in state 3 to those with electrons in state 2 $\frac{n_3}{n_2}$ are shown for the point at which the Hα line has an optical depth of $\tau = 1$. Results are presented for the F10 (top row), F11 (middle row) and F12 (bottom row) beam models.

These are both dependent on a number of free electrons. In stronger flares the hydrodynamic response to a beam injection shifts the line formation regions into deeper layers with higher densities. Combining this with the increased ionisation degree that results from a stronger beam (evident in table 6.1 and Fig.6.3) we have ideal conditions for the broadened lines with stronger wings as the initial energy flux of a beam causing it is increased. Fig.6.2 presents the simulated enhancements in line profiles in the Hα line (top row), Hβ line (middle row) and Hγ line (bottom row) at 4 and 5 s after the onset of a beam. There is an evident pattern in the Balmer series showing the beams with larger initial fluxes producing broader, less pronounced cores of emission lines and more extended wings (Figs.6.1 and 6.2) throughout the beam injection phase.

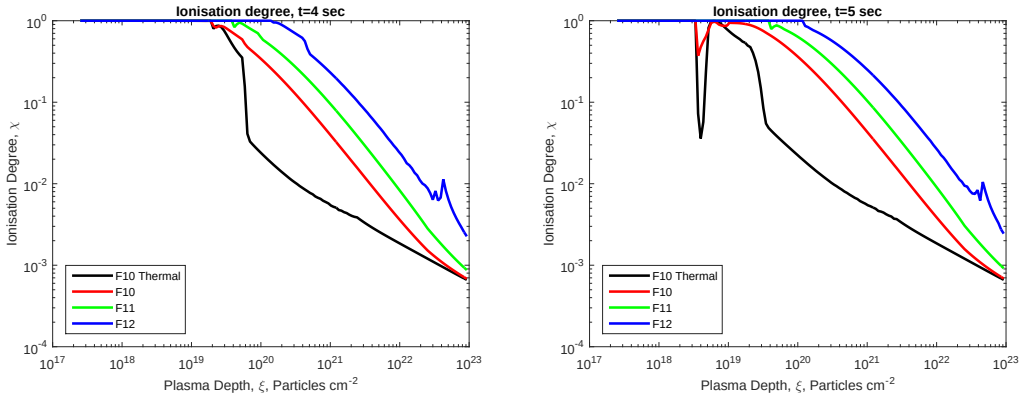

(A) (B)

FIGURE 6.3: The ionisation degree at 4 (a) and 5 (b) seconds plotted against plasma column depth (cm^{-2}) for the thermal (black line), F10 (red line), F11 (green line) and F12 (blue line) models.

Fig.6.3 displays the ionisation degree plotted against column depth for the thermal (black line), F10, F11 and F12 models. Ionisation rates below the flare transition

layer are dominated by the collisions between hydrogen atoms and non-thermal electrons (Zharkova and Kobylinskii, 1993). The ionisation of hydrogen will increase owing to non-thermal inelastic collisions with beam electrons compared to pure thermal case. Additionally, excitation caused by non-thermal electrons will increase the thermal ionisation rates from higher atomic excited states. This leads to the wing intensity increase to be strongly dependent on the initial energy flux of the beam, which is evident across all the Balmer lines at all times (Figs.6.1 and 6.2).

The pattern of wing intensity dependence on non-thermal ionisation and excitation by beam electrons is enhances in the differential studies, where the beam parameters are varied in the radiative code while using the same hydrodynamic response. When we use the joint solutions of radiative and hydrodynamic problems, the wing pattern is still observed. The enhanced Hα wings without strong red shifts are well known and observed as 'moustaches' (Rust and Keil, 1992; Zharkova and Kashapova, 2005). Although, after 4 and 5 s the Hα line profile produced by the F12 flare becomes broadened so much by Stark's effect and shifted to the red wing by Doppler effect to the wavelengths, which extend well beyond the 2.4Å displacement from the line centre plotted in simulated figures (Fig 6.1).

At each column depth where the beam causes increased emission, the optical depths linked to that column depth becomes lower for the Balmer lines through the series from Hα to Hβ to Hγ. As a result the emission profile of the Hα line shows greater core self-absorption than the Hβ line, and both show greater core self-absorption than the Hγ line profile (Fig.6.2a, b, c).

6.1.2 Macro-velocity: Effects on line profiles

We generate the hydrogen emission profiles for lines with a central wavelength λ_0 using the modelled depth points in the flaring atmosphere. The emission from each layer has its own profile and associated Doppler shift $\Delta\lambda_i = \frac{V_m(i)}{c}\mu\lambda_0$ from the layer i, due to its macro-velocity $V_m(i)$ (see section 3.2). For smoothing the contributions of different layers considered, cubic splines were applied to the line profile merged from these layers. Fig.6.4 displays the Hα line profile intensity enhancements and Fig.6.6 the Pα for the F10 (red), F11 (green), and F12 (blue) models at 2, 3, 4, and 5 s from panel (a) to (d) respectively.

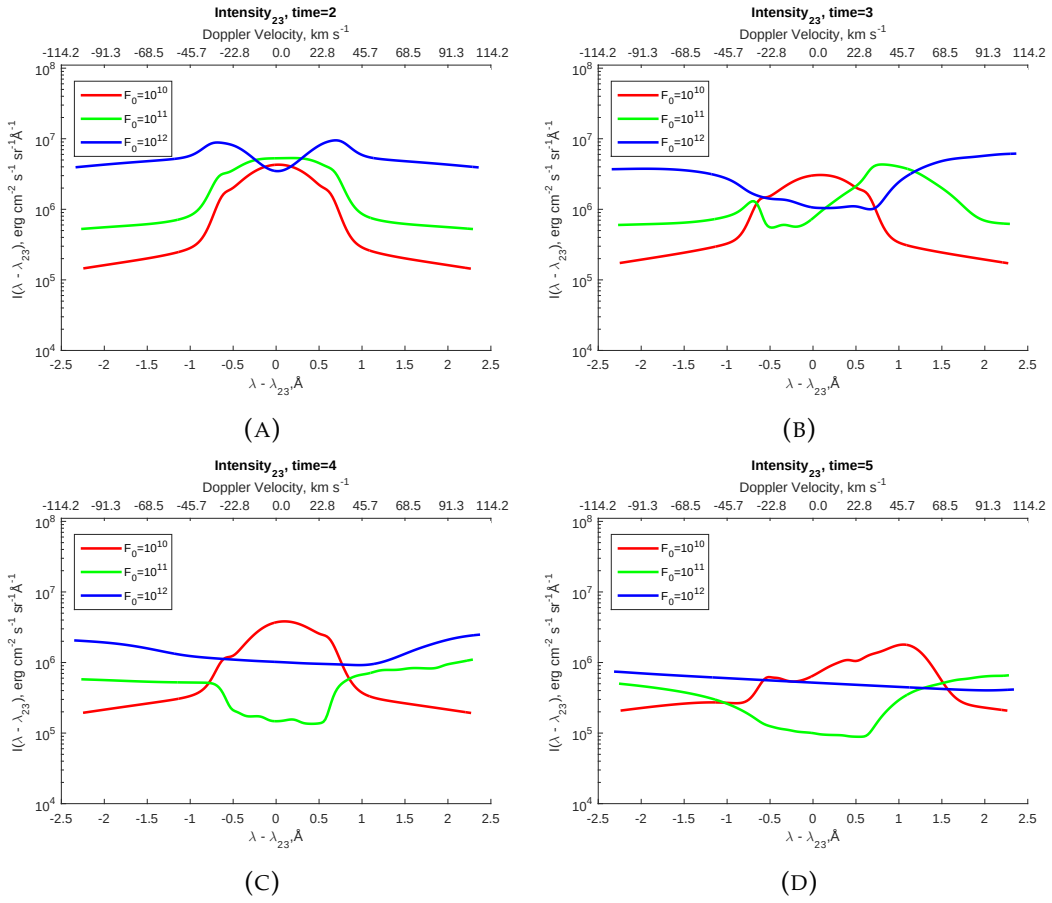

FIGURE 6.4: The Hα line intensity enhancements with macro-velocity effects included for the the F10 (Red), F11 (Green), and F12 (Blue) models. Profiles are shown for (a) $t = 2s$, (b) $t = 3s$, (c) $t = 4s$, (d) $t = 5s$, in erg·cm^{-2}·s^{-1}·sr^{-1}· Å^{-1} against distance from line centre in Å.

It is important to avoid inferring erroneous Doppler velocities from line profiles that form over a large range of depths in the atmosphere, or are observed in low spatial resolution. By considering the contribution functions (see section 3.3.3) one can see that plasma from different column depths, with very different velocities, can contribute to the overall emission profile in a spectral line. In fact, large errors are known to occur in Doppler velocity calculations using the bisector methods when working with the line profiles that contain large deformations due to emission contributions from plasma with a range of velocities (Deng et al., 2013). This issue is highlighted by the different Doppler velocities inferred using different techniques in the work of Brown, Fletcher, and Labrosse, 2016. To avoid such issues, it is practical to use the maxima in the emission intensity profiles. Red-shifts occur when the hydrodynamic shock moving downward enters the line formation region. In the Hα line there is a slight skewing of the core to the red wing for the F10 flare model at 3 s and 4 s (Fig.6.4b and c, red line). At 5 s the red-shifted core peak is visible at a wavelength of 1Å from the line centre wavelength and the blue wing forms a slight horn at -0.5Å. The peak shift suggests a Doppler velocity of 4.5×10^6cm·s^{-1} (45 km·s^{-1}). At the column depths that contribute most to the emission, we find macro-velocities in the range $3.91 - 5.36 \times 10^6$cm·s^{-1}.

By comparing profiles of the F10 flare at 5 seconds and the F11 flare at 3 seconds (Fig.6.4d, red line and Fig.6.4b, green line), we see that a $+0.8$Å shift in the maximum of the line profile occurs earlier in the beam injection phase in the F11 case. Likewise, comparing the F12 and F11 cases at 3 and 5 seconds respectively (Fig.6.4d, green line and Fig.6.4b, blue line), we see that the delay between beginning of the impulsive phase and the time when the hydrodynamic shock enters the Hα formation region decreases with the increasing initial energy flux of a beam. This is due to larger macro-velocities generated by hydrodynamic responses of flaring atmospheres to the injection of beam electrons with larger initial fluxes.

In the F12 flare model the core is shifted from the central wavelength of the spectral line out of the wavelength window used in our simulation 2-3 seconds after the beam injection phase begins, as the hydrodynamic shock hits the Hα line core formation region. Thus, one would expect the macro-velocities in the line formation region could exceed the maximum value captured by our wavelength window

(±2Å), and reach 1.05×10^7cm·s^{-1}, or 3.5Å, for this model, which is beyond the 2Å window in Fig.6.4. The main formation region (identified via the contribution functions) has the temperatures around 18,000K, and associated macro-velocities of around 2.1×10^7cm·s^{-1}.

Hence, summarising the above we can conclude that the Hα red wing enhancements in these simulations are clearly associated with the plasma down-flows, which can be found entering the formation region between 2 and 3 seconds, around 1 second after the shock is formed in the formation region of the Lyman lines (see chapter 5). The scale of the line deformation remains less noticeable for weaker flares, which generate lower maximum macro-velocities in their down-flows. Maximum values of down-flow velocities in the Hα line formation region are found at the peak of the initial flux, after 5 seconds.

If the core emission is red-shifted thus having smaller optical thickness appropriate to the wing wavelength, this leaves the wing intensity contribution from this region overlapping with the core emission coming from greater optical depths in the central wavelength. This results in a self-absorbed profile (Figs 6.4c& d, 6.6c& d and F11 and F12 models). However, if there is a very strong intensity in the line wing generated in the core formation region, for example due to Stark's wings and collisional effects, as was the case in the F12 Hα line, then this can compensate for the red-shifted core intensity being obscured by these effects (Fig.6.4c, 6.4d).

In Fig.6.5a there are shown the enhancements to the Hγ line profiles for the F11 model from $t = 2$ s (light green line) to $t = 5$ s (black line). During the beam injection the Hβ and Hγ line profiles show similar temporal evolution to Hα line profiles. The Hγ line profiles in the F11 model show Doppler red shifts with the emission enhancements peaking for Doppler velocities around 150 km·s^{-1} at 4 s and 5 s.

In Fig.6.5b the enhancements are shown to the profiles of the first three lines in the Balmer series (Hα in orange, Hβ in red and Hγ in black) calculated for the F10 model at $t = 5$. At 5 s The core of the Hα line is red-shifted because the hydrodynamic shock travelling downward has entered the Hα core formation region (Fig.6.5, orange line), whereas only around half of the core emission produced in the Hβ line has been red-shifted (Fig.6.5, red line). This is because at 5 s the core formation region of Hβ extends to depths below the hydrodynamic shock. Only a small

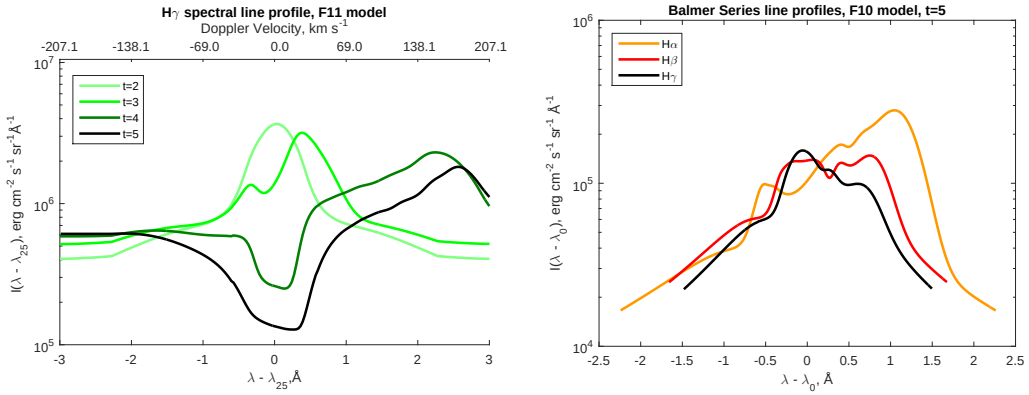

(A) (B)

FIGURE 6.5: (a) The spectral profiles of the Hγ line for $t = 2$ s (light green) to $t = 5$ s (black). (b) The Hα, Hβ and Hγ line profiles at $t = 5$ for the F10 model. Intensities (I) are simulated in erg·cm^{-2}·s^{-1}·sr^{-1}·Å^{-1} against distance from line centre ($\lambda - \lambda_0$) in Å.

proportion of the core emission in the Hγ line is red-shifted (Fig.6.5, black line) as the majority of core intensity is produced from depths below the large downward macro-velocities. This figure highlights the greater importance of contributions to emission from greater column depths in the higher lines of the Balmer series. In the F10 model at 5 s the ratio of the maximum intensity in the red wing compared to that in the centre / blue horn is 2.8 for Hα, 1.1 for Hβ, and 0.62 for Hγ. Hence, by using simultaneous, high cadence observations of Hα, Hβ, and Hγ line profiles during a beam injection it is plausible to track the propagation of a hydrodynamic shock through the chromosphere by comparing the line profiles.

Additional information about the beam can be provided by Paschen lines, which are formed over a broader range of the chromospheric depths if affected by beams. Here we inspect the results for the Pα line (Fig.6.6).

By inspecting the contribution functions for the emission it can be seen that the higher part of the Pα formation region overlaps with the formation region of Balmer lines. This causes a co-temporal onset of the red-shifts appearing in the line profiles for each flare model. The fact that the formation region of Paschen line cores extends to greater column depths results in a smaller proportion of the emission from the line core being red shifted at these times. This can be seen by comparing the line profiles from 5 s for the F10 profile of the Hα (Fig.6.4d, red line) and Pα (Fig.6.6d, red line) lines. Indeed, in the F10 flare model the hydrodynamic shock caused by the beam

does no penetrate into a significant proportion of the Pα formation region at 5 s. The effect of the hydrodynamic shock entering the formation region can be seen in the Doppler shift of the bowing of the red wing, and the shape of the line core at this time (Fig.6.6d, red line).

However, using the same comparison for the F11 and F12 models, one can observe that both the Pα and Hα line have a large proportion of their line cores red shifted away from the central wavelength. This is because, as shown in chapter 4 and Figs. 4.1 and 4.2, the Paschen line cores become highly optically thick in the case of powerful beams. Therefore, in strong flares (with powerful beams) the Paschen and Balmer line profiles reflect the conditions in the upper flaring chromosphere, with the similar proportion of the line core being Doppler-shifted from the central wavelength. However, for weaker beams with optically thinner Paschen line cores one observes a smaller fraction of the Paschen line core being Doppler-shifted away from the central wavelength than in the Balmer lines at the same time.

6.2 Comparison with Hα line observations

Wuelser and Marti, 1989 reported the observations of flare kernels in Hα wavelengths for the M1 solar flare on May 24^{th} 1987 taken with the Specola Solare Ticinese at Locarno-Monti (see Fig.6.7c,d). In particular, the profile presented for the A1 kernel at the peak of the HXR burst shows a little sign of any pre-flare heating. The normalised Hα profile extracted from data in the A1 kernel at the time of the peak in the HXR signal (15:24:55 UT) shown in their Fig.3 was digitally recorded (Fig.6.7c, green line). The quiet Sun profile presented in their Fig.3 (Fig.6.7c, grey line) was subtracted to find the enhancement in Hα emission (Fig.6.7c, pink line). The resulting profiles are shown with normalised intensity on the y-axis and the wavelength relative to the Hα line central wavelength shown on the x-axis.

As shown in a number of studies (Jess et al., 2008; Kowalski et al., 2017) the small (<1″) impulsive flaring kernels associated with beam electrons are also particularly associated with chromospheric line profiles with asymmetric red-wing emission. The pixel size of the observations by Wuelser and Marti, 1989 was 3″×3″ implying that the authors were unable to resolve the locations of individual beam injections,

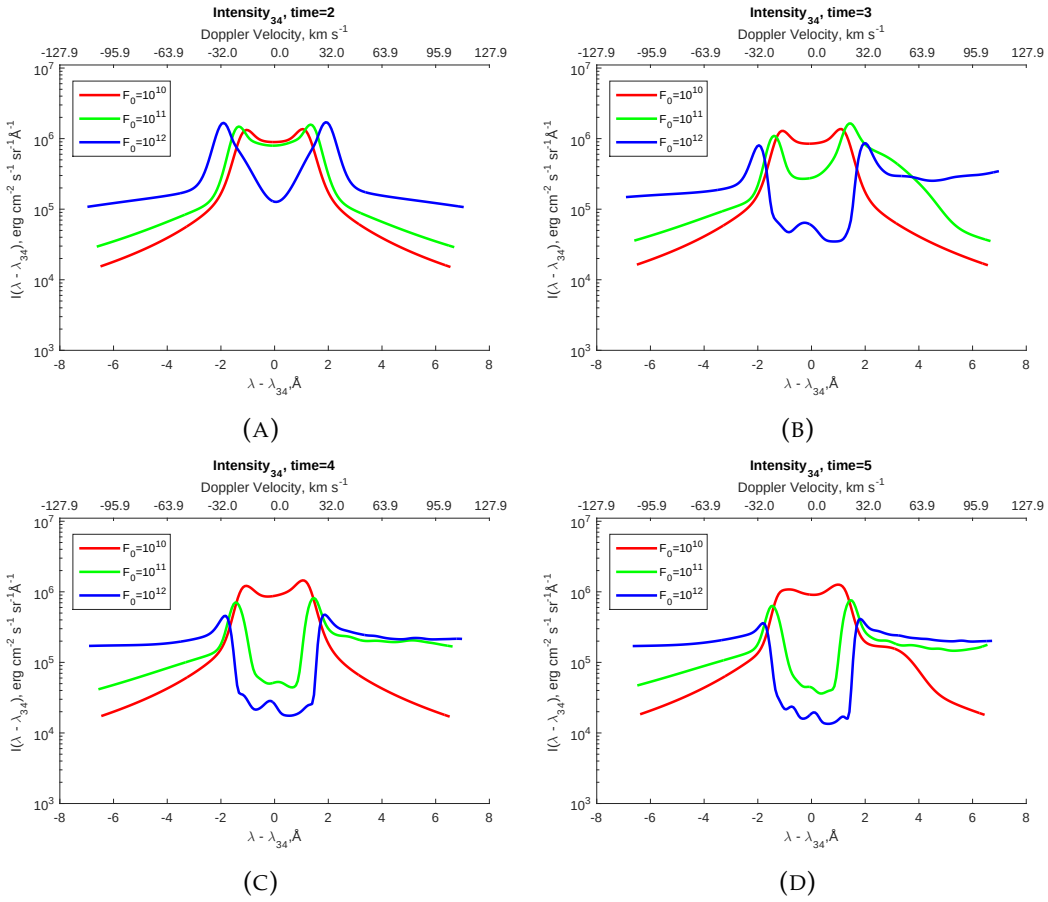

FIGURE 6.6: The Pα line profiles versus distance in Å from the line centre wavelength calculated at (a) $t = 2$, (b) $t = 3$, (c) $t = 4$, (d) $t = 5$, in erg·cm^{-2}·s^{-1}·sr^{-1}·Å^{-1} .

covering much wider areas instead produced by the background solar atmosphere. This fact explains the large enhancement in the Hα emission in a central wavelength shown in Fig.6.7c because only a small part of the region used to generate the emission profile undergoes a large red shift due to the hydrodynamic shocks caused by non-thermal beam injections.

Therefore, in order to identify the emission from regions with beam injections and to avoid accounting for the background, we need to calculate the excess emission in the red wing at the wavelength $\lambda_0 + \Delta\lambda$ as shown in Fig.6.7d by subtracting the normalised intensity enhancement of the profile at a wavelength of $\lambda_0 - |\Delta\lambda|$ from the intensity enhancement at $\lambda_0 + \Delta\lambda$. Of course, such the comparisons should be approached with a caution, but they are preferable to those directly comparing simulations from 1D flux tube models with the complete emission profiles or background subtracted profiles that have been integrated over a large area of the whole active region. This is because during the subtraction we reduce the background emission and pick out the feature of line profiles specifically associated with the beam injection rather than look at the kernel emission aggregated with the emission from bright ribbons and neighbouring thermal contributions, in addition to that from a beam. Selected simulated Hα line profiles which show red wing excesses inside the modelled wavelength window are displayed in Fig.6.7a for the F10 model at 5 s (red line) and the F11 model at 3 and 5 s (light and dark green lines), and the F12 model at 3 s (blue line). The red wing excesses for these profiles is shown in Fig.6.7b. Both the graphs are plotted with enhancement to emission intensity on the y-axis, against wavelength relative to the central frequency of the Hα line, λ_0, in Å on the x-axis.

The emission profiles shown in Fig.1.21 from a flare kernel show a great red wing enhancement in the Hα line at 15:24:55 UT, co-temporal with the HXR peak intensity (Wuelser and Marti, 1989). The red shifted profile had an intensity peak at around 2Å from the line centre wavelength at these times, corresponding to a down-flow of around 90 km·s^{-1} that represents velocities between the simulated maximum down-flow velocities in the F10 and F11 hydrodynamic models. Additionally, there was enhancement in emission extending up to around 4Å, suggesting that strong Stark's

wings had been generated. Both of these features are evident in the profile of the excess emission in the red wing (Fig.6.7d). This description fits the Hα line profile enhancements and red wing excesses for beams with fluxes between 10^{10} erg·cm^{-2}·s^{-1} and 10^{11} erg·cm^{-2}·s^{-1}.

Additionally, a peak in the red excess at around 1-3Å also indicates the presence of a shock caused by a beam with a lower initial flux in the kernel area. We use the profile produced by the F10 model at 5 s as a template for that which results from an electron beam injection with the initial flux slightly lower than 10^{10} erg·cm^{-2}·s^{-1} to fit this peak, and to combine it linearly with the red-excess modelled for a flare with the incident flux somewhat lower than the F11 model. The resulting red excess is shown by the black line in Fig.6.7d, and fits the observed red wing emission excess very closely. This suggests that the large kernel area used in the observation could have injections from at least two beams with fluxes around $10^{10} - 10^{11}$ erg·cm^{-2}·s^{-1}.

6.2.1 Temporal variations

The observations of Kaempfer and Magun, 1983 report three kernels for the flare on June 17^{th} 1982. One of the kernels (L) has co-temporal peaks in HXR and Hα intensities in the 0.25Å window. The other two kernels (M and R) exhibit a 30 s delay in the maximum of emission intensity of the Hα line. From this the authors suggest that different energy transport mechanisms are at play in the different flare kernels. Although, this cause can not be ruled out, imagining the observations of Wuelser and Marti, 1989 conducted using a narrow wavelength band (such as the 0.25Å window used in Kaempfer and Magun, 1983) provides a cautionary tale.

The maximum of the HXR spectra occured at around 15:25:00 UT, according to Wuelser and Marti, 1989 Fig.3. In the same figure it is shown that that a maximum of the emission intensities in the red wing at 1.5 and 3Å occurred at around 15:25:09 UT in the A1 kernel. For the same kernel there was a second set of intensity maxima in the line centre, the red, and the blue wings of the Hα line profile at around 15:25:30 UT, which would be the only peak recorded using a spectral window of 0.25Å around the line centre. Therefore, a 30 s delay between the peak of the response in the Hα line core and the peak of the HXR would have been reported.

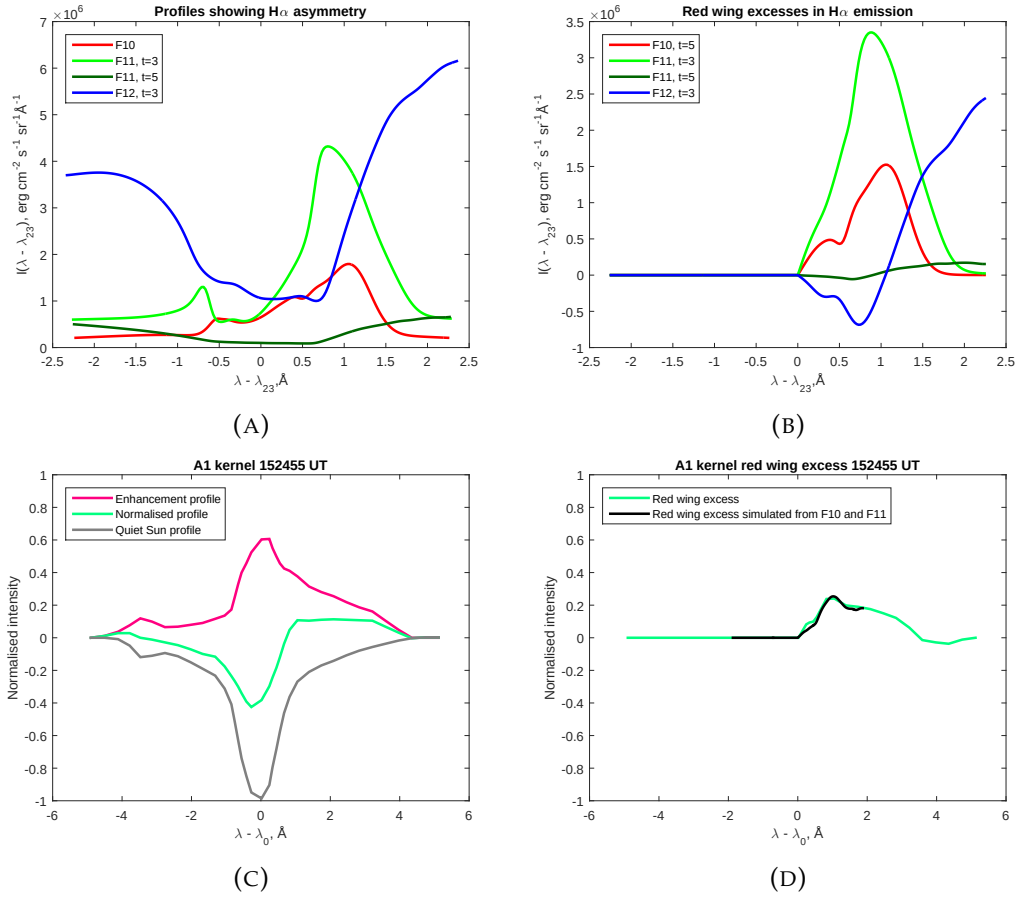

FIGURE 6.7: (a) Simulated Hα profiles showing red wing enhancement for the F10 (red line), F11 (green line) and F12 (blue line) models. Intensity enhancement is on the y-axis, and wavelength relative to the Hα profile line centre on the x-axis. (b) The excess of emission in the red wing of the profiles in panel 'a' relative to the emission in the blue wing. (c) Normalised Hα profiles from the M1 solar flare on May 24^{th} 1987 reported in Wuelser and Marti, 1989. The normalised Hα profile (green line), the quiet Sun background level (grey line) and the enhancement in emission (red line) are shown for the A1 kernel at the time of the maximum of the HXR (15:24:55 UT). The y-axis shows normalised intensity and the wavelength relative to the Hα line central wavelength is shown on the x-axis. (d) The excess emission in the red wing, compared to the blue wing for the A1 kernel at 15:24:55 UT (green line). The black line shows a simulated fit of this excess based on a linear combination of contributions based on the F10 and F11 models

This time delay occurs because the emission profile has a maximum value that is Doppler shifted into the red wing, well beyond 0.25Å (see, for example, the simulated profiles in Fig. 6.4). The B1 kernel with its pre-heated enhancements exhibited a very slight delay between the HXR peak intensity and that in Hα line profile. It is perfectly possible, rather it is a prediction of our models, for delays such those reported in Kaempfer and Magun, 1983 to be evident at the onset of a beam injection. This delay results from the red-shifts caused by plasma down-flows resulting from a hydrodynamic response of flaring atmosphere to an non-thermal beam injection. The Hα line emission is shifted to the red wing and the filter with the given size observes only the blue wing of this shifted profile. Only at later times, after the beam is switched off and the plasma stopped mowing downward, the line profile returns to the profile centred on the central wavelength, which can be observed by the given filter.

We suggest that for capturing the full dynamics of Hα line profiles during the impulsive phase of solar flares larger wavelength windows are essential and recommended in new instruments.

6.2.2 C1.5-class flare on 30th June 2013

This flare is studied in detail and presented as a case study in chapter 7.

6.3 Discussion

Hα radiative response:

Hydrogen line emission originates in the low-temperature condensation of a flaring chromosphere below the flare's transition region. Therefore, in the HYDRO2GEN models the beams with greater initial fluxes push the chromospheric plasma of the quiet Sun, or the hydrogen line formation regions, to greater column depths and larger densities (see table 6.1). However, our simulations for the F10 to F12 models show that these still do not reach the regions with very high densities ($10^{15} - 10^{16}$ cm^{-3}), in which the negative Hydrogen ions appear (Aboudarham and Henoux, 1987). Electrons beams with larger initial fluxes cause higher non-thermal excitation

to the upper atomic states of the transitions in the Balmer and Paschen series, raising the ratio of the electron abundances in the upper state compared to those in the lower state (see table 6.1). This increases the intensity of hydrogen emission produced in the cores and the wings of spectral lines (Figs.6.1 & 6.2). Since the ambient densities and temperatures in the flaring chromosphere are also increased by the beam heating, hydrogen spectral lines become broadened.

Besides heating, beam electrons also raise ionisation degree of hydrogen atoms below the flare transition region because the ionisation rates from inelastic collisions between beam electrons and hydrogen atoms dominate over the ionisation rates caused by thermal electrons (Fig.6.3). A growth of ionisation degree caused by non-thermal electrons extends the spectral line wings, owing to the increased local electric fields (Stark's effect). Therefore, the beams with higher initial fluxes produce a larger intensity in wings and more broadened and flattened cores of Balmer and Pashen lines (Figs.6.1 & 6.2) that confirm the previous conclusions by (Aboudarham and Henoux, 1986; Zharkova and Kobylinskii, 1993). Additionally, in the current study we are able to identify the hydrodynamic effects of beam electrons causing in the line cores (see section 6.1.1).

The magnitudes of Doppler shifts in the spectral line profiles indicate the macro-velocities of the shocks when they pass through the formation regions of a given spectral line. As a result, the Hα line undergoes largest red-wing enhancements among the hydrogen lines presented in our simulations, because it is formed at upper chromospheric depths where the macro-velocities of the shock are the largest. The lines formed at deeper atmospheric depths, such as the Hγ or Pα lines, have a smaller proportion of their core emission being red-shifted (Fig.6.5b). By comparing the Hα, Hβ and Hγ line profiles observed with a high cadence during the first minute or two after a flare (beam injection) onset, the observers can track propagation of the hydrodynamic shocks through the whole flaring chromosphere (Fig.6.5). The time delay between a beam onset and the instance of hydrodynamic shocks entering the formation regions of hydrogen lines is much shorter for the beams with greater initial fluxes. This occurs because the beams with higher initial fluxes produce the shocks with larger downward macro-velocities (section 6.1.2).

In our F10 model the downward chromospheric shocks produce red wing enhancement in the Hα profiles with a 1 Å Doppler shift at the very first 5 s after a beam onset (our Fig.4b). The scale of the Doppler shifts in these profiles agrees with those of Canfield and Gayley, 1987 for a similar flux. However, in Canfield and Gayley, 1987 the peak in emission intensity remains firmly in the blue horn of the simulated profiles. The first radiative hydrodynamic simulations by Heinzel et al., 1994 showed blue horn asymmetries due to absorption in the red wing of Hα at wavelengths around 1 Å. More recent radiative hydrodynamic model by Allred et al. (2005) simulated for the same beam parameters as in our model F10, does not show any significant shocks moving downward in the chromosphere and, thus, no red-shifted Hα line profiles (see their Fig.8). Moreover, Allred et al. (2005)'s F11 model allowed them to obtain a downward velocity only of 40 km·s^{-1}, while our F11 model produces the downward velocities up to 200 km·s^{-1}, providing the red-shift up to 3Å in Hα line profiles, similar to those reported from observations.

In addition, apart from the chromospheric evaporation simulated for coronal temperatures detectable in soft X-rays and extra ultra-violet emission, our hydrodynamic simulations do not show any significant upward motions in the flaring chromosphere, a formation region of the Balmer or Paschen series during a beam injection phase (Fig.2.3). Thus, our models do not produce not observable blue shifted Balmer or Paschen line emission, in contrast to the other radiative hydrodynamic simulations (Allred et al., 2005; Rubio da Costa et al., 2016).

Hα observations:

During the impulsive phase of solar flares observed Hα line profiles often reveal strong red shifts of 1-4 Å (Ichimoto and Kurokawa, 1984; Wuelser and Marti, 1989; Wuelser et al., 1994). These profiles cannot be explained by changes in the maximum opacity (Kuridze et al., 2015). The HYDRO2GEN models presented in this paper explain these profiles by the Doppler effect of the plasma macromotion due to hydrodynamic shocks produced by a non-thermal electron beam (Figs.6.4, 6.5 & 6.6).

The HYDRO2GEN F10 model produces enhancements in Hα line profiles that address the concerns raised by Rubio da Costa et al., 2016, while interpreting Hα

emission from an X1.0-class flare. Rubio da Costa et al., 2016 suggested red asymmetries peaking around 1 Å are to be likely caused by the downflows missing from their simulations. The enhancements of the Hα emission intensity in the core and red wing observed by Rubio da Costa et al. (2016) at these times are within a factor of 2-4 of those generated using the HYDRO2GEN F10 model. Moreover, the wing enhancements of the Hα profiles presented in Rubio da Costa et al., 2016 are naturally explained by our simulated profiles, owing to Stark's effect, caused by the additional ionisation of a flaring chromosphere by beam electrons (see our Figs.6.1, 6.4).

The maximal red shift, somewhat under 1 Å, in their Hα line profiles is achieved for the F11 model by Allred et al., 2005 occurring 5 seconds after the beam onset and disappearing 6 seconds later, being replaced with a large blue shift (see Fig.9 in Allred et al., 2005). While our simulations with higher initial fluxes can match the maximum Doppler shifts of 3-4 Å reported by Ichimoto and Kurokawa (1984) and Wuelser and Marti (1989) at the peak of the HXR emission and lasting for minutes. For stronger beams HYDRO2GEN also generates stronger Hα line wings, similar to those often observed, and explains that them to be caused by an increased number of the ambient electrons (Stark's effect) appearing owing to strong ionisation by electron beams (section 6.1.1 and Fig.6.1).

By extracting the relevant line intensities from our full Hα line profiles using a narrow wavelength window of about 0.25 Å and inspecting the observations by Kaempfer and Magun, 1983; Wuelser and Marti, 1989, we can derive that with such the narrow wavelength window it is not possible to capture any large red-shifted emission caused by a strong chromospheric downflow. Instead, the instrument with such the narrow spectral window would observe blue wings of the shifted Hα line profiles with very low intensity until the red-shifted Hα line returns back to its normal spectral position as reported by these observations. Since downflow velocities of the shocks can be rather high, they can produce large red shifts of up to 4Å. This offers a very physical alternative explanation of the delays between HXR and Hα emission reported by Kaempfer and Magun, 1983. Hence, larger wavelength windows are essential to capturing the full behaviour of Hα line profiles during the impulsive phase of solar flares.

Paschen Pα radiative response:

The Pashen emission in a flaring chromosphere is also strongly affected by electron beams, which cause the Paschen Pα and Pβ line cores to become highly optically thick (Figs.4.1c & 4.2b). For the beams with larger initial fluxes (F11 and F12 models) the Paschen Pα and Pβ line cores are formed in the upper flaring chromosphere, whereas for the F10 model they are formed throughout the lower chromosphere. As a result, in our simulations there is a great red wing excess occurring at the peak of beam fluxes as shown in the Pα line for the F11 and F12 models, whereas only a small proportion of the Paschen Pα core emission was red shifted in the F10 model (Fig.6.6) where the hydrodynamic shock had not yet reached the lower chromosphere.

In summary,

(6.1) Excitation by non-thermal beam electrons increases emission in the Balmer and Paschen lines during the impulsive phase of solar flares. The emission in these lines is simultaneously broadened by the heating of the plasma caused by the beam and the Stark effect due to the ionisation by the beam electrons

(6.2) The magnitudes of Doppler shifts in the spectral line profiles indicate the macro-velocities of the shocks when they pass through the formation regions of a given spectral line. The lines formed at deeper atmospheric depths than Hα, such as the Hγ or Pα lines, have a smaller proportion of their core emission being red-shifted in the impulsive phase (Fig.6.5b). By comparing the Hα, Hβ and Hγ line profiles observed with a high cadence, the propagation of the hydrodynamic shocks caused by the beam can be tracked through the flaring chromosphere (Fig.6.5).

(6.3) The time delay between a beam onset and the hydrodynamic shocks entering the formation regions of hydrogen lines is much shorter for the beams with greater initial fluxes, because the beams with higher initial fluxes produce shocks with larger downward macro-velocities (section 6.1.2).

(6.4) The shocks take longer to reach the formation regions of the Balmer and Paschen lines than the Lyman lines, because they are formed at greater column depths in the atmospheres.

(6.5) In contrast to the Lyman lines, the Balmer and Paschen lines contain very little blue shifted emission until around 100s of the simulation, because evaporation occurs only from the top of the chromosphere and in the transition region.

(6.6) In our F10 model the downward chromospheric shocks produce red wing enhancement in the Hα profiles with a 1 Å Doppler shift at the very first 5 s after a beam onset (our Fig.4b). This is a much greater Doppler shift than is simulated by models using the FCA for a similar flux. Moreover (Allred et al., 2005), Allred et al. (2005)'s F11 model allowed them to obtain a downward velocity only of 40 km·s^{-1}, while our F11 model produces the downward velocities up to 200 km·s^{-1}, providing the red-shift up to 3Å in Hα line profiles, similar to those reported from observations Ichimoto and Kurokawa (1984) and Wuelser and Marti (1989).

(6.7) The Pashen emission in a flaring chromosphere is also strongly affected by electron beams. Non-thermal excitation causes the Paschen Pα and Pβ line cores to become highly optically thick in the middle of the chromosphere (Figs.4.1c & 4.2b) for the beams with larger initial fluxes (F11 and F12 models). For the F10 model the lines are formed throughout the lower chromosphere. As a result, in our simulations there is a great red wing excess occurring at the peak of beam fluxes as shown in the Pα line for the F11 and F12 models, whereas only a small proportion of the Paschen Pα core emission was red shifted in the F10 model (Fig.6.6).

6.4 Notes

Much of the work in this chapter is taken from the published paper Druett and Zharkova, 2018, and was completed in collaboration between Prof. Valentina Zharkova and I.

Chapter 7

C1.5-class flare on 30th June 2013

In this section we confirm the earlier observations of Hα line profiles with strong red shifts during the impulsive phase of the flare (Ichimoto and Kurokawa, 1984; Wuelser and Marti, 1989; Wuelser et al., 1994) by using observations recorded at the Swedish Solar Telescope (SST) of a C1.5-class flaring event onset. These profiles are interpreted with the F10 HYDRO2GEN model (see chapters 2, and 3).

7.1 Observations

7.1.1 Active region topology and HXR emission

The C1.5 class flare occurred on 30th June 2013 in the active region (AR) 11778 during the time 09:11-09:27 UT, as per the GOES light curve in the 1.0-8.0 Å channel (Fig.7.1a: black line, with peak indicated by the grey horizontal line). The flare originated in a complex configuration of magnetic field with the opposite polarity connected to another active region located in the south east (Figs.7.1c and d). The initial flare started at 09:13:54 UT (event 1) in the north-east location of the negative polarity region of the AR11778 (Fig.7.1c).

At 09:15:54 UT it continued in the south-west location of the same region (event 2) (Fig.7.1c) where the Hα ribbons were formed and the line profiles observed. A few minutes later HXR emission appeared at the location of the south east active region (event 3) (Fig.7.1d). The GOES light curves include the contributions from all three events of this active region. Event 2 (Fig.7.1d) contributes to this light curve at the times indicated between the vertical lines in Fig.7.1a. The data from the Helioseismic

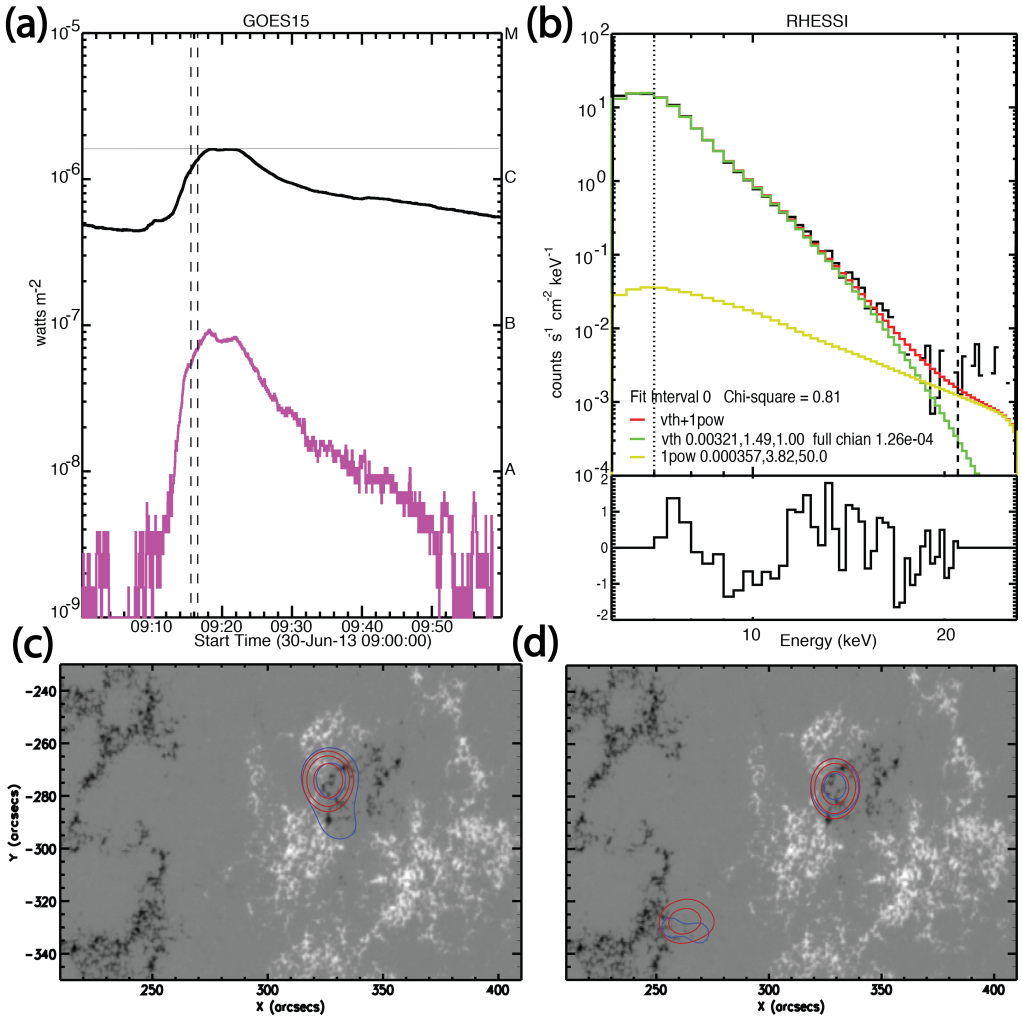

FIGURE 7.1: The active region topology and HXR emission. (a) The GOES X-Ray light curves of the flare in the 1-8 Å (black) and 0.5-4.0 Å (magenta) channels. The vertical dashed lines correspond to the time interval of the RHESSI spectrum in event 2. (b) RHESSI photon flux spectrum for event 2 with residuals derived with CLEAN in the 20 s interval around the time of Hα emission for thermal (green line) plus single power-law (yellow line) components, giving the total (magenta line). HXR emission is mostly of thermal nature with a small non-thermal component (see for details the section 7.1.3) with the parameters: spectral index about 3.8 and initial energy flux can be a factor (0.7-3) of $F_0 = 10^{10}$ erg·cm^{-2}·s^{-1}. (c) The HXR emission contours appearing in event 1 (top) and event 2 (Bottom, blue contour) coinciding with the times of the observations of Hα kernels with red-shifts in the ribbon (09:16 UT). These are overlaid onto the HMI magnetogram. The response in the 5-12 keV channel is shown using red contours, and the response in the 12-25 keV channel with blue. (d) HXR emission overlaid on the HMI magnetogram appearing with the event 3 occurring ∼4 minutes later (09:20 UT), during the maximum in GOES light curve.

and Magnetic Imager (HMI) did not detect any sunquakes (Zharkov et al., 2011) in these events.

Fig.7.1b displays the HXR photon spectrum for event 2 measured by RHESSI with detectors 4, 5, and 9. The spectrum was fitted from 09:15:54 to 09:16:14 UT over the energy range 7 to 21 keV using Object Spectral Executive (OSPEX) and thermal (green line) plus single power-law (yellow line) components, giving the total (magenta line). The background period was 09:38:40 to 09:40:56 UT. The photon spectrum for event 2 can be also fitted by a thermal function only with the similar accuracy (χ^2). This indicates that HXR emission in the vicinity of event 2 has a strong thermal component related to a difference in spatial resolution for HXR and Hα observations (see section 7.1.3). For this reason, the HXR energy spectrum presented in Fig.7.1b) is for a demonstration only of a weak non-thermal component with spectral index of 3.8 and a lower cut-off energy of about 7-10 keV.

The HXR contour images in Figs.7.1c and d were made using the CLEAN algorithm and detectors 3 to 8 with 20 s integration times. The contour levels in 6-12 keV (red) and 12-25 keV (blue) are at 30%, 50%, and 70% of the maximum intensity, covering the area 6-8 pixels for the latter. The initial energy flux for event 2 was about 10^{26} erg·s^{-1}. The range of initial energy fluxes F_0 for this event 2 is discussed in section 7.1.3.

7.1.2 Hα line and coronal jet images

Hα images. The Hα line observation sequence occurred from 09:15.54 UT to 10:17:18 UT and was carried out by SST using the CRisp Imaging Spectro-Polarimeter (CRISP) (Scharmer, 2006). CRISP is especially suited for spectroscopic imaging of the chromosphere in the popular Hα line (6562.8 Å), being equipped with three high-speed, low-noise CCD cameras that operate at a frame rate of 36 fps. The C1.5 class flare under investigation was captured in Hα line within the CRISP Field-of-View (FOV) of 55×55″ centred at heliocentric coordinates [323.4″ ,-287.9″] (see Fig.7.2a). We refer to section 7.1.3 for a description of the reduction technique used for the CRISP data.

Coronal jet images. The images obtained by AIA instrument aboard on the Solar Dynamic Observatory (SDO) (Lemen et al., 2011) were used for the background in Fig.7.2 to locate the Hα ribbons. To achieve sub-AIA pixel accuracy in the temporal

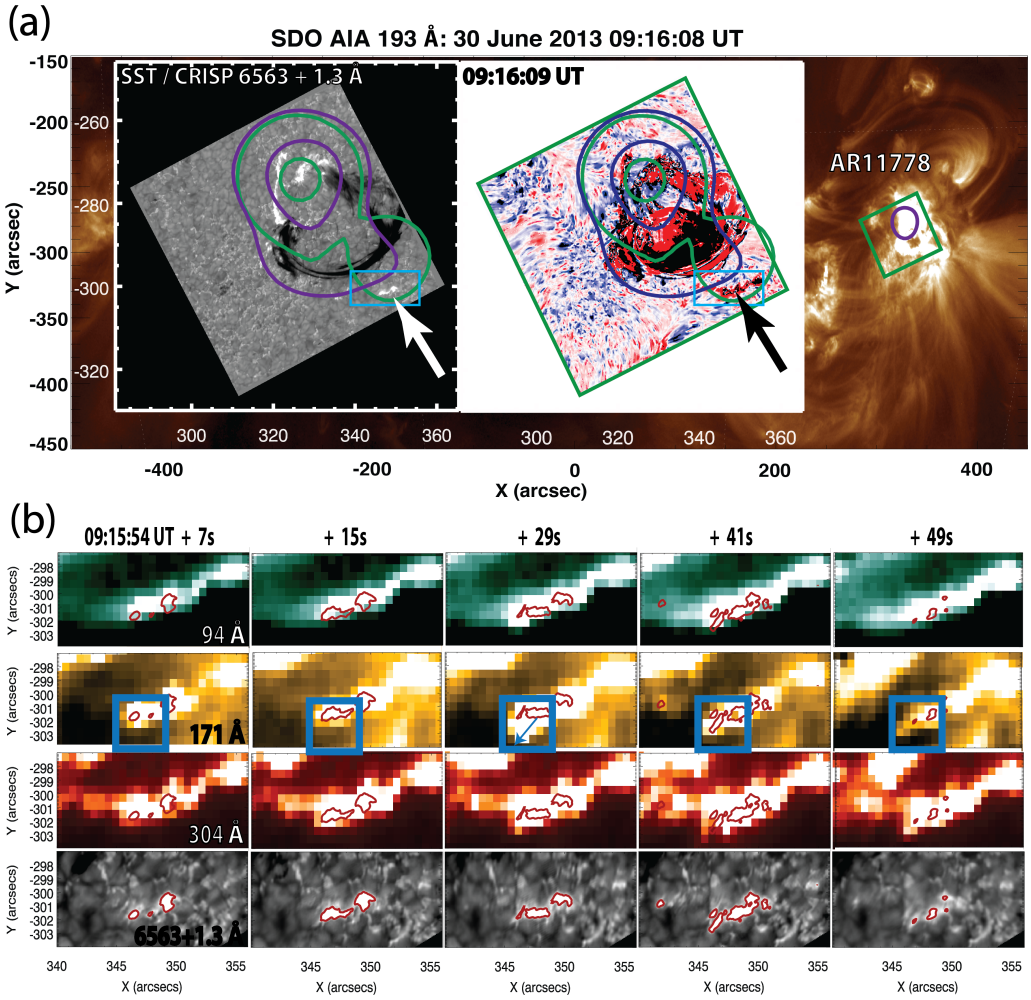

FIGURE 7.2: Observations with AIA. (a) *Background*: A context image for the observation in AIA 193 Å overlaid with the CRISP FOV outlined in green within AR11778. *Inset left*: The co-temporal (09:16:09 UT) CRISP image in the Hα line far red wing reveals bright flare ribbons pointed to by the white arrow for event 2 that are co-spatial within RHESSI imaging contours in 6-12 keV (green) and 12-25 keV (purple). *Inset right*: The Hα dopplergram for the 33 pt. spectral scan per pixel, containing blue/red-shifted motions marked by the relevant colour presented in the range of $\pm$20 km$\cdot$s^{-1}. The blue boxes in the insets (a) highlight the section of the ribbon formation in event 2, which is displayed in panel (b). (b) The image sequence describing evolution of the ribbon in the AIA 94 Å, 171 Å and 304 Å channels from top to bottom, respectively. These are co-spatial and co-temporal with the bright ribbon features (contoured in red), in the Hα far red-wing images of +1.3 Å (bottom panel). The 171 Å channel reveals a bright jet-like protrusion (within the blue boxed region) that appears to form between the time frames 09:15:54 UT +15 s and +29 s (corresponding to 93 km$\cdot$s^{-1}) in the direction of the blue arrow and disappears by the time frame +49 s.

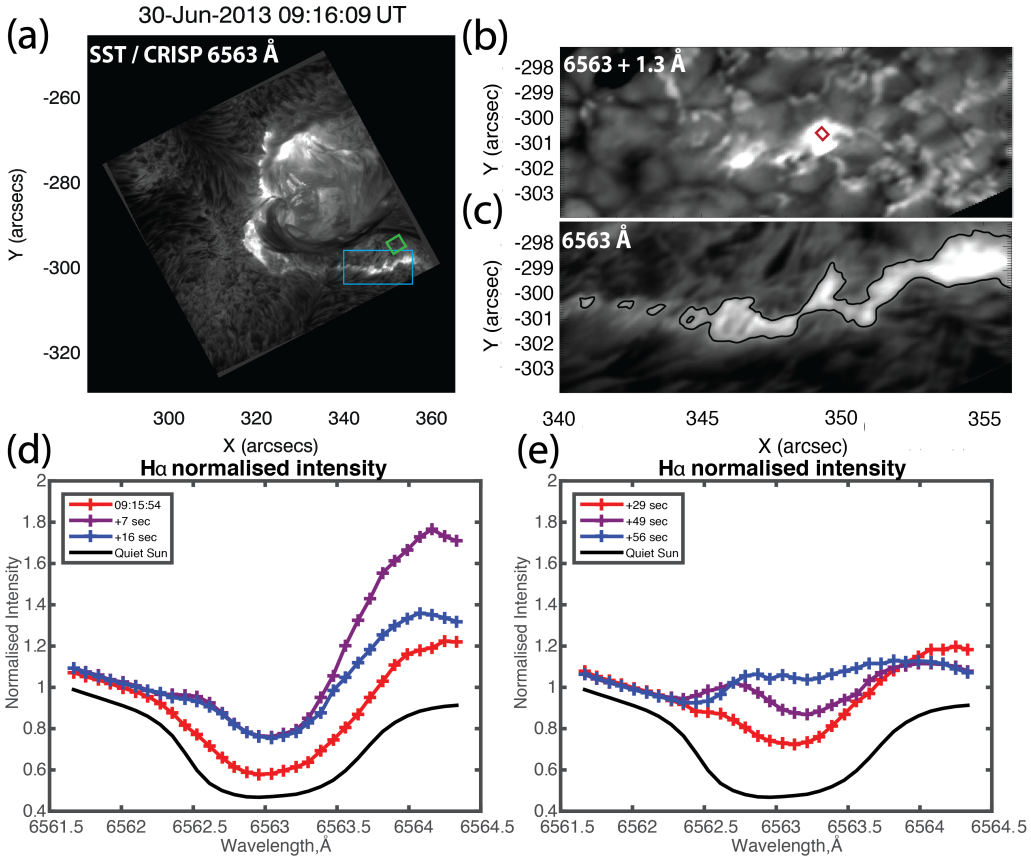

FIGURE 7.3: Hα line profile observations using SST. (a) The CRISP Hα line core image (6563Å) with a blue box outlining the part of the flare ribbon under investigation. The green box corresponds to the pixels selected to construct the average quiet Sun spectral profiles, i.e. close to the ribbon formation and free of any activity, within the time interval of the ribbon formation. (b) The corresponding FOV for the Hα far red wing intensity at +1.3 Å, with a red box corresponding to the region where the spectral profiles of interest are extracted. (c) The contoured ribbons of the Hα line core image for the blue box region is presented. (d) The averaged and normalized Hα spectral line profiles, determined from the red box pixels, are presented for time intervals corresponding to the 1st (09:15:54 UT: red solid line), the 2nd (+7 s: purple solid line) and the 3rd (+16 s: blue solid line) time frames. The Hα line profiles display exceptionally strong red-shifts. (e) The averaged and normalized Hα spectral line profiles for significantly later time frames corresponding to +29 s (red solid line), +49 s (purple solid line) and +56 s (blue solid line) when there were no longer strong red-shifts but rather core emission with peaks in both blue and red near wings. The black solid lines describes the averaged QS background Hα profile, deduced from the region defined by the green box in (a). Intensities were normalised against the background levels using the QS intensity of 9890 counts per pixel at 6561.7 Å as a reference.

and spatial co-alignment of CRISP images with AIA, the photospheric bright points common to both FOV were cross-correlated. The AIA images (Fig.7.2b) for the hotter channels (i.e. transition region - He II 304 Å; Corona - Fe XII 171 Å; Flaring/hot Corona - Fe XXIII 94 Å) were reduced and aligned to 1700 Å, via the *aia_prep* routine in SolarSoft (IDL). Subsequent images in all AIA channels were de-rotated to the CRISP start time (see Fig.7.2). The SST telescope turret continually tracked the starting target. Therefore, throughout the observation the CRISP image sequences are excellently co-aligned with AIA and RHESSI images.

7.1.3 Hα-line profiles

The CRISP observation of event 2 (see section 7.1.1 and Fig.7.1) began at 09:15:54 UT, just before the peak of flux in the GOES light curve produced by all three events. The Hα observations consisted of equidistant scanning of 33 wavelength points from -1.38 Å to +1.38 Å about the Hα line centre, resulting in an effective observation cadence of $\sim$7.27 s. The image quality of the time series data significantly benefited from the correction of atmospheric distortions by the SST adaptive optics system (Scharmer et al., 2003). Post-processing was applied to the data sets with the image restoration technique Multi-Object Multi-Frame Blind Deconvolution (MOMFBD)(van Noort, Rouppe van der Voort, and Löfdahl, 2005). Consequently, every image is close to the theoretical diffraction limit for the SST with respect to the observed wavelengths. We followed the standard procedures in the reduction pipeline for the CRISP data (de la Cruz Rodríguez et al., 2015).

Fig.7.3a shows the full CRISP field of view image in the Hα line core (6563 Å) at 09:16:01 UT. The green box shows the 31$\times$31 pixel square (1333 km^2) used for the QS reference intensity, which had no interference from overlying structures during the relevant observational frames. The blue rectangle in Fig.7.3a displays the zoomed field of view used in panels b and c. In Fig.7.3b we see the image taken in the red wing of Hα at 6564.376 Å and Fig.7.3c show the line core. To assess the feature identified, data was extracted from a 5$\times$5 pixel square (215 km^2), which contained the region of greatest red wing enhancement in the 09:16:01 UT frame. This kernel area is highlighted by the red square in Fig.7.3b.

The mean Hα profile intensities were taken in each of the 33 spectral positions of the QS and the flare kernel. Then the data was smoothed, to remove an instrumental spiking effect between adjacent spectral positions, by creating 32 interpolated spectral data points that are the mean of the two adjacent data points. Intensities were normalised against background levels using the QS average of 9890 counts per pixel at 6561.7 Å as a reference. After 7 s, the kernel produced 10949 counts per pixel at the 6561.7 Å spectral position and 17651 counts per pixel at the peak of the red-shifted intensity (6564.2 Å).

From the CRISP Hα red wing image taken at the time of greatest red wing enhancement (Fig.7.3b), a strong, transient enhancement at 6563+1.3Å can be registered (depending on the emission level) in a range of 266-712 SST pixels with the resolution of 0.0592". Then a single RHESSI pixel (2"x2") contains 33×33 ≈1100 SST pixels. Since the RHESSI area was too big (6-8 pixels) and the resolution too low, the areas of Hα flaring kernels for event 2 were used. Taking into account that $1'' = 725$ km$= 7.25 \times 10^7$ cm, the area is estimated to vary within $(0.3-1.4) \times 10^{16}$cm^2. This leads to the estimation of initial energy flux of HXR emission for event 2 in the location of Hα ribbon of about $F_0 \approx (0.7 - 3.0) \times 10^{10}$ erg·cm^{-2}·s^{-1}.

In order to derive the observed Hα profile, we used a flaring kernel in (5×5=) 25 pixels of the SST event 2. The area covered by other (1100-25=) 1075 SST pixels (98% of a single RHESSI pixel) is the neighbouring area of this active region, which is not directly affected by this particular electron beam. This difference in the spatial resolutions of RHESSI and SST data also can explain a good fitting to thermal emission in the RHESSI data (coming from the pixels not associated with the Hα enhancements). Therefore, the RHESSI data should be (and was) only used for estimating the order of magnitude of the beam flux, while the other means confirming the precise beam flux are required, e.g. from fitting of the Hα line profiles.

The resulting Hα line profiles are shown in Figs.7.3d and e. The CRISP observation captured the onset of a strong chromospheric downflow in the second ribbon area highlighted by the blue box in Fig.7.3a. The red wing enhancement started in the 09:15:54 UT frame (Fig.7.3d, red line), increased between 09:15:54 and 09:16:01 UT and peaked at 09:16:01 UT (Fig.7.3d, purple line), 7 s after the flare onset. Contrary to the symmetric Hα line profile of the QS, the emission in the red

wing exhibited a single-peaked profile (Fig.7.3d). This suggests that the peak can be attributed to a strong downflow in the chromosphere with Doppler velocity of 45-50 km·s^{-1}. This red wing enhancement was reduced 9 s later, while the core emission remained at a slightly raised level, compared to the QS (Fig.7.3d, blue line).

Throughout observations the blue wing had only a slightly raised intensity (without peaks) compared to the QS, in agreement with the wing intensity enhancement, or background level increase, appropriate to flares. 29 to 56 s later, the red wing enhancement was reduced towards the flare background level and the core intensity was increased for the times when the Hα line was in emission (Fig.7.3e, blue line).

7.2 Interpretation of the observations

7.2.1 Hydrodynamic Response

For physical conditions in a flaring atmosphere and with respect to findings from HXR emission, we used the models described in section 2.3.2. A hydrodynamic response of the ambient plasma in this event can also be caused by a high-energy thermal beam because the HXR flux derived from RHESSI can be equally well fit by the thermal curve (see the section 7.1.1). However, as simulated by Somov, Sermulina, and Spektor, 1982, the hydrodynamic response of a flaring atmosphere to a thermal beam is similar to that of a power-law beam, while raising the additional problem of thermal conductivity saturation. In order to avoid this problem, in our simulation for event 2, we chose to heat the flaring plasma by a power-law beam instead.

Heating by electron beam is found to sweep the plasma from the QS chromosphere towards deeper atmospheric levels converting the QS chromosphere into a flaring atmosphere with its own corona, transition region and chromosphere (Somov, Spektor, and Syrovatskii, 1981; Zharkova and Zharkov, 2007). This is different from the hydrodynamic models which use semi-empirical (pre-heated) flaring chromospheres VAL F (Vernazza, Avrett, and Loeser, 1981) with the attached quiet Sun corona as the initial condition (Fisher, Canfield, and McClymont, 1985; Allred et al., 2005). Thus, they are skipping the phase of conversion of the quiet Sun chromosphere into a flaring corona, flaring transition region and flaring chromosphere.

The pre-heated hydrodynamic models work perfectly well for flares with pre-flare events, while our model is more applicable for the initial flaring events without prior heating.

The parameters of an injected beam are selected close to the range of parameters of HXR emission derived from RHESSI for event 2 (see section 7.1.1): a single power-law energy spectrum with a spectral index of about 4 based on a comparison of spectral indices using Fokker-Planck approach (see Fig.11 in Zharkova and Gordovskyy, 2006), a lower cut-off energy of 7-10 KeV (from the total range 7-21 keV recorded by RHESSI). The limits of initial energy flux of beam electrons in event 2 was estimated from HXR emission utilising the areas of Hα kernels because of strong contamination of HXR with thermal emission of the background corona owing to a much lower spatial resolution of the RHESSI (2") versus SST (0.06") pixels (section 7.1.3).

7.2.2 Probing hydrodynamic results with the AIA observations

In the considered hydrodynamic model plasma evaporation (Figs.2.3a, b, box 1) (that can be called 'smooth evaporation' (Somov, Spektor, and Syrovatskii, 1981; Fisher, Canfield, and McClymont, 1985; Polito et al., 2016)) starts from the first second of the beam injection and continues for 100 s (and above, not shown here). For F10 - 3F10 models it reaches velocities of 50-100 km·s^{-1} in the lower flaring corona and several hundred km·s^{-1} in the upper flaring corona (see Fig.2.3).

AIA observations of event 2 in 94 Å, 171 Å and 304 Å channels presented in Fig.7.2 have shown rather variable signatures. A bright, transient jet-like protrusion of plasma from the ribbon in the 171 Å AIA channel was detected between 15-29 s after the event onset, which appeared linked to the strong down-flow regions in Hα emission (red contours) (Fig.7.2b). At the same time, there are no jets seen in the 94 Å or 304 Å emission.

The jet velocity in 171 Å, measured 29 s after event 2 (beam injection) began, was 93 km·s^{-1}. This was derived from the apparent motion of the jet within the AIA image set in the 171 Å channel. The error in measurements is sensitive to a pixel size (0.6″), reaching about $\pm$30 km·s^{-1} in the time frame of jet propagation. This estimation is accounted for by a height of the box 1 within Fig.2.3b, which shows the

macro-velocity within a range of 63-123 km·s^{-1} centred at 93 km·s^{-1}. This velocity is close to other up-flow observations of 100 km·s^{-1} derived for flares with the similar beam parameters(Milligan et al., 2006a; Milligan et al., 2006b).

The hydrodynamic models used in our work include a flaring corona that is obtained from a conversion of the quiet Sun chromosphere, rather than having initially an inherent corona (see Fig.2.3). Although, it should be noted that a large area covered by AIA pixels is the neighbouring corona, because given the difference in spatial resolutions of the AIA (0.6") and SST (0.06") pixels, the minimum area covered by a single AIA pixel includes 10x10=100 SST pixels. Within these, only 25 pixels contain Hα emission while the other 75 pixels are, in fact, the neighbouring corona rather than the flaring event for which our hydrodynamic model is applicable. Therefore, our model does not intend to explain the contributions of any neighbouring coronal pixels to the emission of a flaring corona captured also by AIA, because our model certainly is not intended and does not solve the quiet coronal heating problem.

Each passband in the images from AIA detects plasmas with different emissivity defined by the local atmospheric temperature and density. The normalised instrumental response functions of the AIA channels are shown in Fig.7.4 plotted against $\log_{10}$ of T (temperature) for the spectral lines of interest (94 Å, 171 Å and 304 Å). The AIA 94 Å channel has its largest sensitivity peak close to 10 MK combined with a secondary sensitivity peak close to the temperature of 1 MK (green line in Fig.7.4), i.e. it is sensitive to the flaring corona temperature peak (1-2 MK, see Fig.2.3a) in the flaring event 2 derived from the F10 model. We therefore expect to observe slightly enhanced emission from the source of the beam injection in the 94 Å channel above the observed background level, in addition to a strong enhancement in the 171 Å channel over the background level (see Fig.7.5a).

Comparison of the models presented in Figs.2.3a and b shows that the coronal temperature variations for 3F10 model would not account for the observed jet in the AIA 171 Å emission. However, the temperature profile evolution for F10 model between 5 and 100 s shown in Fig.2.3a, box 1, reveals that the plasma can be detectable in the temperature range of $\log T = 5.2$ to $\log T = 6.05$ at the depths of the low flaring corona. The 171 Å channel is the most sensitive to this range, compared to other

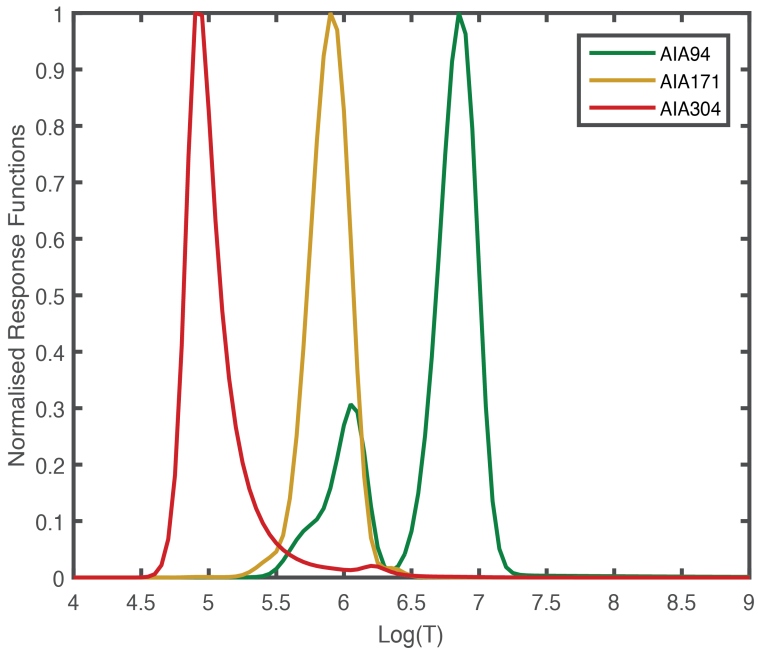

FIGURE 7.4: The normalised response functions of the AIA channels. The normalised response functions of the AIA 94 Å (green line), 171 Å (yellow line) and 304 Å (red line) channels plotted against $\log_{10}$ of T (temperature). The AIA 94 Å channel has its largest sensitivity peak close to 10 MK but it is not limited in sensitivity to that specific temperature. It is shown in the green line that the AIA 94 Å channel has a secondary peak with maximum at the temperature of 1-2 MK.

available AIA channels (see Fig7.4). Moreover, the velocity range derived from the AIA 171 Å channel, averaged at 93 km·s^{-1}, also resembles closely for a given temperature range the predictions of F10 model of a hydrodynamic response to plasma heating by an electron beam shown in Fig.2.3a.

From the hydrodynamic simulations the response in 94 Å channel is expected to be rather weak. This is because the 94 Å emission is detected at a secondary sensitivity peak, at 1 MK relevant for the flaring corona in this event, and not at the main sensitivity peak of 10 MK (see Fig.7.4b, green line). There was slightly increased signal in the 94 Å protrusion (Fig.7.3b, first row), which was most evident in 171 Å images (Fig.7.3b, second row, blue arrow).

The intensity responses, I_i for each of the AIA channels i, were simulated following the AIA calibration method described by Boerner et al., 2012,

$$I_i = \int K_i(T(z)) n_e^2(z) dz, \tag{7.1}$$

where $K_i(T)$ is the temperature response function for the AIA channel i (Boerner et

al., 2012), shown in Fig.7.4, n_e is the electron density, and the integral is performed over the height z, of the model atmosphere.

Fig.7.5a shows the simulated (green line) and observed (green crosses) light-curves for AIA 94 Å channel, and likewise, in yellow, the light curves for the AIA 171 Å channel. There is a small increase above the background levels in the observed AIA 94 Å emission (green crosses) during the first 20-30 s (Fig.7.5a). Due to the secondary sensitivity peak in AIA 94 Å, this flaring F10 model is capable of producing the AIA 94 Å enhancements on the order of $1 - 2 \times 10^2$ in intensity (DN units) (Fig.7.5a, green line) at the temperature of 1-2 MK, hence, confirming that 94Å emission is detectable from this model.

Most importantly, the F10 hydrodynamic model leads to a much greater excess of intensity in the AIA 171 Å channel for some time during and after the beam injection (Fig.7.5a, yellow line), as observed (Fig.7.5a, yellow crosses). This AIA 171 Å enhancement should remain visible during the outflow (jet) process, and is indeed observed (see Fig.7.2b, blue arrow). The *simulated jet* travels at ∼90 km·s^{-1} and the *observed jet* traverses 3 pixels in the image space corresponding to ∼1500 km. Hence, the simulated jet would take ∼15-20 s to appear 3 pixels from the Hα kernel location in the observations (or later if travelling at some angle out of the plane of observation). So the simulation predicts that we should only expect to see the displacement of the jet after this time, in agreement with observations (Fig.7.2b, blue arrow).

The fact that the jet-like feature was seen only in the 171 Å channel and not in 304 Å or not clearly in 94 Å channel can be explained by a fast (tens of seconds) reduction of the plasma temperature and density in the newly formed flaring corona caused by radiative cooling, thermal conduction and plasma motion (Moore and Datlowe, 1975; Antiochos, 1980). Indeed, at the later times (20-30 s), after the beam is off, the coronal temperature was quickly reduced from two million to the sub-million Kelvin range (Fig.2.3a, box 1), and the plasma density was also reduced from the chromospheric (10^{10} cm^{-3}) to coronal 10^9 cm^{-3} density (Fig.2.3c).

The simulated light curves in the two channels were normalised to unity at their peak values (Fig.7.5b) and subtracted, in order to analyse the excess of the AIA171 Å enhancement relative to that in AIA 94 Å. This excess is plotted as a fraction of the enhancement in the AIA 171 Å channel in Fig.7.5c.

The enhancement in AIA 171 Å peaks during the beam injection phase (0-10 s) and decreases afterwards (Fig.7.5a). After 50 s the response in this channel has returned to background level (Fig.7.5a). Because the jet is observed away from the Hα kernel location after 20 s and the AIA cadence is 12 s, the jet should only be visible in AIA 171 Å for 1-2 time frames according to the F10 model (as indicated by the FWHM line plotted in Fig.7.5b), which is indeed the case (Fig.7.2b).

Fig.7.5c shows that at 30 s our model predicts a much greater enhancement over the AIA 171 Å background than over the AIA 94 Å background. Therefore, the F10 model predicts the presence of a jet, outflowing from the chromospheric source of beam heating, that is visible in AIA 171 Å and not AIA 94 Å at around 30 s. The fact that a jet is not observed in AIA 94 Å but only in AIA 171 Å (Fig.7.2b), adds further evidence to support the value of the flux used in the F10 model, because it places an upper boundary on the temperature, T, of the outflow, i.e. T is much less than 10 MK, and limited to 1-2 MK. At the same time, the jet is not observed in AIA 304 Å (Fig.7.2b) resulting in similar implications for the lower temperature. One can conclude that the jet must be also much hotter than 100,000 K (the sensitivity peak for the AIA 304 Å channel). This is why this jet is clearly observed in the AIA 171 Å channel.

The cooling process in hydrodynamic model can quickly reduce the differential emission measure (DEM) of a flaring corona, as demonstrated in Fig.6 of Somov, Spektor, and Syrovatskii, 1981, allowing the coronal emissivity to reach the range matching the AIA sensitivity window. This made the plasma up-flow detectable only in the AIA 171 Å passband at 29 s after the event onset when the coronal temperature in a flaring corona is dropped to the AIA range. Although, the coronal temperature in a flaring atmosphere at this time remains still too high for the intrusion to be clearly seen in the 304 Å passband, it can be observed later (>100 s) after further cooling.

7.2.3 Simulated radiative response in the Hα line

The simulated Hα line profiles were calculated for non-thermal excitation and ionisation by an electron beam with the initial fluxes of 10^{10} erg·cm^{-2}·s^{-1} (F10 model), 3×10^{10} erg·cm^{-2}·s^{-1} (3F10 model), representing an upper estimate of the flux and

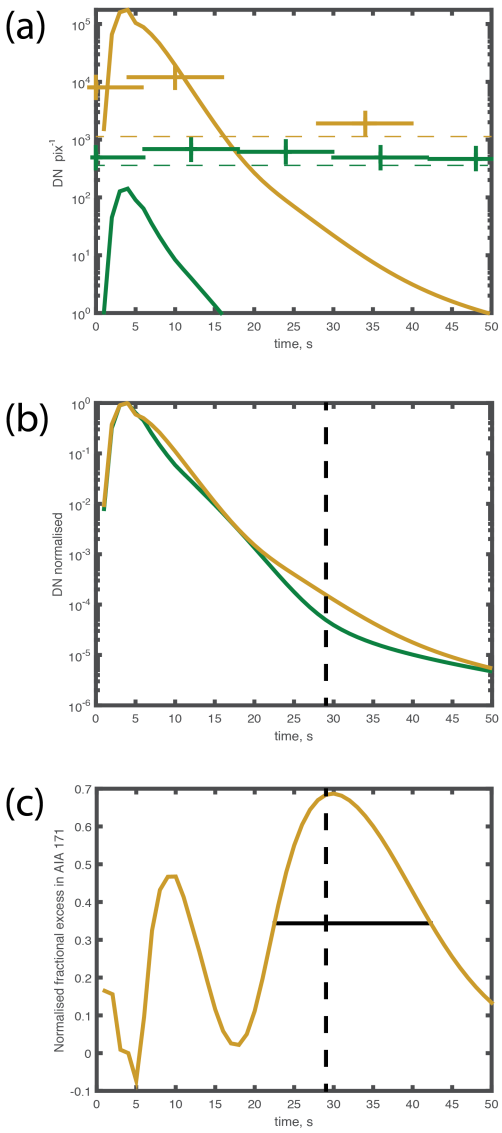

FIGURE 7.5: Simulated and observed AIA light curves. (a) The simulated light curves in the AIA 94 Å (green line) and 171 Å (yellow line) channels for contributions from the flaring corona, transition region and chromosphere. The simulation does not include background from the overlying upper corona or neighbouring corona. Observed values for the 94 Å (green crosses) and 171 Å (yellow crosses) channels including this background are shown. (b) The simulated profiles of the signals in AIA 94 Å (green line) and 171 Å (yellow line) above background. These profiles have been normalised to 1 at their peak values. The AIA 171 Å channel is particularly bright compared to the AIA 94 Å channel at around 30 s. (c) The normalised fractional excess in AIA 171 Å. The normalised light curves in panel b were subtracted to find the relative excess in the 171 Å channel. This excess is plotted as a fraction of the emission in the 171 Å channel at each instant. The full width half maximum (Horizontal black bar) indicates the times at which the jet is particularly bright in AIA 171 Å compared to AIA 94 Å, the vertical bar represents the maximum relative brightness at around 30 s.

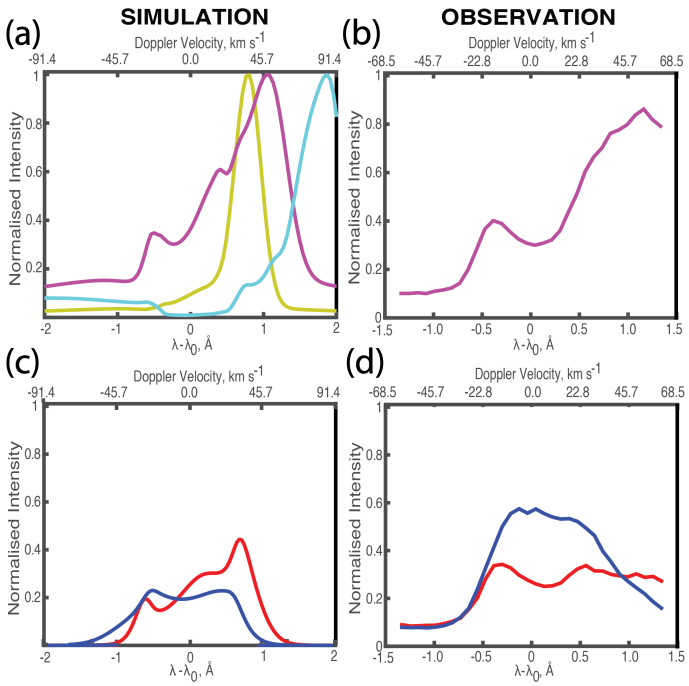

FIGURE 7.6: Simulated and observed Hα line enhancements. (a) the synthetic Hα line normalised intensity versus a distance ($\lambda - \lambda_0$), in Å, from the Hα line central wavelength, $\lambda_0 = 6563$ Å taken from the simulation at +5 s after a beam onset for the F10 model (magenta line), the 3F10 model (cyan line) and a model with initial flux 7×10^9 erg·cm^{-2}·s^{-1} (7F9 model, yellow line) (b) the normalised background-subtracted Hα profile observed +7 s after the ribbon onset in the event 2. (c) The Hα line normalised intensity simulated for the F10 model at later times after the beam onset: +30 s (red solid line) and +70 s (blue solid line) and (d) the observed Hα profiles at the similar times of +29 s (red solid line) and +56 s (blue solid line) after the event 2 onset.

7×10^9 erg·cm^{-2}·s^{-1} (7F9 model), representing a lower estimate with a beam spectral index of 4 (Figs.7.6a and c), as suggested by the RHESSI and tuned by Hα observations (see section 7.1.3). The simulated profiles are normalised in the similar way to the observed profiles.

Non-thermal collisions between beam electrons and hydrogen atoms for all hydrodynamic models using the CEA cause excess excitation to the upper state ($n = 3$) of the Hα line transition, quickly converting the Hα spectral line from absorption into emission. The emission in the near wing wavelengths from the line centre have a lower optical depth and, thus, less absorption, resulting in the small intensity increase in the near wings (± 0.5Å) (called 'horns') (see Fig.7.6). However, the main contribution of energetic beam electrons is to the strong ionisation of hydrogen atoms in a flaring atmosphere causing increase of their ionisation degree by orders of magnitude (Zharkova and Kobylinskii, 1993). This raises density of the ambient electrons, compared to the density expected from their kinetic temperature. This, in turn, produces a significant increase of Hα line wing intensities owing to Stark's effect.

The radiative simulations clearly show that in the first seconds after the beam onset Hα line profiles are dominated by non-thermal ionisation by the beam electrons and the downward motion of the shock (see Fig.2.3b, box 2). For this flaring event the beam has a relatively low initial energy flux about $0.7 - 3.0 \times 10^{10}$ erg·cm^{-2}·s^{-1} resulting in a moderate increase of the Hα wing intensity (see Fig.7.6a). The horn in the near blue wing, about -0.5 Å from the central line wavelength (Fig.7.6a), is in a normal position to be caused by a radiative self-absorption as discussed above. However, the horn in the near red wing reveals a large increase of the intensity caused by a Doppler-shift of the emission wavelength caused by a downward movement of the hydrodynamic shock (see Fig.2.3b, box 2) growing from 35 km·s^{-1} (7F9 model) up to 50 km·s^{-1} (F10 model) or 90 km·s^{-1} (for model 3F10) at the times of maximum beam deposition.

When the beam is switched off, thermal heating and slow recombinations of the ambient electrons with hydrogen atoms become the main sources of sustaining hydrogen atoms' excitation and, thus, Hα emission (see Fig.7.6c and d). One can see a decrease in the total intensity in the line compared to the intensity simulated during

the beam injection (compare Figs.7.6a and c). There is also a decrease of the red wing intensity over the subsequent 60 s (Fig.7.6c). At later times in simulations, after the beam is off, Hα emission profiles become standard thermal profiles, exhibiting after 70 s a small intensity enhancement in the blue horn (Fig.7.6c, blue line).

7.2.4 Comparison with Hα line observations

The simulated Hα line profiles were compared with the profiles observed by CRISP by averaging the emission over all the pixels in the red box of Fig.7.3b (with the quiet Sun background intensity subtracted) during the flare onset (Fig.7.6b) and over the next hundred seconds (Fig.7.6d). The simulation produces intensities of Hα line emission from a flaring atmosphere within the spectral range (± 3.0 Å from a central wavelength) that is broader than the observational range (± 1.5 Å). The simulated profiles are shown to ± 2 Å to demonstrate that the emission profile extended into a far red wing beyond the range (1.5 Å) defined by the CRISP's current spectral filter.

The red-shift in the simulated Hα line profile reaches a maximum at (or just after) 5 s of the electron beam onset when the downward velocity in hydrodynamic model is maximal (see Fig.2.3b, box 2). Only for the F10 model the shape of simulated Hα line profile and a magnitude of the red shift is closely matched by the Hα line profile observed by CRISP over the similar interval (7 s) after the event onset (Fig.7.6d), while the beam with lower or higher energy fluxes produce much smaller or much higher red shifts, than those observed.

The Hα line core in model F10 is formed at depths of a hydrodynamic shock, whose downward motion makes the line intensity red-shifted by around 1 Å from the central wavelength ($\lambda_0 = 6563$ Å), corresponding to a Doppler velocity of 47 km·s^{-1} (Fig.7.6a). This is very close to the velocities of $45 - 50$ km·s^{-1} derived from the observed profile (Fig.7.6b). Hence, we present the first successful interpretation of Hα line red-shifted profiles observed at the onset of a flare that has been long overdue for the past three decades (Ichimoto and Kurokawa, 1984; Wuelser and Marti, 1989).

This comparison confirms that the observed red shift in Hα line can be only caused by beam electrons with the initial flux close to 10^{10} erg·cm^{-2}·s^{-1}. Measuring

Doppler shift of the emission outside of the horns of the Hα line profile is an alternative method for determining the parameters of electron beam, allowing us to tune the estimations of initial energy flux derived from the low-resolution RHESSI data (see section 7.1.3).

7.3 Discussion

In this chapter we presented multi-wavelength observations of a flaring event onset obtained with highest temporal and spatial resolution from CRISP/SST, AIA/SDO and RHESSI. The C1.5 class flare observed on 30 June 2013 in AR 11778 produced 3 flaring events, which contribute to its HXR and SXR light curves. The flaring event 2 produced two Hα ribbons, in one of which Hα line profiles were recorded in 5x5 pixels using CRISP/SST with the maximum downward velocity of $45 - 50$ km·s^{-1}. There are also plasma up-flows of 93 km·s^{-1} observed in the 171 Å AIA channel 29 s after the event onset, occurring just above the Hα line ribbon with the downward motion.

These observations were successfully interpreted with the combined hydrodynamic and full NLTE radiative models (HYDRO2GEN) affected by power-law electron beams (chapters 2 and 3). The beam parameters for this event are estimated using the HXR photon spectrum observed by RHESSI and tuned with the high-resolution Hα observations. Our simulations show that for this flaring event heating of flaring atmosphere by beam electrons in the hydrodynamic model starts from the quiet Sun chromosphere, converting it into a flaring atmosphere with its own corona, transition region and chromosphere. Beam electrons quickly sweep the ambient plasma to deeper atmospheric layers causing, in turn, a fast upward motion of the swept plasma back to the corona and downward motion as hydrodynamic shocks (Somov, Spektor, and Syrovatskii, 1981; Zharkova and Zharkov, 2007).

The upward motion, which occurs from the first seconds after a beam onset, reflects the chromospheric evaporation caused by a hydrodynamic response of the flaring atmosphere to heating by electron beam. The chromospheric plasma in this upward motion for this flaring event is observed injected into a flaring corona 29 s after the event (or beam) onset that fits very well our hydrodynamic model and the

sensitivity windows of the AIA in the different channels (94 Å, 171 Å and 304 Å). The plasma jet becomes only visible in the AIA 171 Å channel, at the times when the temperatures and densities of the flaring corona are reduced to the magnitudes detectable within this AIA passband.

Additional support to the proposed HYDRO2GEN model is provided from fitting the observed Hα-line profiles with large red shifts by the simulated profiles obtained from a full NLTE approach applied to 1D flaring atmospheres being a hydrodynamic response to electron beam heating. The Hα line in flaring atmospheres is shown to be dominated by: *first*, an increase in the line wing intensities is caused by collisional broadening and the Stark effect due to the high number of free electrons in the ambient plasma as a result of non-thermal ionisation of the ambient hydrogen by beam electrons, and *second*, a hydrodynamic shock motion downward leading to large Doppler-shifts. The combination of these effects for this flaring event produces a big increase of the Hα line intensity in the red wing at about 1 Å from the line central wavelength, corresponding Doppler velocities of $45-50$ km·s^{-1} derived from the observation. The latter is closely reproduced by the simulations only for the model F10, clearly restricting the initial energy flux of beam electrons capable of accounting for such the red shift. In addition, this close fit highlights a need to extend the spectral windows for observations of Hα line dynamics in flaring atmospheres, which will allow capture of the profiles with large red shifts occurring in the first 100 s of a flaring event.

It should be noted that the ratio of red-to-blue wing intensities of the simulated Hα line profile is slightly higher than in the observed profile, by a factor of 1.2. In addition, the wavelength of the central reversal (with the maximal absorption) in the simulated Hα line profile at 5 s is slightly blue-shifted from the central wavelength, compared with the observations (compare Figs.7.6a and b). Such blue shifts of the central reversals in Hα lines could be real as they were also observed by Ichimoto and Kurokawa, 1984 for the profiles with strong red shifts (see their Fig.4a at 00:19:59 UT).

It appears that small blue (or red) shifts of the central reversals can reflect the overlying Hα-line emission with strong upward (or downward) motions produced by different layers of a flaring event, so that their superposition could shift the

central reversal emission towards the blue or red wing, accordingly (Ichimoto and Kurokawa, 1984). There is also a possibility that the Hα ribbon emission observed with SST occurred in a much smaller source size than the SST diffraction-limited resolution of 100 km in Hα. This could lead to over-smoothing, or averaging, of the observed Hα line intensity over a larger area than the real emission comes from that causes the differences in the observed and simulated ratios of the red-to-blue horn intensities and the blue-shifted central intensity.

While this scenario is plausible, it still assumes that the observed red-to-blue intensity ratio is perfectly accurate, which may not be the case, given that we do not have infinite spatial resolution in the SST observations. Therefore, this outstanding issue cannot be fully reconciled beyond the limits of the current state-of-the-art SST observations and needs to be progressed with observations by the instruments with higher resolution, such as the Daniel K. Inouye Solar Telescope (DKIST) (Tritschler et al., 2015).

This study provides the first close interpretation of large red-shifted Hα line observations of solar (and possibly stellar) flares indicating a need for broader spectral windows capable to fully capture the dynamics of flaring events.

In summary,

(7.1) The simulated Hα emission in the F10 HYDRO2GEN model is shown to closely match the emission observed in an Hα kernel in the impulsive phase of the C1.5-class flare on 30^{th} June 2013. The match is close in terms of the shape of the profile, the 1Å red-shifted emission, and the ratio of red and blue wing intensities. There is also reasonable agreement between the simulated and observed profiles after the beam is switched off.

(7.2) The beam parameters in the simulation were matched to those suggested using RHESSI observations for the C1.5-class flare on 30^{th} June 2013, and strongly support the interpretation that the highly red-shifted Hα emission observed during the impulsive phases of solar flares is caused by the injection from the corona of a non-thermal electron beam with a power-law energy distribution.

(7.3) Upward motion of plasma was detected above the location of the observed Hα profiles in the C1.5-class flare on 30^{th} June 2013, as a coronal jet in the

AIA 171 channel. This emission showed agreement with the simulated AIA emission, and provides additional confirmation of the speed (~ 93km·s^{-1}) and temperature ($\sim 1MK$) and timing of the evaporation predicted by the F10 model.

7.4 Notes

The work relating to the C1.5-class flare observed on 30^{th} June 2013 is adapted from the paper Druett et al., 2017. In this paper modelling, interpretation and writing input was performed in collaboration with Prof. Valentina Zharkova. Processing and analysis of the observations, as well as the modelling of AIA emission was completed in collaboration with Dr Eamon Scullion. Dr Sergei Zharkov provided assistance with hydrodynamic modelling and checking for a seismic response. The observation was conducted by Prof. Luc Rouppe van der Voort, and RHESSI analysis was conducted by Dr Sarah Matthews.

Chapter 8

Emission in the hydrogen Balmer and Paschen continua

8.1 Simulations of Balmer and Paschen Continua

Despite the expectation that, in flaring atmospheres, most hydrogen continua are optically thin, we have shown that the Lyman continuum has very large optical thicknesses for any beam (see chapter 5) and, thus, fully governs hydrogen ionisation (Zharkova and Kobylinskii, 1993). The Balmer continuum sometimes for stronger beams can also have a non-negligible optical thickness. Because hydrogen continuum radiation is generated by recombination of free electrons with an ionised hydrogen atom (proton), the intensity of emission produced by this process depends strongly on the ionisation degree of the plasma. The ionisation rates in our models are dominated by collisions of hydrogen atoms with non-thermal electrons (see section 3.1.1). Thus, the simulated results for the Balmer and Paschen continua (Fig.8.1) reveal profiles with intensities that are highly sensitive to the beam's initial energy flux.

For all beams the simulated Balmer continuum was the most effectively enhanced, and contained a greater intensity in the continuum head compared to the other hydrogen continua. The Lyman continuum head is optically thick in the chromosphere. Because of this, the Lyman continuum emission only escapes from the top of the chromosphere, and contributions do not emerge from a large fraction of the depths at which the beam causes increased ionisation. Thus, the emerging intensity of Lyman continuum emission is less enhanced than the Balmer continuum.

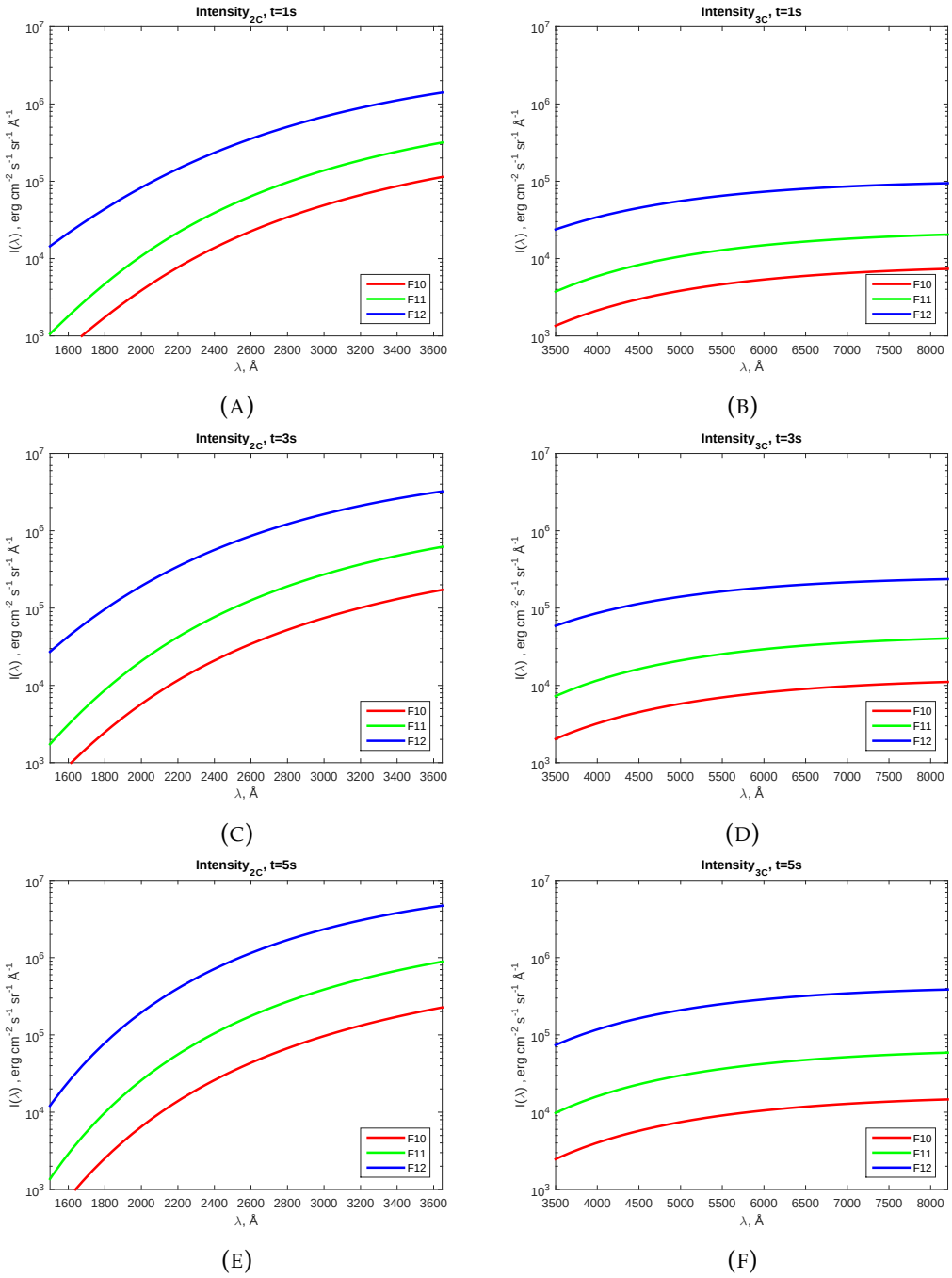

FIGURE 8.1: Intensities of Balmer continuum enhancement at (a) $t = 1$, (c) $t = 3$, (e) $t = 5$, and Paschen continuum enhancement at (b) $t = 1$, (d) $t = 3$, (f) $t = 5$, in erg·cm^{-2}· s^{-1}·sr^{-1}·Å^{-1} against wavelength in Å.

To investigate the relationships between the intensities of emission in the other continua we use the ratios of the intensity in the continuum heads. Tables 8.1 to 8.3 display the ratios of the emission intensity in the Balmer continuum head to that in the Paschen, Bracket and Pfund continuum heads, respectively. The top rows display results for the F12 model, the middle rows contain results for the F11 model and the bottom rows show the F10 model data. The columns indicate the time since the beam injection began, from 1 to 5 s. Over the first 5 s of the injection the ratio of Balmer continuum head intensity to other continua head intensities is reduced by between 18 and 20% for the F12 beam model. For the F11 model the ratio is reduced by between 3 and 4%. For the F10 model there is a negligible change in the ratio over time (Tables 8.1, 8.2, and 8.3). This decrease, or its absence, results from the amount of increase in the ionisation rates by collisions with beam electrons at different depths in the different beam models.

In all the simulated models, the ambient hydrogen is efficiently ionised for a large proportion of the depths that make up the Balmer continuum formation region, but extend to a smaller proportion of the formation regions for the other continua. In models with stronger beams, this increase extends downwards into the depths where subordinate continua are more effectively contributed to, reducing the ratio of the subordinate continuum head intensities compared to the Balmer continuum one.

Beam Model	$t = 1\,sec$	$t = 2\,sec$	$t = 3\,sec$	$t = 4\,sec$	$t = 5\,sec$
F12	14.86	14.33	13.65	12.89	12.12
F11	15.52	15.43	15.32	15.18	15.03
F10	15.44	15.49	15.51	15.52	15.49

TABLE 8.1: $I_{2c}(\lambda_{2c})/I_{3c}(\lambda_{3c})$: The dimensionless continuum head intensity ratios for Balmer and Paschen continua for the F12 model (Top row), F11 model (Middle row) and F10 model (Bottom row). Times, from 1 to 5 s into the beam injection phase, are displayed in each row respectively.

Beam Model	$t = 1\,sec$	$t = 2\,sec$	$t = 3\,sec$	$t = 4\,sec$	$t = 5\,sec$
F12	182.6	175.4	166.3	155.6	144.7
F11	190.1	188.4	186.3	184.1	181.5
F10	189.0	190.1	190.4	190.3	186.9

TABLE 8.2: $I_{2c}(\lambda_{2c})/I_{4c}(\lambda_{4c})$: The dimensionless continuum head intensity ratios for Balmer and Brackett continua

Beam Model	$t = 1\,sec$	$t = 2\,sec$	$t = 3\,sec$	$t = 4\,sec$	$t = 5\,sec$
F12	1001	965.1	915.8	856.5	795.4
F11	1019	1017	1010	1000	987.1
F10	982.3	996.0	1003	1006	1006

TABLE 8.3: $I_{2c}(\lambda_{2c})/I_{5c}(\lambda_{5c})$: The dimensionless continuum head intensity ratios for Balmer and Pfund continua.

By similar reasoning one expects that the same pattern of ratios is present between Paschen head intensity and the subordinate Brackett head intensities. Table 8.4 displays the results in the same format as tables Tables 8.1 to 8.3 and although there is a similar relationship, the magnitude of the effect is negligible even in the F12 flare, as the flaring chromosphere does not span a large fraction of the formation regions of either continuum (Table 8.4).

The Balmer jump is the difference in intensities on either side of the Balmer continuum head wavelength (3646Å) in the continuum spectrum of a star. In order to assess how the initial flux of an electron beam affects the Balmer jump, we inspect our results at the Balmer continuum head wavelength for both Balmer and Paschen continuum radiation. The ratio of intensity of the Balmer continuum to the intensity in the Paschen continuum at the wavelength of the Balmer continuum head (BP ratio) does not show a clear pattern across all flare models (Table 8.5). This results from the fact that the profiles of the continua are affected somewhat by the detailed hydrodynamic response to beam deposition, as well as by the ionisation degree. However, we do see that the ratio is lowered by a greater amount for the F12 model than the F10 and F11 models. This suggests that one would expect to see a smaller Balmer jump developing during beam injection, in the case of beams with high initial fluxes because of strong ionisation increase in the photosphere.

Beam Model	$t = 1\,sec$	$t = 2\,sec$	$t = 3\,sec$	$t = 4\,sec$	$t = 5\,sec$
F12	12.28	12.25	12.18	12.07	11.94
F11	12.25	12.21	12.16	12.13	12.08
F10	12.24	12.27	12.28	12.26	12.24

TABLE 8.4: $I_{3c}(\lambda_{3c})/I_{4c}(\lambda_{4c})$: The continuum head intensity ratios for Paschen and Brackett continua.

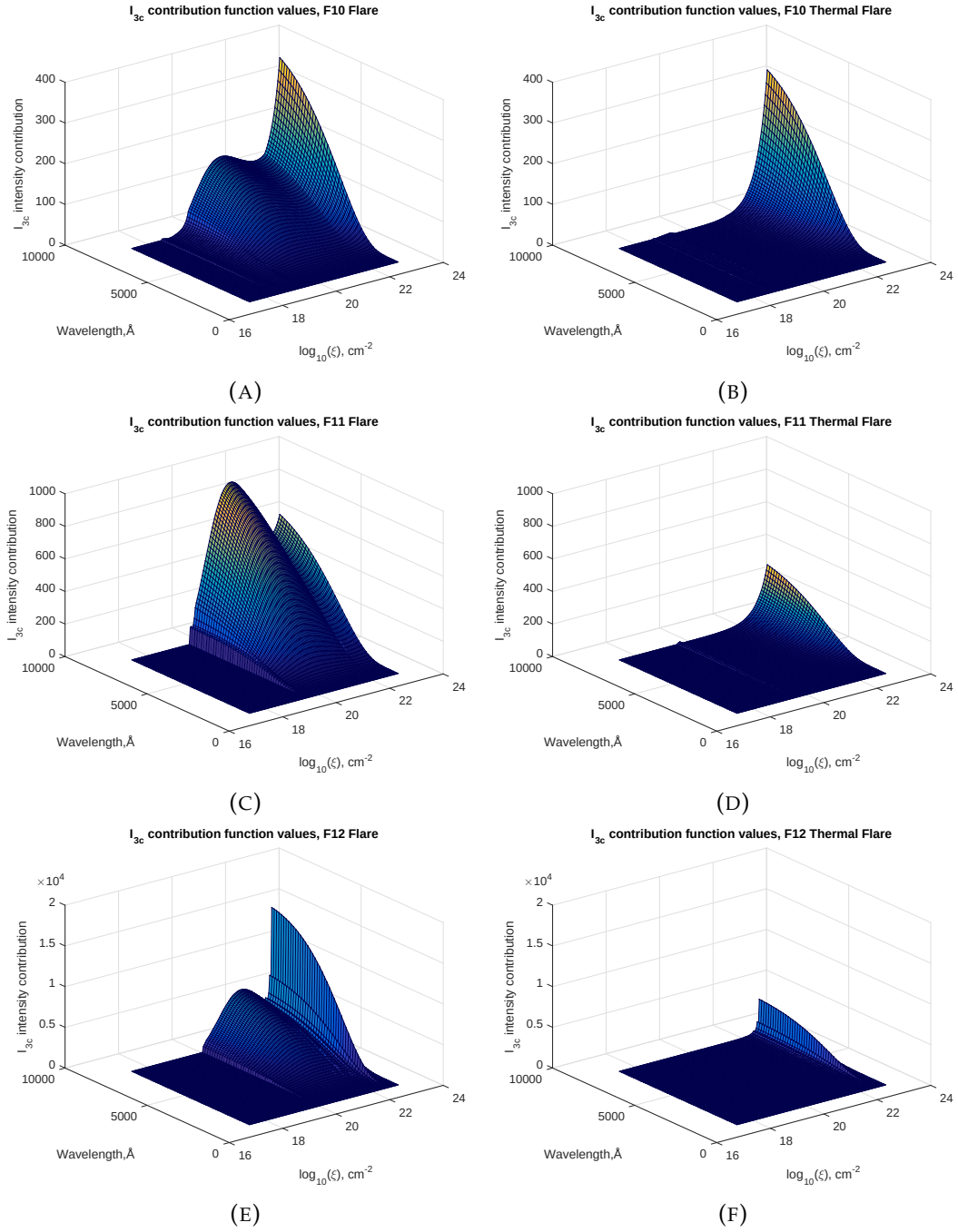

FIGURE 8.2: Paschen continuum's contribution functions (see section 3.3) calculated at $t = 5\ s$. The Z-axis displays the contribution function value, the X- and Y- axes are in terms of wavelength, λ and the logarithm of column depth $log_{10}\xi$. The top row shows results for the F10 flare model, the central row shows the data for the F11 Flare model, and the bottom row shows data for the F12 model. The left panels show the models including excitation and ionisation of hydrogen atoms by non-thermal beam electrons, the right panels display the 'thermal flare' simulations without excitation and ionisation by beam electrons.

Beam Model	$t = 1\,sec$	$t = 2\,sec$	$t = 3\,sec$	$t = 4\,sec$	$t = 5\,sec$
F12	52.26	48.44	48.37	50.42	54.28
F11	72.96	72.29	73.17	73.67	77.22
F10	63.25	72.29	72.78	74.61	78.00

TABLE 8.5: $I_{2c}(\lambda_{2c})/I_{3c}(\lambda_{2c})$: The continuum head intensity ratios for for Balmer and Paschen continua, at the Balmer head wavelength.

8.1.1 Formation regions of Balmer and Paschen continua

Insight into the origin of continuous emission for Balmer and Paschen continua can be gained by inspecting the contribution functions of the hydrogen continua (see section 3.3). Here we consider only Paschen continuum as the source of WL flares. Fig.8.2 displays the Paschen continuum contribution functions at $t = 5\ s$ for the F10, F11, and F12 model simulations in panels a & b, c & d, and e & f respectively. The intensity contributions are plotted on the Z-axis, with wavelength λ, and the column depth in logarithmic scale $\log_{10}\xi$ on the X- and Y-axes, respectively. The left panels show the contribution functions for the models with radiative rates including non-thermal excitation and ionisation by a beam of electrons. Those on the right show the results for 'thermal flares' using the same hydrodynamic model as shown in the left panel, but without non-thermal beam excitation and ionisation included.

In the F10 beam model, non-thermal ionisation causes a great increase in continuum contributions higher in the flaring chromosphere for column depths in a broad range from around $\xi = 10^{19}$ to $10^{22} cm^{-2}$ (compare the beam and thermal model contribution functions in Figs.8.2a and b respectively for column depths from $\xi = 10^{19}$ to $10^{22} cm^{-2}$). However, the contributions from the deeper atmosphere are barely enhanced compared to the thermal model (see Figs.8.2a, b, $\xi = 10^{22}\ cm^{-2}$). This is because, for the beam with a low initial flux, the beam electron densities are reduced to a point where they are not ionising a large amount of the neutral hydrogen at a column depth of $\xi = 10^{22}\ cm^{-2}$. Additionally there is minimal backwarming of the photosphere from the radiative response in the chromosphere.

In the F11 model, contributions from the mid-chromosphere are even more greatly enhanced as a direct result of the increased non-thermal ionisation rates at these depths. Additionally, we observe an increase in contributions from deep in the atmosphere (Fig8.2c, d). This results from both radiative transfer and a more significant

number of beam electrons penetrating to depths greater than $\xi = 10^{22}\ cm^{-2}$.

The F12 model generates a very strong Paschen emission, or WL flare, coinciding with large increase of Balmer continuum radiation produced in the flaring chromosphere. A combination of the effects of radiative transfer with strong non-thermal ionisation in the lower atmosphere produces the extremely large increase of the upper and lower atmospheric contributions (Fig8.2e, f). The F12 flare model produces a non-negligible increase in a temperature in the deep atmosphere (photosphere) (Fig.2.3, left panels), but this is not the source of WL enhancement suggested by the contribution functions presented here. The thermal flare model (only lacking non-thermal excitation and ionisation) produces a much smaller increase in the Paschen continuum, or WL, compared to the model considering the effect of a powerful beam of non-thermal electrons. Hence only the presence of beam electrons can explain the occurrence of WL flares simultaneously with HXR emission reported by many authors (Hudson, 1972; Martínez Oliveros et al., 2012).

The Paschen continuum head intensity ratios for the model with the beam to the thermal flare are of factor 3.53 for the F10 model, 14.4 for the F11 model, and 15.5 for the F12 model. A similar study was conducted for the Balmer continuum that produced the similar results for the ratios of head intensity in models with beam to those for the thermal model, 3.55, 14.0, and 13.0 for the F10, F11, and F12 flares, respectively. The variation of Balmer continuum contribution functions from different column depths also showed similar patterns to those for the Paschen continuum in each simulation (Fig.8.2). The differences were (1) that the contribution functions had higher magnitudes for the Balmer continuum and (2) that there were some differences in the variation of the profiles with wavelength. The results for the Paschen continuum were selected for display in Fig.8.2 to aid the comparison with WL observations carried out in section 8.2.2.

Thus, one can observe that electron beams are highly effective agents for the production of WL emission co-temporally with the beam onset in a flaring atmosphere at higher atmospheric depths, compared with the pure thermal heating. Comparison with observations of Balmer continuum and WL in flares is carried out below, in sections 8.2.1 and 8.2.2.

8.2 Comparison with observations

8.2.1 Balmer continuum enhancement

Heinzel and Kleint, 2014 identified Balmer continuum enhancement during the X1 class flare on 29^{th} March 2014 using IRIS, at a disk position of $\mu = 0.83$ and a wavelength of 2826Å. They report an enhancement of 4.1×10^5 erg·cm^{-2}·s^{-1}·sr^{-1}·Å^{-1} over the background quiet Sun contribution of 3.7×10^5 erg·cm^{-2}·s^{-1}·sr^{-1}·Å^{-1}. Heinzel and Kleint, 2014 state that the RHESSI data suggests, to an order of magnitude, the beam flux for electrons with energies greater than 20 keV was 10^{11}erg·cm^{-2}·s^{-1}, with spectral index $= 5$.

To model this observation Heinzel et al., 2016 simulated Balmer continuum emission using the FLARIX code (Varady et al., 2010). At the peak of an initial flux, $F_0 = 4.5 \times 10^{10}$ erg·cm^{-2}·s^{-1}·sr^{-1}·Å^{-1} FLARIX produces Balmer continuum enhancement of around 6×10^4 erg·cm^{-2}·s^{-1}·sr^{-1}·Å^{-1}, in reasonable agreement with the observation. To evaluate our model, we inspect the simulated Balmer continuum at a wavelength of 2826.5Å, and at the peak of the beam injection ($t = 5\ s$), when a significant amount of the ionisation occurs owing to non-thermal inelastic collisions. With $\mu = 0.83$, the F11 model produces intensities of Balmer continuum that are even closer fits to the observation than those produced using FLARIX, 8.7×10^4 and 3.13×10^5 erg·cm^{-2}·s^{-1}·sr^{-1}·Å^{-1} for $\gamma = 5$ and $\gamma = 3$ respectively. The Balmer continuum intensity produced using FLARIX was very close to the value produced using our F10 model.

Sources of errors between the simulated emission intensities and those observed include: (1) The duration of the beam injection appears to be significantly longer for the observations discussed than the 10 s used in our model. The HXR spectra in Fig.4 of Heinzel and Kleint, 2014 show HXR bursts lasting for times in the order of minutes. (2) The loop footpoint areas are unresolved in RHESSI data, giving lower bounds of the initial energy flux for a beam. (3) The calibration process used to convert the observed data number (DN) units into the CGS units. (4) There is a difference in timing of the observed and simulated continua, with our model representing the first seconds of the flare onset and with an 8 s exposure time and a 75 s cadence in the observations used by Heinzel and Kleint, 2014.

8.2.2 Paschen continuum white light enhancement

Martínez Oliveros et al., 2012 report observations of an M3.5-class flare which occurred on the solar limb, on 24th February 2011 at 07:35 UT (see section sec:WLFs). Data from the 6173Å channel of the Solar Dynamics Observatory (SDO) were used to analyse the white light (WL) enhancement. HXR spectra were generated from RHESSI data in the 30-80 KeV channel over a 45 s exposure that was co-temporal with enhancements in WL. Simultaneous imaging from the Solar-TErrestrial RElations Observatory (STEREO) provided heliographic coordinates of the flare footpoints. A height scale relative to the photosphere was defined, using $\tau = 1$ at 5000Å as the surface of the photosphere.

The HXR sources had centroids located 420 km and 210 km above the quiet Sun photosphere, and the continuum sources had centroids with heights of 230 km and 160 km, in the northern and southern footpoints of the flare respectively. The uncertainty in the measurements of the heights of the HXR sources is ± 240 km, and for the heights of the WL sources the uncertainty is ± 100 km. Thus the sources of the HXR and WL were co-spatial to within instrumental resolution. The authors state that their result, "strongly associates the WL continuum enhancement with the collisional losses of the non-thermal electrons observed via bremsstrahlung HXRs in the impulsive phase of the flare" (Martínez Oliveros et al., 2012). They also note that the observed heights of the sources occurred well below the 800 km height that represents the stopping distance of 50 keV electrons found using the quiet Sun atmosphere of Fontenla et al., 2009. We compare these observations with the strongest beam model presented in this paper (F12), which has the greatest sweeping of chromospheric plasma towards the photosphere (see Fig.2.3k & l, blue lines), in order to assess whether a non-thermal electron beam is a feasible agent for the production of the observed sources of deep, co-temporal HXR and WL.

The column depths of the simulated WL signal, from the contribution functions due to Paschen continuum recombination in the F12 model at the peak of HXR, are shown in Fig.8.2e. At 6173Å the secondary source, produced in the flaring chromosphere, is seen to extend from the column depth of 1.28×10^{20} cm^{-2} to 2.52×10^{22} cm^{-2}, with a peak at 3.44×10^{21} cm^{-2} (Fig.8.2e). The heights in the F12

hydrodynamic model (Fig.2.3, blue lines) are used to identify the vertical heights of these positions above the quiet Sun photospheric level. The top and bottom of this WL signal are 340 km and 180 km above the quiet sun respectively (to the nearest 10 km) with the centroid of the source at a height of 260 km. Thus, for a strong, hard electron beam such as in the F12 beam model, the contribution functions of the simulated Paschen continuum radiation is consistent with the observed height of WL in Martínez Oliveros et al., 2012.

The stopping depths of beam electrons with energies of 30 & 80 keV due to collisional losses are calculated using the method presented in Zharkova and Gordovskyy, 2005b. The column depths calculated are 1.67×10^{20} cm^{-2} and 1.19×10^{21} cm^{-2} respectively. The heights of these column depths in the F12 model are 320 km and 280 km, respectively, at the peak of the beam flux. Hence the stopping depths of the electrons due to collisional losses in Zharkova and Gordovskyy, 2005b are also consistent with the simulated column depths at the height of the signal in the $30 - 80$keV RHESSI channel used in Martínez Oliveros et al., 2012.

Krucker et al., 2015 report the heights of WL ($\lambda = 6173$Å) and HXR sources measured for three limb flares at the peak of the HXR signal in the 30-100 keV range. The M1.7-class flare presented in their work has the HXR profile that most closely matches the form of the beams used in our models: little pre-heating, and a sharp HXR peak followed by a swift decline without repeated injections. The WL source was observed at a height of 799$\pm$70 km above the photosphere and had a radial extent of $\sim$652 km for a full width half maximum of intensity. The F11 model has a centroid of WL at height 771 km with an extent of around 984 km for the full width half maximum (ignoring the deeper, photospheric signal, Fig.8.2c) at the time of the HXR maximum. Therefore, this model presents good agreement with the observations of WL source height for the M1.7 flare, and a reasonable agreement with the observations of the other flares presented in Krucker et al., 2015. It is also possible to alter the extent and height of the WL sources in our models by varying the flux and spectral index of the beam.

8.3 Summary

Radiative responses of the Balmer and Paschen continua:

We show that the effects of electron beams (Fig.8.1) caused by non-thermal collisions between beam electrons and hydrogen atoms define the hydrogen ionisation rates. As result, the Balmer continuum contributions in the flaring chromosphere are most effectively enhanced by the energy delivered by electron beams. The ratio of the intensity enhancement in the Balmer continuum head to that in the heads of other continua is found to decrease with the increasing initial flux of a beam. This occurs because stronger beams (producing stronger flares) deliver greater energies to deeper atmospheric depths where the other continua are formed (Tables 8.1 to 8.3).

Moreover, our simulations demonstrate that a power-law electron beam is the much more effective agent for production of Pashen continuum (or white light (WL)) emission than thermal electrons caused by a temperature increase during flares (Fig.8.2). The non-thermal collisions with beam electrons immediately generate WL emission that begins co-temporally with HXR emission as indicated by Aboudarham and Henoux, 1986. In weaker flares, the WL enhancement due to non-thermal beams is principally generated at upper chromospheric densities. The WL emission for stronger F11 and F12 beam models (derived from the Pashen continuum contribution functions, see Fig.8.2) is also more effectively enhanced at upper chromospheric column depths, in addition to the normal WL emission occurred at the photopheric depths in thermal flares. This is caused by the combined radiative transfer and non-thermal ionisation effects in the Lyman continuum governing hydrogen ionisation affected by electron beams penetrating into the deeper atmospheric layers.

We do not replace the source functions for any transitions with those for black bodies, and consider ionisation by beam electrons from all the excited states of the ambient hydrogen atoms. We fully consider radiative transfer in the Lyman continuum, because this radiation controls the ionization of hydrogen in a flaring atmosphere (see chapter 5). This is an essential difference to many other approaches, such as those used in Ricchiazzi and Canfield, 1983; Allred et al., 2005.

Observations of Balmer and Pashen continua and HXR:

The chromospheric Balmer continuum enhancement in our models results in the close agreement with the enhancement observed using IRIS at a wavelength of 2830Å reported in Heinzel and Kleint, 2014. The column depths at which The WL emission for the F11 and F12 models largely originate are at the locations of stopping depths of lower cut-off electrons (10-20 keV). This is not the case for the thermal flare models where WL sources principally occur at photospheric column depths.

Since HXR emission is mainly produced at the chromospheric footpoints by electrons with such energies of 10-20 keV, this explains the close correlation between the heights of HXR and WL emission observed in the limb flares Martínez Oliveros et al., 2012; Krucker et al., 2015. The heights of these chromospheric sources of WL emission in our models, resulting from the sweeping of the QS plasma downward to the photosphere, due to heating by non-thermal electron beams, are found to be close to the photospheric heights in the quiet Sun seen on the limb. This confirms that electrons beams are the most plausible agents, which can explain solar flare observations on the limb by Martínez Oliveros et al., 2012 and Krucker et al., 2015.

In summary,

(8.1) The non-thermal collisions with beam electrons control the hydrogen ionisation rates in the chromosphere during the impulsive phase of a solar flare. The Balmer continuum is most effectively enhanced at this time because the Balmer continuum radiation forms effectively and escapes over the depths in which the ionisation occurs.

(8.2) Non-thermal ionisation is a much more effective method for the production of white light signatures than thermal emission or temperature increase, and the emission will begin co-temporally with the onset of the beam. For weaker beams (F10 model) this source originates overwhelmingly from contributions in the upper chromosphere. For stronger beams the WL signatures will form at greater depths, towards the photosphere and travel down rapidly under the influence of the hydrodynamic shocks that form as a result of the beam electron injection.

(8.3) The models using the CEA presented here are easily able to explain the heights

of HXR and WL signatures observed close to the photospheric heights in observations of limb flares (Martínez Oliveros et al., 2012; Krucker et al., 2015). This is not true for the other available codes, which use the FCA to beam propagation.

(8.4) The intensities of emission in the Balmer continuum are in reasonable agreement with those observed using IRIS (Heinzel and Kleint, 2014), and are comparable with the intensities produced using simulation with FLARIX (Varady et al., 2010; Heinzel et al., 2016).

8.4 Notes

Much of the work in this chapter is taken from the published paper Druett and Zharkova, 2018, and was completed in collaboration between Prof. Valentina Zharkova and I.

Chapter 9

Conclusions

9.1 Contributions to knowledge

This work presents 1D fully non-LTE radiative models of the responses of hydrogen in the solar atmosphere to injections of non-thermal electron beams, using the CEA to the precipitation of a beam. Therefore, the "HYDRO2GEN" code provides an alternative to the other available codes that rely upon the FCA. Moreover, we consider ionisation from all the excited states of hydrogen in our model, which is seen to be non-negligible in the chromosphere from the beam ionisation rates in Fig. 3.1, panels c and d. This is something that is neglected by the alternative codes currently available.

Using this approach the following conclusions have been derived:

(4.1) The Lyman lines are highly optically thick in the upper chromosphere for all of the simulations. The reductions in optical depth resulting from excitation and ionisation of electrons from the ground state hydrogen caused by collisions with non-thermal beam electrons are negligible when considering the formation regions of these lines. This is also true for the Lyman continuum, which is the only optically thick hydrogen continuum in each of the simulations.

(4.2) Ionisation of the hydrogen atoms by collisions with the non-thermal beam electrons acts to reduce the optical thickness of the Balmer lines. The excitation of electrons to level 2 of hydrogen through collisions with the beam particles acts to increase the optical thickness. This results in Balmer lines becoming optically thinner at the top of the chromosphere during the impulsive phase,

where the ionisation dominates, and simultaneously optically thicker in the lower chromosphere where the excitation dominates.

(4.3) The excitation of electrons to level 3 of hydrogen, by collisions with the non-thermal beam electrons, has a greater influence in increasing the optical thickness of Paschen lines during the impulsive phase than depopulation, by ionisation, has in reducing the optical thickness. Therefore the Paschen lines become optically thick in the chromosphere during the impulsive phase of a flare for beams with high initial fluxes, such as the F11 and F12 models.

(5.1) We predict that the Lyman lines will show an impulsive phase enhancement in the flaring foot-points of the loops due to excitation of the plasma by collisions with the non-thermal electron beam producing the HXR signal.

(5.2) The Lyman line profiles can be used to understand the conditions at the top of the flaring chromosphere. Red-shifted emission will be evident during in the impulsive phase, and blue-shifted emission will occur around 20-80 seconds later, depending on the parameters of the injected beam.

(5.3) Lyman continuum emission shows long lasting enhancement that begins with the onset of the non-thermal HXR as a result of the trapping of optically thick Lyman continuum radiation. The profile of the continuum enhancement shows a lower gradient during the impulsive phase, than in the gradual phase as a result of the higher energy and higher temperature emission at these times.

(5.4) This work addresses the lack of predictions from models, regarding the forthcoming missions that will provide high resolution observations of the Lyman lines and continuum. This was highlighted in point **1** of section 1.3 and discussed in sections 1.1.3, and 1.2.4.

(6.1) Excitation by non-thermal beam electrons increases emission in the Balmer and Paschen lines during the impulsive phase of solar flares. The emission in these lines is simultaneously broadened by the heating of the plasma caused by the beam and the Stark effect due to the ionisation by the beam electrons

(6.2) The magnitudes of Doppler shifts in the spectral line profiles indicate the macro-velocities of the shocks when they pass through the formation regions of a

given spectral line. The lines formed at deeper atmospheric depths than Hα, such as the Hγ or Pα lines, have a smaller proportion of their core emission being red-shifted in the impulsive phase (Fig.6.5b). By comparing the Hα, Hβ and Hγ line profiles observed with a high cadence, the propagation of the hydrodynamic shocks caused by the beam can be tracked through the flaring chromosphere (Fig.6.5).

(6.3) The time delay between a beam onset and the hydrodynamic shocks entering the formation regions of hydrogen lines is much shorter for the beams with greater initial fluxes, because the beams with higher initial fluxes produce shocks with larger downward macro-velocities (section 6.1.2).

(6.4) The shocks take longer to reach the formation regions of the Balmer and Paschen lines than the Lyman lines, because they are formed at greater column depths in the atmospheres.

(6.5) In contrast to the Lyman lines, the Balmer and Paschen lines contain very little blue shifted emission until around 100s of the simulation, because evaporation occurs only from the top of the chromosphere and in the transition region.

(6.6) In our F10 model the downward chromospheric shocks produce red wing enhancement in the Hα profiles with a 1 Å Doppler shift at the very first 5 s after a beam onset (our Fig.4b). This is a much greater Doppler shift than is simulated by models using the FCA for a similar flux. Moreover (Allred et al., 2005), Allred et al. (2005)'s F11 model allowed them to obtain a downward velocity only of 40 km·s^{-1}, while our F11 model produces the downward velocities up to 200 km·s^{-1}, providing the red-shift up to 3Å in Hα line profiles, similar to those reported from observations Ichimoto and Kurokawa (1984) and Wuelser and Marti (1989).

(6.7) The Pashen emission in a flaring chromosphere is also strongly affected by electron beams. Non-thermal excitation causes the Paschen Pα and Pβ line cores to become highly optically thick in the middle of the chromosphere (Figs.4.1c & 4.2b) for the beams with larger initial fluxes (F11 and F12 models). For the F10 model the lines are formed throughout the lower chromosphere.

As a result, in our simulations there is a great red wing excess occurring at the peak of beam fluxes as shown in the Pα line for the F11 and F12 models, whereas only a small proportion of the Paschen Pα core emission was red shifted in the F10 model (Fig.6.6).

(7.1) The simulated Hα emission in the F10 HYDRO2GEN model is shown to closely match the emission observed in an Hα kernel in the impulsive phase of the C1.5-class flare on 30^{th} June 2013. The match is close in terms of the shape of the profile, the 1Å red-shifted emission, and the ratio of red and blue wing intensities. There is also reasonable agreement between the simulated and observed profiles after the beam is switched off.

(7.2) The beam parameters in the simulation were matched to those suggested using RHESSI observations for the C1.5-class flare on 30^{th} June 2013, and strongly support the interpretation that the highly red-shifted Hα emission observed during the impulsive phases of solar flares is caused by the injection from the corona of a non-thermal electron beam with a power-law energy distribution.

(7.3) Upward motion of plasma was detected above the location of the observed Hα profiles in the C1.5-class flare on 30^{th} June 2013, as a coronal jet in the AIA 171 channel. This emission showed agreement with the simulated AIA emission, and provides additional confirmation of the speed ($\sim$ 93km·s^{-1}) and temperature ($\sim$ $1MK$) and timing of the evaporation predicted by the F10 model.

(8.1) The non-thermal collisions with beam electrons control the hydrogen ionisation rates in the chromosphere during the impulsive phase of a solar flare. The Balmer continuum is most effectively enhanced at this time because the Balmer continuum radiation forms effectively and escapes over the depths in which the ionisation occurs.

(8.2) Non-thermal ionisation is a much more effective method for the production of white light signatures than thermal emission or temperature increase, and the emission will begin co-temporally with the onset of the beam. For weaker beams (F10 model) this source originates overwhelmingly from contributions

in the upper chromosphere. For stronger beams the WL signatures will form at greater depths, towards the photosphere and travel down rapidly under the influence of the hydrodynamic shocks that form as a result of the beam electron injection.

(8.3) The models using the CEA presented here are easily able to explain the heights of HXR and WL signatures observed close to the photospheric heights in observations of limb flares (Martínez Oliveros et al., 2012; Krucker et al., 2015). This is not true for the other available codes, which use the FCA to beam propagation.

(8.4) The intensities of emission in the Balmer continuum are in reasonable agreement with those observed using IRIS (Heinzel and Kleint, 2014), and are comparable with the intensities produced using simulation with FLARIX (Varady et al., 2010; Heinzel et al., 2016).

In section 1.3 a number of unresolved issues associated with solar flares were outlined, here we reflect on how this work has address the points raised, and provided an original contribution to knowledge:

(1) The lack of high-resolution observations of Lyman line emission profiles in solar flares and the resulting scarcity of comprehensive studies of these emission profiles is problematic in light of the planned missions that will observe Lyman line emission profiles during solar flares (see sections 1.1.3, and 1.2.4).

(findings) This is addressed by the points **5.1** to **5.4**. A thorough investigation of the modelling of Lyman line emission in solar flares is presented and observable predictions provided.

(2) There is no clear explanation and interpretation of the large red-shifted (1-4Å in Hα) emission in chromospheric line profiles observed during the onsets of solar flares and lasting up to a few minutes (see section 1.1.4).

(3) There are difficulties observing the large red-shifted chromospheric emission resulting from the narrow wavelength windows used in modern spectroscopic observations of Hα (see section 1.1.4).

(findings) The second and third issues are comprehensively addressed by points **6.1** to **6.7** and **7.1** to **7.3**. This work provides the interpretation of large red-shifted emission in the line profiles of chromospheric lines during the impulsive phase of solar flares and effectively highlights the need for wider spectral windows for observations of the Hα line during solar flares.

(4) There is no consistent explanation and modelling that replicates the height and intensity of WL emission observed in the impulsive phase, located at heights close to the photosphere and lasting for minutes after the impulsive phase (see section 1.1.5).

(findings) This has been addressed by points **8.1** to **8.4**, in which simulations were shown to reproduce the observed intensities, timings and heights of the WL and continuous emissions observed during the impulsive phase of solar flares. Non-thermal beams of energetic electrons are shown to be very effective agents for the production of such emission.

(5) As yet there is not clear evidence of the triggering mechanisms responsible for the seismic responses of the Sun associated with solar flares (see section 1.1.6).

(findings) The hydrodynamic models used in this work show that beams of electrons are capable of creating high velocity hydrodynamic shocks in the solar chromosphere that travel to photospheric heights. If a shock reaches the photosphere with speeds greater than the local sound speed then it will generate a seismic response. This work provides the radiative response that would be expected in such an atmosphere and, thus, could provide confirmation of the triggering of a seismic response in flare observations (point **6.2**). Because the required simultaneous spectral line observations were not available at the time of writing, the proposed method remains to be realised by observations, but could be employed using data from the SST in the near future.

9.2 Applications and extensions

Let us highlight some of the numerous extensions of this work that would provide additional insight into solar flares.

Firstly, there are immediate opportunities for observational studies to investigate the further predictions of this work. For example the downward motion of WL signatures that should be visible in high-resolution observations of limb flares using instruments such as CHROMIS at SST (point **8.2**). The predictions of observables in the hydrogen lines can also be investigated, such as the tracking of shocks passing through the chromosphere by simultaneous observations of lines in the Balmer series, or detecting shifts in the formation heights of Paschen lines during the impulsive phase of solar flares (point **6.2**).

Secondly, there is the potential to extend the code. One could simulate the emission from other elements, providing further diagnostics of the flaring atmosphere using observations from a wider variety of instruments. Additionally one could look towards simulating a response with greater consideration of the structure of the plasma surrounding the 1D flux tube as well as energy transfer between the surroundings and the flux tube. Moreover, future investigations could provide greater flexibility regarding the time profile of beam injected into the plasma, or investigate the effects of varying the pitch angle of the flux tube to the vertical. One could expand the code to include the response of hydrogen to mixed beams of protons and electrons.

Thirdly, this work provides the radiative response that could track the propagation of a hydrodynamic shock to the photosphere and, thus, provide confirmation of the triggering of a seismic response in flare observations.

Therefore, in closing, this work has provided new insights into the responses of the solar atmosphere to the injections of energetic electron beams, as well as providing the ground work for future studies in the field.

Bibliography

Abbett, W. P. and S. L. Hawley (1999). "Dynamic Models of Optical Emission in Impulsive Solar Flares". In: *ApJ* 521, pp. 906–919. DOI: 10.1086/307576.

Aboudarham, J. and J. C. Henoux (1986). "Non-thermal excitation and ionization of hydrogen in solar flares. I - Effects on a flaring chromosphere". In: *A&A* 168, pp. 301–307.

— (1987). "Non-thermal excitation and ionization of hydrogen in solar flares. II - Effects on the temperature minimum region Energy balance and white light flares". In: *A&A* 174, pp. 270–274.

— (1989). "Electron beam as origin of white-light solar flares". In: *Sol. Phys.* 121, pp. 19–30. DOI: 10.1007/BF00161685.

Acton, L. W. et al. (1963). "Observations of Solar X-Ray Emission in the 8 to 20 A Band". In: *J. Geophys. Res.* 68, pp. 3335–3344. DOI: 10.1029/JZ068i011p03335.

Alfvén, H. and P. Carlqvist (1967). "Currents in the Solar Atmosphere and a Theory of Solar Flares". In: *Sol. Phys.* 1, pp. 220–228. DOI: 10.1007/BF00150857.

Allen, K. W. (1977). *Astrophysical quantities.*

Allred, J. C. et al. (2005). "Radiative Hydrodynamic Models of the Optical and Ultraviolet Emission from Solar Flares". In: *ApJ* 630, pp. 573–586. DOI: 10.1086/431751.

Anderson, K. A. and J. R. Winckler (1962). "Solar Flare X-Ray Burst on September 28, 1961". In: *J. Geophys. Res.* 67, pp. 4103–4117. DOI: 10.1029/JZ067i011p04103.

Antiochos, S. K. (1980). "Radiative-dominated cooling of the flare corona and transition region". In: *ApJ* 241, pp. 385–393. DOI: 10.1086/158351.

Antonucci, E. and B. R. Dennis (1983). "Observation of chromospheric evaporation during the Solar Maximum Mission". In: *Sol. Phys.* 86, pp. 67–76. DOI: 10.1007/BF00157175.

Antonucci, E., M. A. Dodero, and R. Martin (1990a). "Velocity-temperature distribution in the evaporating plasma during the impulsive phase of solar flares". In: *ApJS* 73, pp. 147–158. DOI: 10.1086/191446.

— (1990b). "Velocity-Temperature Distribution in the Evaporating Plasma during the Impulsive Phase of Solar Flares: Erratum". In: *ApJS* 74, p. 830. DOI: 10.1086/191520.

Antonucci, E. et al. (1982). "Impulsive phase of flares in soft X-ray emission". In: *Sol. Phys.* 78, pp. 107–123. DOI: 10.1007/BF00151147.

Arnoldy, R. L., S. R. Kane, and J. R. Winckler (1968). "Energetic Solar Flare X-Rays Observed by Satellite and Their Correlation with Solar Radio and Energetic Particle Emission". In: *ApJ* 151, p. 711. DOI: 10.1086/149470.

Aschwanden, M. J. (2004). "Pulsed Particle Injection in a Reconnection-Driven Dynamic Trap Model in Solar Flares". In: *ApJ* 608, pp. 554–561. DOI: 10.1086/392494.

— (2007). "RHESSI Timing Studies: Multithermal Delays". In: *ApJ* 661, pp. 1242–1259. DOI: 10.1086/516814.

Bai, T. and P. A. Sturrock (1989). "Classification of solar flares". In: *ARA&A* 27, pp. 421–467. DOI: 10.1146/annurev.aa.27.090189.002225.

Bamba, Y. et al. (2017). "Study on Precursor Activity of the X1.6 Flare in the Great AR 12192 with SDO, IRIS, and Hinode". In: *ApJ* 840, 116, p. 116. DOI: 10.3847/1538-4357/aa6dfe. arXiv: 1704.05158 [astro-ph.SR].

Battaglia, M. and A. O. Benz (2006). "Relations between concurrent hard X-ray sources in solar flares". In: *A&A* 456, pp. 751–760. DOI: 10.1051/0004-6361:20065233. eprint: astro-ph/0606353.

Battaglia, M. and E. P. Kontar (2011). "Height structure of X-ray, EUV, and white-light emission in a solar flare". In: *A&A* 533, L2, p. L2. DOI: 10.1051/0004-6361/201117605. arXiv: 1107.3808 [astro-ph.SR].

Battaglia, M. et al. (2015). "How Important Are Electron Beams in Driving Chromospheric Evaporation in the 2014 March 29 Flare?" In: *ApJ* 813, 113, p. 113. DOI: 10.1088/0004-637X/813/2/113. arXiv: 1509.09186 [astro-ph.SR].

Benz, A. O. (1977). "Spectral features in solar hard X-ray and radio events and particle acceleration". In: *ApJ* 211, pp. 270–280. DOI: 10.1086/154928.

Boerner, P. et al. (2012). "Initial Calibration of the Atmospheric Imaging Assembly (AIA) on the Solar Dynamics Observatory (SDO)". In: *Sol. Phys.* 275, pp. 41–66. DOI: 10.1007/s11207-011-9804-8.

Bradshaw, S. J. and P. J. Cargill (2006). "Explosive heating of low-density coronal plasma". In: *A&A* 458, pp. 987–995. DOI: 10.1051/0004-6361:20065691.

Brosius, J. W., A. N. Daw, and A. R. Inglis (2016). "Quasi-periodic Fluctuations and Chromospheric Evaporation in a Solar Flare Ribbon Observed by Hinode/EIS, IRIS, and RHESSI". In: *ApJ* 830, 101, p. 101. DOI: 10.3847/0004-637X/830/2/101.

Brown, J. C. (1971). "The Deduction of Energy Spectra of Non-Thermal Electrons in Flares from the Observed Dynamic Spectra of Hard X-Ray Bursts". In: *Sol. Phys.* 18, pp. 489–502. DOI: 10.1007/BF00149070.

— (1973). "Thick Target X-Ray Bremsstrahlung from Partially Ionised Targets in Solar Falres". In: *Sol. Phys.* 28, pp. 151–158. DOI: 10.1007/BF00152919.

Brown, J. C. and J. M. Loran (1985). "Possible evidence for stochastic acceleration of electrons in solar hard X-ray bursts observed by SMM". In: *MNRAS* 212, pp. 245–255. DOI: 10.1093/mnras/212.2.245.

Brown, S. A., L. Fletcher, and N. Labrosse (2016). "Doppler speeds of the hydrogen Lyman lines in solar flares from EVE". In: *A&A* 596, A51, A51. DOI: 10.1051/0004-6361/201628390. arXiv: 1610.04007 [astro-ph.SR].

Byram, E. T. et al. (1953). "Lyman-Alpha Radiation in the Solar Spectrum". In: *Physical Review* 91, pp. 1278–1279. DOI: 10.1103/PhysRev.91.1278.

Cameron, R. and I. Sammis (1999). "Tangential Field Changes in the Great Flare of 1990 May 24". In: *ApJ* 525, pp. L61–L64. DOI: 10.1086/312328.

Canfield, R. C. and R. G. Athay (1974). "Theoretical Chromospheric Flare Spectra. I: Hydrogen Equilibrium for the Kinematic Flare-Shock Models of Nakagawa et al. (1973)". In: *Sol. Phys.* 34, pp. 193–206. DOI: 10.1007/BF00149612.

Canfield, R. C. and K. G. Gayley (1987). "Impulsive H-alpha diagnostics of electron-beam-heated solar flare model chromospheres". In: *ApJ* 322, pp. 999–1009. DOI: 10.1086/165795.

Canfield, R. C., T. A. Gunkler, and P. J. Ricchiazzi (1984). "The H-alpha spectral signatures of solar flare nonthermal electrons, conductive flux, and coronal pressure". In: *ApJ* 282, pp. 296–307. DOI: 10.1086/162203.

Canfield, R. C. and R. C. Puetter (1981). "Theoretical quasar emission line ratios. I - Transfer and escape of radiation. II - Hydrogen L-alpha, Balmer, and Paschen lines, and the Balmer continuum". In: *ApJ* 243, pp. 381–403. DOI: 10.1086/158605.

Canfield, R. C., R. C. Puetter, and P. J. Ricchiazzi (1981). "The Lyman-alpha/H-alpha ratio in solar flares and quasars". In: *ApJ* 249, pp. 383–389. DOI: 10.1086/159295.

Canfield, R. C. and M. E. van Hoosier (1980). "Observed L-alpha profiles for two solar flares - 14:12 UT 15 June, 1973 and 23:16 UT 21 January, 1974". In: *Sol. Phys.* 67, pp. 339–350. DOI: 10.1007/BF00149811.

Canfield, R. C. et al. (1990). "H-alpha spectra of dynamic chromospheric processes in five well-observed X-ray flares". In: *ApJ* 363, pp. 318–325. DOI: 10.1086/169345.

Carlsson, M. and R. F. Stein (1992). "Non-LTE radiating acoustic shocks and CA II K2V bright points". In: *ApJ* 397, pp. L59–L62. DOI: 10.1086/186544.

Chubb, T. A. et al. (1957). "Rocket Observation of X-Ray Emission in a Solar Flare". In: *Nature* 179, pp. 861–862. DOI: 10.1038/179861a0.

Chupp, E. L. et al. (1973). "Solar Gamma Ray Lines observed during the Solar Activity of August 2 to August 11, 1972". In: *Nature* 241, pp. 333–335. DOI: 10.1038/241333a0.

Cody, W. J., Kathleen A. Paciorek, and Henry C. Thacher, Jr. (1970). "Chebyshev Approximations for Dawson's Integral". In: *Mathematics of Computation* 24.109, pp. 171–178. ISSN: 0025-5718 (print), 1088-6842 (electronic).

Cox, D. P. and W. H. Tucker (1969). "Ionization Equilibrium and Radiative Cooling of a Low-Density Plasma". In: *ApJ* 157, p. 1157. DOI: 10.1086/150144.

Craig, I. J. D. and A. N. McClymont (1976). "Mass motions in a heated flare filament". In: *Sol. Phys.* 50, pp. 133–151. DOI: 10.1007/BF00206198.

Craig, I. J. D., A. N. McClymont, and J. H. Underwood (1978). "The Temperature and Density Structure of Active Region Coronal Loops". In: *A&A* 70, p. 1.

Culhane, J. L. et al. (1992). "Observations of several small flares with the Bragg Crystal Spectrometer on YOHKOH". In: *PASJ* 44, pp. L101–L106.

de la Cruz Rodríguez, J. et al. (2015). "CRISPRED: A data pipeline for the CRISP imaging spectropolarimeter". In: *A&A* 573, A40, A40. DOI: 10.1051/0004-6361/201424319.

De Pontieu, B. et al. (2014). "The Interface Region Imaging Spectrograph (IRIS)". In: 289, pp. 2733–2779. DOI: 10.1007/s11207-014-0485-y.

Del Zanna, G. (2008). "Flare lines in Hinode EIS spectra". In: *A&A* 481, pp. L69–L72. DOI: 10.1051/0004-6361:20079033.

Del Zanna, G. and T. N. Woods (2013). "Spectral diagnostics with the SDO EVE flare lines". In: *A&A* 555, A59, A59. DOI: 10.1051/0004-6361/201220988.

Deng, N. et al. (2013). "High-cadence and High-resolution Hα Imaging Spectroscopy of a Circular Flare's Remote Ribbon with IBIS". In: *ApJ* 769, 112, p. 112. DOI: 10.1088/0004-637X/769/2/112. arXiv: 1304.4171 [astro-ph.SR].

Ding, M. D. and H. Schleicher (1997). "Lyman continuum as a diagnostic for non-thermal processes in solar flares." In: *A&A* 322, pp. 674–678.

Dobranskis, R. R. and V. V. Zharkova (2015). "Updated analytical solutions of continuity equation for electron beams precipitation - I. Pure collisional and pure ohmic energy losses". In: *MNRAS* 453, pp. 229–241. DOI: 10.1093/mnras/stv1571.

Dodson, H. W., E. R. Hedeman, and R. R. McMath (1956). "Photometry of Solar Flares." In: *ApJS* 2, p. 241. DOI: 10.1086/190027.

Donea, A. (2011). "Seismic Transients from Flares in Solar Cycle 23". In: *Space Sci. Rev.* 158, pp. 451–469. DOI: 10.1007/s11214-011-9787-7.

Donea, A.-C. and C. Lindsey (2005). "Seismic Emission from the Solar Flares of 2003 October 28 and 29". In: *ApJ* 630, pp. 1168–1183. DOI: 10.1086/432155.

Donea, A.-C. et al. (2006). "Seismic Emission from A M9.5-Class Solar Flare". In: *Sol. Phys.* 239, pp. 113–135. DOI: 10.1007/s11207-006-0108-3.

Donnelly, R. F. (1967). "The Solar Flare Radiations Responsible for Sudden Frequency Deviations". In: *J. Geophys. Res.* 72, p. 5247. DOI: 10.1029/JZ072i021p05247.

Donnelly, R. F. (1968). "The X-Ray and Extreme Ultraviolet Radiation of the August 28, 1966 Proton Flare as Deduced from Sudden Ionospheric Disturbance Data". In: *Sol. Phys.* 5, pp. 123–126. DOI: 10.1007/BF00147126.

Druett, M. and V. Zharkova (2018). "HYDRO2GEN: Non-thermal hydrogen Balmer and Paschen emission in solar flares generated by electron beams". In: *A&A* 610, p. 68. DOI: https://doi.org/10.1051/0004-6361/201731053.

Druett, M. et al. (2017). "Beam electrons as a source of Hα flare ribbons". In: *Nature Communications* 8, 15905, p. 15905. DOI: 10.1038/ncomms15905.

Duijveman, A., B. V. Somov, and A. R. Spektor (1983). "Evolution of a flaring loop after injection of energetic electrons". In: *Sol. Phys.* 88, pp. 257–273. DOI: 10.1007/BF00196191.

Emslie, A. G. (1978). "The collisional interaction of a beam of charged particles with a hydrogen target of arbitrary ionization level". In: *ApJ* 224, pp. 241–246. DOI: 10.1086/156371.

— (1981). "On the importance of reverse current ohmic losses in electron-heated solar flare atmospheres". In: *ApJ* 249, pp. 817–820. DOI: 10.1086/159339.

Emslie, A. G. et al. (2003). "RHESSI Hard X-Ray Imaging Spectroscopy of the Large Gamma-Ray Flare of 2002 July 23". In: *ApJ* 595, pp. L107–L110. DOI: 10.1086/378931.

Falchi, A. and P. J. D. Mauas (2002). "Chromospheric models of a solar flare including velocity fields". In: *A&A* 387, pp. 678–686. DOI: 10.1051/0004-6361:20020454.

Finn, G. D. and D. Mugglestone (1965). "Tables of the line broadening function H(a,v)". In: *MNRAS* 129, p. 221. DOI: 10.1093/mnras/129.2.221.

Fisher, G. H., R. C. Canfield, and A. N. McClymont (1985). "Flare loop radiative hydrodynamics. V - Response to thick-target heating. VI - Chromospheric evaporation due to heating by nonthermal electrons. VII - Dynamics of the thick-target heated chromosphere". In: *ApJ* 289, pp. 414–441. DOI: 10.1086/162901.

Fisher, G. H. et al. (2012). "Global Forces in Eruptive Solar Flares: The Lorentz Force Acting on the Solar Atmosphere and the Solar Interior". In: *Sol. Phys.* 277, pp. 59–76. DOI: 10.1007/s11207-011-9907-2. arXiv: 1006.5247 [astro-ph.SR].

Fletcher, L. and H. S. Hudson (2002). "Spectral and Spatial Variations of Flare Hard X-ray Footpoints". In: *Sol. Phys.* 210, pp. 307–321. DOI: 10.1023/A:1022479610710.

— (2008). "Impulsive Phase Flare Energy Transport by Large-Scale Alfvén Waves and the Electron Acceleration Problem". In: *ApJ* 675, 1645-1655, pp. 1645–1655. DOI: 10.1086/527044. arXiv: 0712.3452.

Fletcher, L. et al. (2011). "An Observational Overview of Solar Flares". In: *Space Sci. Rev.* 159, pp. 19–106. DOI: 10.1007/s11214-010-9701-8. arXiv: 1109.5932 [astro-ph.SR].

Fontenla, J. M. et al. (2009). "Semiempirical Models of the Solar Atmosphere. III. Set of Non-LTE Models for Far-Ultraviolet/Extreme-Ultraviolet Irradiance Computation". In: *ApJ* 707, pp. 482–502. DOI: 10.1088/0004-637X/707/1/482.

Frost, K. J. (1969). "Rapid Fine Structure in a Burst of Hard Solar X-Rays Observed by OSO-5". In: *ApJ* 158, p. L159. DOI: 10.1086/180455.

Glencross, W. M. (1973). "Continuous Energy Injection at Numerous Bright Points During Soft X-Ray Flare Enhancement". In: *Sol. Phys.* 29, pp. 429–439. DOI: 10.1007/BF00150823.

Gordovskyy, M. et al. (2005). "Proton versus electron heating in solar flares". In: *Advances in Space Research* 35, pp. 1743–1751. DOI: 10.1016/j.asr.2005.07.004.

Graham, D. R. and G. Cauzzi (2015). "Temporal Evolution of Multiple Evaporating Ribbon Sources in a Solar Flare". In: *ApJ* 807, L22, p. L22. DOI: 10.1088/2041-8205/807/2/L22.

Grigis, P. C. and A. O. Benz (2004). "The spectral evolution of impulsive solar X-ray flares". In: *A&A* 426, pp. 1093–1101. DOI: 10.1051/0004-6361:20041367. eprint: astro-ph/0407431.

— (2008). "Spectral Hardening in Large Solar Flares". In: *ApJ* 683, 1180-1191, pp. 1180–1191. DOI: 10.1086/589826. arXiv: 0708.2472.

Hall, L. A. (1971). "Solar Flares in the Extreme Ultraviolet". In: *Sol. Phys.* 21, pp. 167–175. DOI: 10.1007/BF00155787.

Hallam, K. L. (1964). "Solar Flares in the Light of Hydrogen Lyman-Alpha". In: *NASA Special Publication* 50, p. 63.

Harris III, D. L. (1948). "On the Line-Absorption Coefficient due to Doppler Effect and Damping." In: *ApJ* 108, p. 112. DOI: 10.1086/145047.

Harvey, K. L. (1971). "The Explosive Phase of Solar Flares". In: *Sol. Phys.* 16, pp. 423–430. DOI: 10.1007/BF00162485.

Harvey, K. L., F. Tang, and V. Gaizauskas (1986). "The association of chromospheric and coronal phenomena with the evolution of the quiet sun magnetic fields". In: *NASA Conference Publication*. Ed. by A. I. Poland. Vol. 2442. NASA Conference Publication.

Heinzel, P. and L. Kleint (2014). "Hydrogen Balmer Continuum in Solar Flares Detected by the Interface Region Imaging Spectrograph (IRIS)". In: *ApJ* 794, L23, p. L23. DOI: 10.1088/2041-8205/794/2/L23.

Heinzel, P. et al. (1994). "Chromospheric and transition-region heating phenomena: coordinated GBO and SOHO observations". In: *Solar Dynamic Phenomena and Solar Wind Consequences, the Third SOHO Workshop*. Ed. by J. J. Hunt. Vol. 373. ESA Special Publication, p. 369.

Heinzel, P. et al. (2016). "Numerical RHD simulations of flaring chromosphere with Flarix". In: *ArXiv e-prints*. arXiv: 1602.00016 [astro-ph.SR].

Hiei, E. (1987). "Review of optical observations of solar flares". In: *Sol. Phys.* 113, pp. 249–256. DOI: 10.1007/BF00147705.

Holman, G. D. et al. (2003). "Electron Bremsstrahlung Hard X-Ray Spectra, Electron Distributions, and Energetics in the 2002 July 23 Solar Flare". In: *ApJ* 595, pp. L97–L101. DOI: 10.1086/378488.

Holman, G. D. et al. (2011). "Implications of X-ray Observations for Electron Acceleration and Propagation in Solar Flares". In: *Space Sci. Rev.* 159, pp. 107–166. DOI: 10.1007/s11214-010-9680-9. arXiv: 1109.6496 [astro-ph.SR].

Holt, S. S. and T. L. Cline (1968). "On the Generation of Synchrotron and X-Ray Emission from Electrons with Energy Below mc^{2} in Solar Flares". In: *ApJ* 154, p. 1027. DOI: 10.1086/149823.

Holt, S. S. and R. Ramaty (1969). "Microwave and Hard X-Ray Bursts from Solar Flares". In: *Sol. Phys.* 8, pp. 119–141. DOI: 10.1007/BF00150663.

Hudson, H. S. (1972). "Thick-Target Processes and White-Light Flares". In: *Sol. Phys.* 24, pp. 414–428. DOI: 10.1007/BF00153384.

Hudson, H. S. and F. Fárník (2002). "Spectral variations of flare hard X-rays". In: *Solar Variability: From Core to Outer Frontiers*. Ed. by A. Wilson. Vol. 506. ESA Special Publication, pp. 261–264.

Hudson, H. S., G. H. Fisher, and B. T. Welsch (2008). "Flare Energy and Magnetic Field Variations". In: *Subsurface and Atmospheric Influences on Solar Activity*. Ed. by R. Howe et al. Vol. 383. Astronomical Society of the Pacific Conference Series, p. 221.

Hudson, H. S. et al. (1992). "White-light flares observed by YOHKOH". In: *PASJ* 44, pp. L77–L81.

Hurford, G. J. et al. (2003). "First Gamma-Ray Images of a Solar Flare". In: *ApJ* 595, pp. L77–L80. DOI: 10.1086/378179.

Ichimoto, K. and H. Kurokawa (1984). "H-alpha red asymmetry of solar flares". In: *Sol. Phys.* 93, pp. 105–121. DOI: 10.1007/BF00156656.

Ivanov, V. V. and V. M. Serbin (1984). "The transfer of line radiation. I - General analysis of approximate solutions". In: *Soviet Ast.* 28, pp. 405–409.

Jess, D. B. et al. (2008). "Do All Flares Have White-Light Emission?" In: *ApJ* 688, L119, p. L119. DOI: 10.1086/595588. arXiv: 0810.1443.

Jin, M. and M. Ding (2008). "Loop-Like Hard X-Ray Emission in a 2005 January 20 Flare". In: *PASJ* 60, pp. 835–842. DOI: 10.1093/pasj/60.4.835.

Johnson, L. C. (1972). "Approximations for Collisional and Radiative Transition Rates in Atomic Hydrogen". In: *ApJ* 174, p. 227. DOI: 10.1086/151486.

Kaempfer, N. and A. Magun (1983). "Observed time delays between solar H-alpha flares and microwave bursts as evidence for various energy transport mechanisms". In: *ApJ* 274, pp. 910–915. DOI: 10.1086/161503.

Kahler, S. W. and R. W. Kreplin (1971). "The Observation of Nonthermal Solar X-Radiation in the Energy Range 3 $<$ E $<$ 10 KeV". In: *ApJ* 168, p. 531. DOI: 10.1086/151107.

Kane, S. R. (1973). "Acceleration of Electrons During the Flash Phase of Solar Flares". In: *International Cosmic Ray Conference* 2, p. 1607.

— (1974). "Impulsive /flash/ phase of solar flares - Hard X-ray, microwave, EUV and optical observations". In: *Coronal Disturbances*. Ed. by G. A. Newkirk. Vol. 57. IAU Symposium, pp. 105–141.

Kane, S. R. and R. F. Donnelly (1971). "Impulsive Hard X-Ray and Ultraviolet Emission during Solar Flares". In: *ApJ* 164, p. 151. DOI: 10.1086/150826.

Karlický, M. (2014). "Solar flares: radio and X-ray signatures of magnetic reconnection processes". In: *Research in Astronomy and Astrophysics* 14, 753-772, pp. 753–772. DOI: 10.1088/1674-4527/14/7/002.

Kelly, P. T. and W. A. Rense (1972). "Solar Flares in the EUV Observed from OSO-5". In: *Sol. Phys.* 26, pp. 431–440. DOI: 10.1007/BF00165285.

Kennedy, M. B. et al. (2015). "Radiative hydrodynamic modelling and observations of the X-class solar flare on 2011 March 9". In: *A&A* 578, A72, A72. DOI: 10.1051/0004-6361/201425144.

Kerr, G. S. et al. (2015). "IRIS observations of the Mg ii h and k lines during a solar flare". In: *A&A* 582, A50, A50. DOI: 10.1051/0004-6361/201526128. arXiv: 1508.03813 [astro-ph.SR].

Kerr, G. S. et al. (2016). "Simulations of the Mg II k and Ca II 8542 lines from an AlfvÉn Wave-heated Flare Chromosphere". In: *ApJ* 827, 101, p. 101. DOI: 10.3847/0004-637X/827/2/101. arXiv: 1605.05888 [astro-ph.SR].

Kleint, L. et al. (2014). "Detection of Supersonic Downflows and Associated Heating Events in the Transition Region above Sunspots". In: *ApJ* 789, L42, p. L42. DOI: 10.1088/2041-8205/789/2/L42.

Kleint, L. et al. (2016). "Continuum Enhancements in the Ultraviolet, the Visible and the Infrared during the X1 Flare on 2014 March 29". In: *ApJ* 816, 88, p. 88. DOI: 10.3847/0004-637X/816/2/88. arXiv: 1511.04161 [astro-ph.SR].

Kobylinskii, V. A. and V. V. Zharkova (1996). "Hydrogen H-alpha line emissions and radiative losses in the impulsive solar events". In: *Advances in Space Research* 17, pp. 129–. DOI: 10.1016/0273-1177(95)00554-R.

Kontar, E. P. and A. L. MacKinnon (2005). "Regularized Energy-Dependent Solar Flare Hard X-Ray Spectral Index". In: *Sol. Phys.* 227, pp. 299–310. DOI: 10.1007/s11207-005-1101-y. eprint: astro-ph/0506097.

Kontar, E. P. et al. (2011). "Deducing Electron Properties from Hard X-ray Observations". In: *Space Sci. Rev.* 159, 157, p.6, footnote. DOI: 10.1007/s11214-011-9804-x.

Kosovichev, A. G. (2006a). "Direct Observations of Acoustic Waves Excited by Solar Flares and their Propagation in Sunspot Regions". In: *Solar MHD Theory and Observations: A High Spatial Resolution Perspective*. Ed. by J. Leibacher, R. F. Stein, and H. Uitenbroek. Vol. 354. Astronomical Society of the Pacific Conference Series, p. 154.

— (2006b). "Properties of Flares-Generated Seismic Waves on the Sun". In: *Sol. Phys.* 238, pp. 1–11. DOI: 10.1007/s11207-006-0190-6.

Kosovichev, A. G. and V. V. Zharkova (1998). "X-ray flare sparks quake inside Sun". In: *Nature* 393, pp. 317–318. DOI: 10.1038/30629.

— (1999). "Variations of Photospheric Magnetic Field Associated with Flares and CMEs". In: *Sol. Phys.* 190, pp. 459–466. DOI: 10.1023/A:1005226802279.

— (2001). "Magnetic Energy Release and Transients in the Solar Flare of 2000 July 14". In: *ApJ* 550, pp. L105–L108. DOI: 10.1086/319484.

Kostiuk, N. D. and S. B. Pikelner (1974). "Gas dynamics of a flare region heated by a flux of high-velocity electrons". In: *AZh* 51, pp. 1002–1016.

Kotrč, P., O. Procházka, and P. Heinzel (2016). "New Observations of Balmer Continuum Flux in Solar Flares. Instrument Description and First Results". In: *Sol. Phys.* 291, pp. 779–789. DOI: 10.1007/s11207-016-0860-y. arXiv: 1601.04610 [astro-ph.SR].

Kowalski, A. F. et al. (2017). "The Atmospheric Response to High Nonthermal Electron Beam Fluxes in Solar Flares. I. Modeling the Brightest NUV Footpoints in the X1 Solar Flare of 2014 March 29". In: *ApJ* 836, 12, p. 12. DOI: 10.3847/1538-4357/836/1/12. arXiv: 1609.07390 [astro-ph.SR].

Kreplin, R. W., T. A. Chubb, and H. Friedmann (1962). "X-Ray and Lyman-Alpha Emission from the Sun as Measured from the NRL SR-1 Satellite". In: *J. Geophys. Res.* 67, pp. 2231–2253. DOI: 10.1029/JZ067i006p02231.

Krucker, S. et al. (2008). "Hard X-ray emission from the solar corona". In: *A&A Rev.* 16, pp. 155–208. DOI: 10.1007/s00159-008-0014-9.

Krucker, S. et al. (2015). "Co-Spatial White Light and Hard X-Ray Flare Footpoints Seen Above the Solar Limb". In: *ApJ* 802, 19, p. 19. DOI: 10.1088/0004-637X/802/1/19.

Kuridze, D. et al. (2015). "Hα Line Profile Asymmetries and the Chromospheric Flare Velocity Field". In: *ApJ* 813, 125, p. 125. DOI: 10.1088/0004-637X/813/2/125.

Kurokawa, H., T. Takakura, and K. Ohki (1988). "Close relationship between H-alpha and hard X-ray emissions at the impulsive phase of a solar flare". In: *PASJ* 40, pp. 357–367.

Kuznetzov, S. N. et al. (2006). "High-Energy Emission Measurements of the 20 January 2005 Solar Flare onboard CORONAS-F". In: *36th COSPAR Scientific Assembly*. Vol. 36. COSPAR Meeting.

Křivsky, L. and L. N. Kurochka (1974). "On Lyman's Emission of Solar Flares". In: *Bulletin of the Astronomical Institutes of Czechoslovakia* 25, p. 52.

Lemaire, P., M. Choucq-Bruston, and J.-C. Vial (1984). "Simultaneous H and K CA II, H and K MG II, L-alpha and L-beta H I profiles of the April 15, 1978 solar flare observed with the OSO-8/L.P.S.P. experiment". In: *Sol. Phys.* 90, pp. 63–82. DOI: 10.1007/BF00153785.

Lemaire, P. et al. (2004). "Flare observation of the Sun as a star by SUMER/SOHO in the hydrogen Lyman continuum". In: *A&A* 418, pp. 737–742. DOI: 10.1051/0004-6361:20034405.

Lemen, J. R. et al. (2011). "The Atmospheric Imaging Assembly (AIA) on the Solar Dynamics Observatory (SDO)". In: *Sol. Phys.* Pp. 241–+. DOI: 10.1007/s11207-011-9776-8.

Li, D., Z. J. Ning, and Q. M. Zhang (2015). "Observational Evidence of Electron-driven Evaporation in Two Solar Flares". In: *ApJ* 813, 59, p. 59. DOI: 10.1088/0004-637X/813/1/59. arXiv: 1509.07226 [astro-ph.SR].

Li, H. (2016). "The Lyman-α Solar Telescope (LST) for the ASO-S mission". In: *Solar and Stellar Flares and their Effects on Planets*. Ed. by A. G. Kosovichev, S. L. Hawley, and P. Heinzel. Vol. 320. IAU Symposium, pp. 436–438. DOI: 10.1017/S1743921316000533.

Li, Y. et al. (2017). "Imaging Observations of Magnetic Reconnection in a Solar Eruptive Flare". In: *ApJ* 835, 190, p. 190. DOI: 10.3847/1538-4357/835/2/190. arXiv: 1612.09417 [astro-ph.SR].

Lin, R. P., B. R. Dennis, and A. O. Benz, eds. (2003). *The Reuven Ramaty High-Energy Solar Spectroscopic Imager (RHESSI) - Mission Description and Early Results*.

Lin, R. P. and R. A. Schwartz (1987). "High spectral resolution measurements of a solar flare hard X-ray burst". In: *ApJ* 312, pp. 462–474. DOI: 10.1086/164891.

Lindsey, C. and D. C. Braun (2000). "Basic Principles of Solar Acoustic Holography - (Invited Review)". In: *Sol. Phys.* 192, pp. 261–284. DOI: 10.1023/A:1005227200911.

Litvinenko, Y. E. (1996). "Particle Acceleration in Reconnecting Current Sheets with a Nonzero Magnetic Field". In: *ApJ* 462, pp. 997–+. DOI: 10.1086/177213.

Liu, W. et al. (2015). "Mg ii Lines Observed During the X-class Flare on 29 March 2014 by the Interface Region Imaging Spectrograph". In: *Sol. Phys.* 290, pp. 3525–3543. DOI: 10.1007/s11207-015-0814-9. arXiv: 1511.00480 [astro-ph.SR].

Machado, M. E. and R. W. Noyes (1978). "Lyman continuum observations of solar flares". In: *Sol. Phys.* 59, pp. 129–140. DOI: 10.1007/BF00154936.

Martínez-Oliveros, J. C. and A.-C. Donea (2009). "Magnetic field variations and seismicity of solar active regions". In: *MNRAS* 395, pp. L39–L42. DOI: 10.1111/j.1745-3933.2009.00637.x. arXiv: 0902.3856 [astro-ph.SR].

Martínez Oliveros, J.-C. et al. (2012). "The Height of a White-light Flare and Its Hard X-Ray Sources". In: *ApJ* 753, L26, p. L26. DOI: 10.1088/2041-8205/753/2/L26. arXiv: 1206.0497 [astro-ph.SR].

Mason, H. E. et al. (1986). "Spectral line profiles of Fe XXI 1354.1 A from the Solar Maximum Mission". In: *ApJ* 309, pp. 435–448. DOI: 10.1086/164615.

Matthews, S. A., S. Zharkov, and V. V. Zharkova (2011). "Anatomy of a Solar Flare: Measurements of the 2006 December 14 X-class Flare with GONG, Hinode, and RHESSI". In: *ApJ* 739, p. 71. DOI: 10.1088/0004-637X/739/2/71.

Matthews, S. A. et al. (2015). "Spectroscopic Signatures Related to a Sunquake". In: *ApJ* 812, 35, p. 35. DOI: 10.1088/0004-637X/812/1/35. arXiv: 1508.07216 [astro-ph.SR].

Mauas, P. J. D. and D. O. Gómez (1997). "Fokker-Planck Description of Electron Beams in the Solar Chromosphere". In: *ApJ* 483, pp. 496–506.

McClymont, A. N. and R. C. Canfield (1983). "Flare loop radiative hydrodynamics. I - Basic methods". In: *ApJ* 265, pp. 483–506. DOI: 10.1086/160692.

McKenzie, D. L., D. W. Datlowe, and L. E. Peterson (1973). "Spectral Development of a Solar X-Ray Burst Observed on OSO-7". In: *Sol. Phys.* 28, pp. 175–185. DOI: 10.1007/BF00152922.

Meekins, J. F. et al. (1970). "Solar Soft X-Ray Flare Spectra from OSo-4". In: *Sol. Phys.* 13, pp. 198–212. DOI: 10.1007/BF00963952.

Meunier, N. and A. Kosovichev (2002). "Fast photospheric flows in a flaring active region". In: *SOLMAG 2002. Proceedings of the Magnetic Coupling of the Solar Atmosphere Euroconference*. Ed. by H. Sawaya-Lacoste. Vol. 505. ESA Special Publication, pp. 505–508.

Mihalas, D. (1978). *Stellar atmospheres /2nd edition/*.

Milligan, R. O. and P. C. Chamberlin (2016). "Anomalous temporal behaviour of broadband Lyα observations during solar flares from SDO/EVE". In: *A&A* 587, A123, A123. DOI: 10.1051/0004-6361/201526682.

Milligan, R. O. and B. R. Dennis (2009). "Velocity Characteristics of Evaporated Plasma Using Hinode/EUV Imaging Spectrometer". In: *ApJ* 699, pp. 968–975. DOI: 10.1088/0004-637X/699/2/968.

Milligan, R. O. et al. (2006a). "Observational Evidence of Gentle Chromospheric Evaporation during the Impulsive Phase of a Solar Flare". In: *ApJ* 642, pp. L169–L171. DOI: 10.1086/504592.

Milligan, R. O. et al. (2006b). "RHESSI and SOHO CDS Observations of Explosive Chromospheric Evaporation". In: *ApJ* 638, pp. L117–L120. DOI: 10.1086/500555.

Moore, R. L. and D. W. Datlowe (1975). "Heating and cooling of the thermal X-ray plasma in solar flares". In: *Sol. Phys.* 43, pp. 189–209. DOI: 10.1007/BF00155153.

Moore, R. L. et al. (1984). "Magnetic changes observed in a solar flare". In: *ApJ* 276, pp. 379–390. DOI: 10.1086/161622.

Moradi, H. et al. (2007). "Helioseismic analysis of the solar flare-induced sunquake of 2005 January 15". In: *MNRAS* 374, pp. 1155–1163. DOI: 10.1111/j.1365-2966.2006.11234.x. arXiv: 0704.3472.

Moreton, G. E. (1964). "The Association of Bremsstrahlung X Rays With Explosive Flares". In: *NASA Special Publication* 50, p. 209.

Morozhenko, N. N. (1983). "The spectral properties of filamentary and physical non-homogeneous prominences. III - The structure and stratification of physical conditions". In: *Astrometriia i Astrofizika* 48, pp. 16–25.

— (1984). "The spectral properties of fibrous physically inhomogeneous prominences. IV - Excitation and ionization of CA II". In: *Astrometriia i Astrofizika* 53, pp. 3–10.

Morozhenko, N. N. and V. V. Zharkova (1980). "Spectral features of filamentary and physically inhomogeneous prominences. I - Hydrogen /excitation/". In: *Astrometriia i Astrofizika* 41, pp. 3–11.

— (1982). "The spectral properties of filamentary, physically inhomogeneous prominences. II - Hydrogen (second level excitation, ionization)". In: *Astrometriia i Astrofizika* 47, pp. 34–41.

Mrozek, T., M. Tomczak, and S. Gburek (2007). "Solar impulsive EUV and UV brightenings in flare footpoints and their connection with X-ray emission". In: *A&A* 472, pp. 945–955. DOI: 10.1051/0004-6361:20077652.

Nagai, F. and A. G. Emslie (1984). "Gas dynamics in the impulsive phase of solar flares. I Thick-target heating by nonthermal electrons". In: *ApJ* 279, pp. 896–908. DOI: 10.1086/161960.

Neidig, D. F. and S. R. Kane (1993). "Energetics and timing of the hard and soft X-ray emissions in white light flares". In: *Sol. Phys.* 143, pp. 201–204. DOI: 10.1007/BF00619106.

Neidig, D. F. and P. H. Wiborg Jr. (1984). "The hydrogen emission spectrum in three white-light flares". In: *Sol. Phys.* 92, pp. 217–225. DOI: 10.1007/BF00157247.

Neupert, W. M. (1968). "Comparison of Solar X-Ray Line Emission with Microwave Emission during Flares". In: *ApJ* 153, p. L59. DOI: 10.1086/180220.

Neupert, W. M., R. J. Thomas, and R. D. Chapman (1974). "Spatial Distribution of Soft X-Ray and EUV Emission Associated with a Chromospheric Flare of Importance 1B on August 2, 1972". In: *Sol. Phys.* 34, pp. 349–375. DOI: 10.1007/BF00153673.

Parks, G. K. and J. R. Winckler (1969). "Simultaneous observations of 5- to 15-second period modulated energetic electron fluxes at the synchronous altitude and the auroral zone". In: *J. Geophys. Res.* 74, p. 4003. DOI: 10.1029/JA074i016p04003.

Patterson, A. and H. Zirin (1981). "Transient magnetic field changes in flares". In: *ApJ* 243, pp. L99–L101. DOI: 10.1086/183451.

Pesnell, W. D., B. J. Thompson, and P. C. Chamberlin (2012). "The Solar Dynamics Observatory (SDO)". In: *Sol. Phys.* 275, pp. 3–15. DOI: 10.1007/s11207-011-9841-3.

Peterson, L. E., D. W. Datlowe, and D. L. McKenzie (1973). "Thermal and Nonthermal X-ray Bursts Observed from OSO-7". In: *NASA Special Publication* 342, p. 132.

Petrie, G. J. D. (2012). "The Abrupt Changes in the Photospheric Magnetic and Lorentz Force Vectors during Six Major Neutral-line Flares". In: *ApJ* 759, 50, p. 50. DOI: 10.1088/0004-637X/759/1/50. arXiv: 1211.2210 [astro-ph.SR].

— (2013). "A Spatio-temporal Description of the Abrupt Changes in the Photospheric Magnetic and Lorentz-Force Vectors During the 15 February 2011 X2.2 Flare". In: *Sol. Phys.* 287, pp. 415–440. DOI: 10.1007/s11207-012-0071-0. arXiv: 1202.4192 [astro-ph.SR].

Petrie, G. J. D. and J. J. Sudol (2010). "Abrupt Longitudinal Magnetic Field Changes in Flaring Active Regions". In: *ApJ* 724, pp. 1218–1237. DOI: 10.1088/0004-637X/724/2/1218. arXiv: 1009.4656 [astro-ph.SR].

Petrosian, V. and P. A. Sturrock (1973). "A Model for Impulsive Solar X-Ray Bursts". In: *Bulletin of the American Astronomical Society*. Vol. 5. BAAS, p. 278.

Petschek, H. E. (1964). "Magnetic Field Annihilation". In: *NASA Special Publication* 50, p. 425.

Piana, M. et al. (2003). "Regularized Electron Flux Spectra in the 2002 July 23 Solar Flare". In: *ApJ* 595, pp. L127–L130. DOI: 10.1086/378171.

Pietenpol, W. B. et al. (1953). "Lyman Alpha-Line Photographed in the Sun's Spectrum". In: *Physical Review* 90, pp. 156–156. DOI: 10.1103/PhysRev.90.156.

Pintér, Š. (1970). "Limb flares associated with solar soft X-ray bursts". In: *Bulletin of the Astronomical Institutes of Czechoslovakia* 21, p. 241.

Polito, V. et al. (2016). "Simultaneous IRIS and Hinode/EIS Observations and Modelling of the 2014 October 27 X2.0 Class Flare". In: *ApJ* 816, 89, p. 89. DOI: 10.3847/0004-637X/816/2/89.

Polito, V. et al. (2017). "Analysis and modelling of recurrent solar flares observed with Hinode/EIS on March 9, 2012". In: *A&A* 601, A39, A39. DOI: 10.1051/0004-6361/201629703. arXiv: 1612.03504 [astro-ph.SR].

Priest, E. and T. Forbes (2000). "Magnetohydrodynamics". In: *Encyclopedia of Astronomy and Astrophysics*. Ed. by P. Murdin. DOI: 10.1888/0333750888/1983.

Régnier, S. and B. Fleck (2004). "Magnetic Field Evolution of AR 0486 Before and after the X17 Flare on October 28, 2003". In: *SOHO 15 Coronal Heating*. Ed. by R. W. Walsh et al. Vol. 575. ESA Special Publication, p. 519.

Reid, J. H. (1963). "Classification of Solar Flares". In: *Irish Astronomical Journal* 6, p. 45.

Ricchiazzi, P. J. and R. C. Canfield (1983). "A static model of chromospheric heating in solar flares". In: *ApJ* 272, pp. 739–755. DOI: 10.1086/161336.

Rubio da Costa, F. et al. (2009). "Observations of a solar flare and filament eruption in Lyman α and X-rays". In: *A&A* 507, pp. 1005–1014. DOI: 10.1051/0004-6361/200912651. arXiv: 0909.4705 [astro-ph.SR].

— (2010). "Integrated Ly-alpha intensity emission in ribbon flares". In: *Memorie della Societa Astronomica Italiana Supplementi* 14, p. 193.

Rubio da Costa, F. et al. (2012). "Solar flares in Halpha and Ly-alpha : observations vs simulations." In: *Memorie della Societa Astronomica Italiana Supplementi* 19, p. 117.

Rubio da Costa, F. et al. (2016). "Data-driven Radiative Hydrodynamic Modeling of the 2014 March 29 X1.0 Solar Flare". In: *ApJ* 827, 38, p. 38. DOI: 10.3847/0004-637X/827/1/38.

Rust, D. M. and F. Hegwer (1975). "Analysis of the August 7, 1972 white light flare - Light curves and correlation with hard X-rays". In: *Sol. Phys.* 40, pp. 141–157. DOI: 10.1007/BF00183158.

Rust, D. M. and S. L. Keil (1992). "A search for polarization in Ellerman bombs". In: *Sol. Phys.* 140, pp. 55–65. DOI: 10.1007/BF00148429.

Ryan, D. F. et al. (2012). "The Thermal Properties of Solar Flares over Three Solar Cycles Using GOES X-Ray Observations". In: *ApJS* 202, 11, p. 11. DOI: 10.1088/0067-0049/202/2/11.

Rybicki, G. B. (1984). "Escape probability methods". In: *Methods in Radiative Transfer*. Ed. by W. Kalkofen, pp. 21–64.

Sánchez-Andrade Nuño, B., K. G. Puschmann, and F. Kneer (2007). "Observations of a flaring active region in H[alpha]". In: *Modern solar facilities - advanced solar science*. Ed. by F. Kneer, K. G. Puschmann, and A. D. Wittmann, p. 273.

Scharmer, G. B. (2006). "Comments on the optimization of high resolution Fabry-Pérot filtergraphs". In: *A&A* 447, pp. 1111–1120. DOI: 10.1051/0004-6361:20052981.

Scharmer, G. B. et al. (2003). "Adaptive optics system for the new Swedish solar telescope". In: *Innovative Telescopes and Instrumentation for Solar Astrophysics*. Ed. by S. L. Keil and S. V. Avakyan. Vol. 4853. Society of Photo-Optical Instrumentation Engineers (SPIE) Conference Series, pp. 370–380.

Scharmer, G. B. et al. (2008). "CRISP Spectropolarimetric Imaging of Penumbral Fine Structure". In: *ApJ* 689, pp. L69–L72. DOI: 10.1086/595744.

Schunker, H. and A.-C. Donea (2003). "Variations of the magnetic fields in large solar flares". In: *Space Sci. Rev.* 107, pp. 99–102. DOI: 10.1023/A:1025559319434.

Severny, A. (1964). "Solar Magnetic Fields". In: *Space Sci. Rev.* 3, pp. 451–486. DOI: 10.1007/BF00214468.

Sharykin, I. N., A. G. Kosovichev, and I. V. Zimovets (2015). "Energy Release and Initiation of a Sunquake in a C-class Flare". In: *ApJ* 807, 102, p. 102. DOI: 10.1088/0004-637X/807/1/102. arXiv: 1405.5912 [astro-ph.SR].

Shmeleva, O. P. and S. I. Syrovatskii (1973). "Distribution of Temperature and Emission Measure in a Steadily Heated Solar Atmosphere". In: *Sol. Phys.* 33, pp. 341–362. DOI: 10.1007/BF00152423.

Simões, P. J. A. et al. (2016). "Observations and Modelling of Helium Lines in Solar Flares". In: *Coimbra Solar Physics Meeting: Ground-based Solar Observations in the Space Instrumentation Era*. Ed. by I. Dorotovic, C. E. Fischer, and M. Temmer. Vol. 504. Astronomical Society of the Pacific Conference Series, p. 197. arXiv: 1512.03477 [astro-ph.SR].

Siversky, T. V. and V. V. Zharkova (2009). "Particle acceleration in a reconnecting current sheet: PIC simulation". In: *Journal of Plasma Physics* 1, p. xx. DOI: 10.1017/S0022377809008009.

Smith, D. F. and L. H. Auer (1980). "Thermal models for solar hard X-ray bursts". In: *ApJ* 238, pp. 1126–1133. DOI: 10.1086/158078.

Smith, D. M. et al. (2011). "Solar Hard X-ray Observations with NuSTAR". In: *AAS/High Energy Astrophysics Division*. Vol. 12. AAS/High Energy Astrophysics Division, p. 43.09.

Solov'ev, A. A., E. A. Kirichek, and V. V. Ganiev (2013). "Unique solar flare of September 22, 2011: The suction effect". In: *Geomagnetism and Aeronomy* 53, pp. 981–984. DOI: 10.1134/S0016793213080240.

Somov, B. V., ed. (2000). *Cosmic Plasma Physics*. Vol. 251. Astrophysics and Space Science Library.

Somov, B. V., B. J. Sermulina, and A. R. Spektor (1982). "Hydrodynamic response of the solar chromosphere to an elementary flare burst. II - Thermal model". In: *Sol. Phys.* 81, pp. 281–292. DOI: 10.1007/BF00151302.

Somov, B. V., A. R. Spektor, and S. I. Syrovatskii (1981). "Hydrodynamic response of the solar chromosphere to an elementary flare burst. I - Heating by accelerated electrons". In: *Sol. Phys.* 73, pp. 145–155. DOI: 10.1007/BF00153151.

Somov, B. V. et al. (1999). "Three-dimensional Reconnection in the Solar Corona Related to Yohkoh Observations". In: *Magnetic Fields and Solar Processes*. Ed. by A. Wilson and et al. Vol. 448. ESA Special Publication, p. 883.

Song, Y. L. and M. Zhang (2016). "On the Relationship Between Sunspot Structure and Magnetic Field Changes Associated with Solar Flares". In: *ApJ* 826, 173, p. 173. DOI: 10.3847/0004-637X/826/2/173. arXiv: 1605.01163 [astro-ph.SR].

Spirock, T. J., V. B. Yurchyshyn, and H. Wang (2002). "Rapid Changes in the Longitudinal Magnetic Field Related to the 2001 April 2 X20 Flare". In: *ApJ* 572, pp. 1072–1076. DOI: 10.1086/340431.

Sturrock, P. A. (1968). "A Model of Solar Flares". In: *Structure and Development of Solar Active Regions*. Ed. by K. O. Kiepenheuer. Vol. 35. IAU Symposium, p. 471.

— (1972). "Magnetic Models of Solar Flares". In: *Progress in Astronautics and Aeronautics* 30, p. 163.

Sudol, J. J. and J. W. Harvey (2004). "Changes in the Longitudinal Magnetic Field during Solar Flares". In: *SOHO 14 Helio- and Asteroseismology: Towards a Golden Future*. Ed. by D. Danesy. Vol. 559. ESA Special Publication, p. 643.

Sudol, J. J. and J. W. Harvey (2005). "Longitudinal Magnetic Field Changes Accompanying Solar Flares". In: *ApJ* 635, pp. 647–658. DOI: 10.1086/497361.

Sui, L., G. D. Holman, and B. R. Dennis (2007). "Nonthermal X-Ray Spectral Flattening toward Low Energies in Early Impulsive Flares". In: *ApJ* 670, pp. 862–871. DOI: 10.1086/522198.

Svestka, Z. (1986). "On the varieties of solar flares". In: *The lower atmosphere of solar flares; Proceedings of the Solar Maximum Mission Symposium, Sunspot, NM, Aug. 20-24, 1985 (A87-26201 10-92). Sunspot, NM, National Solar Observatory, 1986, p. 332-355.* Ed. by D. F. Neidig, pp. 332–355.

Sweet, P. A. (1958). "The Neutral Point Theory of Solar Flares". In: *Electromagnetic Phenomena in Cosmical Physics*. Ed. by B. Lehnert. Vol. 6. IAU Symposium, p. 123.

Sylwester, B. and J. Sylwester (1999). "Flaring Structures Observed in Deconvolved SXT Images". In: *Acta Astron.* 49, pp. 85–102.

— (2000). "Evolution of White-Light Flares Observed by YOHKOH". In: *Sol. Phys.* 194, pp. 305–325. DOI: 10.1023/A:1005255532540.

Syrovatskii, S. I. (1963). "The Stability of Plasma in a Nonuniform Magnetic Field and the Mechanism of Solar Flares". In: *Soviet Ast.* 6, p. 768.

— (1969). "On the mechanism of solar flares". In: *Solar Flares and Space Research*. Ed. by C. de Jager and Z. Svestka, p. 346.

Syrovatskii, S. I. and O. P. Shmeleva (1972). "Heating of Plasma by High-Energy Electrons, and Nonthermal X-Ray Emission in Solar Flares". In: *Soviet Astronomy* 16, pp. 273–+.

Takakura, T. (1971). "Acceleration of Electrons and Solar Flares Due to Quasi-Static Electric Field". In: *Sol. Phys.* 19, pp. 186–201. DOI: 10.1007/BF00148833.

Teske, R. G. (1967). "Observations of Solar Soft X Rays from OSO-llI: First Results." In: *AJ* 72, p. 832. DOI: 10.1086/110520.

Tomczak, M. and T. Ciborski (2007). "Footpoint versus loop-top hard X-ray emission sources in solar flares". In: *A&A* 461, pp. 315–323. DOI: 10.1051/0004-6361:20066115. eprint: astro-ph/0610409.

Tritschler, A. et al. (2015). "DKIST: Observing the Sun at High Resolution". In: *18th Cambridge Workshop on Cool Stars, Stellar Systems, and the Sun*. Ed. by G. T. van

Belle and H. C. Harris. Vol. 18. Cambridge Workshop on Cool Stars, Stellar Systems, and the Sun, pp. 933–944.

Uchida, Y. and H. Hudson (1972). "Search for Weak White-Light Flares by Time-Wise Photographic Cancellation". In: *Sol. Phys.* 26, pp. 414–417. DOI: 10.1007/BF00165283.

Švestka, Z., M. Kopecký, and M. Blaha (1961). "Qualitative discussion of 244 flare spectra". In: *Bulletin of the Astronomical Institutes of Czechoslovakia* 12, p. 229.

— (1962). "Qualitative discussion of 244 flare spectra. II. Line asymmetry and helium lines". In: *Bulletin of the Astronomical Institutes of Czechoslovakia* 13, p. 37.

van Allen, J. A. (1967). "Soft X-Ray (λ <14) Emission by the Sun Since 1 July 1966." In: *AJ* 72, p. 833. DOI: 10.1086/110468.

van Beek, H. F., L. D. de Feiter, and C. de Jager (1974). "Time profiles and photon spectra of solar hard X-rays". In: *Correlated Interplanetary and Magnetospheric Observations*. Ed. by D. E. Page. Vol. 42. Astrophysics and Space Science Library, pp. 533–543. DOI: 10.1007/978-94-010-2172-2_34.

van Noort, M., L. Rouppe van der Voort, and M. G. Löfdahl (2005). "Solar Image Restoration By Use Of Multi-frame Blind De-convolution With Multiple Objects And Phase Diversity". In: *Sol. Phys.* 228, pp. 191–215. DOI: 10.1007/s11207-005-5782-z.

Varady, M. et al. (2010). "Modeling of Solar Flare Plasma and Its Radiation". In: *IEEE Transactions on Plasma Science* 38, pp. 2249–2253. DOI: 10.1109/TPS.2010.2057449.

Vernazza, J. E., E. H. Avrett, and R. Loeser (1981). "Structure of the solar chromosphere. III - Models of the EUV brightness components of the quiet-sun". In: *ApJS* 45, pp. 635–725. DOI: 10.1086/190731.

Vilmer, N., A. L. MacKinnon, and G. J. Hurford (2011). "Properties of Energetic Ions in the Solar Atmosphere from γ-Ray and Neutron Observations". In: *Space Sci. Rev.* 159, pp. 167–224. DOI: 10.1007/s11214-010-9728-x. arXiv: 1110.2432 [astro-ph.SR].

Vorpahl, J. and H. Zirin (1970). "Identification of the hard X-ray pulse in the flare of September 11 12, 1968". In: *Sol. Phys.* 11, pp. 285–290. DOI: 10.1007/BF00155227.

Vorpahl, J. A. (1972). "X-Radiation (E> 10 keV), Hα and Microwave Emission During the Impulsive Phase of Solar Flares". In: *Sol. Phys.* 26, pp. 397–413. DOI: 10.1007/BF00165282.

Wang, H. (2006). "Rapid Changes of Photospheric Magnetic Fields around Flaring Magnetic Neutral Lines". In: *ApJ* 649, pp. 490–497. DOI: 10.1086/506320.

Wang, H. and C. Liu (2012). "Circular Ribbon Flares and Homologous Jets". In: *ApJ* 760, 101, p. 101. DOI: 10.1088/0004-637X/760/2/101. arXiv: 1207.7345 [astro-ph.SR].

Wang, H. et al. (2002). "Rapid Changes of Magnetic Fields Associated with Six X-Class Flares". In: *ApJ* 576, pp. 497–504. DOI: 10.1086/341735.

Wang, H. et al. (2004a). "Evidence of Rapid Flux Emergence Associated with the M8.7 Flare on 2002 July 26". In: *ApJ* 605, pp. 931–937. DOI: 10.1086/382527.

Wang, H. et al. (2004b). "Rapid Penumbral Decay following Three X-Class Solar Flares". In: *ApJ* 601, pp. L195–L198. DOI: 10.1086/382188.

Warwick, J. W. and H. Zirin (1957). "Rocket Observation of X-Ray Emission in a Solar Flare". In: *Nature* 180, pp. 500–501. DOI: 10.1038/180500b0.

Watanabe, K. et al. (2010). "G-band and Hard X-ray Emissions of the 2006 December 14 Flare Observed by Hinode/SOT and Rhessi". In: *ApJ* 715, pp. 651–655. DOI: 10.1088/0004-637X/715/1/651. arXiv: 1004.4259 [astro-ph.SR].

Winckler, J. R. (1964). "Energetic X-Ray Bursts From Solar Flares". In: *NASA Special Publication* 50, p. 117.

Wood Jr., A. T. and R. W. Noyes (1972). "Solar Flares in the Extreme Ultraviolet. II. Comparisons with Other Observations". In: *Sol. Phys.* 24, pp. 180–196. DOI: 10.1007/BF00231095.

Wood Jr., A. T. et al. (1972). "Solar Flares in the Extreme Ultraviolet. I. The Observations". In: *Sol. Phys.* 24, pp. 169–179. DOI: 10.1007/BF00231094.

Woods, T. N. et al. (2012). "Extreme Ultraviolet Variability Experiment (EVE) on the Solar Dynamics Observatory (SDO): Overview of Science Objectives, Instrument Design, Data Products, and Model Developments". In: *Sol. Phys.* 275, pp. 115–143. DOI: 10.1007/s11207-009-9487-6.

Wuelser, J.-P. and H. Marti (1989). "High time resolution observations of H alpha line profiles during the impulsive phase of a solar flare". In: *ApJ* 341, pp. 1088–1096. DOI: 10.1086/167567.

Wuelser, J.-P. et al. (1994). "Multispectral observations of chromospheric evaporation in the 1991 November 15 X-class solar flare". In: *ApJ* 424, pp. 459–465. DOI: 10.1086/173903.

Yurchyshyn, V. et al. (2004). "Magnetic Field, Hα, and RHESSI Observations of the 2002 July 23 Gamma-Ray Flare". In: *ApJ* 605, pp. 546–553. DOI: 10.1086/382142.

Zarro, D. M. et al. (1988). "Explosive plasma flows in a solar flare". In: *ApJ* 324, pp. 582–589. DOI: 10.1086/165919.

Zhang, Q. M., D. Li, and Z. J. Ning (2016). "Chromospheric Condensation and Quasi-periodic Pulsations in a Circular-ribbon Flare". In: *ApJ* 832, 65, p. 65. DOI: 10.3847/0004-637X/832/1/65. arXiv: 1609.03165 [astro-ph.SR].

Zharkov, S. et al. (2011). "2011 February 15: Sunquakes Produced by Flux Rope Eruption". In: *ApJ* 741, L35, p. L35. DOI: 10.1088/2041-8205/741/2/L35.

Zharkova, V. and S. Zharkov (2015). "On the Generation of Hydrodynamic Shocks by Mixed Beams and Occurrence of Sunquakes in Flares". In: *Sol. Phys.* 290, pp. 3163–3188. DOI: 10.1007/s11207-015-0813-x.

Zharkova, V. V. (1984). "An investigation of second-level excitation and ionization of hydrogen in filamentary prominences". In: *Astrometriia i Astrofizika* 53, pp. 22–30.

— (2008). "The Mechanisms of Particle Kinetics and Dynamics Leading to Seismic Emission and Sunquakes". In: *Sol. Phys.* 251, pp. 641–663. DOI: 10.1007/s11207-008-9216-6.

Zharkova, V. V. and O. V. Agapitov (2009). "The effect of magnetic topology on particle acceleration in a three-dimensional reconnecting current sheet: a test-particle approach". In: *Journal of Plasma Physics* 75, pp. 159–+. DOI: 10.1017/S002237780800771X.

Zharkova, V. V., J. C. Brown, and D. V. Syniavskii (1995). "Electron beam dynamics and hard X-ray bremsstrahlung polarization in a flaring loop with return current and converging magnetic field." In: *A&A* 304, pp. 284–+.

Zharkova, V. V. and R. R. Dobranskis (2016). "Updated analytical solutions of continuity equation for electron beams precipitation - II. Mixed energy losses". In: *MNRAS* 458, pp. 3720–3730. DOI: 10.1093/mnras/stw500.

Zharkova, V. V. and M. Gordovskyy (2004). "Particle Acceleration Asymmetry in a Reconnecting Nonneutral Current Sheet". In: *ApJ* 604, pp. 884–891. DOI: 10.1086/381966.

— (2005a). "Energy spectra of particles accelerated in a reconnecting current sheet with the guiding magnetic field". In: *Monthly Notices of the Royal Astronomical Society* 356, pp. 1107–1116. DOI: 10.1111/j.1365-2966.2004.08532.x.

— (2005b). "The kinetic effects of electron beam precipitation and resulting hard X-ray intensity in solar flares". In: *A&A* 432, pp. 1033–1047. DOI: 10.1051/0004-6361:20041102.

— (2006). "The Effect of the Electric Field Induced by Precipitating Electron Beams on Hard X-Ray Photon and Mean Electron Spectra". In: *ApJ* 651, pp. 553–565. DOI: 10.1086/506423.

Zharkova, V. V. and L. K. Kashapova (2005). "The viewing angle effect on Hα-line impact polarisation in impulsive solar events". In: *A&A* 431, pp. 1075–1081. DOI: 10.1051/0004-6361:20041651.

Zharkova, V. V. and O. V. Khabarova (2012). "Particle Dynamics in the Reconnecting Heliospheric Current Sheet: Solar Wind Data versus Three-dimensional Particle-in-cell Simulations". In: *ApJ* 752, 35, p. 35. DOI: 10.1088/0004-637X/752/1/35.

Zharkova, V. V. and V. A. Kobylinskii (1989a). "Investigation of Nonthermal Excitation and Ionization of Hydrogen in Low-Temperature Flare Plasma - Part One - Rates of Excitation and Ionization of a Hydrogen Atom by an Electron Beam". In: *Soviet Astronomy Letters* 15, p. 366.

— (1989b). "Investigation of Nonthermal Excitation and Ionization of Hydrogen in Low-Temperature Flare Plasma - Part One - Rates of Excitation and Ionization of a Hydrogen Atom by an Electron Beam". In: *Soviet Astronomy Letters* 15, p. 366.

— (1991). "Investigation of Nonthermal Excitation and Ionization of Hydrogen in Low-Temperature Flare Plasma - Part Two - Computational Method". In: *Soviet Astronomy Letters* 17, pp. 34–+.

— (1993). "The effect of non-thermal excitation and ionization on the hydrogen emission in impulsive solar flares". In: *Sol. Phys.* 143, pp. 259–274. DOI: 10.1007/BF00646487.

Zharkova, V. V. and A. G. Kosovichev (2002). "Fast magnetic field variations associated with solar flares". In: *From Solar Min to Max: Half a Solar Cycle with SOHO*. Ed. by A. Wilson. Vol. 508. ESA Special Publication, pp. 159–162.

Zharkova, V. V., A. A. Kuznetsov, and T. V. Siversky (2010). "Diagnostics of energetic electrons with anisotropic distributions in solar flares. I. Hard X-rays bremsstrahlung emission". In: *A&A* 512, A8, A8. DOI: 10.1051/0004-6361/200811486.

Zharkova, V. V. and T. Siversky (2011). "Formation of electron clouds during particle acceleration in a 3D current sheet". In: *Advances in Plasma Astrophysics*. Ed. by A. Bonanno, E. de Gouveia Dal Pino, and A. G. Kosovichev. Vol. 274. IAU Symposium, pp. 453–457. DOI: 10.1017/S1743921311007472.

Zharkova, V. V. and S. I. Zharkov (2007). "On the Origin of Three Seismic Sources in the Proton-rich Flare of 2003 October 28". In: *ApJ* 664, pp. 573–585. DOI: 10.1086/518731.

Zharkova, V. V. et al. (2005). "Toward magnetic field dissipation during the 23 July 2002 solar flare measured with Solar and Heliospheric Observatory/Michelson Doppler Imager (SOHO/MDI) and Reuven Ramaty High Energy Solar Spectroscopic Imager (RHESSI)". In: *Journal of Geophysical Research (Space Physics)* 110.9, pp. 8104–+. DOI: 10.1029/2004JA010934.

Zharkova, V. V. et al. (2011a). "Recent Advances in Understanding Particle Acceleration Processes in Solar Flares". In: *Space Sci. Rev.* 159, pp. 357–420. DOI: 10.1007/s11214-011-9803-y. arXiv: 1110.2359 [astro-ph.SR].

Zharkova, V. V. et al. (2011b). "The effect of energetic particle beams on the chromospheric emission of the 2004 July 25 flare". In: *MNRAS* 411, pp. 1562–1574. DOI: 10.1111/j.1365-2966.2010.17792.x.

Zharkova, Valentina (2012). *Electron and proton kinematics and dynamics in flaring atmospheres*. Wiley-vch.

Zirin, H. (1978). "The L-alpha/H-alpha ratio in solar flares, quasars, and the chromosphere". In: *ApJ* 222, pp. L105–L107. DOI: 10.1086/182702.

Zirin, H. and D. R. Lackner (1969). "The Solar Flares of August 28 and 30, 1966". In: *Sol. Phys.* 6, pp. 86–103. DOI: 10.1007/BF00146799.

Zirin, H., G. Pruss, and J. Vorpahl (1971). "Magnetic Fields, Bremsstrahlung and Synchrotron Emission in the Flare of 24 October 1969". In: *Sol. Phys.* 19, pp. 463–471. DOI: 10.1007/BF00146073.

Zirin, H. and K. Tanaka (1973). "The Flares of August". In: *Bulletin of the American Astronomical Society*. Vol. 5. BAAS, p. 282.

— (1981). "Magnetic transients in flares". In: *ApJ* 250, pp. 791–795. DOI: 10.1086/159429.

Zirin, H. et al. (1969). "De-Occultation X-Ray Events of 2 December, 1967". In: *Sol. Phys.* 9, pp. 269–277. DOI: 10.1007/BF02391648.